DISSERTATION

AUTOMATED EVENT DETECTORS UTILIZED FOR CONTINENTAL INTRAPLATE EARTHQUAKES: APPLICATIONS TO TECTONIC, INDUCED, AND MAGMATIC SEQUENCES

Submitted by

Nicole D. McMahon

Department of Geosciences

In partial fulfillment of the requirements

For the Degree of Doctor of Philosophy

Colorado State University

Fort Collins, Colorado

Fall 2018

Doctoral Committee:

Advisor: Richard C. Aster

Derek L. Schutt
Margaret Cheney
Harley M. Benz

ABSTRACT

AUTOMATED EVENT DETECTORS UTILIZED FOR CONTINENTAL INTRAPLATE EARTHQUAKES: APPLICATIONS TO TECTONIC, INDUCED, AND MAGMATIC SEQUENCES

Event detection is a crucial part of the data-driven science of seismology. With decades of continuous seismic data recorded across thousands of networks and tens of thousands of stations, and an ever-accelerating rate of data acquisition, automated methods of event detection, as opposed to manual/visual inspection, allow scientists to rapidly sift through enormous data sets extracting event information from background noise for further analysis. Automation naturally increases the numbers of detected events and lowers the minimum magnitude of detectable events. Increasing numbers and decreasing magnitudes of detected events, particularly with respect to earthquakes, enables the construction of more complete event catalogs and more detailed analysis of spatiotemporal trends in earthquake sequences. These more complete catalogs allow for enhanced knowledge of Earth structure, earthquake processes, and have potential for informing hazard mitigation.

This study utilizes automated event detection techniques, namely matched filter and subspace detection, and applies them to three different types of continental intraplate earthquake sequences: a tectonic aftershock sequences in Montana, an induced aftershock sequence in Oklahoma, and a magmatic swarm sequence in Antarctica.

In Montana, the combination of matched filtering and multiple-event relocation techniques provided a more complete picture of the spatiotemporal evolution of the aftershock sequence of the large intraplate earthquake that occurred near Lincoln, Montana in 2017. The study reveals movement along an unmapped fault that is antithetical to the main fault system trend in the region and demonstrates the hazards associated with a highly faulted and seismically active region encompassing complex and hidden structures.

In Oklahoma, subspace detection methodology is used in combination with multiple-event relocation techniques to reveal movement along three different faults associated with the 2011 Prague, Oklahoma induced earthquake sequence. The study identifies earthquakes located in both the sedimentary zone of wastewater injection as well as the underlying crystalline basement indicating that faults traverse the unconformity. Injecting fluid into the overlying sediment can easily penetrate to the basement where larger earthquakes nucleate.

In Antarctica, subspace detection is again used in a very remote intraplate region with sparse station coverage to detail the sustained and ongoing magmatic deep, long-period earthquake swarm occurring beneath the West Antarctic Ice Sheet and Executive Committee Range in Marie Byrd Land, Antarctica. These earthquakes indicate the present-day location of magmatic activity, which appears appear to have increased in intensity over the last few years.

This dissertation contributes to the growing bodies of literature around three distinctly interesting types of seismicity that are not associated to the first order with plate tectonic boundaries. Large tectonic intraplate earthquakes are relatively uncommon. Induced seismicity has only drastically increased in the central US during the last decade and created new insights into this process. Deep, long-period, magmatic earthquakes are still a poorly understood type of seismicity in volcanic settings.

ACKNOWLEDGEMENTS

There are several people and entities in my life to whom I owe an abundance of gratitude for motivation on this long, arduous journey.

First, and foremost, I have to thank my family – Mom, Dad, Allyson, and Derek – who have provided me endless encouragement and support throughout this seemingly never-ending saga. Innumerable commuting phone calls, butt-dials, group messages, Christmases, Fourth of Julys, and the constant battle over who the favorite child is always reminded me of what is really important and provided me the strength to continue and reach for a life beyond professional studenthood. I also have to thank my extended family cheering me on from afar (Hey, Aunt Gale!).

My advisor, Rick, who took a chance on me and stuck it out across two universities in two states. You have been a wealth of knowledge, connections, and opportunities and I'm immensely thankful I had the chance to meet you as a PASSCAL intern and continue my graduate education with you.

Salty Em, my ride-or-die and BFF soulmate. You have been my source of inspiration to greater studenthood, my confidante, my fellow Halloween enthusiast, my daily gchat companion, my sanity check, and my ever-welcome reminder that there is life beyond science.

Folahan, for reminding me that there is a fascinating and complex world beyond graduate school and my tiny research bubble. Thank you for being unabashedly you, questioning everything, and providing an endless fount of extracurricular reading material and intellectual discourse. I'm sure The Atlantic also thanks you.

The Garfields, Gulbrandsons, Allens, and Rachids of Fort Collins and Loveland. Thank you for making my time here in The Choice City truly special. A special thank you to Colin for being a source of light in the darkest times as well as my anachronistic, snazzy-dressing, cinephilic, foodie companion.

The faculty, staff, and students of the Earth and Environmental Science Department at New Mexico Tech where this journey began and the Geosciences Department at Colorado State University where it ended as well as the wider universities and towns of Socorro and Fort Collins.

The U.S. Geological Survey and the National Earthquake Information Center in Golden, CO for supporting me as an intern and allowing me access to the world of earthquake science in action. A special thank you to Will Yeck for being an invaluable and instrumental resource to my research and Dan McNamara for allowing me to participate in exciting publications.

And last, but certainly not least, Harley – my supervisor, mentor, and friend. Your constant guidance, support, and encouragement have molded me into a better scientist and helped push

me across the finish line. I will be eternally grateful for the time we worked together, even the times I was forgotten ☺.

DEDICATION

For

The McMahon Clan

TABLE OF CONTENTS

LIST OF TABLES

APPENDIX 4: Hundreds of Earthquakes per Day: The 2014 Guthrie, Oklahoma, Earthquake Sequence

LIST OF FIGURES

CHAPTER 1: Introduction

CHAPTER 2: Spatiotemporal Analysis of the Foreshock-Mainshock-Aftershock Sequence of the 6 July 2017 $\mathbf{M}_W$ 5.8 Lincoln, Montana, Earthquake

CHAPTER 3: Spatiotemporal Evolution of the 2011 Prague, Oklahoma, Aftershock Sequence Revealed Using Subspace Detection and Relocation

CHAPTER 4: Deep, Long-Period Seismicity Beneath the Executive Committee Range, Marie Byrd Land, Antarctica, Studied Using Subspace Detection

APPENDIX 2: Supplementary Information for Chapter 3 – Lincoln, Montana

APPENDIX 3: Supplementary Information for Chapter 4 – Marie Byrd Land, Antarctica

APPENDIX 4: Hundreds of Earthquakes per Day: The 2014 Guthrie, Oklahoma, Earthquake Sequence

LIST OF DATA SETS

APPENDIX 1: Supplementary Information for Chapter 2 – Lincoln, Montana

APPENDIX 2: Supplementary Information for Chapter 3 – Prague, Oklahoma

APPENDIX 4: Hundreds of Earthquakes per Day: The 2014 Guthrie, Oklahoma, Earthquake Sequence

LIST OF ANIMATIONS

APPENDIX 2: Supplementary Information for Chapter 3 – Prague, Oklahoma

LIST OF ACRONYMS, ABBREVIATIONS, AND VARIABLES

ACRONYMS

API	American Petroleum Institute
CEUS	Central and Eastern United States
DLP	Deep, Long-Period (earthquakes)
ECR	Executive Committee Range
FMD	Frequency-Magnitude Distribution (Gutenberg-Richter law)
HF	High-Frequency (earthquakes)
IRIS	Incorporated Research Institutions for Seismology
ISB	Intermountain Seismic Belt
LCL	Lewis and Clark Line
LF	Low-Frequency (earthquakes)
LP	Long-Period (earthquakes)
MBL	Marie Byrd Land
MBMG	Montana Bureau of Mines and Geology
MMI	Modified Mercalli Intensity
NEIC	National Earthquake Information Center
NSHM	National Seismic Hazard Map
OCC	Oklahoma Corporation Commission
OERB	Oklahoma Energy Resources Board
OGS	Oklahoma Geological Survey
PDF	Probability Density Function
RAMP	Rapid Array Mobilization Program
RMA	Rocky Mountain Arsenal
RMT	Regional Moment Tensor
SNR	Signal-to-Noise Ratio
STA/LTA	Short-Term Average / Long-Term Average
ULP	Ultra-Long-Period (earthquakes)
USGS	United States Geological Survey
VEI	Volcanic Explosivity Index
VLP	Very-Long-Period (earthquakes)
VT	Volcano-Tectonic (earthquakes)
WFZ	Wilzetta Fault Zone

ABBREVIATIONS

ComCat	USGS Comprehensive Catalog of Earthquakes (https://earthquake.usgs.gov/data/comcat/)
HiQuake	The Human-Induced Earthquake Database (https://inducedearthquakes.org)
M	Magnitude (generally)
$\mathbf{M_b}$	Body-wave magnitude
$\mathbf{M_d}$	Duration magnitude
$\mathbf{M_L}$	Local magnitude
$\mathbf{M_{rel}}$	Relative magnitude
$\mathbf{M_S}$	Surface-wave magnitude
$\mathbf{M_W}$	Moment magnitude
MOHO	Mohorovičić discontinuity
POLENET/ANET	Antarctic Network component of the Polar Earth Observing Network (POLENET/ANET)

VARIABLES

b-value	Slope of the frequency-magnitude distribution; Describes relative quantity of small to large earthquakes
c-value	Time delay before the onset of the Omori (power) law (related to the modified Omori decay law
M_C	Minimum magnitude of completeness (related to frequency magnitude distribution)
p-value	Aftershock decay rate (related to modified Omori decay law) in Chapters 2-4; probability value for hypothesis testing in Appendix 2

CHAPTER 1

INTRODUCTION

This introductory chapter provides an overview of automated seismic event detection as well as information about the earthquakes and continental intraplate settings to which these detectors were applied and which will be discussed in subsequent chapters. Section 1.1 provides an overview of automated event detection and its importance and contributions to the earthquake seismology community. This section also details two end-member types of event detectors, energy detectors and correlation detectors. Section 1.2 provides a general overview of continental intraplate earthquakes. Section 1.3 provides an overview of tectonic intraplate seismicity and how the Intermountain Seismic Belt contributes to Montana's status as one of the most seismically active states in the contiguous United States. This section also introduces the 2017 Lincoln, Montana, earthquake sequence that is the subject of Chapter 2. Section 1.4 provides an overview of induced seismicity and how it has affected the central and eastern United States, particularly Oklahoma. This section also introduces the 2011 Prague, Oklahoma, earthquake sequence that is the subject of Chapter 3. Section 1.5 provides an overview of volcanic/magmatic seismicity and deep, long-period earthquakes. This section also introduces the subglacial magmatic earthquake sequence that is presently occurring beneath the Executive Committee Range region of Marie Byrd Land, Antarctica that is the subject of Chapter 4. Section 1.6 provides an overview of additional studies to which contributions were by me made during this journey.

1.1 AUTOMATED EVENT DETECTORS

Event detection is a crucial part of the data-driven science of seismology. Seismometers record ground motion from many different types of seismic events, some more exotic than others, including earthquakes, volcanic eruptions, chemical/nuclear explosions, landslides/avalanches/debris flows, tremor, mine/tunnel collapses, cryoseisms or ice/frost quakes, footquakes or celebrations related to exciting plays during sporting events, passing trains, rock concerts, fireworks, bolide explosions, glacier outburst floods, sonic booms, thunder and lightning, and many more.

With decades of continuous seismic data recorded across thousands of networks and tens of thousands of stations, more ubiquitous archival and access via internet channels, and an overall ever-accelerating rate of data acquisition and re-use, automated methods of event detection, as opposed to manual/visual inspection, are increasingly important to allow scientists to rapidly sift through enormous data sets extracting event information from background noise for further analysis. Automation naturally increases the numbers of detected events and lowers the minimum magnitude of detectable events, often to very low levels (i.e., magnitudes smaller than zero).

Increasing numbers and decreasing magnitudes of detected events, particularly with respect to earthquakes, enables the construction of more complete event catalogs and more detailed analysis of spatiotemporal trends in earthquake sequences. These more complete catalogs allow for enhanced knowledge of Earth structure, earthquake processes, and have potential for informing hazard mitigation. Some areas in which automated detection capabilities provide valuable insight include:

- Visualization of subsurface features such as faults [e.g., *Horton et al.*, 2015] and volcanic systems [e.g., *Hansen and Schmandt*, 2015]
- Understanding spatiotemporal trends including aftershock rate decay [e.g., *Peng et al.*, 2006] and seismicity migration patterns [e.g., *Peng and Zhao*, 2009]
- Monitoring oil and gas operations [e.g., *Yoon et al.*, 2017]
- Monitoring remote volcanoes [e.g., *Sparks et al.*, 2012]
- Operational earthquake forecasting [e.g., *Benz et al.*, 2015]
- Microseismic monitoring of mines for rockburst [*Ge*, 2005]
- Geothermal stimulation and energy extraction [e.g., *Rowe et al.*, 2002]

Automated event detectors span the range from energy detectors, in which a transient increase in waveform energy/power is detected and no information about an event's waveform is necessarily known, to correlation detectors, in which event detections are based upon waveform similarity to a known event. These types of event detectors are used to build initial catalogs of events as well as enhance existing catalogs. Details about the advantages and drawbacks of these detectors are found below with a summary in Table 1.1.

ENERGY DETECTORS

Energy detectors function by detecting transient increases of energy/power in continuous seismic data. These detectors are broadly applicable because they require little information about the events to be detected, and can therefore be used to explore seismic data for event signals without *a priori* knowledge. Common energy detector techniques include:

- STA/LTA – Short-term average / Long-term average: STA/LTA detectors compute the ratio of the STA energy in a short time window to the LTA energy in a longer-time window as the windows slide though continuous data. Upon encountering a transient seismic event, the STA energy will increase raising the STA/LTA ratio. A detection is declared when the ratio exceeds a predetermined threshold. While this detector is widely applicable, it does not perform well with low signal-to-noise data, emergent onsets, or overlapping signals [e.g., *Vanderkulk et al*, 1965; *Allen*, 1982].

- Kurtosis: Kurtosis detectors and phase arrival pickers are based on higher-order statistical characteristic functions, namely skewness and kurtosis. Generally, such detectors use sliding windows to automatically identify the transition from Gaussian to non-Gaussian behavior that coincides with the onset of a seismic event [e.g., *Saragiotis et al.*, 2002; *Baillard et al.*, 2014]. Kurtosis improves upon standard STA/LTA practices by enhancing the detection of emergent onsets. This methodology is utilized to pick *S*-phase arrival times in Chapter 3.

- Local Similarity: Local similarity quantifies the signal consistency on an examined station with respect to its nearest neighbors rather than considering each station individually or considering all stations together. This methodology is useful for monitoring ultra-weak microseismicity, identifying both emergent and impulsive onsets, and detecting unusual seismic events in noisy environments [*Li et al.*, 2018].

Energy detectors are broadly applicable and useful in situations where preexisting event templates may not exist, or where a wide variety of events need to be detected. STA/LTA detectors tend to be more insensitive to emergent signal onsets, but Kurtosis and Local Similarity detectors improve upon this issue. However, energy detectors are indiscriminant, picking up all varieties of transient seismic signals (e.g., mine blasts, cultural activities, local earthquakes, teleseisms, or telemetry artifacts) leading to potentially high false alarm rates. Further processing is typically needed to distinguish different types of events.

CORRELATION DETECTORS

As an alternative to energy detectors, correlation detectors correlate previously identified events with continuous seismic data to detect additional events that have high waveform similarity. These detectors take advantage of the fact that nearby seismic events may have similar source mechanisms and ray paths, and thus similar waveforms. Common correlation detector techniques include:

- Matched Filter or Template Matching: Matched filters are a tool used widely in signal processing including many areas outside of seismology (e.g., electrical engineering, communications, astronomy, and image processing). The basic principle is that matched filter is performed by correlating a known signal, or template, with an unknown signal to detect the presence of the template within the unknown signal. In seismology, the finite waveform of a known event is correlated against continuous seismic data to detect additional events with similar waveform appearance [e.g., *Van Trees*, 1968]. This methodology is utilized in Chapter 3.

- Subspace Detection: Whereas the matched filter technique uses a single known event as a template, subspace detection utilizes multiple known events and effects a simultaneous correlation to detect additional events. These detectors invoke a model that represents the signals to be detected as a linear combination of orthogonal basis waveforms formed by the singular value decomposition of a set of known template events [*Harris*, 2006]. The number of orthogonal basis waveforms needed to adequately describe the seismograms from an earthquake sequence (known as the rank of the utilized subspace) is a function of the variability of the observed waveforms, which is related to variations in the source time history, source mechanism, and spatial distribution of the events [*Benz et al.*, 2015]. Typically, the rank of the subspace is much lower than the number of previously identified events in an event catalog making it more computationally efficient than implementing the matched filter technique using all templates. Subspace detectors can excel at identifying smaller events, particularly in low signal-to-noise environments. This methodology is utilized in Chapters 3 and 4 as well as Appendix 4.

- FAST - Fingerprint and Similarity Thresholding: FAST is a computationally efficient similarity search that adapts a data mining algorithm to detect additional events. It first creates compact "fingerprints" of waveforms by extracting key discriminative features, then groups similar fingerprints together within a database to facilitate fast, scalable search for similar fingerprint pairs, and finally generates a list of earthquake detections. This methodology ranks high in detection sensitivity, general applicability, and computational efficiency [*Yoon et al.*, 2015]. This is an early example of an emerging generation of detection strategies that leverage data mining and machine learning for seismic event detection an analysis.

Correlation detectors are highly effective for detecting "repeating" earthquakes that produced nearly identical waveforms, and have been used to study a wide range of seismic events including: foreshocks [e.g., *Kato and Nakagawa*, 2014], aftershocks [e.g., *Peng and Zhao*, 2009], triggered earthquakes [e.g., *Meng et al.*, 2013], volcanic swarms [e.g., *Shelly et al.*, 2013], low-frequency earthquakes in tectonic tremor [e.g., *Tang et al.*, 2010], nuclear explosions [e.g., *Bobrov et al.*, 2014], and microseismic earthquake monitoring in geothermal [e.g., *Rowe et al.*, 2002; *Plenkers et al.*, 2013] and oil and gas reservoirs [e.g., *Song et al.*, 2010]. Correlation detectors have proven to be remarkably sensitive for finding known seismic signals in noisy data. However, correlation detectors rely on predetermined templates as inputs, and are not broadly applicable like energy detectors. As such, correlation detectors naturally tend to only detect events that are similar to input templates. This may be useful for event discrimination (e.g., in Oklahoma where many earthquakes are occurring but a researcher may only be interested in a specific sequence), but may fail to detect events that involve changes in event location and character. Subspace detection and FAST were developed to generalize template matching and allow for more detections of non-repeating sources with greater variations in their waveforms.

1.2 CONTINENTAL INTRAPLATE EARTHQUAKES

The vast majority of earthquakes are int*ER*plate events occurring at tectonic plate boundaries or within zones of broad deformation along the plate boundaries (Fig. 1.1). Int*RA*plate earthquakes, on the other hand, are earthquakes occurring within the interior of tectonic plates, far from the boundaries, and constitute ~2% of all recorded earthquakes [*Steeples and Brosius*, 1996] and ~0.3% of the Earth's annual seismic moment release [*Johnston*, 1989]. Although large intraplate earthquakes are relatively rare, the hazard is still significant when they occur near populous areas as magnitudes can exceed 7 with severe to extreme ground shaking reported. Thus, the study of continental intraplate earthquakes has high societal as well as scientific significance. Due to low attenuation values within stable continental interiors, ground shaking from intraplate events typically reaches larger areas compared to similar magnitude interplate earthquakes [e.g., *Nuttli*, 1973; *Hanks and Johnston*, 1992; *Dalton and Ekström*, 2006]. Aftershock sequences for intraplate earthquakes are also significantly longer than their interplate counterparts lasting decades or centuries [*Stein and Liu*, 2009].

Intraplate earthquakes are most commonly caused by the reactivation of pre-existing geologic features in response to the changes in the stress field or, in the case of induced seismicity, to changes in fault strength. Pre-existing geological features, or zones of weakness, include isolated faults, pluton edges, or failed rifts, for example [*Gangopadhyay and Talwani*, 2003]. Reactivation can occur by a localized buildup of stress due to the ambient stress field, the superposition of a triggering stresses, and the reduction of strength of features by mechanical and/or chemical means [*Talwani*, 1989].

Knowledge of intraplate earthquakes is limited and can be difficult to ascertain. Far fewer earthquake occur in intraplate regions owing to the slow deformation rates within plates and there is no direct way to estimate how often they should occur, unlike at plate boundaries where long-term plate motions provide insight into why and how often earthquakes will occur on average. Several techniques and approaches, however, have yielded important new insights into these issues. Geodesy can measure the slow intraplate deformation, constraining the rates at which stresses accumulate. Paleoseismology extends the short and sparse instrumental record backward in time, constraining recurrence history. Numerical deformation modeling makes it possible to test hypotheses for the stresses causing earthquakes and analyze spatiotemporal variations of seismicity [*Stein and Mazzotti*, 2007].

Although the hazard posed by large continental intraplate earthquakes is small compared to large interplate events, it is still significant. Studies of earthquakes in sparsely or unpopulated populated areas, such as rural Montana/Oklahoma and Antarctica, contribute to the growing body of knowledge of the causes, mechanics, and hazards of intraplate events and makes strides towards mitigation of future disasters.

In this dissertation, automated event detection techniques are utilized to examine the spatiotemporal characteristics of three types of continental intraplate earthquakes sequences: 1) a naturally occurring large earthquake and aftershock sequence in Montana; 2) a large injection-induced earthquake and aftershock sequence in Oklahoma; and, 3) a magmatic deep, long-period earthquake swarm sequence in Marie Byrd Land, Antarctica.

1.3 Lincoln, Montana, and Tectonic Intraplate Seismicity

Overview of Tectonic Intraplate Seismicity

This section refers only to tectonic intraplate seismicity, excluding nontectonic earthquakes associated with induced seismicity (e.g., industry-related earthquakes in South Africa, China, and

Oklahoma; discussed in Section 1.2) and intraplate magmatic centers or volcanic seismicity (e.g., Yellowstone National Park, Hawaii, Antarctica; discussed in Section 1.4). *Okal and Sweet* [2007] found that of the 474,203 global earthquakes recorded between 1963 and 2002 with body-wave magnitude ($\mathbf{M_b}$) greater than or equal to 4, only 2737 of the earthquakes were true intraplate tectonic events, constituting 0.6% of the National Earthquake Information Center's database.

Special zones that have experienced historical tectonic intraplate seismicity affect the U.S. Geological Survey (USGS) National Seismic Hazard Maps (NSHM), showing increased probabilities for damaging earthquakes in specific regions. Four prominent zones of historical tectonic intraplate seismicity in the US include (Fig. 1.2):

- New Madrid: What is now known as the New Madrid Seismic Zone was host to the New Madrid earthquakes of 1811-1812. Three very large earthquakes occurred on 16 December 1811 (**M** ~7.5), 23 January 1812 (**M** ~7.3), and 7 February 1812 (**M** ~7.5) kick starting a robust aftershock sequence that included more than 2000 events in the region between 16 December 1811 and 15 March 1812. Sand blows, river bank failures, landslides, and sunken land were reported [*Johnston and Schweig*, 1996]. Although the region was sparsely populated at the time, the town of New Madrid, Missouri was severely damaged by the third shock [*Williams et al.*, 2011].
- Meers fault: The Meers fault of southwestern Oklahoma is part of a fault system that forms the boundary between the Wichita Mountains and the Anadarko Basin, the deepest intracontinental basin in the United States. Youthful deposits on the scarp indicate that

movement may have produced large earthquakes in the geologically recent past and may be capable of producing large earthquakes in the future [*Luza et al.*, 1987; *Cetin*, 2003].

- Charleston, South Carolina: On 31 August 1886, a **M** ~7.3 earthquake occurred in Charleston, South Carolina. Shaking reached a maximum Modified Mercalli Intensity (MMI) X on a scale from I (not felt) to X+ (extreme shaking). The earthquake was felt from Maine to Florida and as far west as the Mississippi River. This is the most powerful and destructive earthquake in recorded history to strike the eastern seaboard. The earthquake nearly leveled Charleston killing ~100 people and damaging ~2000 buildings. Railroad tracks buckled, trains derailed, fissures opened, land liquefied, and sand blows appeared [*Zalzal*, 2017].
- Mineral, Virginia: A more recent example of U.S. tectonic intraplate seismicity is the 23 August 2011 $\mathbf{M}_{W}$ 5.8 Mineral, Virginia, earthquake which was felt by more people than any other earthquake in U.S. history with felt reports from Georgia to Canada. Shaking intensity reached MMI VIII near the epicenter and caused moderately-heavy damage totaling more than $80 million in Louisa County alone. Wide-spread light-to-moderate damage from central Virginia to southern Maryland was reported, including the Washington Monument and the National Cathedral in Washington, D.C. The earthquake occurred within the well-known Central Virginia Seismic Zone, an area of previously identified as having elevated seismic hazard [*McNamara et al.*, 2014].

The NSHM also shows an area of increased intraplate hazard that extends from northwestern Montana in a curvilinear fashion to southern Nevada/Utah. This zone of increased hazard is known as the Intermountain Seismic Belt (ISB). The ISB has been host to at least 48 earthquakes of **M** 5.0 and larger since 1876 and poses significant risk to the people and infrastructure in the region [*Smith and Arabasz*, 1991; *University of Utah*, 2018].

THE INTERMOUNTAIN SEISMIC BELT AND MONTANA SEISMICITY

Montana is one of the most seismically active states in the conterminous United States owing to the ISB extending through the western third of the state (Figs. 1.2 and 1.3). The ISB is a belt of seismicity that broadly defines the eastern limits of extending crust in the western US [*Lageson and Stickney*, 2000]. It extends in a curvilinear branching pattern 1500 km from the northwest corner of Montana to the Yellowstone National Park region and continues southward along the Idaho-Wyoming border, through Utah, and into southern Nevada and northern Arizona [*Smith and Arabasz*, 1991]. A branch of the ISB, known as the Centennial Tectonic Belt, extends west from Yellowstone National Park through southwestern Montana into Central Idaho [*Montana Bureau of Mines and Geology*, 2018]. The 100 to 200 km wide ISB is characterized by late Quaternary normal faulting, diffuse shallow seismicity (<20 km), and episodic scarp-forming earthquakes associated with intraplate stress within the western North American plate [*Sbar et al.,* 1972; *Arabasz and Smith*, 1981; *Smith and Arabasz*, 1991]. Northeast-southwest intraplate extension drives contemporary ISB deformation [*Stickney and Bartholomew*, 1987]. The north-south trending ISB is disrupted by the northwest-southeast trending Lewis and Clark Line (LCL), which has been suggested to indicate a major, intraplate crustal discontinuity (Fig. 1.3) [*Waldron and Galster*, 1984]. The LCL, interpreted as a rotational shear zone, extends from northern Idaho to east of Helena, Montana [*Sears and Hendrix*, 2004].

Two types of earthquake sequences characterize western Montana seismicity: discrete earthquakes followed by a classically decaying series of aftershocks and geographically finite swarms of earthquakes occurring over weeks to months [*Lageson and Stickney*, 2000]. Notable 20th century earthquakes in western Montana include (Fig. 1.4):

- Clarkston earthquake, June 1925: This surface-wave magnitude ($\mathbf{M_S}$) 6.6 earthquake was the earliest instrumentally recorded event in Montana. The earthquake caused considerable damage within a 1500 km^2 area [*Pardee*, 1926].
- 1935 Helena earthquakes, October 1935: Two earthquakes, $\mathbf{M_S}$ 6.2 and $\mathbf{M_S}$ 6.0, were the largest in a sustained sequence that lasted from October 1935 through December 1936 with more than 2500 recorded earthquakes. Four fatalities and $4 million in property damage were reported [*Stover and Coffman*, 1993; *Stickney*, 2018].
- Hebgen Lake earthquake, August 1959: This $\mathbf{M_W}$ 7.3 earthquake is largest ever recorded in Montana. Shaking reached maximum MMI X causing 28 fatalities and $11 million in property damage [*Stover and Coffman*, 1993].
- Flathead Lake swarms, April 1969 – December 1971: Approximately 350 events were recorded in this swarm. 21 events were felt in the month following the largest **M** 4.7 event. Buildings were damaged and water wells were muddied [*Stover and Coffman*, 1993; *Franz*, 2017].
- Kila swarm, May – June 1995: The largest event of this swarm was **M** 4.1 and 13 events larger than or equal to **M** 2.5 were recorded [*Lageson and Stickney*, 2000; *Franz*, 2017].
- Dillon earthquake, July 2005: The $\mathbf{M_W}$ 5.6 event reach maximum MMI VII damaging 60% of older masonry chimneys in the area [*Stickney*, 2006;2013].

- Lincoln earthquake, July 2017: The $\mathbf{M_W}$ 5.8 resulted in 19,000 reports of felt shaking and maximum MMI VII [*U.S. Geological Survey*, 2017b].

THE 2017 LINCOLN, MONTANA, EARTHQUAKE

On 6 July 2017 (00:30 local time), a $\mathbf{M_W}$ 5.8 earthquake occurred near the town of Lincoln in west-central Montana, 50 km northwest of the capital city, Helena. This was the largest earthquake to occur in Montana since the 1959 $\mathbf{M_W}$ 7.3 Hebgen Lake event in the Yellowstone region. The Lincoln earthquake was felt more than 800 km from the epicenter and garnered more than 19,000 reports of shaking which reached maximum MMI VII (Fig. 1.5). No injuries or serious damage were reported. Items were knocked off shelves in the epicentral region [*U.S. Geological Survey*, 2017b], a power outage affected 1350 homes in Lincoln [*Chaney*, 2017], a gas leak occurred in Helena, Montana, 50 km away [*Billings Gazette*, 2017], a two-story garage suffered damage in Winston, Montana, 80 km away [*U.S. Geological Survey*, 2017b], part of a brick parapet fell from an apartment building in Butte, Montana, 100 km away [*Chaney*, 2017], and an elevator went into seismic mode in Missoula, Montana, 100 km away [*Briggeman*, 2017].

The USGS and the Montana Bureau of Mines and Geology (MBMB) reported one unfelt foreshock, local magnitude ($\mathbf{M_L}$) 2.3, ~19 hours before the mainshock [*U.S. Geological Survey*, 2017a] and more than 1200 aftershocks through the end of 2017, 46 larger than or equal to **M** 3. The largest aftershock of the sequence was an $\mathbf{M_W}$ 5.0 that occurred 5 minutes after the mainshock [*U.S. Geological Survey*, 2017c]. A $\mathbf{M_W}$ 4.0 aftershock 11 days later received hundreds of felt reports out to Spokane, Washington, 380 km away [*U.S. Geological Survey*, 2017d]. Aftershocks were still being felt in September 2018, 14 months after the mainshock. Due to the intraplate setting, aftershocks could potentially continue for decades [*Stein and Liu*, 2009].

The Lincoln earthquake occurred on a previously unknown fault oriented perpendicular to the major known faults in the area. Fortunately, the event occurred in a sparsely populated area where the majority of structures are resistant to earthquake shaking [*U.S. Geological Survey*, 2017b]. The earthquake sequence provides an excellent opportunity to study a relatively uncommon, large tectonic intraplate event and offers insight into the hazard associated with quiescent, unmapped, subsurface geologic structures.

Chapter 2 presents an analysis of the spatiotemporal evolution of the Lincoln, Montana foreshock-mainshock-aftershock sequence. The study details the locations of 685 events larger than or equal to **M** 1 that occurred in the three months following the $\mathbf{M_W}$ 5.8 mainshock. These aftershock locations delineate an unmapped fault plane antithetic to the orientation of the main LCL fault system in the region. The study also identifies 3005 aftershocks detected in the three weeks following the mainshock as well as three previously undetected foreshocks. The sequence is described by a slow aftershock decay rate and a low frequency-magnitude distribution not unlike other intraplate earthquake and aftershock sequences observed globally. This analysis contributes to the body of literature related to moderate-to-large North American Cordilleran tectonic intraplate earthquakes. This analysis also demonstrates that unmapped faults play a role in accommodating regional strain in western Montana, can host significant earthquakes, and can pose significant hazard to population centers.

1.4 Prague, Oklahoma, and Induced Seismicity

Overview of Induced Seismicity

The term "induced seismicity" here refers to earthquakes with anthropogenic origins; that is, earthquakes that have been induced by human activities. It has long been recognized that earthquakes can be induced by perturbing crustal stress. The study of induced earthquakes began in 1894 in Johannesburg, South Africa when earthquakes were first felt and attributed to gold production that had begun eight years earlier [*McGarr et al.*, 2002].

Despite low deformation rates [*Petersen et al.*, 2008], the shear stress of intracontinental regions is near the strength limit of (typically inactive) crustal faults [*Townend and Zoback*, 2000]. This critically stressed nature of the intracontinental crust means that perturbations as small as 0.01 MPa caused by pore pressure changes, volume changes, or applied forces/loads can and do induce earthquakes, even in areas that are typically nearly aseismic [*McGarr et al.*, 2002]. Because induced earthquakes resemble tectonic earthquakes to a great degree, due to their fundamentally identical mechanism, it can be difficult to distinguish naturally occurring earthquakes from induced ones [e.g., *Keranen and Weingarten*, 2018].

Many types of industrial activity that alter stresses and/or weaken faults have been linked to anthropogenic seismicity including: impounding of surface water reservoirs behind dams; erecting tall buildings; engineering coastal sediments; quarrying; extraction of resources including groundwater, coal, minerals/ores, and hydrocarbons (gas and oil); tunnel excavation and collapse; waste fluid disposal (military waste and produced water); hydraulic fracturing; enhanced oil recovery; geothermal engineering; natural gas storage; carbon dioxide sequestration; mine flooding; research projects; and, nuclear explosions (Fig. 1.6a). The Human-Induced Earthquake Database (*HiQuake*), publically available at www.inducedearthquakes.org, contains more than 750 cases, dating back to 1801, of earthquakes potentially induced by such activities [*Foulger et al.*, 2018; *Wilson et al.*, 2018].

Induced earthquakes have been reported on every continent except Antarctica (Fig. 1.6b) and maximum magnitudes vary greatly (Fig. 1.6c) The most commonly reported magnitudes are $3 \leq$ $\mathbf{M} < 4$ (Fig. 1.6d), though it is important to note that large numbers of smaller induced earthquake sequences have not been identified and reported [*Foulger et al.*, 2018].

Induced earthquakes can be large and cause significant damage. The largest magnitude claimed for an induced seismic event is the 2008 $\mathbf{M_W}$ 7.9 earthquake in the Longmen Shan mountains of Wenchuan county, Sichuan province, China. It has been linked with the impoundment of reservoir water behind the Zipingpu dam [*Foulger*, 2018]. As a result of this earthquake, nearly 90,000 people were killed and more than five million buildings collapsed [*U.S. Geological Survey*, 2008]. The shaking reached maximum MMI XI and triggered almost 200,000 landslides [*Xu et al*. 2014] including the Daguanbao landslide, one of the largest earthquake induced landslides ever observed [*Huang and Fan*, 2013; *Fan et al.*, 2018]. The total economic loss for the event was estimated at ~$150 billion (USD) [*Miyamoto et al.*, 2008] making it one of the costliest natural disasters in history.

Within the United States, induced seismicity was first recognized in 1920s and 1930s when earthquakes accompanied ground subsidence after fluid withdrawal in the Goose Creek oil field in Texas [e.g., *Pratt and Johnson*, 1926; *McGarr et al*., 2002; *Keranen and Weingarten*, 2018] and during the impoundment of Lake Mead behind the Hoover Dam [*Mead and Carder*, 1941].

Two of the most famous and informative cases of early induced seismicity in the United States come from Colorado in the 1960s. First, the U.S. Army disposal of waste fluids at Rocky Mountain Arsenal (RMA) triggered the infamous Denver, Colorado earthquakes. In 1961, a deep disposal well was drilled into the Precambrian crystalline basement at RMA northeast of Denver. Disposal of chemical-warfare-manufacturing waste fluids into the well began in March 1962 and continued off and on until February 1966, after a connection between the well and earthquakes was publicly suggested [*Healy et al.*, 1968]. More than 700 earthquakes were recorded in the Denver area from April 1962 through September 1965 ranging from **M** 0.7 to **M** 4.3. These were the first earthquakes reported in the Denver area since 1882 [*Evans*, 1966]. The most economically damaging earthquake in Colorado history, a **M** 5.3 earthquake that struck the Denver area and caused more than $1 million in damage, occurred in August 1967 almost two years after disposal at RMA had ceased [*Colorado Geological Survey*, 2018]. The volume and pressure of fluid injected at RMA appeared to be directly correlated to the frequency of earthquakes, though lower-permeability boundaries slowed pressure dissipation resulting in continued seismicity for years after injection ceased [*Hseigh and Bredehoeft*, 1981; *Kernanen and Weingarten*, 2018].

Following the discovery that high-pressure underground fluid injection was responsible for triggering earthquakes at RMA, experiments on intentional earthquake triggering were conducted at the Rangely oil field in northwest Colorado. Researchers intentionally triggered and modulated seismic activity by alternately injecting and recovering water from wells that penetrated the studied fault zone [*Raleigh et al.*, 1976]. Seismicity rates rose when subsurface pressure was maintained above a critical pressure threshold and decreased when pressure fell below the estimated critical value. Strong temporal correlation between frequency of the seismic activity and variations in fluid pressure confirmed that earthquakes can be induced, and perhaps controlled, by subsurface stress changes induced by fluid injection [*Raleigh et al., 1976; Keranen and Weingarten*, 2018].

Injection-related activities can trigger earthquakes by increasing pore-fluid pressure, thus reducing effective normal stresses and frictional strength on pre-existing fault planes and moving the faults closer to failure (e.g., via wastewater disposal) [*Hubert and Rubey*, 1959*; Nicholson and Wesson*, 1990]. The bulk of injection-induced seismicity is triggered by the disposal of waste fluids into deep formations. These formations may lie directly above and have hydraulic connections to faulted basement rock, or occasionally lie within the basement rock. Alternatively, fractures/faults can be created through high-pressure fluid injection inducing shear failure in rock (e.g., via hydraulic fracturing) [e.g., *Ellsworth*, 2013]. Hydraulic fracturing inherently induces earthquakes by intentionally fracturing rock or opening pre-existing fractures to allow oil and gas to flow more freely through formations. The majority of these hydraulic fracturing earthquakes are very small ($\mathbf{M} \leq 1$) and unfelt [Davies et al., 2013]; however, some hydraulic fracturing operations have induced larger, felt earthquakes (e.g., southern Oklahoma [*Holland*, 2013a], Ohio [*Friberg et al.*, 2014; *Skoumal et al.*, 2015], western Canada [*BC Oil and Gas Commission*, 2012; *Bao and Eaton*, 2016], and the United Kingdom [*de Pater and Baisch*, 2011]).

A dramatic rise in the rate of induced earthquakes in the past decade, particularly in the central and eastern United States (CEUS) (Fig. 1.7), has sparked renewed interest in the seismological and hazard communities and provided a plethora of opportunities to study these events and the processes associated with their nucleation. Prior to 2000, the CEUS experienced an average of 21 earthquakes with magnitudes greater than or equal to 3.0 per year; however, more than 300 occurred in the three years from 2010 to 2012 [*Ellsworth*, 2013] (Fig. 1.7a) and more than 1700 occurred in the three years from 2013 to 2015 [*Keranen and Weingarten*, 2018] (Fig. 1.7b). This unprecedented increase in seismicity has coincided with the expansion of horizontal drilling and hydraulic fracturing operations via fluid injection in tight shale enables the production of oil and gas from previously unproductive formations. Along with increased production of oil and gas comes the increase of produced water. Large quantities of connate brine (dense, saline water trapped in the pores of a rock during its formation) is co-produced in these operations, and the water-to-product ratios can exceed 20 [*Foulger et al.*, 2018]. The produced water contains excessive levels of total dissolved solids as was well as potentially toxic organic and inorganic compounds making it unsuitable for discharge at the surface [*Veil et al.*, 2004]. Instead, produced water is reinjected into depleted oil fields to maintain reservoir pressure or disposed of by injecting it deep underground into receptive geologic formations, similar to what was done at RMA. *Weingarten et al.* [2015] found that the entire increase in the CEUS earthquake rate is associated with fluid injection wells (production and disposal). Prior to 2000, ~20% of all CEUS seismicity was associated with injection wells. From 2011 to 2014 ~87% of all CEUS seismicity was associated with injection wells.

The states most affected by increasing levels of seismicity include Arkansas, Colorado, Kansas, New Mexico, Ohio, Oklahoma, and Texas. Recent high-profile/studied cases of injection-induced seismicity in the CEUS include:

- Guy-Greenbrier, Arkansas
  [e.g., *Horton*, 2012]
- Greeley, Colorado
  [e.g., *Yeck et al.*, 2016a]
- Raton Basin, Colorado/New Mexico
  [e.g., *Rubinstein et al.*, 2014]
- Harper County, Kansas
  [e.g., *Buchanan et al.*, 2014]
- Harrison Township, Ohio
  [e.g., *Friberg et al.*, 2014]
- Poland Township, Ohio
  [e.g., *Skoumal et al.*, 2015]
- Youngstown, Ohio
  [e.g., *Skoumal et al.*, 2014]
- Cushing, Oklahoma
  [e.g., *McNamara et al.*, 2015a]
- Fairview, Oklahoma
  [e.g., *Yeck et al.*, 2016b]
- Guthrie, Oklahoma
  [e.g., *Benz et al.*, 2015]
- Jones, Oklahoma
  [e.g., *Keranen et al.*, 2014]
- Pawnee, Oklahoma
  [e.g., *Yeck et al.*, 2017]
- Prague, Oklahoma
  [e.g., *Keranen et al.*, 2013]
- Azle, Texas
  [e.g., *Hornbach et al.*, 2015]
- Cleburne, Texas
  [e.g., *Justinic et al.*, 2013]
- Cogdell, Texas
  [e.g., *Gan and Frohlich*, 2013]
- Dallas-Fort Worth, Texas
  [e.g., *Frohlich et al.*, 2011]
- Fashing, Texas
  [e.g., *Frohlich et al.*, 2016]
- Timpson, Texas
  [e.g., *Frohlich et al.*, 2014]

The above list includes the 3 September 2016 $\mathbf{M}_{\mathbf{W}}$ 5.8 Pawnee, Oklahoma earthquake. The Pawnee earthquake is currently the largest earthquake alleged to have been induced by fluid injection (in this case, wastewater disposal), and is the largest earthquake ever recorded in the state of Oklahoma. It was felt to distances over 1500 km from the epicenter and reached maximum MMI VII [*U.S. Geological* Survey, 2016b] resulting in one injury, six uninhabitable buildings, collapsed chimneys, and damage to brick masonry buildings [*Yeck et al.*, 2016]. The Oklahoma Governor declared a state of emergency for Pawnee County where the worst damage was located [*News 9*, 2016], and 69 injection wells in the vicinity were subsequently shut down [*Murphy*, 2016; *Querry*, 2016].

While the sharp rise in CEUS seismicity is associated with injection wells, it is important to note that the vast majority of injection wells are not associated with seismicity (Fig. 1.7c). In fact, only ~10% of wells have been associated with induced earthquakes [*Weingarten et al.*, 2015], and that 10% is concentrated in a few geographic regions. Hypotheses proffered for this geographically selective association include:

- High-rate injection wells: Wells injecting more than 300,000 barrels per month are much more likely to be associated with earthquakes than lower-rate wells. 76% of the highest rate disposal wells (injecting more than 1 million barrels per month) are associated with earthquakes [*Weingarten et al.*, 2015].
- Vertical barriers or paths to pressure transmission into basement: Low-permeability basal sedimentary layers may inhibit triggering by preventing pressures from reaching basement faults [*Zhang et al.*, 2013]. Conversely, faults and fractures may provide fast paths that allow injection fluids to easily affect basement formations.
- Injection proximity to basement: Injection high in the sedimentary section relative to basement, such as in North Dakota, means that fluid pressure has fewer direct pathways to the basement where larger earthquakes originate [*Hincks et al.*, 2018; *Keranen and Weingarten, 2018*]. However, *Goebel and Brodsky* [2018] found that injecting fluid into the softer sedimentary layers increased the range of seismic hazard around a well,

generating larger earthquakes farther from the well, whereas harder basement rock better confined the injection fluid.

- Complex subsurface geology: Earthquake hypocenters can cluster around subsurface features (e.g., fossil reefs, unmapped faults) resulting in geographically biased activation potential [*Schultz et al.*, 2016].
- Optimal fault orientation: Faults can be aligned optimally with the regional stress field making them easier to perturb and trigger [*Holland*, 2013b].

The sharp rise in seismicity and tendency toward geographic clustering led the USGS to develop one-year seismic hazard forecast maps that accounted for the prevalence of induced seismicity in the CEUS. Prior to 2014, the USGS's NSHMs, updated every six years, removed nontectonic events due to lack of geographic and temporal permanence (Fig. 1.8a). However, the hazard from recent sustained seismicity resulting from injection activities was deemed quantifiable and ineluctable. The USGS identified 21 zones of induced seismicity (Fig. 1.8b) across the CEUS used to forecast chances of damage (Fig. 1.8c). The new maps show increased chances of damage in a few of the 21 previously identified zones, but the most hazard is present in central and north-central Oklahoma. This map has been updated yearly since 2016 and all updates consistently show increased hazard in central and north-central Oklahoma [*Petersen et al.*, 2014; 2016; 2017; 2018].

INDUCED SEISMICITY IN OKLAHOMA

While several states across the CEUS have experienced the recent uptick in induced seismicity, none have been more affected than Oklahoma. *Weingarten et al*. [2015] found that wells in central and north-central Oklahoma have been the main contributor to the dramatic increase in seismicity across the CEUS since 2008. In the last decade, the state has experienced an exponential increase in the number of earthquakes (Fig. 1.9). Prior to 2009, ~2 earthquakes larger than or equal to **M** 3.5 occurred in the state per year. In 2015 alone, there were 191 earthquakes larger than or equal to **M** 3.5. While Oklahoma was not void of seismicity prior to 2009 [e.g., *Oklahoma Geological Survey*, 2013], the sudden and dramatic increase concerned denizens, resulted in lawsuits, and eventually prompted state officials to take action towards public education and increased industry regulation.

A perfect storm of conditions is present in Oklahoma creating an environment ripe for the proliferation of induced seismicity. Wastewater production volumes are very high. High-rate injection wells dispose of wastewater into the Arbuckle Group, a permeable geological formation that lies directly or closely above the Precambrian basement. Many wells initially disposed directly into the basement. Optimally-oriented, critically-stressed, unmapped faults pervade the Oklahoma basement. The relatively easy communication of water and stress perturbations from the wells to the primed basements faults generates ample seismicity that has rattled the state, caused millions of dollars in damage, and sparked scientific intrigue and a political maelstrom.

The first major event in the post-2008 seismic boom was in 2011 near Prague, Oklahoma (the subject of Chapter 3). A series of three moderately-large events ($\mathbf{M_W}$ 4.8, 5.7, and 4.8) rattled the entire central US, injured two people, caused moderate damage in the epicentral region, and triggered a prolific sequence of aftershocks. The $\mathbf{M_W}$ 5.7 event was, at the time, the largest earthquake ever recorded in the state.

Continued increasing rates of seismicity and citizens' concerns prompted the Oklahoma Geological Survey (OGS) to release a statement in 2014 stating that "some earthquakes may have a relationship to oil and gas activities," however, "the majority… appear to be the result of natural stresses" [*Oklahoma Geological Survey*, 2014]. The OGS's statement contradicted the growing body of literature linking wastewater disposal to increased seismic activity in the state and rest of the CEUS. This may have been due to pressures from university administrators (the OGS is a state agency administered by the University of Oklahoma), state officials, and prominent industry executives to downplay the link in order to protect the immense oil and gas interests in the state [*Jones*, 2017]. The June 2014 economic impact and jobs report commissioned by the Oklahoma Energy Resources Board (OERB) on the oil and natural gas industry stated that Oklahoma ranked in the top five states for production of natural gas and crude oil, one out of five Oklahomans were directly or indirectly supported by the industry, and the industry accounted for one out of every three dollars of gross state product [*Agee*, 2014]. The oil and natural gas industry is the largest source of tax revenue for the state [*Oklahoma Energy Resources Board*, 2017], despite being taxed at some of the lowest rates in the United States [*Cohen and Schneyer*, 2016]. Cushing, Oklahoma is also home to the largest crude oil storage facility in the world [*McNamara et al.*, 2015a].

In May 2014, the USGS and the OGS released a joint statement indicating that the increasing number of small earthquakes in the state increased the probability of a larger, more damaging earthquake [*U.S. Geological Survey and Oklahoma Geological Survey*, 2014]. It was the first time an "earthquake warning" had been issued for a state east of the Rocky Mountains, as such seismic hazard assessments are typically issued for western states following large earthquakes to warn residents of the risk of damaging aftershocks [*Oskin*, 2014].

On 21 April 2015, the OGS changed its position on the cause of the increased seismicity and released a statement considering it "very likely that the majority of recent earthquakes…[were] triggered by the injection of produced water in disposal wells" based on seismicity "observed to follow the oil and gas activities" and seismicity rates increasing as injection volumes increased [*Oklahoma Geological Survey*, 2015]. The OGS also noted, as had many researchers [e.g., *Zoback*, 2012; *Ellsworth*, 2013; *Hand*, 2014], that the primary source of recent earthquakes was not hydraulic fracturing, though some earthquakes have been associated with the process [e.g., *Holland*, 2013a]. Instead, the primary source of earthquakes was the disposal of produced water at sufficient depth to perturb faults in basement formations.

The same day the OGS released its statement linking earthquakes to oil and gas activities, earthquakes.ok.gov was launched as a public resource dedicated to sharing research, regulations, updates, and news items related to Oklahoma's recent earthquakes. The website was a result of the work of the Coordinating Council on Seismic Activity, created in September 2014, and led by Oklahoma's first Secretary of Energy and Environment. The Coordinating Council's participants include the Oklahoma Corporation Commission (OCC – the state's regulatory agency charged with overseeing the oil and gas industry), the OGS, the OERB, the Groundwater Protection Council, university geoscience departments, the Oklahoma Independent Petroleum Association, and the Oklahoma Oil and Gas Association.

The OCC has exclusive jurisdiction in the regulation of class II underground injection wells in the state. In 2013, The OCC initiated a "traffic light" system for disposal well operators, as recommended by the National Academy of Sciences [*National Research Council*, 2013], to review disposal well permits for earthquake inducing potential. In 2015, the OCC implemented measures to shut down or reduce volumes of injection for more than 700 disposal wells throughout a 15,000-square-mile "Area of Interest" in central and north-central Oklahoma, reducing wastewater injection volumes 40% from 2014 levels. The OCC also implemented daily required reports of injection parameters [*Oklahoma Corporation Commission*, 2015].

More than a dozen directives have been implemented by the OCC to reduce the number of felt-earthquakes across the states [*Oklahoma Corporation Commission*, 2017], and the total number of felt and recorded earthquakes have indeed decreased since 2015 [e.g., *Keranen and Weingarten*, 2018]. The decreasing seismicity is most apparent in areas where wastewater disposal decreased which may reflect regulatory actions or economic factors [*Petersen et al.*, 2018].

THE 2011 PRAGUE, OKLAHOMA, EARTHQUAKE

On 6 November 2011 (5 November 2011, 22:53 local time), a $\mathbf{M_W}$ 5.7 earthquake occurred near the town of Prague in central Oklahoma, 50 km east of the capital Oklahoma City. At the time, it was the largest earthquake ever recorded in the state (later surpassed by the 2016 $\mathbf{M_W}$ 5.8 Pawnee, Oklahoma earthquake) and is currently the third largest earthquake recorded in the CEUS after the 2016 Pawnee, Oklahoma and 2011 Mineral, Virginia earthquakes. The Prague earthquake was felt in at least 17 states across the central US from southern Wisconsin to southern Texas and from eastern Colorado to western Tennessee. A 65 km^2 area around the epicenter experienced shaking of MMI VIII (Fig. 1.10). 14 homes were destroyed, many buildings were damaged, highway pavement buckled, and two people were injured [*U.S. Geological Survey*, 2011a] (Fig. 1.11).

The $\mathbf{M_W}$ 5.7 mainshock was preceded by a $\mathbf{M_W}$ 4.8 foreshock ~24 hours earlier and succeeded by the largest aftershock, $\mathbf{M_W}$ 4.8, ~48 hours later. This trio of moderately-sized earthquakes triggered a prolific aftershock sequence of tens of thousands of earthquakes including more than 20,000 in the month following the mainshock [*McMahon et al.*, 2017]. The vast majority of these aftershocks were small, unfelt events with ~300 events larger than **M** 3 occurring since and through 2017.

In March 2013, the Oklahoma Geological Survey released a statement interpreting the Prague sequence a "result of natural causes," based on previously recorded "relatively large, natural earthquakes" in the state, aftershock decay rates "typical of natural seismicity," favorably oriented faults, lack of increasing seismicity with increasing water injection, and under-pressured formations [*Oklahoma Geological Survey*, 2013]. Many scientific studies, however, claimed the earthquakes were induced and linked with oil and gas activities in the region, namely wastewater injection [*Keranen et al.*, 2013, 2014; *van der Elst et al.*, 2013; *Llenos and Michael*, 2013; *Ellsworth*, 2013; *Hough*, 2014; McGarr, 2014; *Sumy et al.*, 2014]. The closest earthquakes at the tip of the first ruptured fault were just ~200 m from active high-volume disposal wells (Fig. 1.12) [*Keranen et al.*, 2013]. In April 2015, the Oklahoma Geological Survey acknowledged the link between the state's increased seismicity, including the Prague earthquake, and the disposal of water associated with oil and gas production [*Oklahoma Geological Survey*, 2015].

At least two earthquake-associated lawsuits have been brought against companies operating wastewater disposal wells in the area. A personal injury lawsuit was settled for an undisclosed amount in 2017 [*Wilmoth*, 2017] and a class action lawsuit comprising of Oklahoma citizens with residential or business properties in the nine counties that suffered damage in the earthquake is set to begin in September 2018 [*Wilmoth*, 2018].

The Prague earthquake sequence has been and continues to be the subject of many scientific studies because it provides a vast amount of data for the study of large induced/intraplate earthquakes and aftershock sequences. These studies help delineate the geometry and activity of subsurface faults, inform the hazards in the region, and provide insight into how induced earthquakes differ from naturally occurring tectonic earthquakes. Interesting findings and hypotheses about this sequence include: occurrence approximately 18 years after injection began in the area [*Keranen et al.*, 2013]; three stages of faulting, large slip regions generally free of aftershocks, and a low stress drop of the mainshock [*Sun and Hartzell*, 2014]; low stress drops of the aftershocks (an order of magnitude lower than typical eastern US intraplate stress drops) [*Sumy et al.*, 2017]; the mainshock occurred on an optimally stress-oriented, unmapped fault [*Holland*, 2013b]; the foreshock potentially trigged a cascading failure of earthquakes, including the mainshock [*Keranen et al*., 2013; *Sumy et al*., 2014]; the foreshock, mainshock, and aftershock may all have been injection induced [*McGarr*, 2014]; low stress drop contributed to less intense shaking at regional distances than typically found with tectonic earthquakes, but the epicenter felt intense shaking due to the shallow hypocenter [*Hough*, 2014]; and repeating earthquakes imply that some precursory slow slip occurred before the main shock [*Savage et al*., 2017].

Chapter 3 presents a peer-review published analysis of the spatiotemporal evolution of the Prague, Oklahoma aftershock sequence through the detection and location of 5262 events in the one month following the 6 November 2011 $\mathbf{M}_{\mathbf{W}}$ 5.7 mainshock. The study details the detection and location of microseismic events, three different faults ruptured by the foreshock, mainshock, and largest aftershock as well as triggered seismicity on an adjacent fault, slow aftershock decay, statistical differences between the overlying sediment (zone of wastewater injection) and crystalline basement, and the relative absence of aftershocks on parts of the fault that experienced large slip. This analysis contributes to the growing body of literature about the Prague, Oklahoma earthquake sequence as well as the hazards associated with wastewater disposal and induced seismicity in Oklahoma and the CEUS.

1.5 MARIE BYRD LAND, ANTARCTICA, AND VOLCANIC SEISMICITY

OVERVIEW OF VOLCANIC SEISMICITY

There are ~1500 potentially active volcanoes on Earth (volcanoes that have erupted in the last 10,000 years) [*Global Volcanism Program*, 2018] and ~12% of the world's population lives within 100 km of these volcanoes [*Small and Naumann*, 2001]. The hazard of living near an active volcano can be tremendous and mitigation is essential. The deadliest volcanic eruption in recent history occurred on November 13, 1985 at Nevado del Ruiz volcano in Colombia. The relatively small paroxysmal eruption (Volcanic Explosivity Index (VEI) 3, on a scale 0-8+)

produced pyroclastic flows and surges that melted part of the summit ice cap which ultimately generated the catastrophic lahars that killed more than 22,000 people and caused more than $212 million in property damage. The eruption culminated a year of intermittent precursory earthquake, fumarolic, and phreatic activity [*Herd*, 1986]. Volcano seismology seeks to understand the nature and dynamics of seismic sources associated with volcanic systems. These seismic sources are often indicative of volcanic unrest and understanding them can aid the mitigation of volcanic hazards through potential eruption forecasting.

There are four basic types of seismic signals identified in volcanic settings: high-frequency events, low-frequency events, explosions, and tremor. Examples of waveforms and spectrograms for these types of events are presented in Figure 1.13. High-frequency (HF) earthquakes, also known as A-type and volcano-tectonic (VT) earthquakes, are indistinguishable from pure tectonic, shallow earthquakes in terms of waveform appearance and broad spectral characteristics. These events have clearly defined *P*- and *S*-phase arrivals, dominant frequencies between 5 and 15 Hz, and tend to occur at shallow depths, 1-20 km. They are often observed in swarms rather than mainshock-aftershocks sequences like their tectonic counterparts and can be triggered by large teleseismic events. HF earthquakes are thought to be caused by shear failure or slip on faults in the volcanic edifice and act as gauges that map stress concentrations distributed over large volumes surrounding magma conduits and reservoirs. [*Chouet*, 1996; *McNutt,* 1996; 2005; *Zobin*, 2017].

Low-frequency (LF) earthquakes, also known as B-type and long-period (LP) earthquakes, are thought to be caused by fluid processes that are still not well understood. The dominant frequencies of these events are typically 0.5 - 5 Hz. The waveforms are characterized by emergent *P*-phases and typically lack *S*-phases. The broadband onsets are followed by coda of decaying harmonic oscillations. LF earthquakes have been interpreted as a broadband, time-localized pressure excitation mechanism followed by the response of a fluid-filled resonator [*Chouet*, 1996; *McNutt*, 2005; *Chouet and Matoza*, 2013].

Explosion earthquakes accompany explosive eruptions and the earthquake magnitudes are related to the magnitude of the eruption. Explosion earthquakes and are often identified by the high-frequency air-shock phase on seismograms, but explosions can also produce long-period waveforms [*McNutt*, 1996; *Kawakatsu and Yamamoto*, 2015; *Zobin*, 2017].

Volcanic tremor is a high-amplitude, continuous signal lasting minutes to years. Two different types of tremor have been recorded at volcanoes, harmonic (or monotonic) tremor and spasmodic tremor. Harmonic tremor is characterized by a narrow frequency range, 1-5 Hz, or sharply peaked spectra with harmonic overtones that can experience spectral gliding. The lowest peak frequency is generally around 1 Hz. In many instances, LF events and harmonic tremor have essentially the same temporal and spectral components indicating that common source processes, differing only in duration, underlie these types of events. Spasmodic tremor is characterized by higher frequencies and a pulsating, irregular signals. Both harmonic and spasmodic tremor are thought to result from resonance due to extended flow of fluid through fractures. Tremor can also be caused by continuous occurrence of HF events, LF events, or explosions so closely spaced in time that they can't be visually separated. Volcanic tremor has been recognized as a common short-term precursor to eruptions as well as an accompaniment to eruptions [*McNutt*, 1996; 2005; *Chouet and Matoza*, 2013; *Kawakatsu and Yamamoto*, 2015; *Zobin*, 2017].

In addition to the above four basic types of signals observed at volcanoes, there many additional types of signals including, very-long-period (VLP) signals, ultra-long-period (ULP) signals, and various types of hybrid signals. There are also several types of signals from surficial processes including glacial movement, landslides, rockfalls, pyroclastic flows, and lahars. Deep, long-period earthquakes are discussed in the following section as well as Chapter 4.

DEEP, LONG-PERIOD EARTHQUAKES

Deep, long-period earthquake (DLPs) are a relatively poorly understood, yet fairly ubiquitous type of seismicity found beneath or near volcanic centers. DLPs are typically smaller magnitude events (**M** < 2) characterized by (1) deep hypocenters below the crustal seismogenic or brittle-ductile transition zone (10-50 km, depending on region), (2) long-period/low-frequency energy (<5 Hz) (Fig. 1.14), (3) monochromatic or harmonic waveforms, (4) long-duration, ringing coda waves, and (5) emergent signals.

DLPs are a part of background seismicity at some volcanoes and can occur persistently over years [e.g., *Aso et al*, 2011; *Lough et al.*, 2013], but they have also been correlated with various forms of volcanic unrest, including eruptions [e.g., *Power et al.*, 2002; 2004]. The clearest example of DLPs related to pre-eruption seismicity is at Mount Pinatubo, Philippines, where ~600 DLPs occurred beneath the volcano in the weeks preceding the paroxysmal 1991 eruption [*White*, 1996]. The initiation of DLP activity was accompanied by the onset of shallow, long-period earthquakes, tremor, and steam emissions approximately three weeks before the eruption. DLP activity waned approximately one week before the eruption with the emergence of a dome inflated by basalt that had recently arrived from the deep crust. The spatiotemporal correlation of the DLP activity with the subsequent surficial activity indicated the seismicity was related to movement of magma in the crust. Although DLPs do not necessarily signal an eruption, they may be one of the earliest indications of deep magmatic movement and renewed volcanic activity, and therefore can be useful in forecasting future eruptions.

DLPs have been observed worldwide beneath or near volcanoes in different types of tectonic regimes including:

- Alaska, Aleutian Arc volcanoes [*Power et al.*, 2004]
- Antarctica [*Lough et al.*, 2013]
- Cascadia, Oregon and Washington [*Pitt et al.*, 2002; *Nichols et al.*, 2011; *Vidale et al.*, 2014; *Han et al.*, 2018]
- Hawaii, Kilauea and Mauna Loa [*Aki and Koyanagi*, 1981; *Okubo and Wolf*, 2008; *Matoza et al.*, 2014]
- Iceland, Askja volcano [*Soosalu et al.*, 2010]
- Japan [*Ukawa and Ohtake*, 1987; *Hasegawa and Yamamoto*, 1994; *Nakamichi et al.*, 2003; *Aso et al.*, 2013]
- The Philippines, Mount Pinatubo [*White*, 1996]
- Northern California [*Hill et al.*, 2002; *Pitt et al.*, 2002]
- Russia, Klyuchevskoy volcano group [*Shapiro et al.*, 2017]

A source mechanism for DLPs has not been well established. Several hypotheses have been proposed to interpret the source of DLPs including dehydration embrittlement of already-serpentinized mantle material [*Vidale et al.*, 2014] and thermal strain from magma cooling [*Aso and Tsai*, 2014]. The most favored source mechanism for DLPs, however, is the movement of fluid or magma or other fluids within a volcano's plumbing system. Long-period earthquakes have been attributed to the pressure fluctuations that result from unsteady mass transport in volcanic systems [e.g., *Chouet and Matoza*, 2013]. Two generally accepted source models for these earthquakes involve unsteady, nonlinear fluid flow along conduits with irregular geometry [*Julian*, 1994] and the resonance of fluid-filled cracks [*Chouet*, 1992]. Several studies have utilized these models to interpret DLPs:

- *White* [1996] suggested DLPs at Mount Pinatubo were produced by the forceful injection of basaltic fluids through cracks into a magma chamber.
- *Hill et al.* [2002] suggested that DLPs beneath Mammoth Mountain resulted from a slug of magmatic fluid moving into a crack.
- *Pitt et al.* [2002] suggest DLPs in northern California reflect an invasion of basaltic magma at midcrustal depths.
- *Power et al.* [2004] suggest the DLPs in the Aleutian arc represent a steady-state process of magma ascent over broad areas in the lower and middle portions of the crust.
- *Okubo and Wolfe* [2008] suggest DLPs beneath Mauna Loa resulted from resonance of a fluid-filled crack that could be modulated by teleseismic events.
- *Soosalu et al.* [2010] suggest DLPs beneath Askja volcano in Iceland represent bursts of magma motion opening dykes.

- *Nichols et al.* [2011] suggest DLPs in Cascadia represent fluid and/or magma transport along pre-existing tectonic structures in the middle crust.
- *Han et al.* [2018] found that DLPs at Mount St. Helens were modulated by solid Earth tidal stresses suggesting that their occurrence is related to magmatic and/or fluid activity.

Spatiotemporal association of DLPs with surface and subsurface activity in these cases strongly supports fluid movement as a possible source mechanism for DLPs.

The DLP Swarms in Marie Byrd Land, Antarctica

Lough et al. [2013] used the Antarctic Network component of the Polar Earth Observing Network (POLENET/ANET) to identify DLPs beneath the volcanic Executive Committee Range (ECR) in Marie Byrd Land (MBL), Antarctica. A total of 1370 events, concentrated primarily in two swarms beginning in January 2010 and March 2011, were detected and located beneath the ice at 25-40 km depth. These events have been interpreted as a present location of active intraplate magmatic activity. It is not believed that eruptions have accompanied the two swarms, as there was no detectable shallower volcanic seismicity or other activity. It is likely, though, that DLPs have accompanied past eruptions.

Chapter 4 presents an analysis on the utilization of subspace detection methodology to study the DLP swarms in MBL. The study details the detection and location of 1158 DLP events in 2010 as well as the detection of sustained DLP activity over 8 years that continues through the most recent data. This analysis contributes to the growing body of literature about DLP earthquakes and seismic sources in Antarctica.

1.6 Additional Studies

In addition to my work presented in Chapters 2, 3, and 4, I also contributed to several U.S. Geological Survey peer-reviewed publications as a secondary author during my internship at the National Earthquake Information Center working on automated event detection. Brief overviews of those studies follow.

Hundreds of Earthquakes per Day: The 2014 Guthrie, Oklahoma, Earthquake Sequence [*Benz et al.*, 2015]

We first applied subspace detection to a single seismic station near a highly energetic induced seismic sequence in Guthrie, Oklahoma. This sequence was part of the remarkable increase in seismic activity rattling Oklahoma since 2009. We detected 51,112 events in a 6.5-month period, from 14 February 2014 through 31 August 2014, supplementing the catalog of 79 earthquakes reported by the USGS. The average number of detections per day was 258 and the maximum was 2462. Interestingly, the dense seismic activity allowed us to study temporal variations in the frequency-magnitude distribution (FMD) *b*-value which was found to sharply increase in the few days prior to the largest observed earthquakes indicating possibly utility in seismic forecasting. This study demonstrated that an optimal set of subspace detectors is effective at targeting and characterizing earthquake sequences, and when combined with observations of time-varying *b*-values, provides possible insight into potential earthquake forecasting. Furthermore, it demonstrated that the USGS catalog of earthquake source parameters for Oklahoma is sufficient to design optimal sets of waveform templates, both retrospectively and in real time, which can vastly improve monitoring of numerous earthquake sequences that have developed throughout Oklahoma in recent years. This study is presented in Appendix 4.

Reactivated faulting near Cushing, Oklahoma: Increased potential for a triggered earthquake in an area of United States strategic infrastructure [*McNamara et al.*, 2015a]

We applied single-station subspace detection to the aftershock sequence of a $\mathbf{M_W}$ 4.3 earthquake that occurred near Cushing, Oklahoma, home of the largest crude oil storage facility in the world. We detected 4245 events in one month between 17 October 2014 and 20 November 2014 indicating intense low-magnitude aftershock activity near the major hub of U.S. oil and gas pipeline transportation system. The study demonstrated that the nearby fault zones are critically stressed enough to increase the likelihood of a large and damaging earthquake. In fact, the fault system hosted a $\mathbf{M_W}$ 5.0 earthquake on 7 November 2016 that injured one person and severely damaged 40 buildings leaving the Cushing downtown area temporarily uninhabitable [*Morison*, 2016; *U.S. Geological Survey*, 2016a].

Efforts to monitor and characterize the recent increasing seismicity in central Oklahoma [*McNamara et al.*, 2015b]

This study delineated numerous reactivated subsurface faults throughout central Oklahoma and found that the majority of them are favorably oriented for earthquake rupture. These necessary first-order observations are required to assess the potential hazards of individual faults in Oklahoma and assess both short-term (traffic-light) and long-term (NSHM) earthquake hazard. The study concluded that the increased rate and occurrence of earthquakes near optimally oriented and long fault structures has raised the earthquake hazard in central Oklahoma and has increased the probability for a damaging earthquake.

1.7 TABLE FOR CHAPTER 1

Table 1.1: Summary of energy and correlation detectors discussed in Section 1.1.

DETECTOR	ENERGY	CORRELATION
Primary Function	Detect transient energy increases	Detect similar waveforms
Pros	• Broadly applicable • No *a priori* knowledge necessary • Less computationally expensive	• Discriminant detection • Microseismic event detection • Good in low signal-to-noise environments
Cons	• Indiscriminant detection • Potentially high false alarm rates	• More computationally expensive • *A priori* knowledge necessary • Insensitive to changes
Useful application	Initial data exploration	Repeating event detection

1.8 FIGURES FOR CHAPTER 1

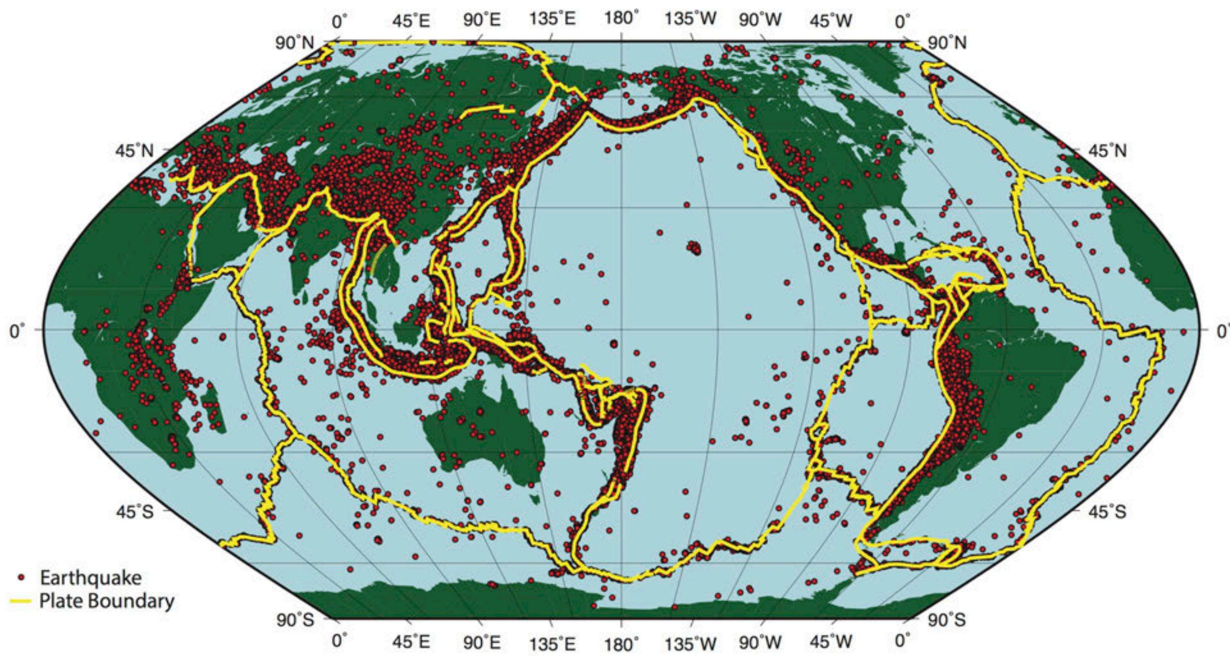

Figure 1.1. Map of 77,752 earthquakes (red dots) larger than or equal to **M** 5 from 1960 through 2017 and tectonic plate boundaries (yellow lines). The vast majority of earthquakes are interplate events occurring at plate boundaries and within broad zones of deformation (e.g., Tibetan Plateau). Earthquake locations are from the U.S. Geological Survey (USGS) Comprehensive Earthquake Catalog (ComCat) and plate boundaries are from University of Texas Institute for Geophysics [http://www-udc.ig.utexas.edu/external/plates/data.htm].

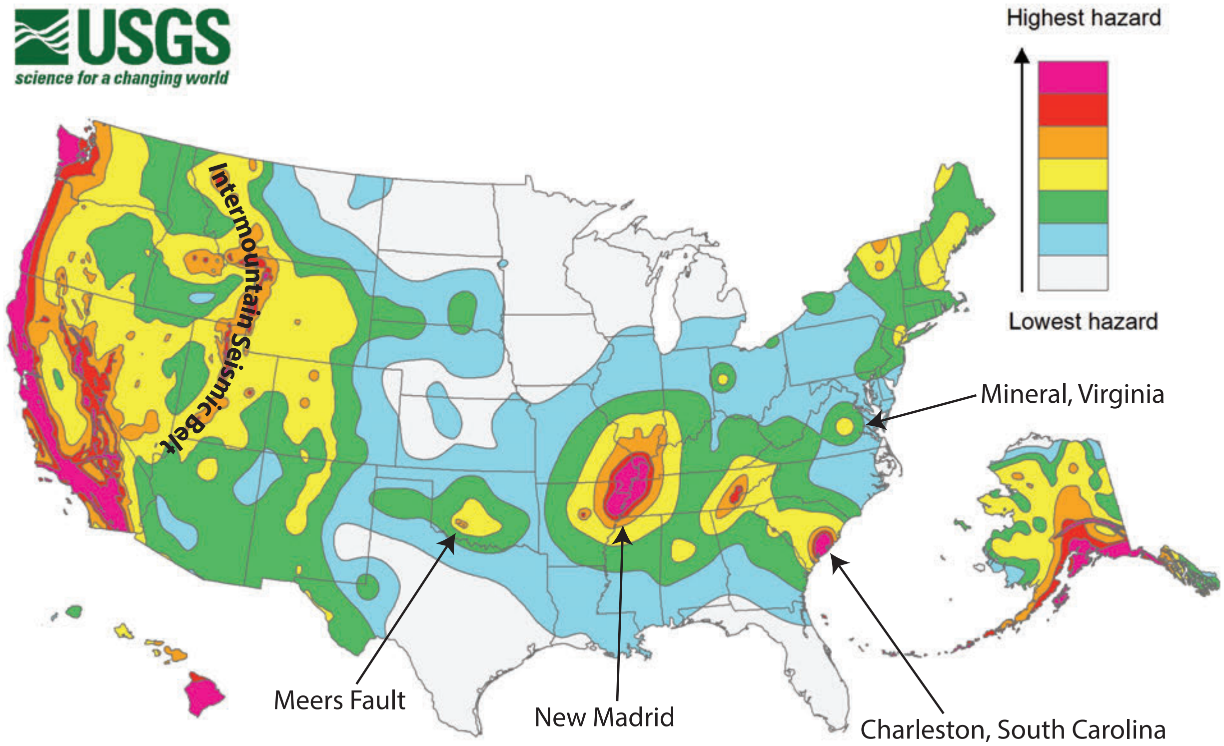

Figure 1.2. USGS 2014 National Seismic Hazard Map (NSHM) with special zones of tectonic intraplate seismicity discussed in Section 1.3 identified. The special zones show increased hazard/probability for damaging earthquakes. Adapted from *Peteresen et al*. [2014].

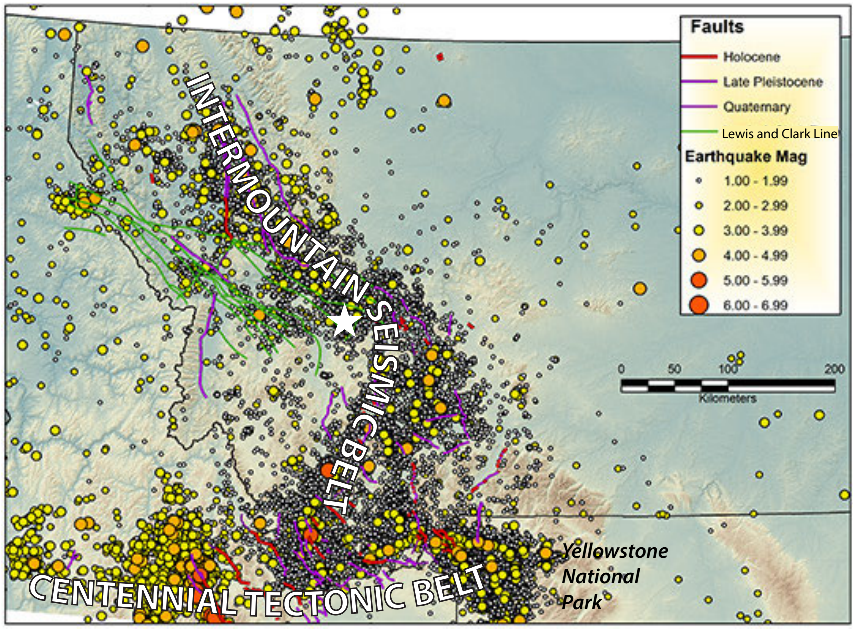

Figure 1.3. Map of historical seismicity in western Montana and surrounding regions. The ISB extends through western Montana and the Centennial Tectonic belt extends west from Yellowstone National Park to central Idaho. The 6 July 2017 **M**$_\mathbf{W}$ 5.8 Lincoln, Montana earthquake (white star) occurred within the Lewis and Clark Line (LCL) (green lines). Adapted from *Montana Bureau of Mines and Geology* [2018].

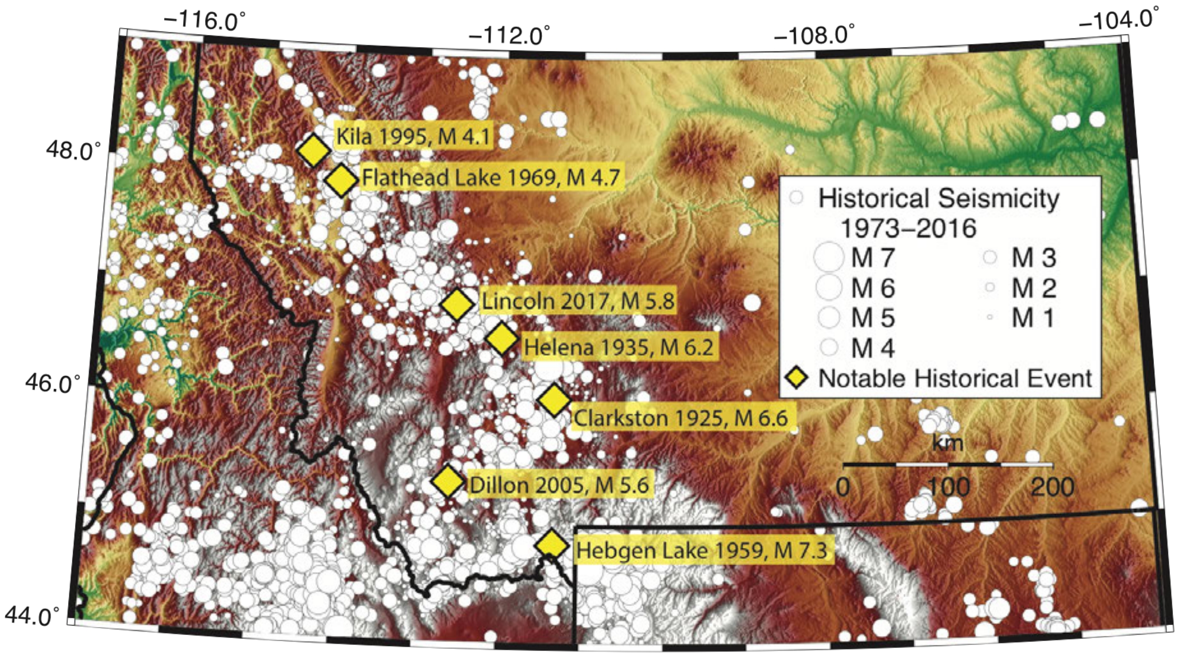

Figure 1.4. Map of historical seismicity in Montana and surrounding regions from 1973 through 2016 contained in the USGS's Comprehensive Catalog of Earthquakes with locations of notable historical events discussed in Section 1.3 identified.

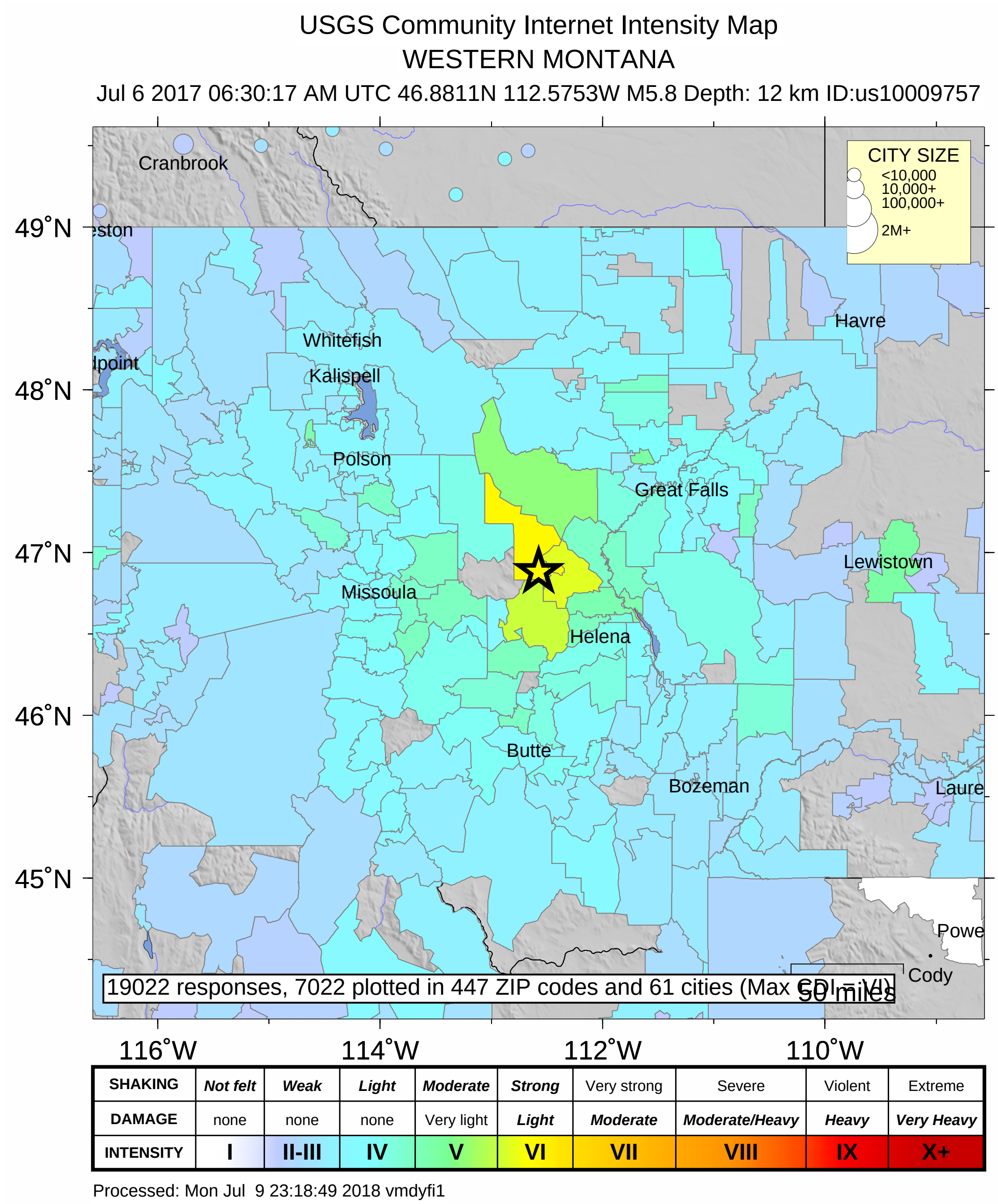

Figure 1.5. Reported shaking intensity map for the 6 July 2017 **M_W** 5.8 Lincoln, Montana earthquake. The star indicates the earthquake epicenter. From *U.S. Geological Survey* [2017b].

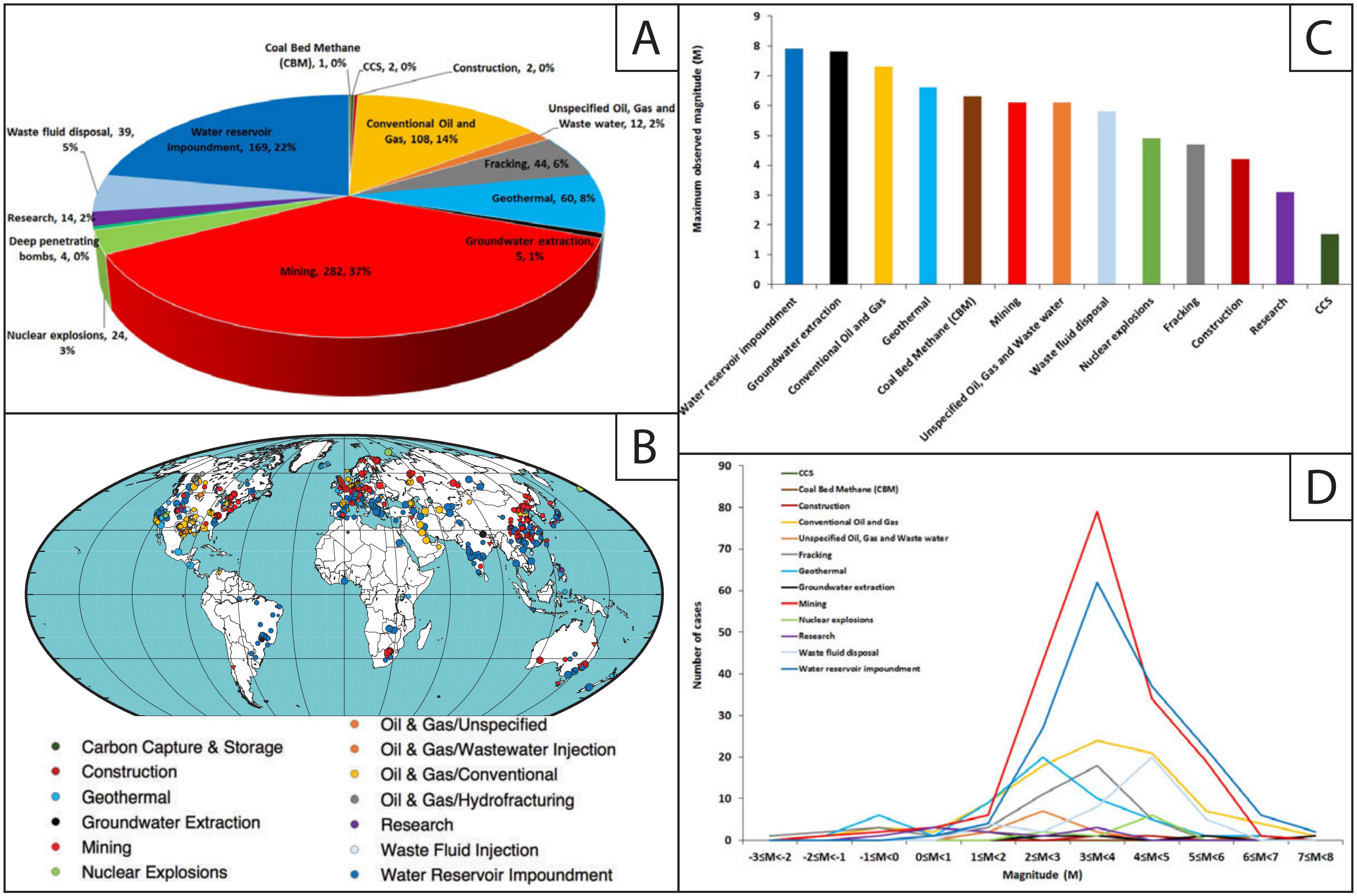

Figure 1.6. Key graphs developed from the *HiQuake* database of induced earthquakes. (A) The graph shows the proportions of cases each activity contributes to *HiQuake*. (B) The map shows the locations of the cases contained in *HiQuake*. (C) The graph shows the maximum observed magnitudes to date for various types of activity. (D) The graph shows the number of cases in *HiQuake* by magnitude range. From *Foulger et al*. [2018] and *Wilson et al*. [2018].

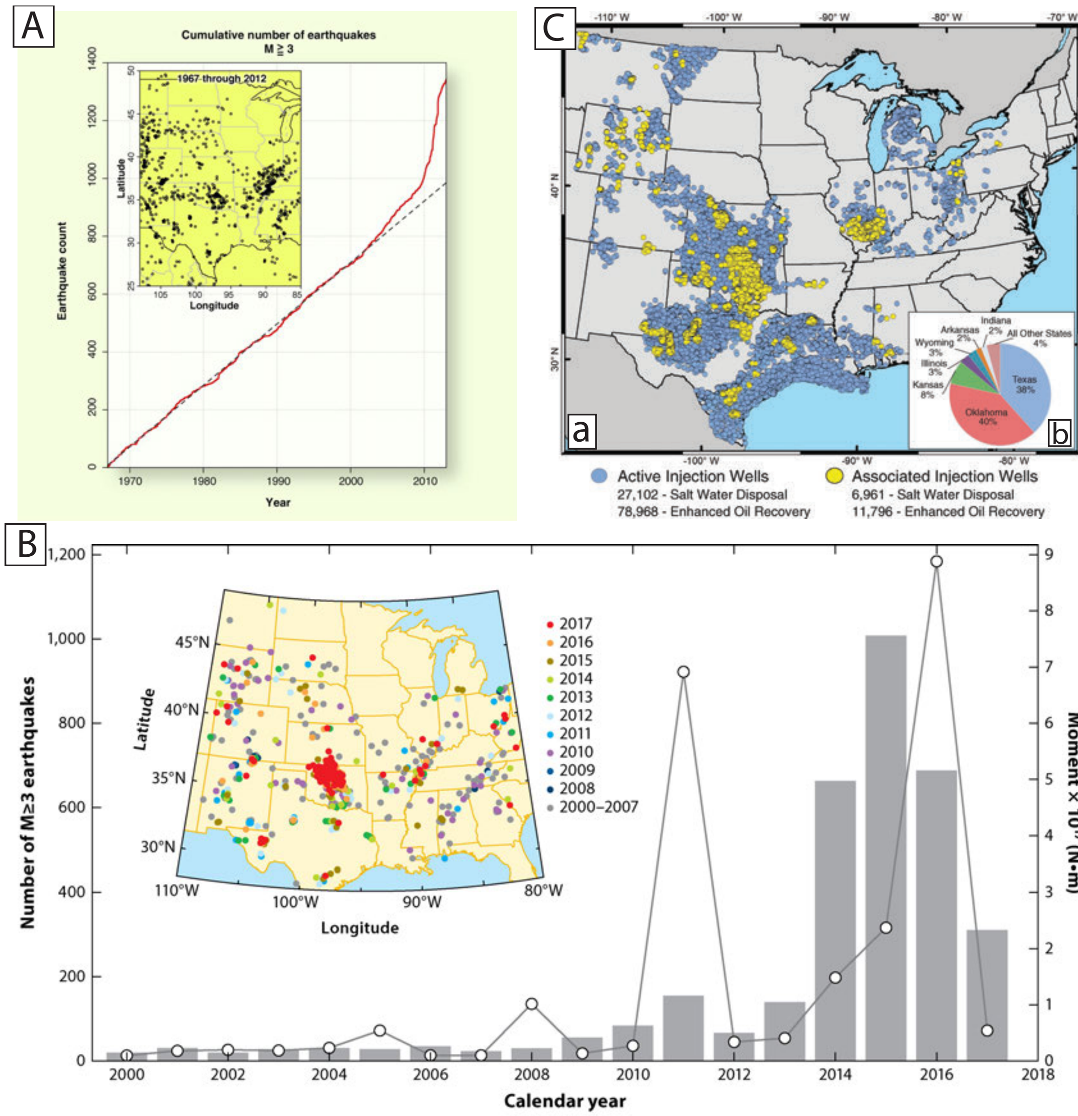

Figure 1.7. (A) Cumulative count of earthquakes of **M** ≥ 3 in the central and eastern United States (CEUS), 1967-2012. The dashed line corresponds to the long-term rate of 21.2 earthquakes/year observed from 1967 to 2000. Inset: Distribution of earthquake epicenters. From *Ellsworth* [2013]. (B) Number of **M** ≥ 3 earthquakes (gray bars) in the CEUS from January 2000 to November 2017, along with summed seismic moment release during each year (white dots). Inset: Distribution of earthquake epicenters colored by year of occurrence. The number of earthquakes peaked in 2015, but total moment release was highest in 2011, when $\mathbf{M_W}$ 5.7 and $\mathbf{M_W}$ 5.4 earthquakes occurred in Prague, Oklahoma, and Raton Basin, Colorado, respectively, and in 2016, when $\mathbf{M_W}$ 5.1, $\mathbf{M_W}$ 5.8, and $\mathbf{M_W}$ 5.0 earthquakes occurred in Fairview, Pawnee, and Cushing, Oklahoma, respectively. From *Keranen and Weingarten* [2018]. (C) Active and associated class II injection wells in the CEUS. (a) Map showing the location of active class II injection wells. Active injection wells are shown as blue circles. Wells associated with earthquakes are shown as yellow circles. (b) The inset pie diagram shows percentage of all associated wells in each state. Only 8% of all injection wells are located in Oklahoma, but 40% of the wells associated with earthquakes are in Oklahoma. From *Weingarten et al.* [2015].

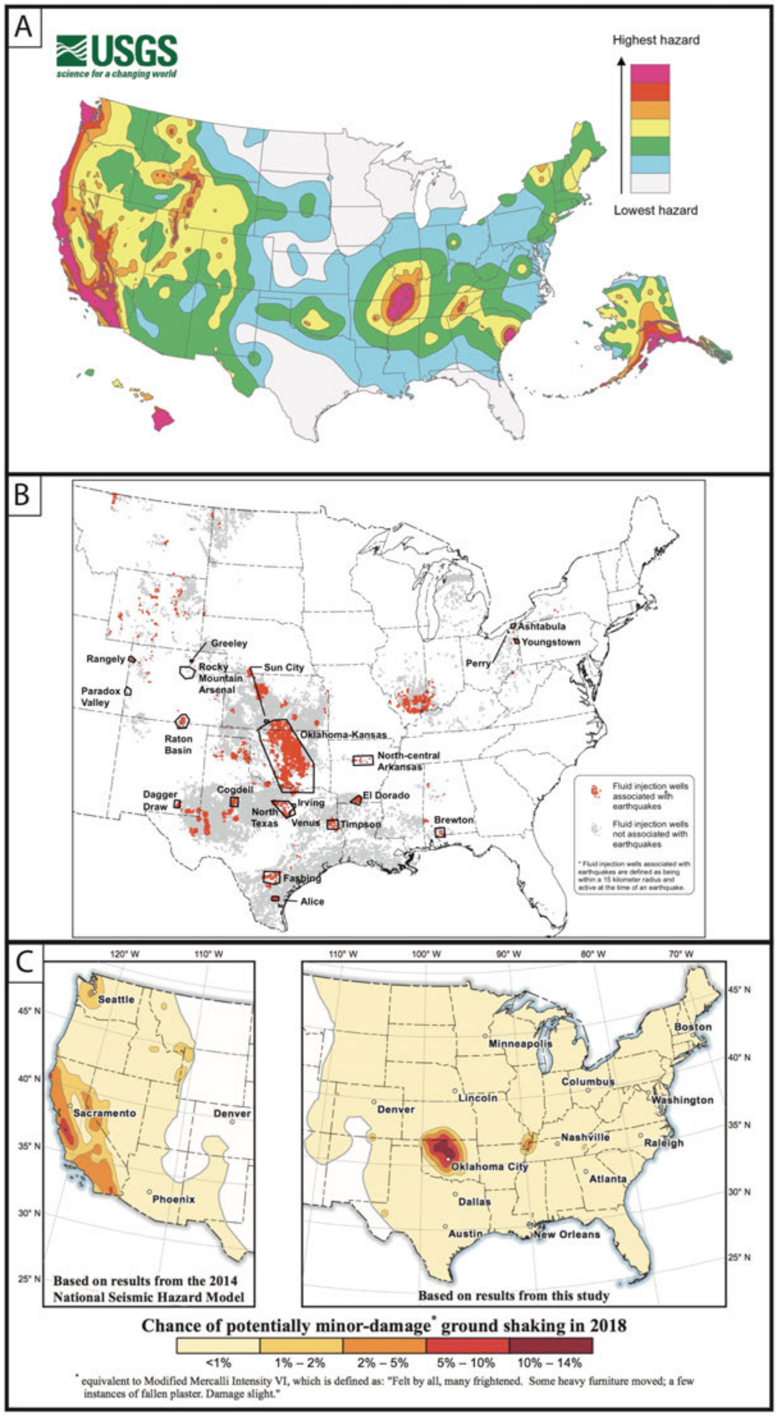

Figure 1.8. (A) USGS 2014 long-term National Seismic Hazard Map with hazard from nontectonic earthquakes removed. From *Petersen et al.* [2014]. (B) 21 zones of induced seismicity identified by the USGS for creation of short-term hazard maps. Red dots are fluid injection wells associated with earthquakes, and grey dots are fluid injection wells not associated with earthquakes. From *Petersen et al.* [2016]. (C) USGS 2018 one-year potential hazard map for natural and human-induced earthquakes. This map shows high hazard in central and north-central Oklahoma. From *Petersen et al.* [2018].

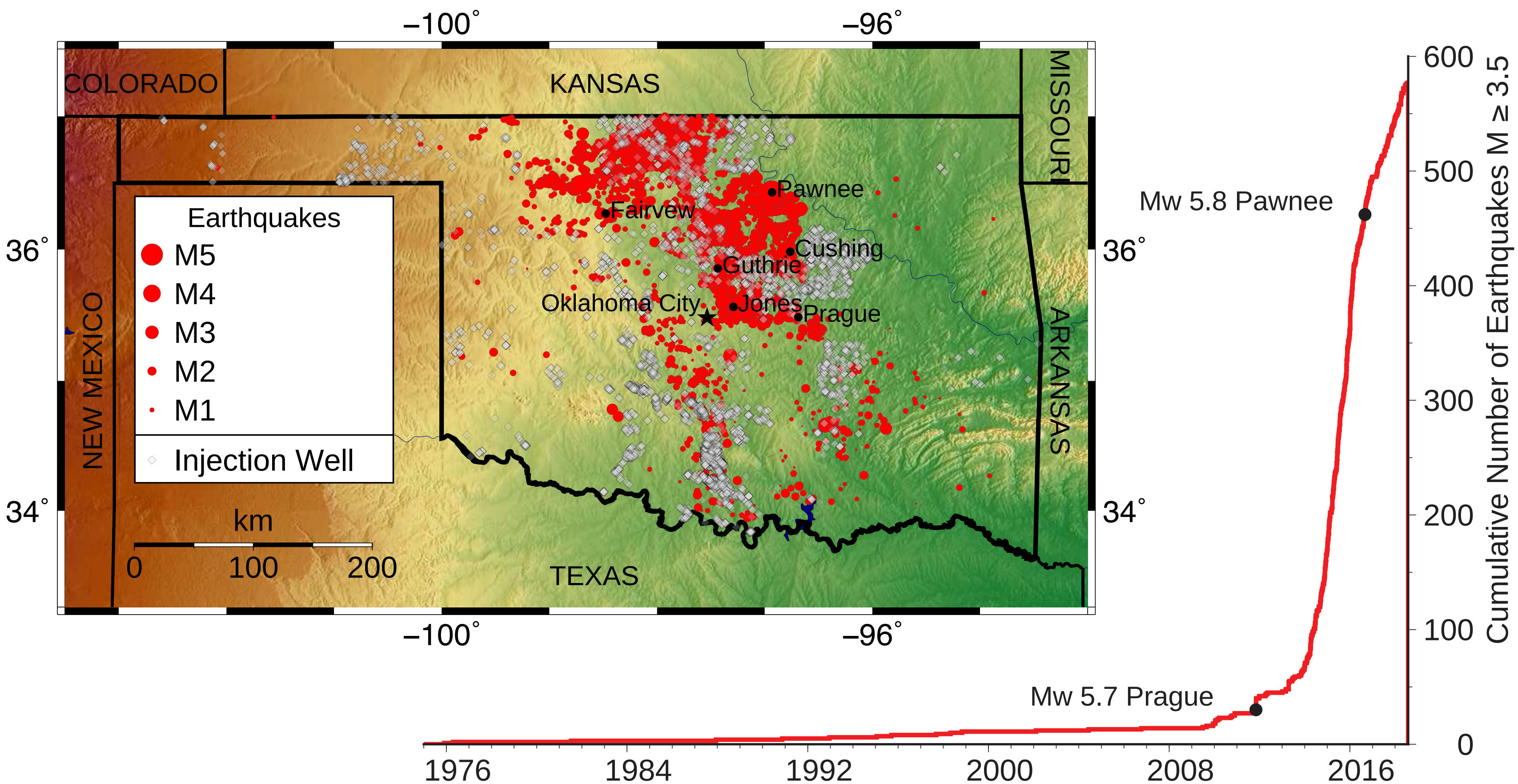

Figure 1.9. (Top left) Location of all historical seismicity and injection wells in Oklahoma through July 2018. (Right bottom) Cumulative number of earthquakes in Oklahoma with magnitudes greater than or equal to 3.5 as a function of year from 1974 through July 2018. Prior to 2009, Oklahoma averaged ~2 earthquakes **M** ≥ 3.5 per year. In 2015, there were 191 earthquakes **M** ≥ 3.5. Times of the 2016 Pawnee and 2011 Prague earthquakes identified, the first and second largest earthquakes recorded in the state.

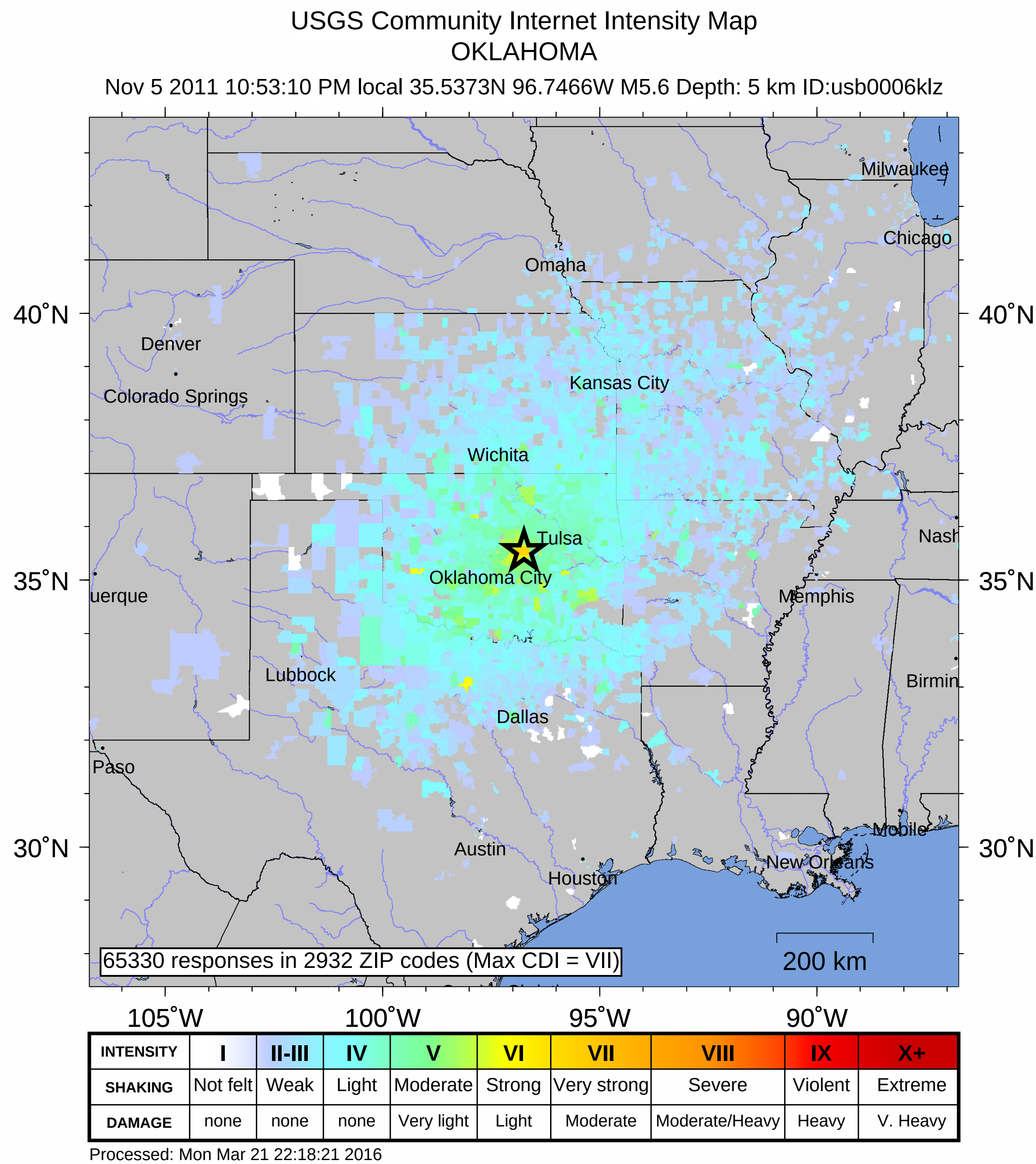

Figure 1.10. Reported shaking intensity map for the 5 November 2011 **M**$_W$ 5.7 Prague, Oklahoma earthquake. The star indicates the earthquake epicenter. From *U.S. Geological Survey* [2011a].

Figure 1.11. Examples of damage incurred from the 2011 $\mathbf{M_W}$ 5.7 Prague, Oklahoma earthquake. (A) Toppled turret on century-old Tudor revival Benedictine Hall at the now closed St. Gregory's University in Shawnee, Oklahoma, 25 km from the epicenter. All four towers were eventually removed and rebuilt due to earthquake damage. (B) Bricks fallen from three sides of a home in Sparks, Oklahoma, ~6 km from the epicenter. (C) Structural engineers condemned a workshop used by monks at St. Gregory's University in Shawnee, Oklahoma. (D) A gaping hole in the ceiling of a house in Sparks, Oklahoma created when the chimney toppled onto the roof. (E) Damaged bathroom in Sparks, Oklahoma. (F) Collapsed chimney in Sparks, Oklahoma. (G) Toppled chimney near epicenter. From *NewsOK* [2011], *U.S. Geological Survey* [2011b], and *Wertz* [2015].

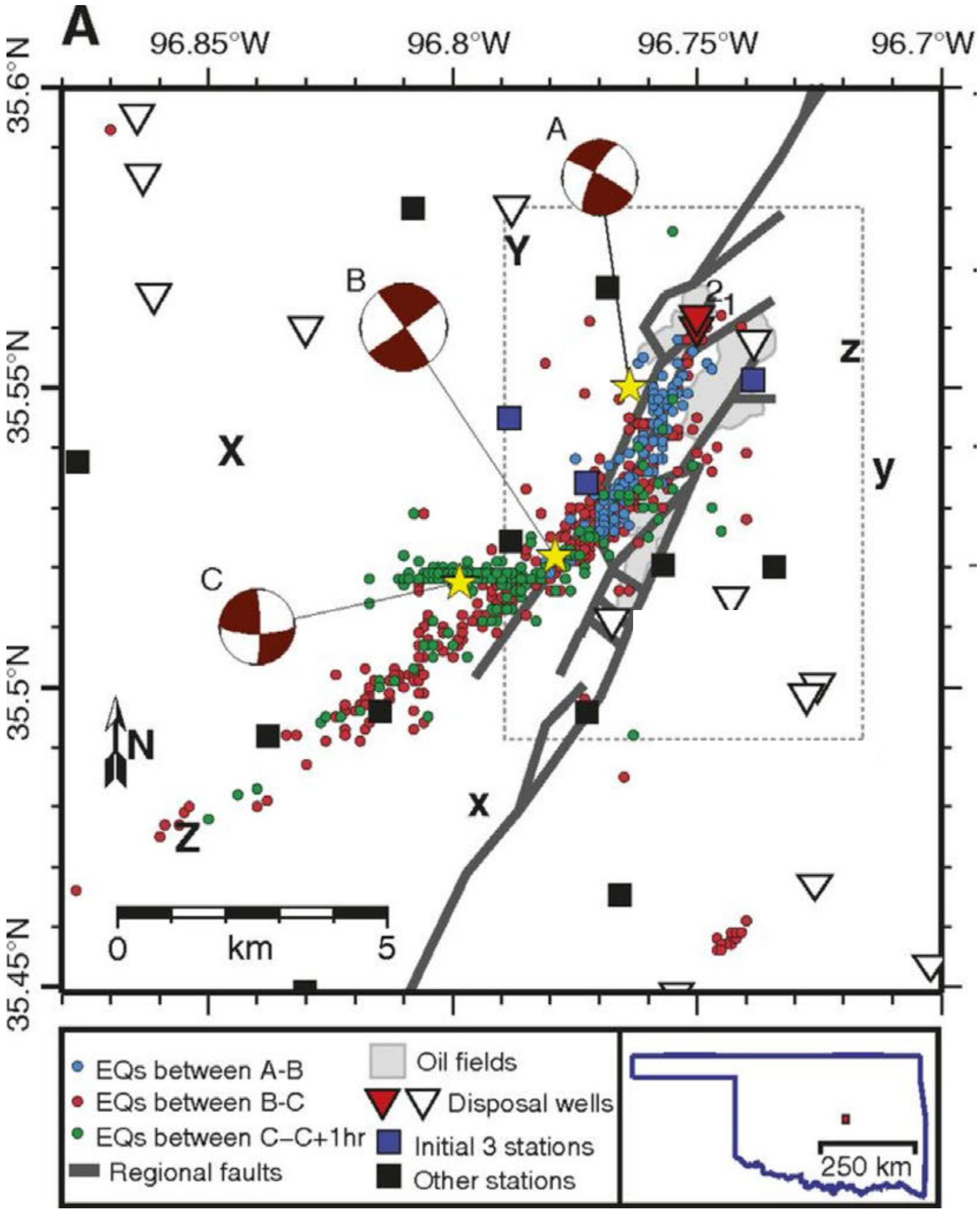

Figure 1.12. Seismicity, centroid moment tensor mechanisms, seismic stations, active disposal wells, and oil fields near the Prague, Oklahoma earthquake. Event A is the $\mathbf{M_W}$ 4.8 foreshock. Event B is the $\mathbf{M_W}$ 5.7 mainshock. Event C is the largest $\mathbf{M_W}$ 4.8 aftershock. Event A likely nucleated on fault defined by aftershock locations (blue dots). Wells 1 and 2 inject near aftershocks of event A. Adapted from *Keranen et al.* [2013].

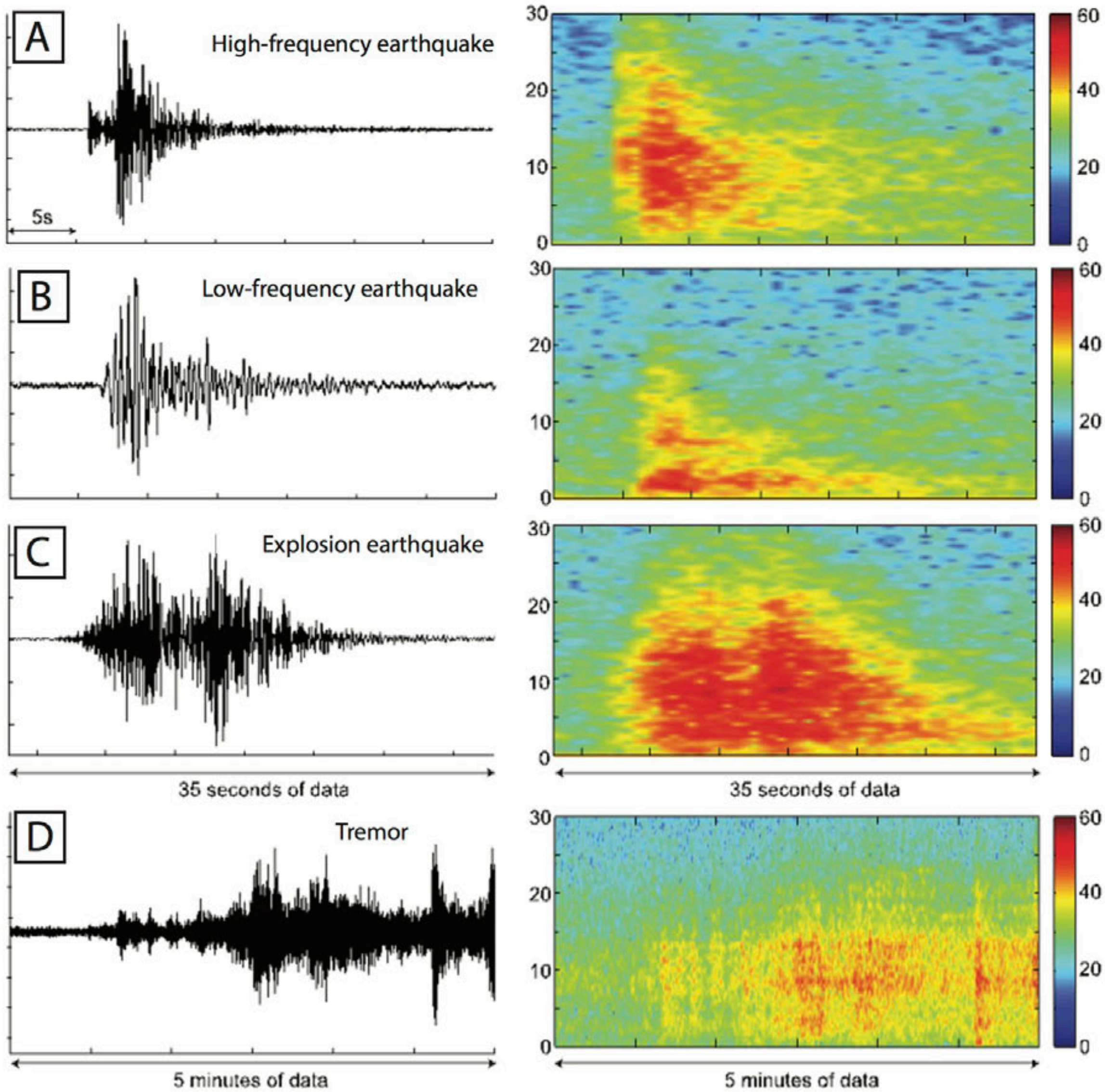

Figure 1.13. Four basic types of seismic signals recorded at a single station on Sinabung volcano in North Sumatra. Left column is the uncorrected, unfiltered signal waveform; right column is the normalized spectrograms with red representing high power values, and blue, low values. Figure parts A-C are 35 s of data and D is 5 min of data. (A) Typical high-frequency (HF) event with defined *P*- and *S*-phase arrivals and a broad spectral range. (B) Typical low-frequency (LF) event with broadband, emergent onset followed by narrow band coda of decaying harmonic oscillations and a lack of *S*-phase. (C) Typical explosion event. (D) Example of tremor composed of repeating, closely spaced events. Adapted from *Gunawan et al.* [2018].

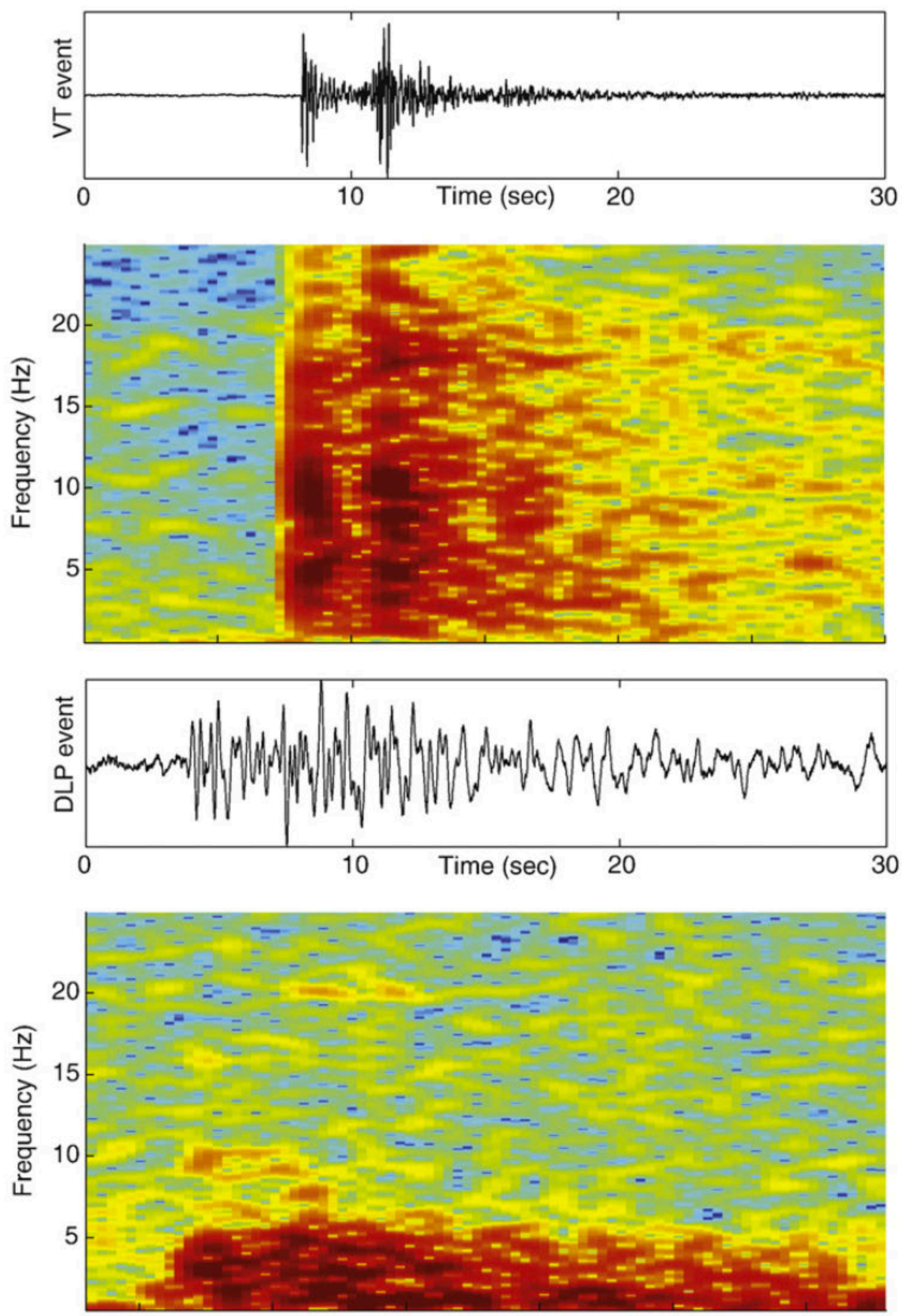

Figure 1.14. Seismograms and spectrograms from two events recorded near Mt. Rainier illustrate the difference in frequency content. (Top) HF event with impulsive onset and energy between 1 and 20 Hz. (Bottom) DLP event with more emergent onset, energy primarily below 5 Hz, and a long, ringing coda. Spectrogram colors represent amplitude intensity and range from blue (low) to yellow (intermediate) to red (high). Adapted from *Nichols et al.* [2011].

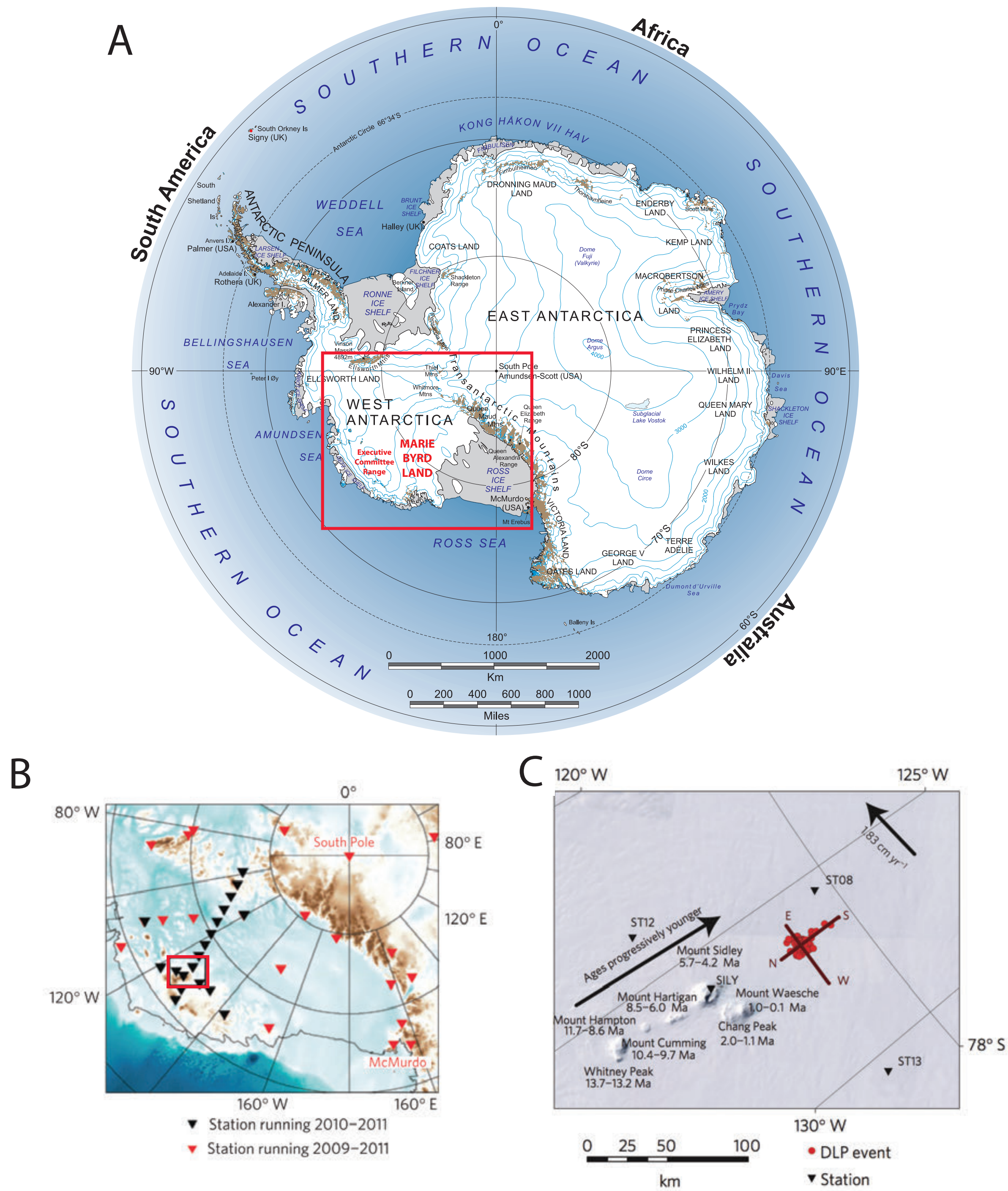

Figure 1.15. (A) Location map of Antarctic features with Marie Byrd Land (MBL) and the Executive Committee Range (ECR) in red text. Red box indicates extent of map in B. Adapted from *https://lima.usgs.gov*. (B) POLENET/ANET stations over bed topography. Red box indicates extent of map in C. (C) ECR volcanoes labeled with dates of known volcanism. DLP swarms occur ~55 km south of Mount Sidley along the age-progression line. Arrow shows HS3-NUVELLA1A plate motions. B and C adapted from *Lough et al.* [2013].

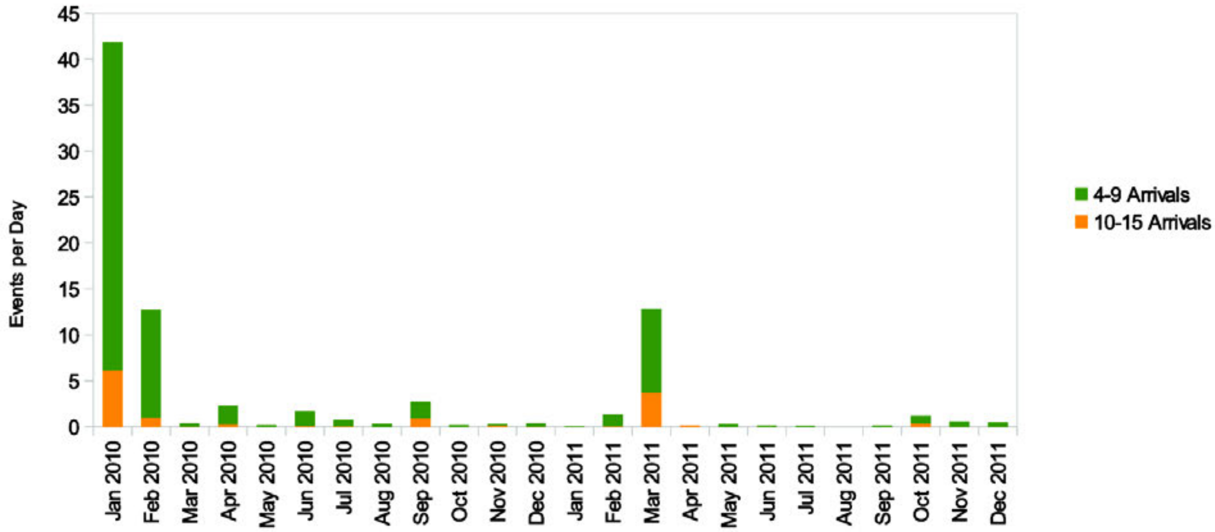

Figure 1.16. Histogram of DLP events detected in 2010-2011 by month. Events are binned by number of arrivals. From *Lough et al.*, [2013].

REFERENCES FOR CHAPTER 1

Agee, S. C. (2014), *Oklahoma's Oil and Natural Gas Industry Economic Impact and Jobs Report – June 2014*, Oklahoma City: Oklahoma: The Steven C. Agee Economic Research and Policy Institute, accessed 26 Aug 2018, https://oerb.com/uploads/press-releases/economicimpact2014-final.pdf.

Aki, K. and R. Koyanagi (1981), Deep volcanic tremor and magma ascent mechanism under Kilauea, Hawaii, *J. Geophys. Res.*, 86(B8), 7095-7109, doi: 10.1029/JB086iB08p07095.

Allen, R. (1982), Automatic phase pickers: Their present use and future prospects, *Bull. Seismol. Soc. Am.*, 72(6B), S225-S242.

Arabasz, W. J. and R. B. Smith (1981), Earthquake prediction in the Intermountain Seismic Belt – An intraplate extensional regime, In D. W. Simpson and P. G. Richards (Eds.), *Earthquake Prediction: An International Review* (Vol. 4, pp. 248-258), Washington, D.C.: American Geophysical Union, doi: 10.1029/ME004p0248.

Aso, N, K. Ohta, and S. Ide (2011), Volcanic-like low-frequency earthquakes beneath Osaka Bay in the absence of a volcano, *Geophys. Res. Lett.*, 38(8), L08303, doi: 10.1029/2011GL046935.

Aso, N. and V. C. Tsai (2014), Cooling magma model from deep volcanic long-period earthquakes*, J. Geophys. Res.-Sol.Ea.*, 119(11), 8442-8456, doi: 10.1002/2014JB011180.

Aso, N., K. Ohta, and S. Ide (2013), Tectonic, volcanic, and semi-volcanic deep low-frequency earthquakes in western Japan, *Tectonophysics*, 600, 27-40, doi: 10.1016/j.tecto.2012.12.015.

Baillard, C., W. C. Crawford, V. Ballu, C. Hibert, and A. Mangeney (2014), An automatic kurtosis-based P- and S-phase picker designed for local seismic networks, *Bull. Seismol. Soc. Am.*, 104(1), 394-409, doi: 10.1785/0120120347.

Bannister, S. and B. L . N. Kennett (2002), Seismic activity in the Transantarctic Mountains – Results from a broadband array deployment, *Terra Antarctica*, 9(1), 41-46.

Bao, X. and D. W. Eaton (2016), Fault activation by hydraulic fracturing in western Canada, *Science*, doi: 10.1126/science.aag2583.

Bassis, J. N., H. A. Fricker, R. Coleman, Y. Bock, J. Behrens, D. Darnell, M. Okal, and J.-B. Minster (2007), Seismicity and deformation associated with ice-shelf rift propagation, *J. Glaciology*, 53(183), 523-536, doi: 10.3189/002214307784409207.

BC Oil and Gas Commission (2012), *Investigation of observed seismicity in the Horn River Basin*, accessed 28 Aug 2018, https://www.bcogc.ca/node/8046/%20download?documentID=1270.

Behrendt, J. C. (2013), The areomagneticc method as a tool to identify Cenozoic magmatism in the West Antarctic Rift System beneath the West Antarctic Ice Sheet – A Review: Theil subglacial volcano as possible source of ash layer in WAISCORE, *Tectonophysics*, 585, 124-136, doi: 10.1016/j.tecto.2012.06.035.

Benz, H. M., N. D. McMahon, R. C. Aster, D. E. McNamara, and D. B. Harris (2015), Hundreds of earthquakes per day: The 2014 Guthrie, Oklahoma, earthquake sequence, *Seismol. Res. Lett.*, 86(5), 1318-1325, doi:10.1785/0220150019.

Bindschadler, R. A., M. A. King, R. B. Alley, S. Anandakrishnan, and L. Padman (2003), Tidally controlled stick-slip discharge of a west Antarctic ice, *Science*, 301(5635), 1087-1089, doi: 10.1126/science.108723.

Bobrov, D., I. Kitov, and L. Zerbo (2014), Perspectives of cross-correlation in seismic monitoring at the International Data Centre, *Pure Appl. Geophys.*, 171(3-5), 439-468, doi: 10.1007/s00024-012-0626-x.

Boger, S. D. (2011), Antarctica – Before and after Gondwana, *Gondwana Res.*, 19(2), 335-271, doi: 10.1016/j.gr.2010.09.003.

Briggeman, K. (2017, Jul 6), Big shake, little damage in western Montana's biggest earthquake, *Missoulian*, accessed 27 Aug 2018, https://missoulian.com/news/local/big-shake-little-damage-in-western-montana-s-biggest-earthquake/article_58beb121-5ae5-5ad0-ad04-f4ab25b339cf.html.

Buchanan, R. C., K. D. Newell, S. Catherine, and R. D. Miller (2014), Induced seismicity: The potential for triggered earthquakes in Kansas, *Kansas Geological Survey Public Information Circular 36*, accessed 15 Sep 2018, http://www.kgs.ku.edu/Publications/PIC/PIC36r.pdf.

Cetin, H. (2003), Comment on "Known and suggested quaternary faulting in the midcontinent United States" by Russel L. Wheeler and Anthony Crone, *Eng. Geol.*, 69(1-2), 193-210, doi: 10.1016/S0013-7952(02)00270-3.

Chaney, R. (2017, Jul 6), Montana escapes significant damage from quake centered near Lincoln, *Billings Gazette*, accessed 27 Aug 2018, https://billingsgazette.com/news/state-and-regional/montana/montana-escapes-significant-damage-from-quake-centered-near-lincoln/article_eeceaecf-80ae-5e58-bb27-c5465f5e8f10.html.

Chouet, B. (1992), A seismic model for the source of long-period events and harmonic tremor, In P. Gasparini, R. Scarpa, and K. Aki (Eds.), *Volcanic Seismology*, *IAVCEI Proceedings in Volcanology* (Vol. 3, pp. 133-156), Berlin: Springer, doi: 10.1007/978-3-642-77008-1_11.

Chouet, B. (1996), Long-period volcano seismicity: Its sources and use in eruption forecasting, *Nature*, 380(6572), 309-216, doi: 10.1038/380309a0.

Chouet, B. and R. Matoza (2013), A multi-decadal view of seismic methods for detecting precursors of magma movement and eruptions, *J. Volcanol. Geoth. Res.*, 252, 108-175, doi: 10.1016/j.jvolgeores.2012.11.013.

Cohen, L. and J. Schneyer (2016, May 17), When the oil boom went bust, Oklahoma protected drillers and squeezed schools, *Reuters Investigates*, accessed 26 Aug 2018, https://www.reuters.com/investigates/special-report/usa-oklahoma-bust/

Colorado Geological Survey (2018), Colorado's largest earthquakes, accessed 26 Aug 2018, http://coloradogeologicalsurvey.org/geologic-hazards/earthquakes/colorados-largest-earthquakes/.

Dalton, C. A. and G. Ekström (2006), Global models of surface wave attenuation, *J. Geophys. Res.*, 111(B5), B05317, doi: 10.1029/2005JB003997.

Danesi, S., S. Bannister, and A. Morelli (2007), Repeating earthquakes from rupture of an asperity under an Antarctic outlet glacier, *Earth Planet Sc. Lett.*, 253(1-2), 151-158, doi: 10.1016/j.epsl.2006.10.023.

Davies, R., G. Foulger, A. Bindley, and P. Styles (2013), Induced seismicity and hydraulic fracturing for the recovery of hydrocarbons, *Mar. Petrol. Geol.*, 45, 171-185, doi: 10.1016/j.marpetgeo.2013.03.016.

de Pater, C. J. and S. Baisch (2011), Geomechanical study of Bowland Shale seismicity, Synthesis report commissioned by Cuadrilla Resources Ltd., accessed 28 Aug 2018, http://energyspeakswv.com/Resources/Docs/Studies/Final_Report_Bowland_Seismicity_02-11-11.pdf.

Ellsworth, W. L. (2013), Injection-induced earthquakes, *Science*, 341(6142), 1225942, doi: 10.1126/science.1225942.

Evans, D. M. (1966), The Denver area earthquakes and the Rocky Mountain Arsenal disposal well, *The Mountain Geologist*, 3(1), 23-36.

Fan, X., C. H. Juang, J. Wasowski, R. Huang, Q. Xu, G. Scaringi, C. J. van Westen, and H. B. Havenith (2018), What we learned from the 2008 Wenchuan earthquake and its aftermath: A decade of research and challenges, *Eng. Geol.*, 241, 25-32, doi: 10.1016/j.enggeo.2018.05.004.

Foulger, G. R., M. P. Wilson, J. G. Gluyas, B. R. Julian, and R. J. Davies (2018), Global review of human-induced earthquakes, *Earth-Sci. Rev.*, 178, 438-514, doi: 10.1016/j.earscirev.2017.07.008.

Franz, J. (2017, Jul 6), Magnitude 5.8 earthquake rattles western Montana, *Flathead Beacon*, accessed 27 Aug 2018, https://flatheadbeacon.com/2017/07/06/5-8-magnitude-earthquake-rattles-western-montana/.

Friberg, P., G. Besana-Ostman, and I. Dricker (2014), Characterization of an earthquake sequence triggered by hydraulic fracturing in Harrison County, Ohio, *Seismol. Res. Lett.*, 85(6), 1295-1307, doi: 10.1785/0220140127.

Frohlich, C., C. Hayward, B. Stump, and E. Potter (2011), The Dallas-Fort-Worth earthquake sequence: October 2008 through May 2009, *Bull. Seismol. Soc. Am.*, 101(1), 327-340, doi: 10.1785/0120100131.

Frohlich, C., H. DeShon, B. Stump, C. Hayward, M. Hornbach, and J. I. Walter (2016), A historical review of induced earthquakes in Texas, *Seismol. Res. Lett.*, 87(4), 1022-1038, doi: 10.1785/0220160016.

Frohlich, C., W. Ellsworth, W. A. Brown, M. Brunt, J. Luetgert, T. MacDonald, and S. Walter (2014), The 17 May 2010 M4.8 earthquake near Timpson, east Texas: An event possibly triggered by fluid injection, *J. Geophys. Res.-Sol. Ea.*, 119(1), 581-593, doi: 10.1002/2013JB010755.

Gan, W. and C. Frohlich (2013), Gas injection may have triggered earthquakes in Cogdell oil field, Texas, *P. Natl. A. Sci. USA*, 110(47), 18786-18791, doi: 10.1073/pnas.1311316110.

Gangopadhyay, A. and P. Talwani (2003), Symptomatic features of intraplate earthquakes, *Seismol. Res. Lett.*, 74(6), 863-883, doi: 10.1785/gssrl.74.6.863.

Ge, M. (2005), Efficient mine microseismic monitoring, *Int. J. Coal Geol.*, 64(1-2), 44-56, doi: 10.1016/j.coal.2005.03.004.

Global Volcanism Program (2018), Holocene Volcano List, accessed 11 Sep 2018, https://volcano.si.edu/list_volcano_holocene.cfm.

Gunawan, H., Surono, A. Budianto, Kristianto, O. Prambada, W. McCausland, J. Pallister, and M. Iguchi (2018), Overview of the eruptions of Sinabung eruption, 2010 and 2013-present and details of the 2013 phreomagmatic phase, *J. Volcan. Geoth. Res.*, in press, doi: 10.1016/j.jvolgeores.2017.08.005.

Han, J., J. E. Vidale, H. Houston, D. A. Schmidt, and K. C. Creager (2018), Deep long-period earthquakes beneath Mount St. Helens: Their relationship to tidal stress, episodic tremor and slip, and regular earthquakes, *Geophys. Res. Lett.*, 45(5), 2241-2247, doi: 10.1002/2018GL077063.

Hand, E. (2014), Injection wells blamed in Oklahoma earthquakes, *Science*, 345(6192), 13-14, doi: 10.1126/science.345.6192.13.

Hanks, T. C. and A. C. Johnston (1992), Common features of the excitation and propagation of strong ground motion for North American earthquakes, *Bull. Seismol. Soc. Am.*, 82(1), 1-23.

Hansen, S. M. and B. Schmandt (2015), Automated detection and location of microseismicity at Mount St. Helens with large-N geophone array, *Geophys. Res. Lett.*, 42(18), 7390-7397, doi: 10.1002/2015GL064848.

Harris, D. B. (2006), *Subspace detectors: Theory* (Rep. UCRL-TR-222758), Livermore, California: Lawrence Livermore National Laboratory.

Hasegawa, A. and A. Yamamoto (1994), Deep, low-frequency microearthquakes in or around seismic low-velocity zones beneath active volcanoes in northeastern Japan, *Tectonophysics*, 233(3-4), 233-252, doi: 10.1016/0040-1951(94)90243-7.

Healy, J. H., W. W. Rubey, D. T. Griggs, and C. B. Raleigh (1968), The Denver earthquakes, *Science*, 161(3848), 1301-1310, doi: 10.1126/science.161.3848.1301.

Heeszel, D. S., H. A. Fricker, J. N. Bassis, S. O'Neel, and F. Water (2014), Seismicity within a propagating ice shelf rift: The relationship between icequake locations and ice shelf structure, *J. Geophys. Res.-Earth*, 119(4), 731-744, doi: 10.1002/2013JF002849.

Herd, D. G. (1986), The 1985 Ruiz Volcano Disaster, *EOS Trans. Am. Geophys. U.*, 67(19), 457-460, doi: 10.1029/EO067i019p00457-03.

Hill, D. P., P. Dawson, M. J. S. Johnston, and A. M. Pitt (2002), Very-long-period volcanic earthquakes beneath Mammoth Mountain, California, *Geophys. Res. Lett.*, 29(10), 1370, doi: 10.1029/2002GL014833.

Holland, A. (2013a), Earthquakes triggered by hydraulic fracturing in south-central Oklahoma, *Bull. Seismol. Soc. Am.*, 103(3), 1784-1792, doi: 10.1785/0120120109.

Holland, A. (2013b), Optimal fault orientations within Oklahoma, *Seismol. Res. Lett.*, 84(5), 876-890, doi: 10.1785/0220120153.

Hornbach M. J., H. R. DeShon, W. L. Ellsworth, B. W. Stump, C. Hayward, C. Frohlich, H. R. Oldham, J. E. Olson, M. B. Magnani, C. Brokaw, and J. H. Luetgert (2015), Causal factors for seismicity near Azle, Texas, *Nat. Commun.*, 6(6728), doi: 10.1038/ncomms7728.

Horton, J. W., A. K. Shah, D. E. McNamara, S. L. Snyder, and A. M. Carter (2015), Aftershocks illuminate the 2011 Mineral, Virginia, earthquake causative fault zone and nearby active faults, In J. W. Horton, M. C. Chapman, and R. A. Green (Eds.), *The 2011 Mineral, Virginia, earthquake, and its significance for seismic hazards in eastern North America*, Geological Society of America, doi: 10.1130/2015.2509(14).

Horton, S. (2012), Disposal of hydrofracking waste fluid by injection into subsurface aquifers triggers earthquake swarm in central Arkansas with potential for damaging earthquake, *Seismol. Res. Lett.*, 83(2), 250-260, doi: 10.1785/gssrl.83.2.250.

Hough, S. E. (2014), Shaking from injection-induced earthquakes in the central and eastern United States, *Bull. Seismol. Soc. Am.*, 104(5), 2619-2626, doi: 10.1785/0120140099.

Hseigh, P. A. and J. D. Bredehoeft (1981), A reservoir analysis of the Denver earthquakes: A case of induced seismicity, *J. Geophys. Res. - Sol. Ea.*, 86(B2), 903-920, doi: 10.1029/JB086iB02p00903.

Huang, R. and X. Fan (2013), The landslide story, *Nat. Geosci.*, 6(5), 325-326, doi: 10.1038/ngeo1806.

Hubert, M. K. and W. W. Rubey (1959), Role of fluid pressure in mechanics of overthrust faulting: I. Mechanics of fluid-filled porous solids and its application to overthrust faulting, *GSA Bull*., 70(2), 115-166, doi: 10.1130/0016-7606(1959)70[115:ROFPIM]2.0.CO;2**.**

Johnston, A. C. (1989), The seismicity of "stable continental interiors", In S. Gregersen and P. W. Basham (Eds.), *Earthquakes at North-Atlantic passive margins: Neotectonics and postglacial rebound* (Vol. 266, pp. 299-327), Dordecht, Netherlands: Springer, doi: 10.1007/978-94-009-2311-9_18.

Johnston, A. C. and E. S. Schweig (1996), The enigma of the New Madrid earthquakes of 1811-1812, *Annu. Rev. Earth Pl. Sc.*, 24, 339-384, doi: 10.1146/annurev.earth.24.1.339.

Jones, C. (2017, Nov 15), Deposition: Former state seismologists felt pressured not to link Oklahoma quakes with man-made causes, *Tulsa World*, accessed 26 Aug 2018, https://www.tulsaworld.com/earthquakes/deposition-former-state-seismologist-felt-pressured-not-to-link-oklahoma/article_19c0dfb1-fc12-5a9f-8aa7-eea06d829d8e.html.

Julian, B. R. (1994), Volcanic tremor: Nonlinear excitation by fluid flow, *J. Geophys. Res.*, 99(B6), 11859-11877, doi: 10.1029/93JB03129.

Justinic, A. H., B. Stump, C. Hayward, and C. Frohlich (2013), Analysis of the Cleburne, Texas, earthquake sequence from June 2009 to June 2010, *Bull. Seismol. Soc. Am.*, 103(6), 3083-3093, doi: 10.1785/0120120336.

Kato, A. and S. Nakagawa (2014), Multiple slow-slip events during a foreshock sequence of the 2014 Iquique, Chile Mw 8.1 earthquake, *Geophys. Res. Lett.*, 41(15), 5420-5427, doi: 10.1002/2014GL061138.

Kawakatsu, H. and M. Yamamoto (2015), *Volcano seismology*, In G. Schubert (Ed.), *Treatise on Geophysics* (Ed. 2, Vol. 4, pp. 389-419), Elsevier, doi: 10.1016/B978-0-444-53802-4.00081-6.

Keranen, K. M. and M. Weingarten (2018), Induced Seismicity, *Annu. Rev. Earth Pl. Sc.*, 46, 149-174, doi: 10.1146/annurev-earth-082517-010054.

Keranen, K. M., H. M. Savage, G. A. Abers, and E. S. Cochran (2013), Potentially induced earthquakes in Oklahoma, USA: Links between wastewater injection and the 2011 M_w 5.7 earthquake sequence, *Geology*, 41(6), 699-702, doi: 10.1130/G34045.1.

Keranen, K. M., M. Weingarten, G. A. Abers, B. A. Bekins, and S. Ge (2014), Sharp increase in central Oklahoma seismicity since 2008 induced by massive wastewater injection, *Science*, 345(6195), 448-451, doi: 10.1126/science.1255802.

Knox, H. A. (2012), Eruptive characteristics and glacial earthquakes investigation on Erebus Volcano, Antarctica, PhD dissertation, Dept. Earth and Env. Sci., New Mexico Inst. Of Mining and Tech., Socorro, New Mexico.

Lageson, D. R. and M. C. Stickney (2000), Seismotectonics of northwest Montana, USA, In R. A. Schall and E. H. Johnson (Eds.), *Montana Geological Society 50th Anniversary Symposium, Montana/Alberta Thrust Belt and Adjacent Foreland* (Vol. 1, pp. 109-126), Montana Geological Society.

Li, Z., Z. Peng, D. Hollis, L. Zhu, and J. McClellan (2018), High-resolution seismic event detection using local similarity for large-N arrays, *Sci. Rep*., 8, 1646, doi: 10.1038/s41598-018-19728-w.

Llenos, A. L. and A. J. Michael (2013), Modeling earthquake rate changes in Oklahoma and Arkansas: Possible signatures of induced seismicity, *Bull. Seismol. Soc. Am.*, 103(5), 2850-2861, doi: 10.1785/0120130017.

Lough, A. C. (2014), Studies of seismic sources in Antarctica using an extensive deployment of broadband seismographs, PhD dissertation, Dept. of Earth and Planetary Sci., Washington Univ., St. Louis, Missouri.

Lough, A. C., D. A. Weins, C. Grace Barcheck, S. Anandakrishnan, R. C. Aster, D. D. Blankenship, A. D. Huerta, A. Nyblade, D. A. Young, and T. J. Wilson (2013), Seismic detection of an active subglacial magmatic complex in Marie Byrd Land, Antarctica, *Nat. Geosci.*, 6(12), 1031-1035, doi: 10.1038/ngeo1992.

Luza, K. V., R. F. Madole, and A. J. Crone (1987), *Investigation of the Meers fault, southwestern Oklahoma*, Oklahoma Geological Survey Special Publication (Vol. 87-1), Oklahoma Geological Survey.

Matoza, R. S., P. M. Shearer, and P. G. Okubo (2014), High-precision relocation of long-period events beneath the summit region of Kilauea volcano, Hawaii, from 1986-2009, *Geophys. Res. Lett.*, 41(10), 3413-3421, doi: 10.1002/2014GL059819.

McGarr, A. (2014), Maximum magnitude earthquakes induced by fluid injection, *J. Geophys. Res.-So. Ea.*, 119(2), 1008-1019, doi: 10.1002/2013JB010597.

McGarr, A., D. Simpson, and L. Seeber (2002), Case histories of induced and triggered seismicity, In W. Lee, P. Jennings, C. Kisslinger, and H. Kanamori (Eds.), *International Handbook of Earthquake and Engineering Seismology* (Vol. 81, Part A, pp. 647-661), San Francisco: Academic Press.

McMahon, N. D., R. C. Aster, W. L. Yeck, D. E. McNamara, and H. M. Benz (2017), Spatiotemporal evolution of the 2011 Prague, Oklahoma, aftershock sequence revealed using subspace detection and relocation, *Geophys. Res. Lett.*, 44(14), 7149-7158, doi: 10.1002/2017GL072944.

McNamara, D. E., G. P. Hayes, H. M. Benz, R. A. Williams, N. D. McMahon, R. C. Aster, A. Holland, T. Sickbert, R. Herrmann, R. Briggs, G. Smoczyk, E. Bergman, and P. Earle (2015a), Reactivated faulting near Cushing, Oklahoma: Increased potential for a triggered earthquake in an area of United States strategic infrastructure, *Geophys. Res. Lett.*, 42(20), 8328-8332, doi: 10.1002/2015GL064669.

McNamara, D. E., H. M. Benz, R. B. Herrmann, E. A. Bergman, P. Earle, A. Meltzer, M. Withers, and M. Chapman (2014), The M_W 5.8 Mineral, Virginia, earthquake of August 2011 and aftershock sequence: constraints on earthquake source parameters and fault geometry, *Bull. Seismol. Soc. Am.*, 104(1), 40-54, doi: 10.1785/0120130058.

McNamara, D. E., J. L. Rubinstein, E. Myers, G. Smoczyk, H. M Benz, R. A. Williams, G. Hayes, D. Wilson, R. Herrmann, N. D. McMahon, R. C. Aster, E. Bergman, A. Holland, and P. Earle (2015b), Efforts to monitor and characterize the recent increasing seismicity in central Oklahoma, *The Leading Edge*, 34(6), 628-639, doi: 10.1190/tle34060628.1.

McNutt, S. R. (1996), Seismic monitoring and eruption forecasting of volcanoes: A review of the state-of-the-art and case histories, In R. Scarpa and R. I. Tilling (Eds.), *Monitoring and mitigation of volcano hazards* (pp. 99-146), Berlin: Springer-Verlag, doi: 10.1007/978-3-642-80087-0_3.

McNutt, S. R. (2005), Volcanic seismology, *Annu. Rev. Earth Pl. Sc.*, 33, 461-491, doi: 10.1146/annurev.earth.33.092203.122459.

Mead, T. C. and D. S. Carder (1941), Seismic investigations in the Boulder Dam area in 1940, *Bull. Seismol. Soc. Am.*, 31(4), 321-324.

Meng, X., Z. Peng, and J. L. Hardebeck (2013), Seismicity around Parkfield correlates with static shear stress changes following the 2003 Mw6.5 San Simeon earthquake, *J. Geophys. Res.-Sol.Ea.*, 118(7), 3576-3591, doi: 10.1002/jgrb.50271.

Miyamoto, H. K., A. S. Gilani, and A. Wada (2008), *Reconnaissance report of the 2008 Sichuan earthquake, damage survey of buildings and retrofit options*, Abstract presented at 2008 World Conferences on Earthquake Engineering, Beijing, China.

Montana Bureau of Mines and Geology (2018), Seismicity in Montana, accessed 27 Aug 2018, http://www.mbmg.mtech.edu/quakes/quake-seismicity.html.

Morrison, O. (2016, Nov 7), Update on Oklahoma earthquake: 45 evacuated, one injured, *The Wichita Eagle*, accessed 19 Sep 2018, https://www.kansas.com/news/local/article113029143.html.

Murphy, S. (2016, Sept 12), Oklahoma, EPA shutter 32 wells in new earthquake-prone area, *Associated Press*, accessed 26 Aug 2018, https://apnews.com/612b2303f71641f388b0224fb6dab557/oklahoma-epa-shutter-32-wells-new-earthquake-prone-area.

Nakamichi, H., H. Hamaguchi, S. Tanaka, S. Ueki, T. Nishimura, and A. Hasegawa (2003), Source mechanisms of deep and intermediate-depth low-frequency earthquakes beneath Iwate volcano, northeastern Japan, *Geophys. J. Int.*, 154(3), 811-828, doi: 10.1046/j.1365-246X.2003.01991.x.

National Research Council (2013), *Induced seismicity potential in energy technologies*, Washington, D.C.: The National Academic Press, doi: doi.org/10.17226/13355.

Nettles, M. and G. Ekström (2010), Glacial earthquakes in Greenland and Antarctica, *Annu. Rev. Earth Pl. Sc.*, 38, 467-491, doi: 10.1146/annurev-earth-040809-152414.

News9 (2016, Sept 3), Gov. Fallin declares state of emergency for Pawnee County after quake, accessed 26 Aug 2018, http://www.news9.com/story/33008800/state-responds-to-56-earthquake.

NewsOK (2011, Nov 7), Magnitude 4.7 earthquake reported in Oklahoma's Lincoln County, accessed 26 Aug 2018, https://newsok.com/article/3621066/magnitude-47-earthquake-reported-in-oklahomas-lincoln-county.

Nichols, M. L., S. D. Malone, S. C. Moran, W. A. Thelen, and J. E. Vidale (2011), Deep long-period earthquakes beneath Washington and Oregon volcanoes, *J. Volcanol. Geoth. Res.*, 200(3-4), 116-128, doi: 10.1016/j.jvolgeores.2010.12.005.

Nicholson, C. and R. L. Wesson (1990), Earthquake hazard associated with deep well injection – A report to the U.S. Environmental Protection Agency, *U.S. Geol. Surv. Bull.*, 1951, doi: 10.3133/b1951.

Nuttli, O. W. (1973), Seismic wave attenuation and magnitude relations for eastern North America, *J. Geophys. Res.*, 78(5), 876-885, doi: 10.1029/JB078i005p00876.

Okal, E. A. and J. R. Sweet (2007), Frequency-size distributions for intraplate earthquakes, In S. Stein and S. Mazzotti (Eds.), *Continental intraplate earthquakes: Science, hazard, and policy issues*, Geological Society of America Special Papers (Vol. 425, pp. 59-71), Geological Society of America, doi: 10.1130/2007.2425(05).

Oklahoma Corporation Commission (2015, Jul 17), OCC announces next step in continuing response to earthquake concerns: 200-plus more wells added to action list, accessed 26 Aug 2018, https://occeweb.com/News/DIRECTIVE-2.pdf.

Oklahoma Corporation Commission (2017, Feb 24), Earthquake response summary (as of February 24, 2017), accessed 26 Aug 2018, http://www.occeweb.com/News/2017/02-24-17EARTHQUAKE%20ACTION%20SUMMARY.pdf.

Oklahoma Energy Resources Board (2017), Oklahoma's Oil and Natural Gas Industry Economic Impact Fact Sheet, accessed 26 Aug 2018, https://www.oerb.com/uploads/economicimpact-factsheet.pdf.

Oklahoma Geological Survey (2013, Mar 22), Statement on the Prague Earthquake Sequence from the Oklahoma Geological Survey on March 22, 2013, accessed 26 Aug 2018, http://www.ogs.ou.edu/earthquakes/OGS_PragueStatement201303.pdf.

Oklahoma Geological Survey (2014, Feb 17), Position statement on earthquake activity from the Oklahoma Geological Survey on February 17, 2014, accessed 26 Aug 2018, http://www.ogs.ou.edu/pdf/OGS_POSITION_STATEMENT_2_18_14.pdf.

Oklahoma Geological Survey (2015, Apr 21), Summary statement on Oklahoma seismicity from the Oklahoma Geological Survey on April 21, 2015, *Earthquakes in Oklahoma*, accessed 26 Aug 2018, http://earthquakes.ok.gov/wp-content/uploads/2015/04/OGS_Summary_Statement_2015_04_20.pdf.

Okubo, P. G. and C. J. Wolfe (2008), Swarms of similar long-period earthquakes in the mantle beneath Mauna Loa volcano, *J. Volcanol. Geoth. Res.*, 178(4), 787-794, doi: 10.1016/j.jvolgeores.2008.09.007.

Oskin, B. (2014, May 5), Rare earthquake warning issued for Oklahoma, *Live Science*, accessed 26 Aug 2018, https://www.livescience.com/45361-oklahoma-earthquake-risk-rising.html.

Pardee, J. T. (1926), The Montana earthquake of June 27, 1925, In W. C. Mendenhall (Ed.), *Shorter Contributions to General Geology: Professional Paper 147* (pp. 7-23), Washington, D.C.: Dept. of the Interior and U.S. Geological Survey, doi: 10.3133/pp147.

Peng, Z. and P. Zhao (2009), Migration of early aftershocks following the 2004 Parkfield earthquake, *Nat. Geosci.*, 2, 877-881, doi: 10.1038/ngeo697.

Peng, Z., J. E. Vidale, and H. Houston (2006), Anomalous early aftershock decay rate of the 2004 Mw6.0 Parkfield, California, earthquake, *Geophys. Res. Lett.*, 33(17), L17307, doi: 10.1029/2006GL026744.

Petersen, M. D., A. D. Frankel, S. C. Harmsen, C. S. Mueller, K. M. Haller, R. L. Wesson, Y. Zeng, O. S. Boyd, D. M. Perkins, N. Luco, E. H. Field, C. J. Willis, and K. S. Rukstales (2008), *Documentation for the 2008 update of the United State national seismic hazard maps* (USGS Open-File Rep. 2008-1128), U.S. Geological Survey, accessed 15 Sep 2018, https://pubs.usgs.gov/of/2008/1128/pdf/OF08-1128_v1.1.pdf.

Petersen, M. D., C. S. Mueller, M. P. Moschetti, S. M. Hoover, A. L. Llenos, W. L. Ellsworth, A. J. Michael, J. L. Rubinstein, A. F. McGarr, and K. S. Rukstales (2016), *2016 one-year seismic hazard forecast for the Central and Eastern United States from induced and natural earthquakes* (USGS Open-File Rep. 2016-1035), U.S. Geological Survey, doi: 10.3133/ofr20161035.

Petersen, M. D., C. S. Mueller, M. P. Moschetti, S. M. Hoover, A. M. Shumway, D. E. McNamara, R. A. Williams, A. L. Llenos, W. L. Ellsworth, A. J. Michael, J. L. Rubinstein, A. F. McGarr, and K. S. Rukstales (2017), 2017 one-year seismic-hazard forecast for the Central and Eastern United States from induced and natural earthquakes, *Seismol. Res. Lett.*, 88(3), 772-783, doi: 10.1785/0220170005.

Petersen, M. D., C. S. Mueller, M. P. Moschetti, S. M. Hoover, K. S. Rukstales, D. E. McNamara, R. A. Williams, A. M. Shumway, P. M. Powers, P. S. Earle, A. L. Llenos, A. J. Michael, J. L. Rubinstein, J. H. Norbeck, and E. S. Cochran (2018), 2018 one-year seismic hazard forecast for the Central and Eastern United States from induced and natural earthquakes, *Seismol. Res. Lett.*, 89(3), 1049-1061, doi: 10.1785/0220180005.

Petersen, M. D., M. P. Moschetti, P. M. Powers, C. S. Mueller, K. M. Haller, A. D. Frankel, Y. Zeng, S. Rezaeian, S. C. Harmsen, O. S. Boyd, N. Field, R. Chen, K. S. Rukstales, N. Luco, R. L. Wheeler, R. A. Williams, and A. H. Olsen (2014), *Documentation for the 2014 Update of the United States national seismic hazard maps* (USGS Open-File Rep. 2014-1091), U.S. Geological Survey, doi: 10.3133/ofr20141091.

Pitt, A. M., D. P. Hill, S. W. Walter, and M. J. S. Johnson (2002), Midcrustal, long-period earthquakes beneath northern California volcanic areas, *Seismol. Res. Lett.*, 73(2), 144-152, doi: 10.1785/gssrl.73.2.144.

Plenkers, K., K. R. R. Ritter, and M. Schindler (2013), Low signal-to-noise event detection based on waveform stacking and cross-correlation: Application to stimulation experiment, *J. Seimol.*, 17(1), 27-49, doi: 10.1007/s10950-012-9284-9.

Power, J. A., S. D. Stihler, R. A. White, and S. C. Moran (2004), Observations of deep long-period (DLP) seismic events beneath Aleutian arc volcanoes; 1989-2002, *J. Volcanol. Geoth. Res.*, 138(3-4), 243-266, doi: 10.1016/j.jvolgeores.2004.07.005.

Power. J. A., A. D. Jolly, C. J. Nye, and M. L. Harbin (2002), A conceptual model of the Mount Spurr magmatic system from seismic and geochemical observations of the 1992 Crater Peak eruption sequence, *Bull. Volcanol.*, 64, 206-218, doi: 10.1007/s00445-002-0201-x.

Pratt, W. E. and D. W. Johnson (1926), Local subsidence of the Goose Creek oil field, *J. Geol.*, 34, 577-590.

Querry, K. (2016, Sept 3), USGS: 5.6 magnitude earthquake shakes Oklahoma, *Oklahoma's News 4*, accessed 26 Aug 2018, https://kfor.com/2016/09/03/usgs-5-6-magnitude-earthquake-shakes-oklahoma/.

Raleigh, C. B., J. H. Healy, and J. D. Bredehoeft (1976), An experiment in earthquake control at Rangely, Colorado, *Science*, 191(4233), 1230-1237, doi: 10.1126/science.191.4233.1230.

Reading, A. M. (2007), The seismicity of the Antarctic plate, In S. Stein and S. Mazzotti (Eds.), *Continental intraplate earthquakes: Science, hazard, and policy issues*, Geological Society of America Special Papers (Vol. 425, pp. 59-71), Geological Society of America, doi: 10.1130/2007.2425(18).

Rowe, C. A., R. C. Aster, P. R. Kyle, and J. W. Schlue (1998), Broadband recording of Strombolian explosions and associated very-long period seismic signals on Mount Erebus volcano, Ross Island, Antarctica, *Geophys. Res. Lett.*, 25(13), 2297-2300, doi: 10.1029/98GL01622.

Rowe, C. A., R. C. Aster, P. R. Kyle, R. R. Dribble, J. W. Schlue (2000), Seismic and acoustic observations at Mount Erebus Volcano, Ross Island, Antarcica, 1994-1998, *J. Volcanol. Geoth. Res.*, 101(1-2), 105-128, doi: 10.1016/S0377-0273(00)00170-0.

Rowe, C. A., R. C. Aster, W. S. Phillips, R. H. Jones, B. Borchers, and M. C. Fehler (2002), Using automated, high-precision repicking to improve delineation of microseismic structures at the Soultz geothermal reservoir, *Pure Appl. Geophys.*, 159(1-3), 563-596, doi: 10.1007/PL00001265.

Rubinstein, J. L., W. L. Ellsworth, A. McGarr, and H. M. Benz (2014), The 2001-present induced earthquake sequence in the Raton Basin of northern New Mexico and southern Colorado, *Bull. Seismol. Soc. Am.*, 104(5), 2162-2181, doi: 10.1785/0120140009.

Saragiotis, C. D., L. J. Hadjileontiadis, and S. M Panas (2002), PAI-S/: A robust automatic seismic P phase arrival identification scheme, *IEEE T. Geosci. Remote*, 40(6), 1395-1404, doi: 10.1109/TGRS.2002.800438.

Savage, H. M., K. M. Keranen, D. P Schaff, and C. Dieck (2017), Possible precursory signals in damage zone foreshocks, *Geophys. Res. Lett.*, 44(11), 5411-5417, doi: 10.1002/2017GL073226.

Sbar, M. L., M. Barazangi, J. Dorman, C. H. Scholz, and R. B. Smith (1972), Tectonics of the Intermountain Seismic Belt, western United States: Micro earthquake seismicity and the composite fault place solutions, *Geol. Soc. Am. Bull.*, 83(1), 13-28, doi: 10.1130/0016-7606(1972)83[13:TOTISB]2.0.CO;2.

Schultz, R., H. Corlett, K. Haug, K. Kocon, K. MacCormack, V. Stern, and T. Shipman (2016), Linking fossil reefs with earthquakes: Geologic insight to where induced seismicity occurs in Alberta, *Geophys. Res. Lett.*, 43(6), 2534-2542, doi: 10.1002/2015GL067514

Sears, J. W. and M. Hendrix (2004), Lewis and Clark line and the rotational origin of the Alberta and Helena salient, North American Cordillera, In A. J. Susan and A. B. Weil (Eds.), *Orogenic curvature: Integrating paleomagnetic and structural analysis*, Geological Society of America Special Papers (Vol. 383, pp. 173-186), Geological Society of America, doi: 10.1130/0-8137-2383-3(2004)383[173:LACLAT]2.0.CO;2.

Shapiro, N. M., D. V. Droznin, S. Ya. Droznina, S. L. Senyukov, A. A. Gusev, and E. I. Gordeev (2017), Deep and shallow long-period volcanic seismicity linked by fluid-pressure transfer, *Nat. Geosci.*, 10(6), 442-455, doi: 10.1038/ngeo2952.

Shelly, D. R., D. P. Hill, F. Massin, J. Farrell, R. B. Smith, and T. Taira (2013), A fluid-driven earthquake swarm on the margin of the Yellowstone caldera, *J. Geophys. Res.-Sol. Ea.*, 118(9), 4872-4886, doi: 10.1002/jgrb.50362.

Skoumal, R. J., M. R. Brudzinski, and B. S. Currie (2015), Earthquakes induced by hydraulic fracturing in Poland Township, Ohio, *Bull. Seismol. Soc. Am.*, 105(1), 189-197, doi: 10.1785/0120140168.

Skoumal, R. J., M. R. Brudzinski, B. S. Currie, and J. Levy (2014), Optimizing multi-station earthquake template matching through re-examination of the Youngstown, Ohio, sequence, *Earth Planet Sc. Lett.*, 405, 274-280, doi: 10.1016/j.epsl.2014.08.033.

Small, C. and T. Naumann (2001), The global distribution of human population and recent volcanism, *Environ. Hazards*, 3(3), 93-109, doi: 10.3763/ehaz.2001.0309.

Smith, R. B. and W. J. Arabasz (1991), Seismicity of the intermountain seismic belt, In D. B. Slemmons, E. R. Engdahl, M. D. Zoback, and D. D. Blackwell (Eds.), *Neotectonics of North America* (pp. 185-228), Geological Society of America, doi: 10.1130/DNAG-CSMS-NEO.185.

Song, F., H. S. Kuleli, M. N. Toksöz, E. Ay, and H. Zhang (2010), An improved method for hydrofracture-induced microseismic event detection and phase picking, *Geophysics*, 75(6), A47-A52, doi: 10.1190/1.3484716.

Soosalu, H., J. Key, R. S. White, C. Knox, P. Einarsson, and S. S. Jacobsdóttir (2010), Lower-crustal earthquakes caused by magma movement beneath Askja volcano on the north Iceland rift, *Bull. Volcan.*, 72, 55-62, doi: 10.1007/s00445-009-0297-3.

Sparks, R. S. J., J. Biggs, and J. W. Neuberg (2012), Monitoring volcanoes, *Science*, 335(6074), 1310-1311, doi: 10.1126/science.1219485.

Steeples, D. W. and L. Brosius (1996), Earthquakes, *Kansas Geological Survey Public Information Circular 3*, accessed 20 Sep 2018, http://www.kgs.ku.edu/Publications/pic3/PIC3_2014_revision.pdf.

Stein, S. and M. Liu (2009), Long aftershock sequences within continents and implications for earthquake hazard assessment, *Nature*, 462, 87-89, doi: 10.1038/nature08502.

Stein, S. and S. Mazzotti (2007), *Continental intraplate earthquakes: Science, Hazard, and Policy Issues*, Geological Society of America Special Papers (Vol. 425), Geological Society of America, doi: 10.1130/SPE425.

Stickney, M. C. (2006), The 26 July 2005 M_W 5.6 Dillon, Montana earthquake, *Seismol. Res. Lett.*, 77(2), 209, doi: 10.1785/gssrl.77.2.160.

Stickney, M. C. (2013), The 2005 Dillon, Montana earthquake: A moderate-sized intermountain seismic belt earthquake on a blind normal fault and its effects on local seismicity rates, *Seismol. Res. Lett.*, 84(2), 298, doi: 10.1785/0220130011.

Stickney, M. C. (2018), *Written communication on 4 May 2018*.

Stickney, M. C. and M. J. Bartholomew (1987), Seismicity and Quaternary faulting of the northern basin and range province, Montana and Idaho, *Bull. Seismol. Soc. Am.*, 77(5), 1602-1625.

Stover, C. W. and J. L. Coffman (1993), *Seismicity of the United States, 1568-1989 (Revised)*, U.S. Geological Survey Professional Paper 1527, U.S. Geological Survey, doi: 10.3133/pp1527.

Sumy, D. F., C. J. Neighbors, E. S. Cochran, and K. M. Keranen (2017), Low stress drops for aftershocks of the 2011 Mw 5.7 Prague, Oklahoma, earthquake, *J. Geophys. Res.-So. Ea.*, 122(5), 3813-3834, doi: 10.1002/2016JB013153.

Sumy, D. F., E. S. Cochran, K. M. Keranen, M. Wei, and G. A. Abers (2014), Observations of static Coulomb stress triggering of the November 2011 M5.7 Oklahoma earthquake sequence, *J. Geophys. Res. Solid Earth*, 119, 1904-1923, doi:10.1002/2013JB010612.

Sun, X., and S. Hartzell (2014), Finite-fault slip model of the 2011 Mw 5.6 Prague, Oklahoma earthquake from regional waveforms, *Geophys. Res. Lett.*, 41, 4207-4213, doi: 10.1002/2014GL060410.

Talwani, P. (1989), Characteristic features of intraplate earthquakes and the models proposed to explain them, In S. Gregersen and P. W. Basham (Eds.), *Earthquakes at North-Atlantic passive margins: Neotectonics and postglacial rebound* (Vol. 266, pp. 563-579), Dordecht, Netherlands: Springer, doi: 10.1007/978-94-009-2311-9_33.

Tang, C.-C., Z. Peng, K. Chao, C.-H. Chen, and C.-H. Lin (2010), Detecting low-frequency earthquakes within non-volcanic tremor in southern Taiwan triggered by the 2005 Mw8.6 Nias earthquake, *Geophys. Res. Lett.*, 37(16), L16307, doi: 10.1029/2010GL043918.

Townend, J. and M. D. Zoback (2000), How faulting keeps the crust strong, *Geology*, 28(5), 399-402, doi: 10.1130/0091-7613(2000)28<399:HFKTCS>2.0.CO;2.

U.S. Geological Survey (2008), Earthquake summary M 7.9 – eastern Suchuan, China, accessed 26 Aug 2018, https://earthquake.usgs.gov/earthquakes/eventpage/usp000g650 - executive.

U.S. Geological Survey (2011a), Earthquake summary M 5.7 – Oklahoma, accessed 26 Aug 2018, https://earthquake.usgs.gov/earthquakes/eventpage/usp000jadn - executive.

U.S. Geological Survey (2011b), House damage from 2011 Oklahoma earthquake, accessed 26 Aug 2018, https://www.usgs.gov/media/images/house-damage-2011-oklahoma-earthquake.

U.S. Geological Survey (2016a), Earthquake summary M 5.0 – 3km W of Cushing, Oklahoma, accessed 19 Sep 2018, https://earthquake.usgs.gov/earthquakes/eventpage/us100075y8#executive.

U.S. Geological Survey (2016), Earthquake summary M 5.8 – 14km NW of Pawnee, Oklahoma, accessed 26 Aug 2018, https://earthquake.usgs.gov/earthquakes/eventpage/us10006jxs#executive

U.S. Geological Survey (2017a), Earthquake summary M 2.3 – 12 km SE of Lincoln, Montana, accessed 27 Aug 2018, https://earthquake.usgs.gov/earthquakes/eventpage/mb80223214#executive.

U.S. Geological Survey (2017b), Earthquake summary M 5.8 – 11km SE of Lincoln, Montana, accessed 27 Aug 2018, https://earthquake.usgs.gov/earthquakes/eventpage/us10009757#executive.

U.S. Geological Survey (2017c), Earthquake summary M 5.0 – 15 km S of Lincoln, Montana, accessed 27 Aug 2018, https://earthquake.usgs.gov/earthquakes/eventpage/us1000975k#executive.

U.S. Geological Survey (2017d), Earthquake summary M 4.0 – 12 km ESE of Lincoln, Montana, accessed 27 Aug 2018, https://earthquake.usgs.gov/earthquakes/eventpage/us20009ww4#executive.

U.S. Geological Survey and Oklahoma Geological Survey (2014), Record number of Oklahoma tremors raises possibility of damaging earthquakes, accessed 26 Aug 2018, https://earthquake.usgs.gov/earthquakes/byregion/oklahoma/newsrelease_05022014.php.

Ukawa, M. and M. Ohtake (1987), A monochromatic earthquake suggesting deep-seated magmatic activity beneath the Izu-Ooshima volcano, Japan, *J. Geophys. Res.*, 92(B12), 12649-12663, doi: 10.1029/JB092iB12p12649.

University of Utah (2018), Intermountain seismic belt historical earthquake project, accessed 13 Sep 2018, http://quake.utah.edu/regional-info/intermountain-seismic-belt-historical-earthquake-project.

van der Elst, N. J., H. M. Savage, K. M. Keranen, and G. A. Abers (2013), Enhanced remote earthquake triggering at fluid-injection sites in the Midwestern United States, *Science*, 341(6142), 164-167, doi: 10.1126/science.1238948.

Van Trees, H. L. (1968), *Detection, Estimation and Modulation Theory* (Vol. 1), New York: John Wiley and Sons.

Vanderkulk, W., F. Rosen, and S. Lorenz (1965), Larger aperture seismic array signal processing study, IBM Final Report, ARPA Contract Number SD-296.

Veil, J. A., M. G. Puder, D. Elcock, and R. J. Redweick Jr. (2004), A white paper describing produced water from production of crude oil, natural gas, and coal med methane, Prepared for U.S. Dept. of Energy, accessed 28 Aug 2018, http://www.ipd.anl.gov/anlpubs/2004/02/49109.pdf.

Vidale, J. E., D. A. Schmidt, S. D. Malone, A. J. Hotovec-Ellis, S. C. Moran, K. C. Creager, and H. Houston (2014), Deep long-period earthquakes west of the volcanic arc in Oregon: Evidence of serpentine dehydration in the fore-arc mantle wedge, *Geophys. Res. Lett.*, 41(2), 370-376, doi: 10.1002/2013GL059118.

Waldron, H. H. and R. W. Galster (1984), Comparative seismic hazards study of western Montana, In *Proceedings of the Eighth World Conference on Earthquake Engineering* (Vol. 1, pp. 31-38), Prentice-Hall.

Weingarten, M., S. Ge, J. W. Godt, B. A. Bekins, and J. L. Rubinstein (2015), High-rate injection is associated with the increase in U.S. mid-continent seismicity, *Science*, 348(6241), 1336-1340, doi: 10.1126/science/aab1345.

Wertz, J. (2015, Jul 16), Years after earthquake, Oklahoma college still shaken by cracked budgets and broken buildings, *State Impact Oklahoma,* accessed 26 Aug 2018, https://stateimpact.npr.org/oklahoma/2015/07/16/years-after-earthquake-oklahoma-college-still-shaken-by-cracked-budgets-and-broken-buildings/.

White, R. A. (1996), Precursory deep long-period earthquakes at Mount Pinatubo: Spatio-temporal link to basaltic trigger, In C. G. Newhall and R. S. Punongbayan (Eds.), *Fire and mud: Eruptions and lahars of Mount Pinatubo, Philippines* (pp. 307-328), U.S. Geological Survey, accessed 15 Sep 2018, https://pubs.usgs.gov/pinatubo/.

Williams, R. A., N. S. McCallister, and R. L. Dart (2011), 20 cool facts about the New Madrid Seismic Zone – Commemorating the bicentennial of the New Madrid earthquake sequence, December 1811-February 1812, *U.S. Geological Survey General Information Product 134*, accessed 27 Aug 2018, https://pubs.usgs.gov/gip/134/.

Wilmoth, A. (2017, Oct 20), Companies, resident settle Prague earthquake lawsuit, *NewsOK*, accessed 26 Aug 2018, https://newsok.com/article/5568757/companies-resident-settle-prague-earthquake-lawsuit.

Wilmoth, A. (2018, May 22), Earthquake lawsuit gains class-action status, *NewsOK*, accessed 26 Aug 2018, https://newsok.com/article/5595410/earthquake-lawsuit-gains-class-action-status.

Wilson, M. P., G. R. Foulger, J. G. Gluyas, R. J. Davies, and B. R. Julian (2018), *HiQuake: The Human-Induced Earthquake Database*, Department of Earth Sciences, Durham University, UK, accessed 15 Sep 2018, www.inducedearthquakes.org.

Winberry, J. P. and S. Anandakrishnan (2003), Seismicity and neotectonics in West Antarctica, *Geophys. Res. Lett.*, 30(18), 1931, doi: :10.1029/2003GL018001.

Winberry, J. P. and S. Anandakrishnan (2004), Crustal structure of the West Antarctica rift system and Marie Byrd Land hotspot, *Geology*, 32(11), 977-980, doi: 10.1130/G20768.1.

Xu, C., X. Xu, X. Yao, and F. Dai (2014), Three (nearly) complete inventories of landslides triggered by the May 12, 2008 Whenchuan Mw 7.9 earthquake of China and their spatial distribution statistical analysis, *Landslides*, 11(3), 441-461, doi: 10.1007/s10346-013-0404-6.

Yeck, W. L., A. F. Sheehan, H. M. Benz, M. Weingarten, and J. Nakai (2016a), Rapid response, monitoring, and mitigation of induced seismicity near Greeley, Colorado, *Seismol. Res. Lett.*, 87(4), 837-847, doi: 10.1785/0220150275.

Yeck, W. L., G. P. Hayes, D. E. McNamara, J. L. Rubinstein, W. D. Barnhart, P. S. Earle, and H. M. Benz (2017), Oklahoma experiences largest earthquake during ongoing regional wastewater injection hazard mitigation efforts, *Geophys, Res. Lett.*, 44(2), 711-717, doi: 10.1002/2016GL071685.

Yeck, W. L., M. Weingarten, H. M. Benz, D. E. McNamara, E. A. Bergmen, R. B. Herrmann, J. L. Rubinstein, and P. S. Earle (2016b), Far-field pressurization likely caused one of the largest injection induced earthquakes by reactivating a large preexisting basement fault structure, *Geophys. Res. Lett.*, 43(19), 10198-10207, doi: 10.1002/2016GL070861.

Yoon, C. E., O. O'Reilly, K. J. Bergen, and G. C. Beroza (2015), Earthquake detection through computationally efficient similarity search, *Sci. Adv.*, 1(11), e1501057, doi: 10.1126/sciadv.1501057.

Yoon, C. E., Y. Huang, W. L. Ellsworth, and G. C. Beroza (2017), Seismicity during the initial stages of the Guy-Greenbrier, Arkansas, earthquake sequence, *J. Geophys. Res.-Sol. Ea.*, 122(11), 9253-9274, doi: 10.1002/2017JB014946.

Zalzal, K. S. (2017, Aug 31), Benchmarks: August 31, 1886: Magnitude-7 earthquake rocks Charleston, South Carolina, *Earth Magazine*, August 2017, accessed 27 Aug 2018, https://www.earthmagazine.org/article/benchmarks-august-31-1886-magnitude-7-earthquake-rocks-charleston-south-carolina.

Zhang, Y., M. Person, J. Rupp, K. Ellett, M. A. Celia, C. W. Gable, B. Bowne, J. Evans, K. Bandilla, P. Mozley, T. Dewers, and T. Elliot (2013), Hydrogeologic control on induced seismicity in crystalline basement rocks due to fluid injection into basal reservoirs, *Groundwater*, 51(4), 525-538, doi: 10.1111/gwat.12071.

Zoback, M. D. (2012, Apr 17), Managing the seismic risk posed by wastewater disposal, *Earth Magazine*, April 2012, accessed, 26 Aug 2018, https://www.earthmagazine.org/article/managing-seismic-risk-posed-wastewater-disposal.

Zobin, V. M. (2017), *Introduction to volcanic seismology* (Ed. 3), Amsterdam: Elsevier, doi: 10.1016/C2015-0-00304-5.

CHAPTER 2

SPATIOTEMPORAL ANALYSIS OF THE FORESHOCK-MAINSHOCK-AFTERSHOCK SEQUENCE OF THE 6 JULY 2017 M_W 5.8 LINCOLN, MONTANA, EARTHQUAKE [1]

SUMMARY

An $\mathbf{M_W}$ 5.8 earthquake occurred on 6 July 2017 at 12.2-km depth, 11 km southeast of Lincoln in west-central Montana. No major damage or injuries were reported; however, the widely felt mainshock generated a prolific aftershock sequence with more than 1200 located events through the end of 2017. The Lincoln event is the latest in a series of moderate to large earthquakes that have affected western Montana. We characterize the spatiotemporal evolution of the sequence using matched filter detection and multiple event relocation techniques. Moment tensor solutions and aftershock locations indicate faulting occurred on a 9-km-long NNE-striking, near-vertical, strike-slip fault antithetic to the Lewis and Clark Line, the main through-going fault system. Seismicity primarily occurs between 6- and 16-km depth, which is broadly consistent with seismicity in the Intermountain Seismic Belt. We estimate a fault rupture area of ~64 km^2 and ~30 cm of average fault displacement. We identified four foreshocks during the three days before and 3005 aftershocks in the three weeks after the mainshock. The supplemented catalog frequency-magnitude distribution has a *b*-value of 0.79 and a minimum magnitude of completeness of 0.7. The overall decay rate is consistent with a modified Omori decay law *p*-

---

[1] **This chapter has been accepted and is currently in press for publication:**

McMahon, N. D., W. L. Yeck, M. C. Stickney, R. C. Aster, H. R. Martens, and H. M. Benz (2018), Spatiotemporal analysis of the foreshock-mainshock-aftershock sequence of the 6 July 2017 M_W 5.8 Lincoln, Montana, Earthquake, *Seismol. Res. Lett.*, in press.

value of 0.76 and *c*-value of 0.32. This event demonstrates that unmapped faults antithetic to major geologic structures play a role in accommodating regional strain in western Montana and can host significant earthquakes.

2.1 INTRODUCTION

On 6 July 2017, a moment magnitude ($\mathbf{M_W}$) 5.8 earthquake occurred 11 km southeast of the town of Lincoln in west-central Montana (population ~1000), 50 km northwest of the capital city, Helena (population ~31,000), and 100 km east of the state's second most populous city, Missoula (population ~72,000). This earthquake, which we refer to as the Lincoln earthquake, is the largest to occur in Montana since the 1959 $\mathbf{M_W}$ 7.3 Hebgen Lake event in the Yellowstone region, and notably occurred 50 km northwest of the 1935 Helena earthquake sequence within the same regional fault system (Fig. 2.1). The Lincoln earthquake was felt to epicentral distances of more than 800 km with a maximum Modified Mercalli Intensity (MMI) of VIII. No serious damage or injuries were reported. More than 1200 aftershocks of duration magnitude ($\mathbf{M_d}$) -1 and larger were located by the U.S. Geological Survey (USGS) and the Montana Bureau of Mines and Geology (MBMG) through the end of 2017. The distribution of aftershocks aligns with one nodal plane of the USGS *W*-phase moment tensor [*Hayes et al*., 2009] indicating slip on a near-vertical, NNE-striking, left-lateral strike-slip fault at a mid-crustal depth of 12 km (Fig. 2.2). The largest aftershock was an $\mathbf{M_W}$ 5.0 that occurred approximately 5 min after the mainshock. A total of 47 $\mathbf{M_W}$ 3 or larger earthquakes have occurred as a part of this sequence through 19 April 2018.

The causative fault is antithetic to principal faults that compose the Lewis and Clark Line (LCL), a 400-km east-southeast trending fault zone of subparallel faults dominated by steeply dipping strike-slip, dip-slip, and oblique-slip motions [*Wallace et al.*, 1990]. The Lincoln earthquake occurred on a previously unmapped fault at depth, likely related to broad-scale deformation associated with the LCL.

Montana is one of the most seismically active states in the contiguous United States, with the Intermountain Seismic Belt (ISB) extending through the western third of the state (Fig. 2.1). The ISB is a north-south-trending zone of shallow (<20 km), intraplate seismicity approximately 100-200 km wide that extends 1500 km from southern Nevada to northwestern Montana [*Smith and Arabasz*, 1991]. The ISB is characterized by late Quaternary normal-faulting, diffuse shallow seismicity, and episodic scarp-forming earthquakes associated with intraplate stress within the western North American plate [*Sbar et al.,* 1972; *Arabasz and Smith*, 1981]. Northeast-southwest intraplate extension drives contemporary ISB deformation [*Stickney and Bartholomew*, 1987]. The north-south trending ISB is disrupted by the northwest-southeast trending LCL, forming a major, intraplate crustal discontinuity [*Waldron and Galster*, 1984]. The LCL faults have movement histories ranging from middle Proterozoic through Quaternary, and they extend from northern Idaho to east of Helena, Montana. The LCL width increases from 40 to 80 km west to east, and the predominant strikes rotate from east to southeast [*Wallace et al.*, 1990]. *Sears and Hendrix* [2004] interpret the LCL as an Early Cretaceous to late Paleocene rotational shear zone between the northeastward rotating Lewis-Eldorado-Hoadley block to the north and the eastward rotating Sapphire and Lombard blocks to the south, with deformation spanning the fold-thrust belt formation of the northern Rocky Mountains. Following formation of the fold-thrust belt, principal faults of the LCL accommodated up to 28 km of dextral shear [*Wallace et al.*, 1990] and development of basin and range to the south [*Reynolds*, 1979; *Lageson and Stickney*, 2000].

Several notable twentieth century earthquakes have occurred in the region (Fig. 2.1). The surface-wave magnitude **(M_S)** 6.6 Clarkston earthquake in June 1925, approximately 100 km to the south, was the earliest instrumentally recorded event in Montana. It caused considerable damage within a 1500 km^2 area and was preceded by two small foreshocks [*Pardee*, 1926]. The **M_S** 6.2 and **M_S** 6.0 Helena earthquakes of October 1935, approximately 50 km to the southeast, were the largest events of a sustained sequence that lasted from October 1935 through December 1936. The earthquakes caused an estimated $4 million in property damage and four fatalities [*Stover and Coffman*, 1993]. Focal mechanisms for the two largest shocks indicated strike-slip movement with the east-west nodal planes consistent with nearby LCL fault orientations [*Doser*, 1989]. More than 2500 earthquakes were felt in the swarm from October 1935 through November 1936. The Lewis and Clark County Disaster and Emergency Services department has estimated that an **M_W** 6.3 earthquake in this region today could cause more than $500 million in damage [*Lewis and Clark County Disaster and Emergency Services Website*]. The 1959 **M_W** 7.3 Hebgen Lake earthquake, the largest recorded earthquake in Montana, was felt across nine western states and three Canadian provinces, with MMI X near the epicenter. The 1959 earthquake caused 30 km of surface rupture of up to 6 m along two principal faults and a host of minor faults. It caused $11 million in damage, 28 fatalities, and a massive landslide [*Stover and Coffman*, 1993]. The **M_W** 5.6 earthquake near Dillon, Montana (170 km south of Lincoln) in July 2005 reached MMI VII, damaged 60% of older masonry chimneys in the area, and occurred at

10-km depth on a previously unknown normal fault that lacked surface expression [*Stickney*, 2006; 2013].

The 6 July 2017 $\mathbf{M_W}$ 5.8 Lincoln earthquake has source characteristics consistent with these historical moderate-to-large-sized earthquakes occurring in western Montana. As Montana's largest historical earthquakes preceded regional network monitoring, these important events are poorly documented in terms of source parameters (e.g. mechanism, depth) and their relation to the regional geologic structures. Studying the 2017 Lincoln earthquake sequence provides an opportunity to better constrain fault geometry, source depths, and seismicity distribution, which helps contextualize earthquake hazards and scenario studies of western Montana. Here, we provide refined locations of a foreshock, the mainshock, and aftershocks in the sequence, documenting kinematic details of the seismicity in relation to the geologic structures. Furthermore, we identify additional, small-magnitude earthquakes that substantially lower the catalog's magnitude of completeness for a more detailed analysis of spatiotemporal evolution of the sequence.

2.2 DATA

We analyzed waveform data from the 14 closest seismic stations to the earthquake sequence (Table 2.1; Fig. 2.2a). This includes seven permanent stations from the Montana Regional Seismic Network [network code MB] [*Montana Bureau of Mines and Geology/Montana* Tech, 2001] and one permanent station from the U.S. National Seismic Network [network code US] [*Albuquerque Seismological Laboratory*, 1990] operating at distances of 22-107 km from the mainshock epicenter. To ensure minimally biased earthquake locations and good depth control on aftershocks, the USGS deployed three temporary seismic stations within four days after the mainshock [network code GS] [*Albuquerque Seismological Laboratory*, 1980] located at distances of 4-26 km from the mainshock epicenter. This temporary network was supplemented by three seismic stations deployed by the University of Montana 50 days after the mainshock located within 12 km of the epicenter (Fig. 2.2) [network code UM] [*University of Montana*, 2017].

2.3 METHODOLOGY

EVENT RELOCATIONS

We collected earthquake source parameters (i.e., moment tensor solutions, hypocenter locations, magnitudes, and phase data) for 685 well-located earthquakes larger than or equal to **M** 1 occurring between 5 July and 15 October 2017 from the USGS Comprehensive Catalog of Earthquakes (ComCat) (Table A1.1). We manually checked and repicked, when necessary, *P*- and *S*-phase first arrivals, primarily *Pg*, *Pn*, *Sg*, and *Sn*, for these events on the 11 MB, US, and GS stations and supplemented the dataset with USGS analyst picks from more distant stations. Additionally, we manually picked *P*- and *S*-phase first arrivals for each of the events on the UM seismic stations occurring between 24 August 2017, when the first station was deployed in the epicentral region, and 15 October 2017. Combining ComCat phase arrival times with additional UM phase arrival times, we relocated the earthquakes using a hypocentroid decomposition (HD) multiple event relocation approach [*Jordan and Sverdrup*, 1981; *Bergman*, 2014] utilizing a velocity model similar to that derived for western Montana [*Zeiler et al.*, 2005] (Table 2.3). The HD method separates the location problem into that of the cluster hypocentroid and event-specific cluster vectors, which locate the event relative to the hypocentroid. To reduce bias introduced by unmodeled velocity structure and ambiguity at the *Pg*/*Pn* and *Sg*/*Sn* crossovers, we only use the data within 1.0° of an event when solving for the hypocentroid. All arrival-time data available are used when solving for the cluster vectors. Cluster vectors are estimated using cataloged absolute-time picks, but in a differential sense and therefore are less sensitive to unmodeled velocity perturbations. Using this procedure, the entire dataset is minimally biased in terms of absolute location due to reliance on near-source observations while maintaining good relative locations. The resulting dataset of 685 earthquakes have average epicentral and depth uncertainties (90% confidence) on the order of 1 km, ensuring an accurate set of earthquake locations to better constrain the active structures. The final hypocenter locations are included in Data Set A1.1.

ADDITIONAL EVENT DETECTION

In addition to relocating the events contained in ComCat, we sought to supplement the catalog with unreported, lower magnitude events to better understand earthquake rates and temporal evolution of the sequence. We utilized the matched filter technique [*Van Trees*, 1968] to detect additional events. We cross-correlated 303 known events (templates) identified on the 11 MB, US, and GS stations against the respective stations' continuous waveform data from 1 June through 27 July 2017, one month before the mainshock to three weeks after. These template events ranged from local magnitude ($\mathbf{M_L}$) -0.3 to $\mathbf{M_W}$ 5.8. All templates included the full waveform from the *P*- through the *S*-phases, started 0.1 s before the *P*-phase arrival, and ranged in length from 4 to 16 s. We empirically determined the detection threshold for each station to account for station noise characteristics and dominant event frequencies. Table 2.1 lists template construction and correlation parameters.

Using this approach, templates constructed from different events on individual stations will often detect the same event. All detections on a station within an estimated 1-s phase arrival window were declared a single event, but we chose the detection with the highest correlation coefficient as the new detection on the respective station. After detections were completed and multiple detections accounted for, we associated the detections between stations into events based on estimated origin times, given the template event's known travel-time. We classified all detection origin times within a 2-s window as single events for subsequent processing. We selected for further study all events detected on at least five stations with correlation coefficients greater than 0.5. For newly detected events, we computed magnitudes relative to the highest correlated templates. We used a length of waveform corresponding to the respective station's template length (Table 2.1) capturing the *P*- and *S*-phases and the method of *Benz et al.* [2015] to calculate relative magnitude at each station. We then averaged across all stations for each event to determine the final relative event magnitude ($\mathbf{M_{rel}}$).

We did not add the newly detected earthquakes to the multiple event relocation processing because they are typically smaller events recorded on far fewer stations; consequently, their location uncertainties are larger. The fundamental importance of these newly detected events is for aftershock statistics with associated implications regarding the seismotectonic properties of the fault. We included the final catalog of 3009 events (303 original template events and 2706 additional events) in Data Sets A1.2 and A1.3. To calculate the event frequency-magnitude distribution of the catalog [e.g., *Gutenberg and Richter*, 1944] and the modified Omori decay parameters, *p* and *c* [e.g., *Omori*, 1894; *Utsu et al.*, 1995], we utilized the ZMAP program [*Wiemer*, 2001].

2.4 RESULTS

EVENT RELOCATIONS

The 685 well-located earthquakes delineate an ~9 km long, nearly vertical fault, striking N6°E and dipping 86°E (Figs. 2.2b and 2.3). This aftershock distribution orientation is generally consistent with the NNE-striking nodal plane of the USGS *W*-phase moment tensor solution which strikes at N11°E and dips 83°E with associated uncertainties of ±10° [*U.S. Geological Survey*, 2017; *Duputel et al.*, 2012]. The vast majority of the aftershocks (94%) occurred in a depth range of 6-16 km, consistent with the broad shallow seismic activity of the ISB. The aftershock activity is concentrated in an ~8 km horizontal by 8 km vertical area on a NNE-striking fault plane, with some sparse activity outside this zone. We use the *Wells and Coppersmith* [1994] equation relating moment magnitude to rupture area, $\log (RA) = a + b * M$, where RA is the rupture area, M (5.8) is the moment magnitude, and a (-3.42) and b (0.9) are empirically derived coefficients for strike-slip faults, to calculate a rupture area of ~63 km^2. This estimation is on par with the 64 km^2 zone of concentrated aftershock activity defining the rupture area of the mainshock. Using $M_0 = \mu AD$ [*Aki*, 1966] where M_0 is the seismic moment, μ is the shear modulus, A is the fault surface area, and D is the average displacement during rupture and assuming a 6.407×10^{17} N-m seismic moment from the USGS W-phase moment tensor calculation, a 64-km^2 fault surface area, and a 32-GPa crustal shear modulus, we calculate an average rupture displacement of ~30 cm. Dispersed seismicity was also observed on a NW-SE-trending structure oriented parallel to primary LCL faults.

Although early in the sequence we observed no significant spatiotemporal patterns other than the delineation of the causative fault, the aftershocks do appear to cluster late in the studied time frame. After ~23 September 2017, the aftershocks appear to be concentrated in the shallower depths of the southern end of the fault and in a narrower zone along the fault. We found no significant patterns in magnitude as a function of time or position on the fault. We observed more and larger events occurring on the NW-SE-trending structure to the west of the fault and fewer events occurring on the structure as a whole later in the studied time frame.

Five of the six largest aftershocks for which moment tensors were computed have focal mechanisms that are similar to the mainshock, indicating near-vertical, left-lateral strike-slip motion. Only the $\mathbf{M_W}$ 4.4 aftershock that occurred 24 hours after the mainshock at the northern terminus of activity has a notably more oblique-normal faulting mechanism, which is a common feature of ISB seismicity and similar to reported slip orientation on portions of the LCL [*Waldron and Galster*, 1984].

ADDITIONAL EVENT DETECTION

We cross-correlated a total of 303 earthquakes occurring from 5 July through 27 July 2017 with continuous seismic data from 11 stations recording during 1 June through 27 July 2017. This resulted in a combined 66,585 detections across 11 stations with correlation coefficients greater than or equal to 0.5 (Fig. 2.4). Detections were then associated across stations resulting in 2989 events with detection on at least five of the 11 stations. The 46,003 unassociated detections were likely from events that were too small to be recorded on the requisite five stations as well as detections from nonseismic sources. We further supplemented our catalog with 20 larger events from ComCat that went undetected because the amplitude-clipped waveforms on nearby stations were unusable for cross-correlation. The final catalog contains 3009 earthquakes occurring between 2 July and 28 July 2017 with magnitudes between $\mathbf{M}_{\mathbf{rel}}$ -0.3 and $\mathbf{M}_{\mathbf{rel}}$ 5.8, which is a 10-fold increase from ComCat for this three-week time period (Figs. 2.4 and 2.5).

Our analysis identified three additional foreshocks, $\mathbf{M}_{\mathbf{rel}}$ 0.9, 1.1, and 0.7, which occurred 3 days, 2 days, and 2 minutes, respectively, before the $\mathbf{M}_{\mathbf{L}}$ 2.3 foreshock reported by the MBMG. Utilizing the modified maximum curvature method of *Benz et al*. [2015] and the maximum likelihood algorithm of *Weimer* [2001], we calculate the complete catalog *b*-value at 0.79 ± 0.02 [*Shi and Bolt*, 1982] with a minimum magnitude of completeness, M_C, of 0.7, thus extending the catalog's M_C down 1.8 units of magnitude compared to the initial catalog of 303 template events while maintaining the general nature of the frequency magnitude distribution (Fig. 2.6a). This *b*-value is lower than the global mean value near 1.0 [e.g., *Frohlich and Davis, 1993*], but on par with lower *b*-values associated with intraplate earthquakes. A global review of intraplate earthquakes found *b*-values between 0.6 and 0.85 [*Okal and Sweet*, 2007] and a global review of aftershock sequences associated with stable continental regions found an average *b*-value of 0.865 ± 0.226 [*Ebel*, 2009]. The greater New York City-Philadelphia area had *b*-values around 0.70 ± 0.13 [*Sykes et al.*, 2008]. Recent aftershock sequences near Mount Carmel, Illinois, and Mineral, Virginia, have *b*-values of 0.6 [*Yang et al.*, 2009] and 0.747 ± 0.04 [*McNamara et al.*, 2014], respectively. These low *b*-values may reflect the strike-slip nature of some of the sequences [*Frohlich and Davis*, 1993], the reactivation of pre-existing faults [*Friberg et al.*, 2014], large levels of stress accumulated in and around the source volume controlled by asperities along the fault [Wyss, 1973], or, alternatively, that the mainshocks released most of the slip or strain on the fault [*McNamara et al.*, 2014].

The number of detected aftershocks decays steadily after the mainshock (Figs. 2.4 and 2.6c), with the exception of 13, 17, and 23 July having relatively high numbers of aftershocks caused by large-magnitude events occurring on these days ($\mathbf{M_L}$ 3.7, M_W 4.0, and $\mathbf{M_L}$ 3.7, respectively). The overall decay rate is consistent with a modified Omori decay law [*Utsu et al.*, 1995] *p*-value of 0.76 and *c*-value of 0.32 days for aftershocks above $M_C = 0.7$ (Fig. 2.6b,c). By comparison, the initial catalog of 303 template events used for correlation presented a *p*-value of 0.76 and a *c*-value of 0.01 days with events above $M_C = 2.5$. The *p*-value describes the rate of decay for an aftershock sequence, with typical global values between 0.9 and 1.5 [*Utsu et al.*, 1995]. A *p*-value of 0.76 in the final catalog indicates a slower than average decay, a characteristic attributed to intraplate settings [*Zhao et al.*, 1992]. The *c*-value describes the time delay before the onset of the Omori (power) law. Before time *c* the detection of aftershocks is incomplete because of frequent earthquakes with overlapping seismograms, and therefore the *c*-value is sensitive to catalog completeness [*Utsu et al.*, 1995; *Narteau et al.*, 2002; *Holschneider et al.*, 2012]. Thus, it is logical that the *c*-value increases as we decrease the magnitude of catalog completeness; more time is needed to escape the supersaturated early sequence at $M_C = 0.7$ (final catalog, $c = 0.32$ days) than at $M_C = 2.5$ (initial catalog, $c = 0.01$ days). Although we increase the number of aftershocks 10-fold, decrease M_C by 1.8 units of magnitude, and subsequently increase the *c*-value, we observe a consistent aftershock decay rate relative to the original ComCat catalog.

2.5 CONCLUSIONS

The combination of matched filtering and multiple event relocation techniques gives rise to a more complete picture of the spatiotemporal evolution of the Lincoln earthquake sequence. Our observations show that although WNW-trending faults of the LCL dominate the structural grain in this part of western Montana, associated antithetic structures also play a key role in accumulating and releasing regional strain. The $\mathbf{M}_W$ 5.8 Lincoln, Montana, earthquake occurred on a NNE-SSW trending, left-lateral strike-slip fault antithetic to the LCL. The mainshock and its associated aftershocks are primarily concentrated in an 8 x 8 km area between 6- and 16-km depth with a total lateral extent of about 9 km. The corresponding faulting area of 64 km^2 is consistent with the empirical source scaling relationship of *Wells and Coppersmith* [1994] and an average displacement rupture of ~30 cm. The relatively low *b*-value of 0.79 is broadly consistent with intraplate earthquakes and aftershock sequences observed globally. Studying the Lincoln event and similar earthquakes demonstrates anew the hazards associated with a highly faulted and seismically active region encompassing complex and hidden fault structures and adds to the body of literature related moderate-to-large North American Cordilleran intraplate earthquakes that are unassociated with induced or triggered seismicity.

2.6 Data and Resources

The waveform data from MB, US, GS, and UM network stations are available from the IRIS Data Management Center [http://www.iris.edu/mda/MB, http://www.iris.edu/mda/US, http://www.iris.edu/mda/GS, http://www.iris.edu/mda/UM, all last accessed April 2018]. We obtained earthquake location and magnitudes from the USGS Comprehensive Catalog of Earthquakes [https://earthquake.usgs.gov/earthquakes/search/, last accessed November 2017]. Fault data were obtained from the USGS Mineral Resources On-Line Spatial Data at https://mrdata.usgs.gov/geology/state/state.php?state=MT, https://mrdata.usgs.gov/geology/state/state.php?state=ID, https://mrdata.usgs.gov/geology/state/state.php?state=WY, https://mrdata.usgs.gov/geology/state/state.php?state=WA [all last accessed November 2017]. The catalog of 3009 event detections is available at the USGS ScienceBase website https://www.sciencebase.gov/catalog/item/5b83f32ee4b05f6e321b4ee2 [last accessed August 2018] [*McMahon et al.*, 2018]. We created some figures using the Generic Mapping Tools (GMT) software of *Wessel and Smith* [1991]. We calculated the *b*-, *p*-, and *c*-values using the software package ZMAP of *Wiemer* [2001] obtained at http://www.seismo.ethz.ch/static/stat_2010_website/stat-website-pre2010/www.earthquake.ethz.ch/software/zmap.html [last accessed February 2018]. Lewis and Clark County Disaster and Emergency Services website is available at https://www.lccountymt.gov/des.html [last accessed February 2018].

2.7 Acknowledgements

This research was supported by the U.S. Geological Survey (USGS) National Earthquake Hazards Reduction Program. The authors thank the U.S. Geological Survey (USGS) Albuquerque Seismological Laboratory for their efforts in deploying temporary seismic stations in the vicinity of Lincoln, Montana, and University of Montana graduate and undergraduate students for their field efforts. The Montana Bureau of Mines and Geology and the USGS National Earthquake Information Center provided high-quality earthquake source parameters and observations used in this analysis. The authors thank S. Hoover, E. Morton, and two anonymous reviewers for providing thoughtful comments that improved this article. The authors thank J. Slate and J. McCarthy for editorial reviews.

2.8 TABLES FOR CHAPTER 2

Table 2.1: Table of seismic station information and correlation parameters.

Network	Station	Start Recording (Days post-mainshock)	Distance from Mainshock (km)	Instrument and Sampling Rate	Correlation Parameters	
					Bandpass (Hz)	Template Length (s)
MB	BEMT	0	22.2	L4C Vertical – 100 Hz	1.4 – 4.4	5.0
	BPMT	0	85.1	L4C Vertical – 100 Hz	1.4 – 4.4	16.0
	CHMT	0	54.0	L4C Vertical – 100 Hz	1.4 – 4.4	9.0
	ELMT	0	40.5	L4C Vertical – 100 Hz	1.4 – 4.4	8.0
	HRY	0	57.5	S-13 Vertical – 100 Hz	1.4 – 4.4	10.0
	LYMT	0	21.4	L4C Vertical – 100 Hz	1.4 – 4.4	5.0
	OVMT	0	39.8	L4C Vertical – 100 Hz	1.4 – 4.4	8.0
US	MSO	0	106.5	STS-2 3-comp – 40 Hz	1.4 – 4.4	16.0
GS	MT01	2.4 7/8 16:00	11.5	Trillium Compact 3-comp – 100 Hz	2.0 – 8.0	7.0
	MT02	3.7 7/10 00:00	25.9	Trillium Compact 3-comp – 100 Hz	2.0 – 8.0	6.0
	MT03	3.7 7/9 23:00	4.6	Trillium Compact 3-comp – 100 Hz	2.0 – 8.0	4.0
UM	GBMT	49.5 8/24 18:00	7.1	MBB-2 3-comp – 100 Hz		
	LGMT	49.6 8/24 21:00	4.8	MBB-2 3-comp – 100 Hz		
	NVMT	50.4 8/25 17:00	11.7	MBB-2 3-comp – 100 Hz		

Table 2.2: Velocity model used for event relocations.

Depth (km)	P velocity (km/s)	S Velocity (km/s)
0.0	5.800	3.357
7.0	5.800	3.357
7.0	6.220	3.597
19.8	6.220	3.597
19.8	6.530	3.731
38.7	6.530	3.731
MOHO*		
38.7	8.050	4.620
120.0	8.050	4.620

* MOHO = Mohorovičić discontinuity

2.9 FIGURES FOR CHAPTER 2

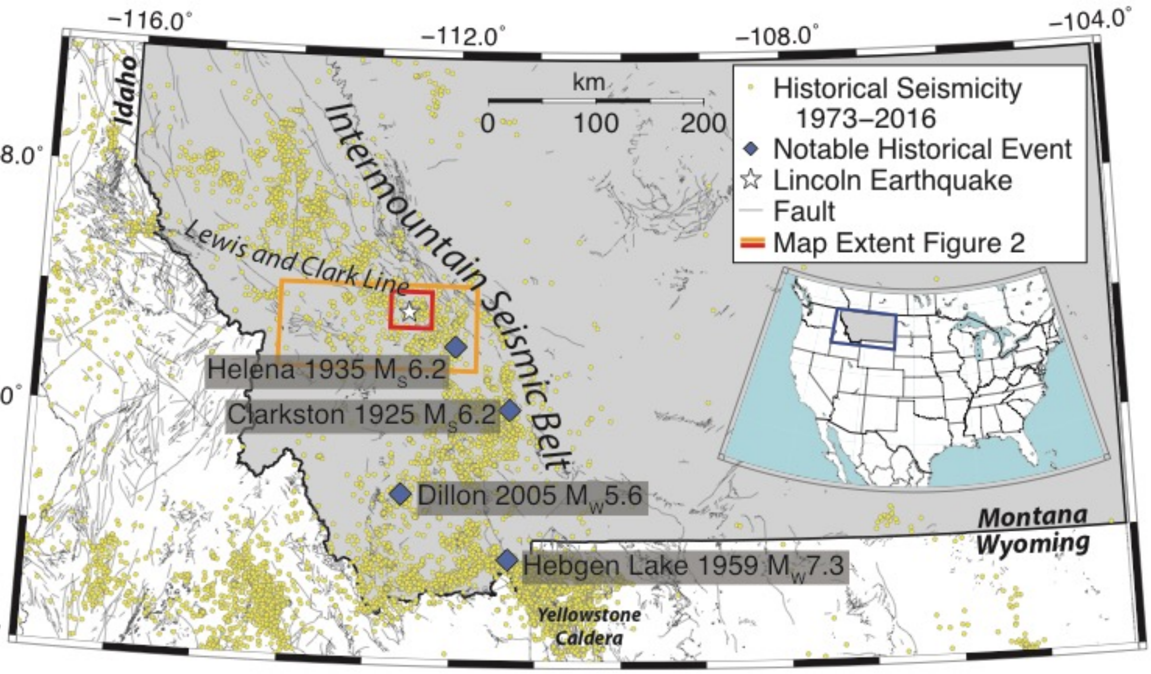

Figure 2.1. Historical seismicity (yellow circles) in and around Montana and adjacent states through 2016. Activity is primarily associated with the Intermountain Seismic Belt (ISB) and Yellowstone caldera. Orange and red boxes indicate map extents in Figure 2.2. Blue diamonds are locations of notable historical earthquakes referred to in the introduction. The inset map (lower left) shows the map extent (blue box) within the United States.

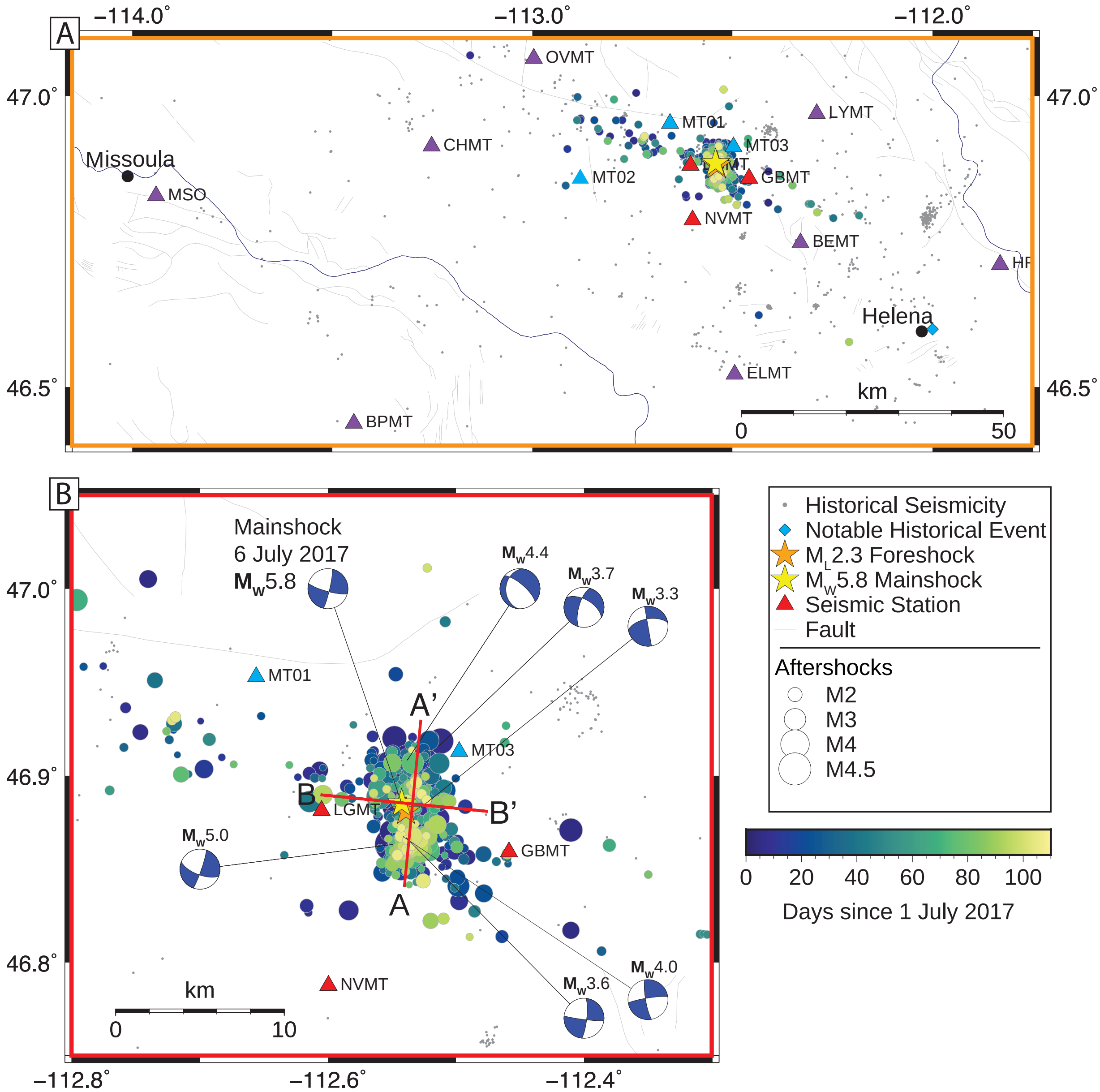

Figure 2.2. Maps of relocated earthquakes for the 6 July 2017 **Mw** 5.8 sequence. (A) Regional view (orange box in Figure 2.1) of the **Mw** 5.8 mainshock and 14 seismic stations used for this study. Purple triangles are the MB and US seismic stations used in this study; blue triangles are the GS stations deployed shortly after the mainshock; red triangles are the UM stations deployed 50 days after the mainshock. Earthquakes are colored as a function of time since 1 July 2017. (B) Tighter view (red box in Figure 2.1) of the 685 relocated earthquakes, computed focal mechanisms, and cross-section locations (shown in Figure 2.3).

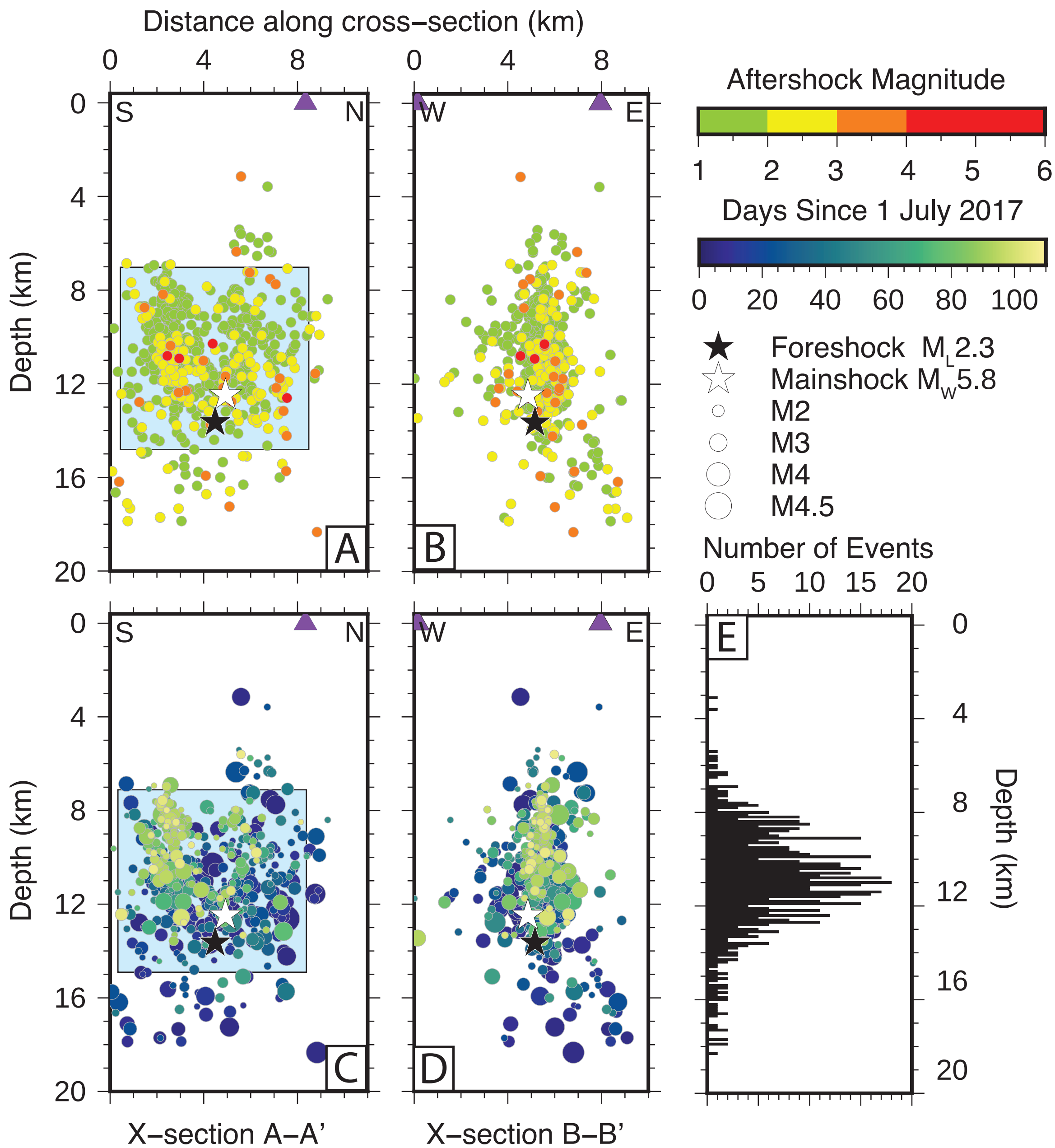

Figure 2.3. Cross-sections for 685 relocated events indicated in Figure 2.1. (A,B) Cross-sections A-A’ and B-B’ with earthquakes colored by magnitude. The light blue region indicates the 8 x 8 km^2 plane of concentrated activity discussed in the Event Relocations portion of the Results (section 2.4). (C,D) Cross-sections with earthquakes colored as a function of time since 1 July 2017 and sized as a function of magnitude. (E) Histogram of number of earthquakes as a function of depth in 0.1-km bins.

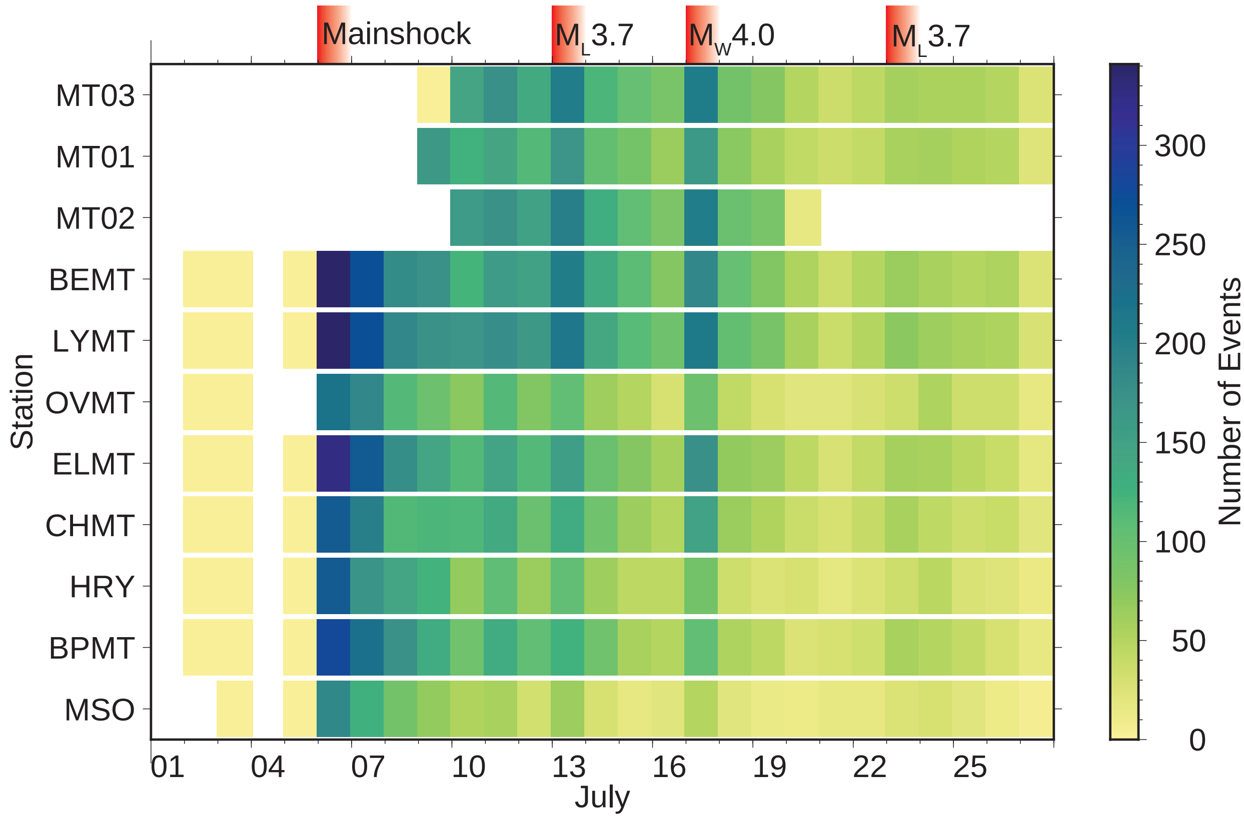

Figure 2.4. Event counts at each station detected using matched filtering resulting in the final catalog of 3009 events. The color scale represents the daily number of detections on each station with cross-correlation coefficients greater than or equal to 0.5. The red markers indicate the times of the mainshock and three significant aftershocks that resulted in sharply higher numbers of detections and deviations from steady aftershock rate decay.

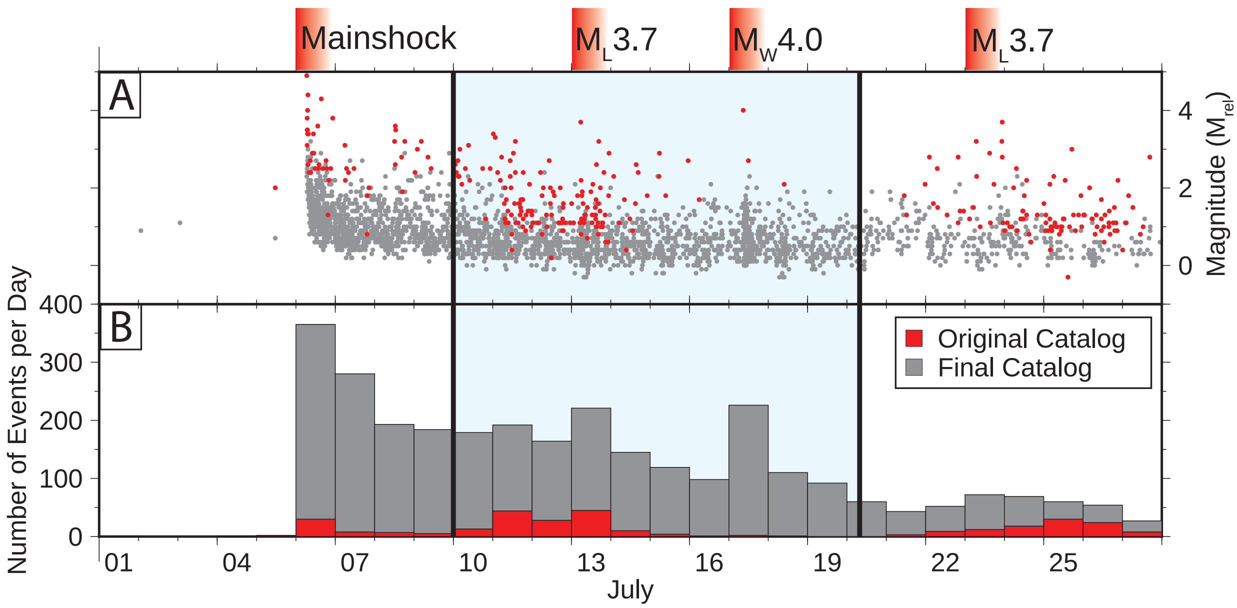

Figure 2.5. Magnitudes and daily event counts for the final catalog. (A) Magnitudes for the final 3009 events as a function of time of occurrence. The red dots indicate the 303 template earthquakes, and the gray dots indicate newly detected events. The blue shaded area indicates the time period when all 11 MB, US, and GS stations utilized in this study were simultaneously functional. (B) Daily event counts for this period. The red bars indicate template earthquakes, and the gray bars indicate event counts for the final catalog. The red markers on the top indicate the times of the mainshock and three significant aftershocks that resulted in sharply higher numbers of detections and deviations from steady aftershock rate decay.

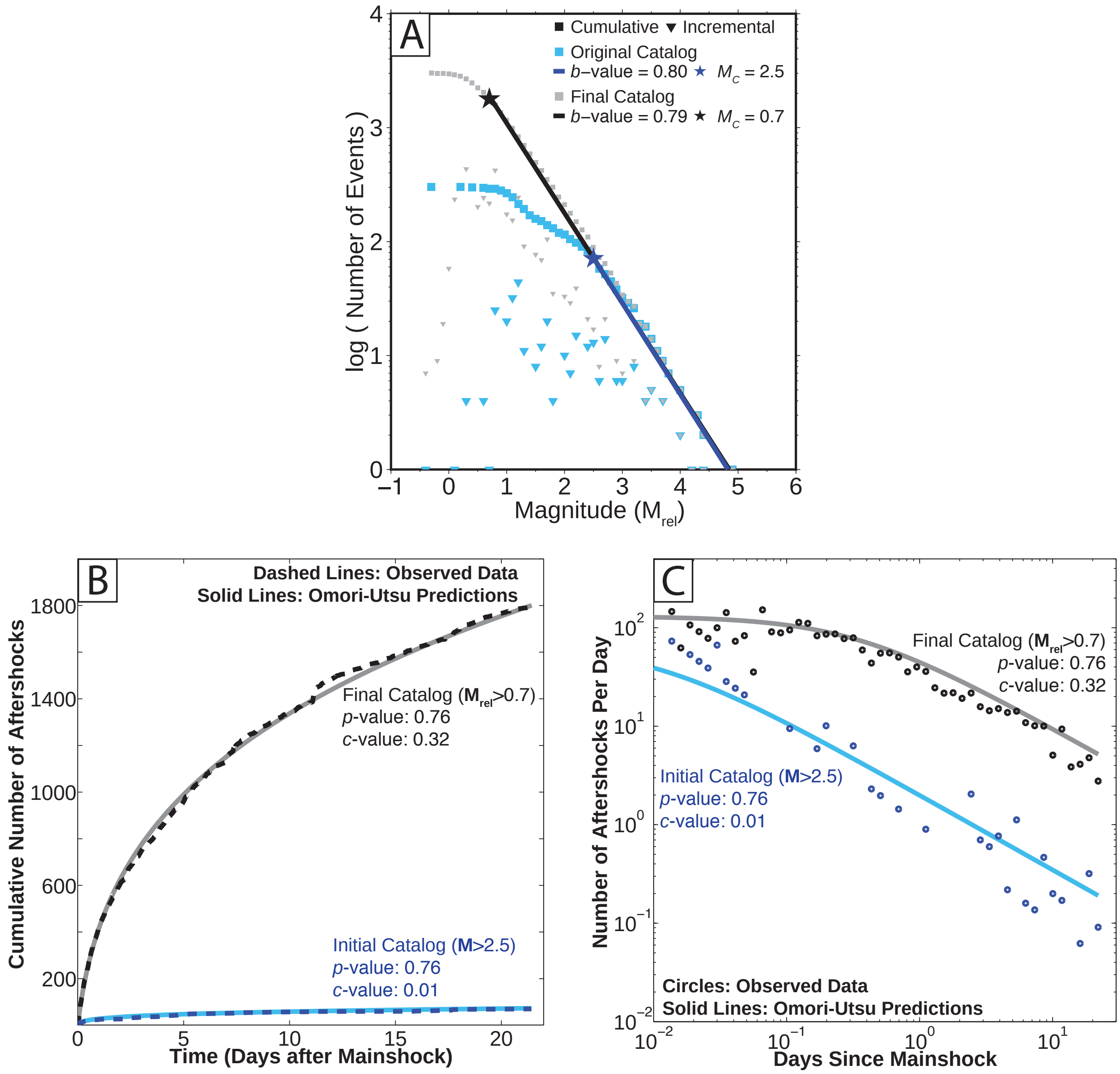

Figure 2.6. (A) Frequency-magnitude distributions for the original catalog (blue; initial 303 template events) and final catalog (grey; 3009 detected events). Triangles are incremental event counts, squares are cumulative event counts, stars show minimum magnitudes of completeness, M_C, and solid lines show *b*-value trends. Modified Omori Law predictions for the initial and final catalogs shown as a function of cumulative number of aftershocks (B) and aftershock rate (C). Dashed lines in B and circles in C are observed data, and solid lines in B and C are Omori-Utsu predictions with the indicated *p*- and *c*-values. Blue lines are the initial catalog and gray lines are the final catalog.

REFERENCES FOR CHAPTER 2

Aki, K. (1966), Generation and propagation of *G* waves from the Niigata earthquake of June 16, 1964, Part 2: Estimation of earthquake moment, released, energy, and stress-strain drop from the G wave spectrum, *Bull. Earthq. Res. Inst. Tokyo Univ.*, (44), 73-88.

Albuquerque Seismological Laboratory (ASL)/USGS (1980), U.S. Geological Survey Networks, *International Federation of Digital Seismograph Networks*, Other/Seismic Network, doi: 10.7914/SN/GS.

Albuquerque Seismological Laboratory (ASL)/USGS (1990), United States National Seismic Network, *International Federation of Digital Seismograph Networks*, Other/Seismic Network, doi: 10.7914/SN/US.

Arabasz, W. J. and R. B. Smith (1981), Earthquake prediction in the Intermountain Seismic Belt – An intraplate extensional regime, In D. W. Simpson and P. G. Richards (Eds.), *Earthquake Prediction: An International Review* (Vol. 4, pp. 248-258), Washington, D.C.: American Geophysical Union, doi: 10.1029/ME004p0248.

Benz, H. M., N. D. McMahon, R. C. Aster, D. E. McNamara, and D. B. Harris (2015), Hundreds of earthquakes per day: The 2014 Guthrie, Oklahoma, earthquake sequence, *Seismol. Res. Lett.*, 86(5), 1318-1325, doi: 10.1785/0220150019.

Bergman, E. A. (2014), *Multiple event relocation at the National Earthquake Information Center* (Final Technical Rep. Award G11AP20016), U.S. Geological Survey.

Doser, D. I. (1989), Source parameters of Montana earthquakes (1925-1964) and tectonic deformation in the northern Intermountain Seismic Belt, *Bull. Seismol. Soc. Am.*, 79(1), 31-50.

Duputel, Z., L. Rivera, H. Kanamori, and G. Hayes (2012), *W* phase source inversion for moderate to large earthquakes (1990-2010), *Geophys. J. Int.*, 189(2), 1125-1147, doi: 10.1111/j.1365-246X.2012.05419.x.

Ebel, J. E. (2009), Analysis of aftershock and foreshock activity in stable continental regions: Implications for aftershock forecasting and the hazard of strong earthquakes, *Seismol. Res. Lett.*, 80(6), 1062-1068, doi: 10.1785/gssrl.80.6.1062.

Friberg, P. A., G. M. Besana-Ostman, and I. Dricker (2014), Characterization of an earthquake sequence triggered by hydraulic fracturing in Harrison County, Ohio, *Seismol. Res. Lett.*, 85(6), 1295-1307, doi: 10.1785/0220140127.

Frohlich, C. and S. D. Davis (1993), Teleseismic *b* values; Or, much ado about 1.0, *J. Geophys. Res.*, 98(B1), 631-644, doi:10.1029/92JB01891.

Gutenberg, B., and C. F. Richter (1944), Frequency of earthquakes in California, *Bull. Seismol. Soc. Am.*, 34(4), 185-188.

Hayes, G. P., L. Rivera, and H. Kanamori (2009), Source inversion of the *W*-Phase: Real-time implementation and extension to low magnitudes, *Seismol. Res. Lett.*, 80(5), 817-822, doi: 10.1785/gssrl.80.5.817.

Holschneider, M., C. Narteau, P. Shebalin, Z. Peng, and D. Schorlemmer (2012), Bayesian analysis of the modified Omori law, *J. Geophys. Res.*, 117(B6), doi: 10.1029/2011JB009054.

Jordan, T. H. and K. A. Sverdrup (1981), Teleseismic location techniques and their application to earthquake clusters in the south-central Pacific, *Bull. Seismol. Soc. Am.*, 71(4), 1105-1130.

Lageson, D. R. and M. C. Stickney (2000), Seismotectonics of northwest Montana, USA, In R. A. Schall and E. H. Johnson (Eds.), *Montana Geological Society 50th Anniversary Symposium, Montana/Alberta Thrust Belt and Adjacent Foreland* (Vol. 1, pp. 109-126), Montana Geological Society.

Lewis and Clark County Disaster and Emergency Services Website: http://www.lccountymt.gov/des/potential-hazards/earthquakes.html.

McMahon, N. D., W. L. Yeck, M. C. Stickney, R. C. Aster, H. R. Martens, and H. M. Benz (2018), Spatiotemporal analysis of the foreshock-mainshock-aftershock sequence of the 6 July 2017 M5.8 Lincoln, Montana, earthquake, *U.S. Geol. Surv. Data Release*, doi: 10.5066/P9KTXZMK.

McNamara, D. E., H. M. Benz, R. B. Herrmann, E. A. Bergman, P. Earle, A. Meltzer, M. Withers, and M. Chapman (2014), The M_W 5.8 Mineral, Virginia, earthquake of August 2011 and aftershock sequence: Constraints on earthquake source parameters and fault geometry, *Bull. Seismol. Soc. Am.*, 104(1), 40-54, doi: 10.1785/0120130058.

Montana Bureau of Mines and Geology/Montana Tech (MBMG, MT USA) (2001), Montana Regional Seismic Network, *International Federation of Digital Seismograph Networks*, Other/Seismic Network, doi:10.7914/SN/MB.

Narteau, C., P. Shebalin, and M. Holschneider (2002), Temporal limits of the power law aftershock decay rate, *J. Geophys. Res.*, 107(B12), doi:10.1029/2002JB001868.

Okal, E. A. and J. R. Sweet (2007), Frequency-size distributions for intraplate earthquakes, In S. Stein and S. Mazzotti (Eds.), *Continental intraplate earthquakes: Science, hazard, and policy issues*, Geological Society of America Special Papers (Vol. 425, pp. 59-71), Geological Society of America, doi: 10.1130/2007.2425(05).

Omori, F. (1894), On the after-shocks of earthquakes, *J. Coll. Sci. Imp. Univ. Tokyo*, 7, 111-200.

Pardee, J. T. (1926), The Montana earthquake of June 27, 1925, In W. C. Mendenhall (Ed.), *Shorter Contributions to General Geology: Professional Paper 147* (pp. 7-23), Washington, D.C.: Dept. of the Interior and U.S. Geological Survey, doi: 10.3133/pp147.

Reynolds, M. W. (1979), Character and extent of Basin-Range faulting, western Montana and east-central Idaho, in G. W. Newman and H. D. Goode (Eds.), *Basin and Range Symposium and Great Basin Field Conference* (pp. 185-193), Rocky Mountain Association of Geologists and Utah Geological Association.

Sbar, M. L., M. Barazangi, J. Dorman, C. H. Scholz, and R. B. Smith (1972), Tectonics of the Intermountain Seismic Belt, western United States: Micro earthquake seismicity and the composite fault place solutions, *Geol. Soc. Am. Bull.*, 83(1), 13-28, doi: 10.1130/0016-7606(1972)83[13:TOTISB]2.0.CO;2.

Sears, J. W. and M. Hendrix (2004), Lewis and Clark line and the rotational origin of the Alberta and Helena salient, North American Cordillera, In A. J. Susan and A. B. Weil (Eds.), *Orogenic curvature: Integrating paleomagnetic and structural analysis*, Geological Society of America Special Papers (Vol. 383, pp. 173-186), Geological Society of America, doi: 10.1130/0-8137-2383-3(2004)383[173:LACLAT]2.0.CO;2.

Shi, Y. and B. A. Bolt (1982), The standard error of the magnitude-frequency *b* value, *Bull. Seismol. Soc. Am.*, 72(5), 1677-1687.

Smith, R. B. and W. J. Arabasz (1991), Seismicity of the intermountain seismic belt, In D. B. Slemmons, E. R. Engdahl, M. D. Zoback, and D. D. Blackwell (Eds.), *Neotectonics of North America* (pp. 185-228), Geological Society of America, doi: 10.1130/DNAG-CSMS-NEO.185.

Stickney, M. C. (2006), The 26 July 2005 M_W 5.6 Dillon, Montana earthquake, *Seismol. Res. Lett.,* 77(2), 209, doi:10.1785/gssrl.77.2.160.

Stickney, M. C. (2013), The 2005 Dillon, Montana earthquake: A moderate-sized intermountain seismic belt earthquake on a blind normal fault and its effects on local seismicity rates, *Seismol. Res. Lett.*, 84(2), 298, doi: 10.1785/0220130011.

Stickney, M. C. and M. J. Bartholomew (1987), Seismicity and Quaternary faulting of the northern Basin and Range province, Montana and Idaho, *Bull. Seismol. Soc. Am.*, 77(5), 1602-1625.

Stover, C. W. and J. L. Coffman (1993), *Seismicity of the United States, 1568-1989 (Revised)*, U.S. Geological Survey Professional Paper 1527, U.S. Geological Survey, doi: 10.3133/pp1527.

Sykes, L. R., J. Armbruster, W. Y. Kim, and L. Seeber (2008), Observations and tectonic setting of historic and instrumentally located earthquakes in the greater New York City-Philadelphia area, *Bull. Seismol. Soc. Am.*, 98(4), 1696-1719, doi: 10.1785/0120070167.

U.S. Geological Survey (2017), Earthquake summary M 5.8 – 11km SE of Lincoln, Montana, https://earthquake.usgs.gov/earthquakes/eventpage/us10009757#executive.

University of Montana (2017), University of Montana Seismic Network, *International Federation of Digital Seismograph Networks*, Other/Seismic Network, doi: 10.7914/SN/UM.

Utsu, T., Y. Ogata, and R. Matsu'ura (1995), The centenary of the Omori formula for a decay law of aftershocks activity, *J. Phys. Earth*, 43(1), 1-33, doi:10.4294/jpe1952.43.1.

Van Trees, H. L. (1968), *Detection, Estimation and Modulation Theory* (Vol. 1), New York: John Wiley and Sons.

Waldron, H. H. and R. W. Galster (1984), Comparative seismic hazards study of western Montana, In *Proceedings of the Eighth World Conference on Earthquake Engineering* (Vol. 1, pp. 31-38), Prentice-Hall.

Wallace, C. A., D. J. Lidke, and R. G. Schmidt (1990), Faults of the central part of the Lewis and Clark line and fragmentation of the Late Cretaceous foreland basin in west-central Montana, *Geol. Soc. Am. Bull.*, 102(8), 1021-1037, doi: 10.1130/0016-7606(1990)102<1021:FOTCPO>2.3.CO;2.

Wells, D. L. and K. J. Coppersmith (1994), New empirical relationships among magnitude, rupture length, rupture width, rupture area and surface displacement, *Bull. Seismol. Soc. Am.*, 84(4), 974-1002.

Wessel, P. and W. H. F. Smith (1991), Free software helps map and display data, *EOS Trans. AGU*, 72(41), 441-446, doi:10.1029/90EO00319.

Wiemer, S. (2001), A software package to analyze seismicity: ZMAP, *Seismol. Res. Lett.*, 72(3), 373-382, doi:10.1785/gssrl.72.3.373.

Wyss, M. (1973), Towards a physical understanding of the earthquake frequency distribution, *Geophys. J. Roy. Astron. Soc.*, 31(4), 341-359, doi: 10.1111/j.1365-246X.1973.tb06506.x.

Yang, H., L. Zhu, and R. Chu (2009), Fault-plane determination of the 18 April 2009 Mount Carmel, Illinois, earthquake by detecting and relocating aftershocks, *Bull. Seismol. Soc. Am.*, 99(6), 3413-3420, doi: 10.1785/0120090038.

Zeiler, C. P., M. C. Stickney, and M. A. Speece (2005), Revised velocity structure of western Montana, *Bull. Seismol. Soc. Am.*, 95(2), 759-762, doi:10.1785/0120040088.

Zhao, Z., K. Qike, K. Matsumura, and J. Xu (1992), *p*-values of continental aftershock activity in China, *Acta Seismol. Sin.*, 5(4), 683-690, doi:10.1007/BF02651015.

CHAPTER 3

Spatiotemporal Evolution of the 2011 Prague, Oklahoma, Aftershock Sequence Revealed Using Subspace Detection and Relocation [2]

Summary

The 6 November 2011 $\mathbf{M}_W$ 5.7 earthquake near Prague, Oklahoma, is the second largest earthquake ever recorded in the state. A $\mathbf{M}_W$ 4.8 foreshock and the $\mathbf{M}_W$ 5.7 mainshock triggered a prolific aftershock sequence. Utilizing a subspace detection method, we increase by fivefold the number of precisely located events between 4 November and 5 December 2011. We find that while most aftershock energy is released in the crystalline basement, a significant number of the events occur in the overlying Arbuckle Group, indicating that active Meeker-Prague faulting extends into the sedimentary zone of wastewater disposal. Although the number of aftershocks in the Arbuckle Group is large, comprising ~40% of the aftershock catalog, the moment contribution of Arbuckle Group earthquakes is much less than 1% of the total aftershock moment budget. Aftershock locations are sparse in patches that experienced large slip during the mainshock.

---

[2] **This chapter has been previously published:**

McMahon, N. D., R. C. Aster, W. L. Yeck, D. E. McNamara, and H. M. Benz (2017), Spatiotemporal evolution of the 2011 Prague, Oklahoma, aftershock sequence revealed using subspace detection and relocation, *Geophys. Res. Lett.*, 44(14), 7149-7158, doi: 10.1002/2017GL072944.

3.1 INTRODUCTION

In the 2011 **M**$_W$ 5.7 Prague, Oklahoma, sequence, three relatively large earthquakes (**M**$_W$ 4.8, 5.7, and 4.8) on 5, 6, and 8 November 2011, respectively, were likely induced by deep wastewater injection at a nearby well [*Keranen et al.*, 2013]. The mainshock is currently the second largest instrumentally recorded earthquake in Oklahoma history [*Keranen et al.*, 2013; *Sumy et al.*, 2014], only recently succeeded by the **M**$_W$ 5.8 Pawnee, Oklahoma, earthquake on 3 September 2016 [*Yeck et al.*, 2017]. The largest aftershock of the sequence, a **M**$_W$ 4.8, occurred 2 days after the mainshock. Much of this seismicity sequence occurred along the Meeker- Prague fault, a 20 km splay off the Wilzetta fault zone (WFZ). The WFZ is a complex, ~200 km long, Pennsylvanian-aged fault system that trends NE-SW through central Oklahoma [*Way*, 1983; *Joseph*, 1987]. Focal mechanisms and aftershock locations reveal a steeply dipping right-lateral strike-slip fault [*Dycus*, 2013; *Holland*, 2013b; *Sumy et al.*, 2014].

We apply subspace detectors and multiple-event relocation to the 2011 **M**$_W$ 5.7 Prague, Oklahoma, aftershock sequence to significantly lower the magnitude of completeness of the catalog and to better understand the spatiotemporal evolution of seismicity. Subspace detection is a powerful tool for detecting seismic events in low signal-to-noise environments and/or during high rates of seismicity. Subspace detectors improve upon simple cross correlation or matched filtering techniques by using multiple orthogonal waveform templates that approximately span the signals from all previously identified events within a data set; subspace detectors are also typically more computationally efficient [*Harris*, 2006]. The subspace methodology has been increasingly used for the characterization of large earthquake swarms [*Harris*, 2006; *Morton*, 2013; *Harris and Dodge*, 2011; *Barrett and Beroza*, 2014]; low-frequency earthquakes within nonvolcanic tremor [*Maceira et al.*, 2010]; extensive aftershock sequences [*Harris and Dodge*, 2011]; microseismic monitoring of hydrofracturing sequences [*Song et al.*, 2014]; exploration of deep, long-period magmatic events [*McMahon et al.*, 2016]; characterization of coal mine-related seismicity [*Chambers et al.*, 2015]; and investigation of induced seismicity clusters [*Benz et al.*, 2015b; *Skoumal et al.*, 2015].

3.2 Observational Waveform Data

We utilized waveform data from 21 temporary seismic stations: 18 from the Oklahoma RAMP network [*Keranen*, 2011] and 3 from the U.S. Geological Survey (USGS) network [*Albuquerque Seismological Laboratory*, 1980], all deployed within 1 week after the $\mathbf{M_W}$ 4.8 foreshock (Table A2.1). Stations were deployed around the aftershock sequence at distances between 0.7 and 14.7 km from the $\mathbf{M_W}$ 5.7 mainshock epicenter (Figure 3.1). Data from nine EarthScope USArray Transportable Array stations [*IRIS Transportable Array*, 2003] and an Oklahoma Seismic Network [*Oklahoma Geological Survey*, 1978] station were also utilized to better capture the foreshock-mainshock-aftershock activity and to enhance detection and location capabilities prior to full functionality of the temporary networks. The last deployed temporary stations became fully operational on 11 November 2011. We analyzed data from 4 November 2011, 1 day prior to the foreshock, through 5 December 2011.

3.3 Methodology

We utilized the catalog of *McNamara et al*. [2015] (Data Set A2.1) as the initial catalog for our subspace detector construction. A total of 998 events in the month following the foreshock were identified, located, and manually reviewed.

Detectors were developed exclusively for the *S*-phase, which observationally is the simplest in complexity and the largest amplitude signal. We followed the methodology of *Benz et al*. [2015b] for subspace detector construction, detection, and estimation of *S*-phase arrival time. We found that between 11 and 91 multichannel templates were needed to describe 90% of the observed event waveform energy on each of the stations (Table A2.1). The multichannel templates were simultaneously cross-correlated against continuous data at each station from the time the station became operational for temporary stations and from 4 November 2011 for permanent stations through 5 December 2011 (Table A2.1).

Although they excel at identifying smaller events, our subspace detectors can be insensitive to larger ($\mathbf{M_W} > 3$) events because the extended source duration of the mainshock and largest aftershocks makes them difficult to detect using templates that are derived from small earthquakes. We supplemented the detection catalog with larger event information by adding the *P*- and *S*-phase arrival times of the original catalog. The additional arrival time and station information of precisely located events resulted in a more robust final catalog.

After the arrival times from the detections were associated into events using an arrival time associator [*Benz et al.*, 2015a] and supplemented with large and precisely located event information, we used Bayesloc [*Myers et al.*, 2007, 2009] to estimate hypocenters utilizing the velocity model of *McNamara et al*. [2015] (Table A2.2).

For detected events, magnitudes relative to the nearest original event catalog neighbor were computed at each station using the method of *Benz et al*. [2015b] and averaged across all stations to determine the final event magnitude (Figure A2.2). To calculate the event catalog *b*-value [e.g., *Gutenberg and Richter*, 1944], we utilized the methods of *Benz et al*. [2015b].

The subspace detection methodology was chosen for its computational efficiency over running all the cataloged events as templates. A total of 14,150 events identified on the 31 stations of interest was reduced to 1116 subspace detection templates representing a 92% reduction in the number of templates cross correlated against the continuous data and an equivalent reduction in processing time.

3.4 RESULTS

A total of 577,040 S-phase arrival times from subspace detection were obtained using 31 seismic stations. A total of 191,100 of the arrival times were associated into 20,788 events observed at five or more stations. Most remaining arrival times were likely events observed on fewer than five stations. Few false detections are likely given that we set the detection threshold relatively high. Of the 21,786 events located, 5176 events had estimated epicentral uncertainties less than 500 m and depth uncertainties less than 1 km. After relocation, 184 of the events in the original catalog were excluded due to the uncertainty constraints, bringing the final event count to 5262. These excluded events were added to Figures A2.11–A2.15 for comparative visualization.

Aftershocks align primarily along the known fault strands of the WFZ, as indicated by the initial catalog (Figure 3.2a) and extend down to ~10 km depth. Aftershocks extend southwestward from a pair of active wastewater disposal wells along the main strike of the WFZ (A’-A”) before turning more westerly and extending ~16 km along the main strike of the Meeker-Prague fault

(A-A'), short of the 20 km length previously indicated due to strict uncertainty parameters used in this study. A splay (E-E'; Figure A2.1) extends ~4 km west- ward away from the Meeker-Prague fault. A linear, NE-SW oriented satellite sequence (G-G'; Figure A2.1) appears ~9 km to the southeast of the main aftershock sequence, subparallel to the Meeker-Prague fault. This nearly vertical active fault structure was not clearly visible in the initial catalog.

The 5 November **M**$_W$ 4.8 foreshock ruptured a portion of the main WFZ along A'-A" (Figures 3.2c1–3.2c3). The aftershocks extend southwestward from a pair of active wastewater disposal wells, deepening over a distance of ~3 km to 10 km depth. The **Mw** 5.7 mainshock ruptured the Meeker-Prague fault along A-A' (Figures 3.2b1–3.2b3). Along this fault, most aftershocks are concentrated in an ~9 by 9 km section of the fault extending southwestward away from the intersection with the main WFZ. The largest aftershock, a **M**$_W$ 4.8, ruptured an ~4 km westward trending splay of the Meeker-Prague fault along E-E' (Figure A2.1).

From map view and cross section C-C' we see the geometry of the Meeker-Prague fault striking N55°E and dipping 85° to the northwest which is consistent with the USGS W-phase moment tensor solution striking N56°E and dipping 85° to the northwest.

Common characteristics are visible in the cross sections. First, there is a "lid" of seismicity characterized by dense aftershock occurrence between ~1.4 and 2.6 km depth with relatively few aftershocks occurring immediately above and below this zone. Within this zone, there is a bifurcation in aftershock occurrence at ~1.9 km depth. We note that the input velocity model had an increase at this depth, which may cause this split in location depths in the Arbuckle, but it cannot cause the difference in depths between these events and the deeper, larger basement events. Dense aftershock occurrence is seen on cross sections A-A’ and A’-A” between ~4.7 and 8 km depth with relatively little activity between the top of this zone and the base of the above described lid. While the number of aftershocks shallower than 2.6 km is relatively high, the moment released (Figures 3.2b3, 3.2c3, and 3.2d3) is relatively low, indicating smaller aftershocks occurring above this depth and larger ones below. Additional cross sections can be found in Figure A2.1.

The complete catalog *b*-value is 0.52 with a minimum magnitude of completeness, M_C, of 0.8 extending the initial catalog’s M_C down 1.2 units of magnitude while maintaining the general nature of the frequency-magnitude distribution (Figure 3.3a). We note a difference between the frequency-magnitude distribution of the complete catalog and the catalog of detected events alone. The catalogs have the same magnitude of completeness, but there is a divergence between the number of detected events in the original and subspace detected catalog above **M** 1.5. If we enlarge the subspace catalog by increasing the uncertainty allowed in locations to 2.0 km horizontal error and 5.0 km depth error, while seeing more scatter in locations and less well-defined fault structures, we do not see a significant change in the frequency-magnitude distribution. We noted previously that subspace detection can be insensitive to larger events, and this divergence may suggest, in contrast to a minimum magnitude of completeness, a maximum magnitude of completeness achievable with subspace detection alone.

The number of detected aftershocks decays steadily after the network became fully functional on 11 November 2011 (Figure 3.3c), while the mean magnitude of events remained relatively constant. The decay rate is consistent with a modified Omori decay law [*Utsu et al.*, 1995] *p*-value of 0.61 (Figure 3.3b). This value increases to 0.69 when looking at only aftershocks above the catalog M_C. Both values, however, are smaller than standard *p*-values found globally, 0.9–1.5 [*Utsu et al.,* 1995]. These low values indicate a slower decay rate than most earthquake sequences possibly explained by the intraplate location [*Zhao et al.*, 1992] and low heat-flow values [*Blackwell et al.*, 2011] leading to lower stress relaxation [*Mogi*, 1967; *Kisslinger and Jones*, 1991]. This finding contrasts with the short-term results of *McNamara et al*. [2015], which estimated a *p*-value for the first few months of the Prague aftershock sequence of 1.25 and a rapidly decaying aftershock. This discrepancy between estimated *p*-values likely arises because this study analyzed just 25 days of data (post full network functionality), whereas *McNamara et al*. [2015] studied 95 days of data. The detection and location of low-magnitude events via subspace detection also contribute to this discrepancy, detecting more events over an increased time period slowing the decay rate and subsequently lowering the *p*-value. Both studies note slower aftershock decay in the days immediately following the mainshock, with the decay rate increasing 20–30 days post–mainshock.

A diurnal variation in the number of precisely located earthquakes shows the sensitivity of the subspace detection method to background noise levels. We note a diurnal variation in the temporal decay of aftershocks (Figures 3.4a and 3.4b). Overall, there is a 60% increase in the number of aftershocks detected in the local overnight hours (18:00–06:00) versus local daylight hours (06:00–18:00). We attribute this difference to diurnal variation in anthropogenic noise (e.g., vehicle traffic). This effect increases the catalog's overnight M_C from **M** -1.2 to **M** -0.6

relative to the daylight M_C. When analyzing only aftershocks above the entire catalog's M_C, the difference in numbers of detected aftershocks and mean magnitude is significantly lessened.

3.5 DISCUSSION

Utilizing subspace detection, we increased the number of precisely located events in the catalog fivefold and decrease the M_C by 1.2 units of magnitude to **M** 0.8. Many smaller events are hard to detect at multiple stations because of poor signal-to-noise characteristics, but this is overcome by strategically correlating the *S*-phase recorded on three components (see Figures A2.6–A2.8 for waveform examples). This significant increase in detected and locatable earthquakes allows for more detailed spatiotemporal analysis of the evolution of the aftershock sequence.

The Arbuckle Group, the principal wastewater disposal formation in the Prague region, is composed of late Cambro-Ordovician cyclic carbonate and underlies most of Oklahoma and the adjacent states [*Johnson*, 1991; *Fritz et al.*, 2013]. A high density of very small earthquakes occurring between 1.4 and 2.6 km depth on both the main and off-fault seismicity trends, combined with information from nearby well logs, indicates slip on small WFZ structures extending into this formation.

Overlying the Arbuckle Group is the middle Ordovician Simpson Group, a sequence of basal sandstones grading upward to shales and limestones [*Suhm*, 1997; *Dycus*, 2013]. This group records the first influx of clastic sediments over a region that had previously been the site of a vast amount of carbonate accumulation [*Islam and Crump*, 1990]. The sandy and clastic nature of the Simpson Group sharply contrasting against the underlying Arbuckle Group carbonates may indicate why earthquakes do not propagate to shallower depths in the Prague region. The lithologic change also explains the sharply delineated top of the lid of seismicity at ~1.4 km. Only 16 events in the catalog have hypocentral depths <1.4 km.

Although other studies have noted some seismicity within the Arbuckle Group [e.g., *Keranen et al.*, 2014], the enhanced detection capabilities of subspace detection reveal a great number of aftershocks within the Arbuckle Group, with 40% of the aftershocks identified in this study located between 1.4 and 2.6 km depth (Figure A2.4). The vast majority of these events are very small: 95% were smaller than **M** 0.2. For scale, a **M** 0.2 corresponds to a 70 m^2 fault area slipping 1 mm using equation 1 of *Hanks and Kanamori* [1979] and assuming a shear modulus of 32 GPa. As a consequence, the total moment release for earthquakes in the Arbuckle Group is small, despite the large number of aftershocks, and nearly all of the seismic moment is released in the crystalline basement, with >99.9% of the cumulative moment in the catalog released below 2.6 km depth. All but one of the 168 events larger than **M** 2 occur below 2.6 km depth.

The Arbuckle Group overlies the Precambrian granitic basement. Both *Dycus* [2013] and *Keranen et al*. [2013] put the top of basement at ~2.5 km depth in the aftershock region, which is congruent with the observed base of the small magnitude Arbuckle lid of seismic activity at ~2.6 km. The unconformity between the base of the sedimentary Arbuckle Group and the top of the volcanic basement may explain the sharp contrast in earthquake density and energy release across the formation boundary, reflecting sharply differing stress and/or rheological conditions between the two units.

We note a difference in the frequency-magnitude distributions (FMD) between the Arbuckle Group and the basement (Figure 3.3c). The FMD of the basement resembles that of the original catalog as few small events in the Arbuckle Group were originally detected. The *b*-value of the Arbuckle Group follows more closely with the empirically estimated global *b*-value of 1.0. This disparity across the unconformity is expected as larger events are occurring in the basement decreasing the *b*-value, and only small events are occurring in the Arbuckle Group increasing the *b*-value. *Friberg et al*. [2014] suggest, in hydraulic fracturing sequences, that lower *b*-values are associated with reactivation of preexisting faults rather than the creation of new fractures as intended by the operations. The low *b*-value in the basement may represent the reactivation of the Wilzetta fault zone and therefore be characterized by a lower *b*-value. The higher *b*-value in the Arbuckle Group may represent the creation of new fractures associated with wastewater injection operations. The entire catalog's *b*-value, however, is dominated by basement events.

We also note a difference in the modified Omori decay *p*-values between the Arbuckle Group and the basement (Figure 3.3d). A lower *p*-value in the Arbuckle Group indicates a slower decay in the number of after- shocks over time. This disparity is possibly explained by a larger number of small events being detected in the Arbuckle Group over time due to the proximity to seismic stations. The increase in the decay rate/*p*-value seen in the entire catalog is only found in the Arbuckle Group, however. It is possible that the sedimentary section may be experiencing this change due to the induced nature of the sequence, perhaps taking a few weeks for the fluid pressures and perturbations associated with the wastewater injection to stabilize.

The size of an earthquake is determined by the constitutive properties of the medium [*Lapusta and Rice*, 2003] and the frictional strength of the fault [*Byerlee*, 1978; *Das and Scholz*, 1983]. These principles may explain why larger-magnitude events are not occurring in the shallow sediments in the Prague region. It is unlikely that an event larger than **M** 2–3 will initiate in the Arbuckle Group or **M** 1 in the shallow sediments, and unlikely larger events, such as the $\mathbf{M_W}$ 4.8 foreshock and $\mathbf{M_W}$ 5.7 mainshock, will occur much shallower than 5 km in the Meeker-Prague region (Figure A2.5). We hypothesize that limitations on earthquake magnitudes in the Arbuckle Group could be controlled by physical parameters: the lower shear modulus of the carbonate compared to the basement granite thus producing smaller magnitudes, the change in rheological properties across the Arbuckle-basement unconformity limiting the size of faults and disallowing them to progress downward, or the increased pore fluid pressure lowering the frictional strength of the rocks causing smaller strains to accumulate and hence smaller slips.

The aftershock locations along the Meeker-Prague fault show good correlation with the finite-fault slip model estimated by *Sun and Hartzell* [2014] (Figure 3.4). As shown previously, the large slip patches are predominantly free of aftershocks. Approximately 73% of events locate in cells with less than 10 cm slip and only 5% in cells with more than 30 cm slip which agrees with the observation that aftershocks are preferentially located in low-slip regions of faults [*Mendoza and Hartzell*, 1988; *Beroza and Zoback*, 1993; *Das and Henry*, 2003; *Woessner et al.*, 2006] (Figure A1.3).

In addition to the main faults ruptured during the Prague sequence, a subparallel, unmapped fault approximately 9 km to the southeast of the principal Meeker-Prague fault system was illuminated by aftershock activity along G-G' (Figures A2.1d1–A2.1d3). This fault exhibits characteristics that are similar to the main Meeker-Prague fault: a NE-SW trend similar to a majority of seismogenic faults in Oklahoma, a high density of low-magnitude earthquakes occurring at shallow depths, and larger-magnitude events occurring below this depth. There appears to be a clear lineation of earthquakes at ~2.3 km depth which may demarcate the base of the Arbuckle Group, slightly shallower than the main fault system to the northwest. This new fault appears to have become active on 9 November 2011, and activity may have been statically triggered by the seismicity on the main fault zone.

3.6 CONCLUSIONS

Application of subspace detection methodology increased the number of precisely located events in the Prague, Oklahoma, aftershock catalog more than fivefold. Most events in the updated catalog are located using only the *S*-phase which may be useful for environments in which other body phases may be difficult to discern or pick. We find a large number of earthquakes (~40%) within the Arbuckle Group, the zone of wastewater injection in the Prague region, indicating that the Meeker-Prague fault may extend into the above-basement sediment. These earthquakes, however, are mostly very small, comprising << 1% of moment budget of the entire catalog. We find a previously unmapped, subparallel fault delineated by aftershock locations approximately 9 km to the southeast of the main Meeker-Prague fault. The aftershock locations show good correlation with finite-fault slip models showing that patches that experienced large slip during the mainshock are predominantly free of aftershocks. Via subspace detection, we effectively lowered the catalog's minimum magnitude of completeness to **M** 0.8, detecting microseismic events that may not be possible with more traditional detection techniques and allowing for more detailed analysis of spatiotemporal trends in seismicity.

3.7 Acknowledgements

Most seismic data were obtained from the Incorporated Research Institutions for Seismology Data Management Center (http://www.iris.edu/, last accessed June 2015). IRIS Data Services are funded through the Seismological Facilities for the Advancement of Geoscience and EarthScope (SAGE) Proposal of the National Science Foundation under cooperative agreement EAR-1261681. Seismic data for stations ZQ.LC01-ZQ.LC08 were obtained from the U.S. Geological Survey National Earthquake Information Center archives. The initial catalog of events was obtained through written communication with E. Bergman and D. McNamara. The final aftershock catalog data are available at the U.S. Geological Survey ScienceBase website https://www.sciencebase.gov/catalog/item/ 595276c6e4b062508e3c7650 (last accessed July 2017) [*McMahon*, 2017]. Class II injection well information was obtained from the Oklahoma Corporation Commission electronic well database (http://www.occpermit.com/ WellBrowse/, last accessed May 2015) and oil and gas data files (http://www.occeweb.com/og/ogdatafiles2.htm, last accessed May 2015). Fault data were obtained from the Oklahoma Geological Survey Open-File Report OFR3-2015 [*Holland*, 2015]. Finite-fault slip data were obtained via written communication with S. Hartzell. We thank S. Larson for geological comments on this study and A. Holland, G. Choy, and M. Brudzinski for thoughtful reviews. Some figures were created using the Generic Mapping Tools (GMT) version 5.1.2 (www.soest.hawaii.edu/gmt) [*Wessel et al.*, 2013].

3.8 FIGURES FOR CHAPTER 3

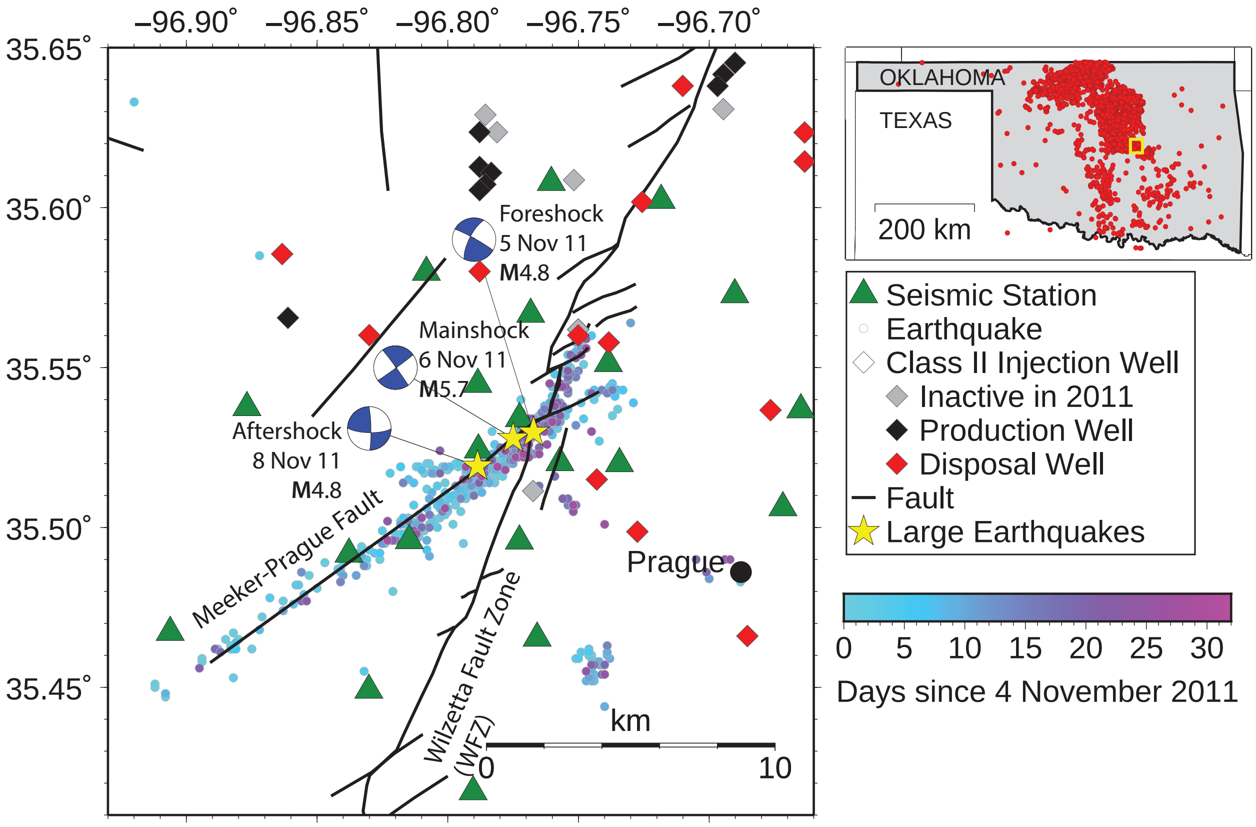

Figure 3.1. Map of aftershocks in the *McNamara et al*. [2015] catalog used for subspace detector construction (circles) colored by time of occurrence after 4 November 2011, seismic stations utilized in the study (green triangles), class II injection wells (diamonds) colored by type of activity, and mapped faults (solid black lines). The earthquakes extend southwestward away from a pair of active wastewater disposal wells. Location map of all historic seismicity above **M**$_W$ 2.5 in Oklahoma complete through July 2016 in the top right. The aftershocks illuminated ~20 km of the Meeker-Prague fault and an off-fault cluster of events to the southeast.

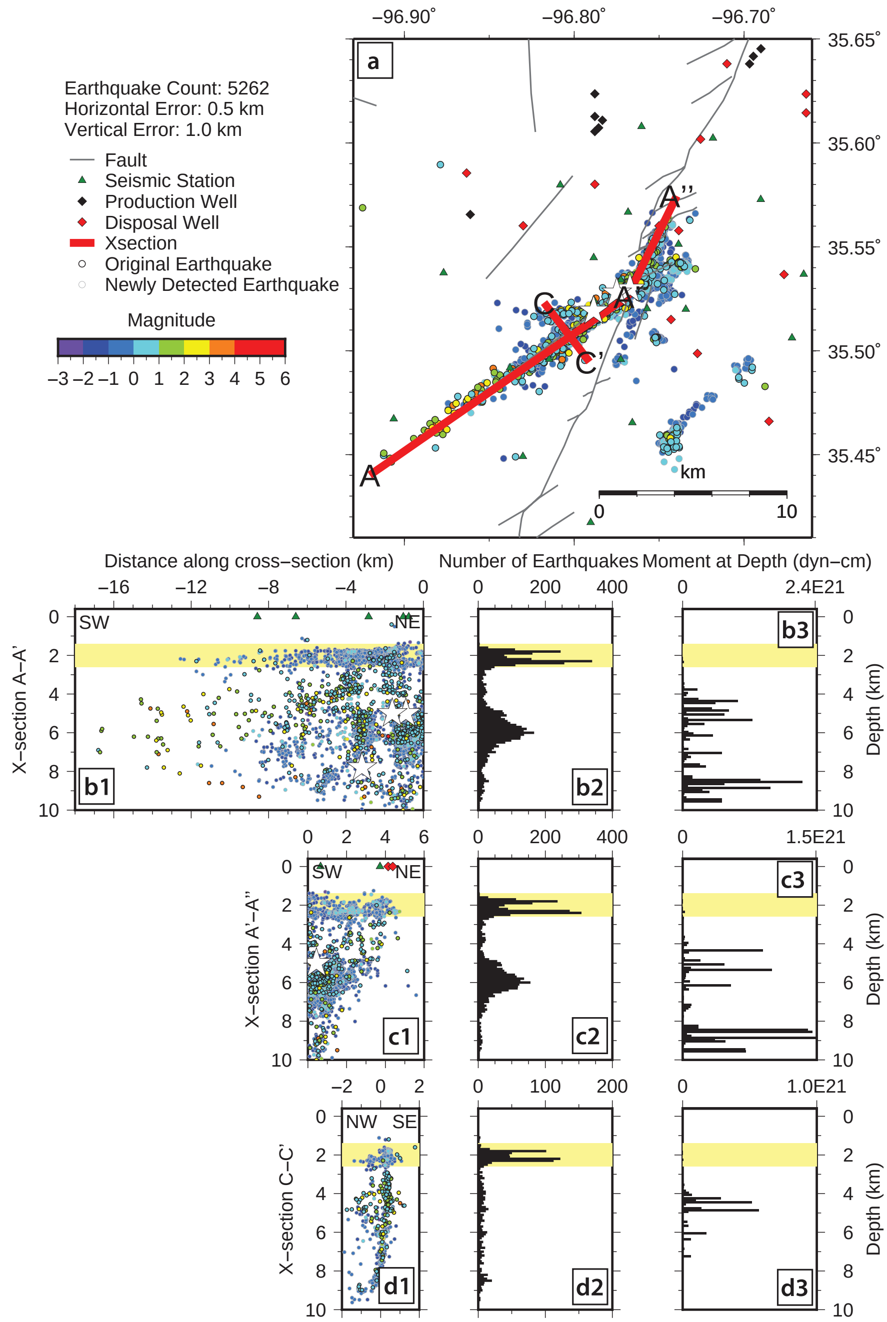

Figure 3.2. (a) Map of final event catalog locations with epicentral uncertainties less than 500 m and depth uncertainties less than 1 km. The yellow depth range depicts the approximate extent of the Arbuckle Group in the region. Events are colored by magnitude as indicated in the legend. The three large events (Figure 3.1) are plotted as white stars, and cross sections are indicated by red lines. (b1) Event locations within 1.5 km of cross section A-A' along the strike Meeker-Prague fault. (b2) Number of earthquakes in cross section A-A' as a function of depth in 0.1 km depth bins. (b3) Seismic moment in cross section A-A' as a function of depth in 0.1 km depth bins. (c1–c3) Follows Figures 3.2b1–3.2b3 for cross section A'-A" along the main strike of the Wilzetta fault zone. (d1–d3) Follows Figures 3.2b1–3.2b3 for cross section C-C' perpendicular to the Meeker- Prague fault.

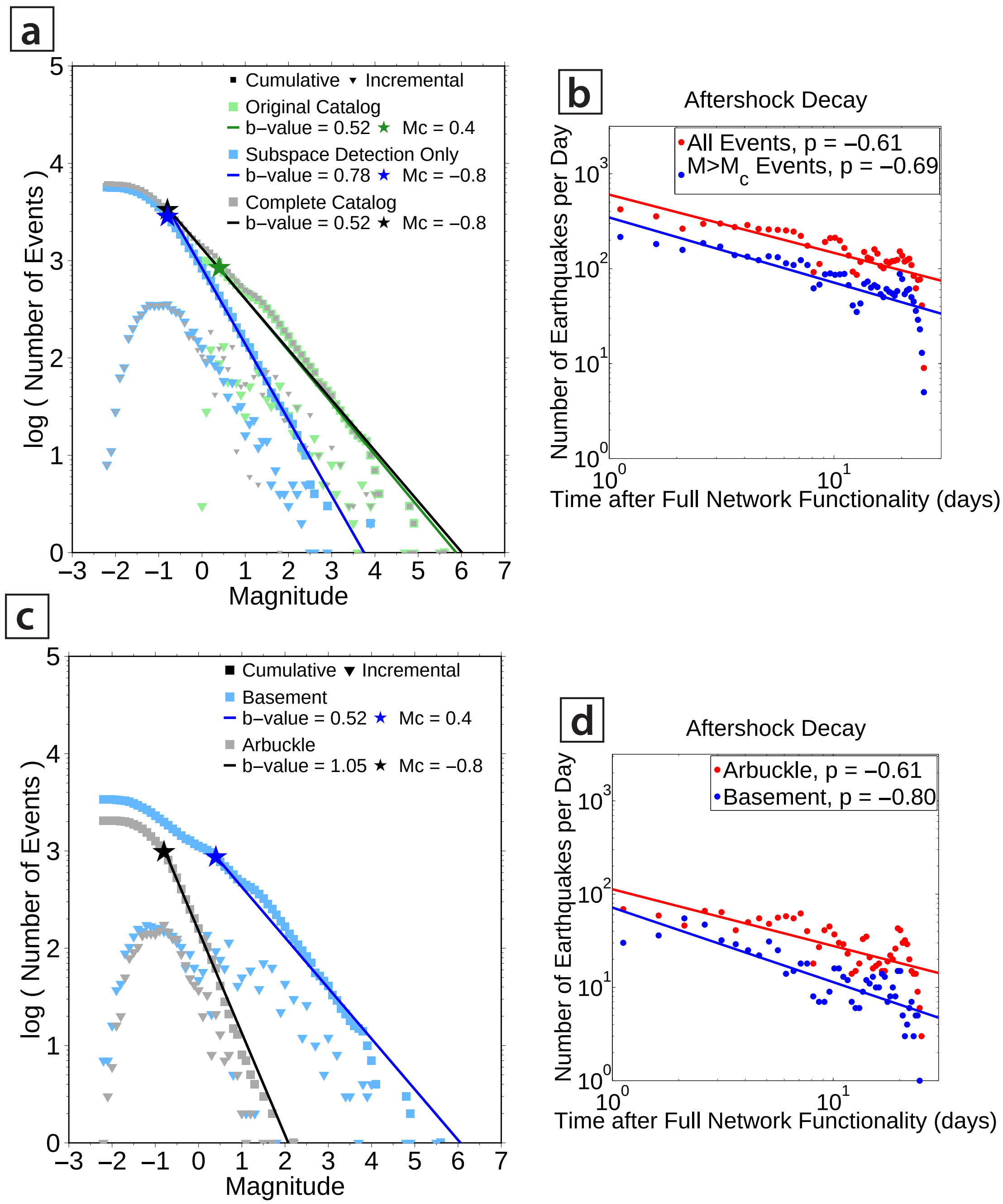

Figure 3.3. (a) Frequency-magnitude distributions for the original catalog of events (green), the catalog using only subspace detected events (blue), and the final catalog amalgamating the two previous catalogs (gray). Minimum magnitude of completeness M_C and *b*-value lines are also plotted. The triangles indicate absolute number of events within respective magnitude bins, and the squares indicate cumulative number of events greater than or equal to respective magnitudes. (b) Modified Omori decay parameter, *p*, using all catalog events (red) and only events above the M_C (blue). (c) Follows Figure 3.3a showing the differing frequency-magnitude distributions between the Arbuckle Group (red) and the crystalline basement (blue). (d) Follows Figure 3.3b showing the differing modified Omori decay parameters between the Arbuckle Group (red) and the basement (blue).

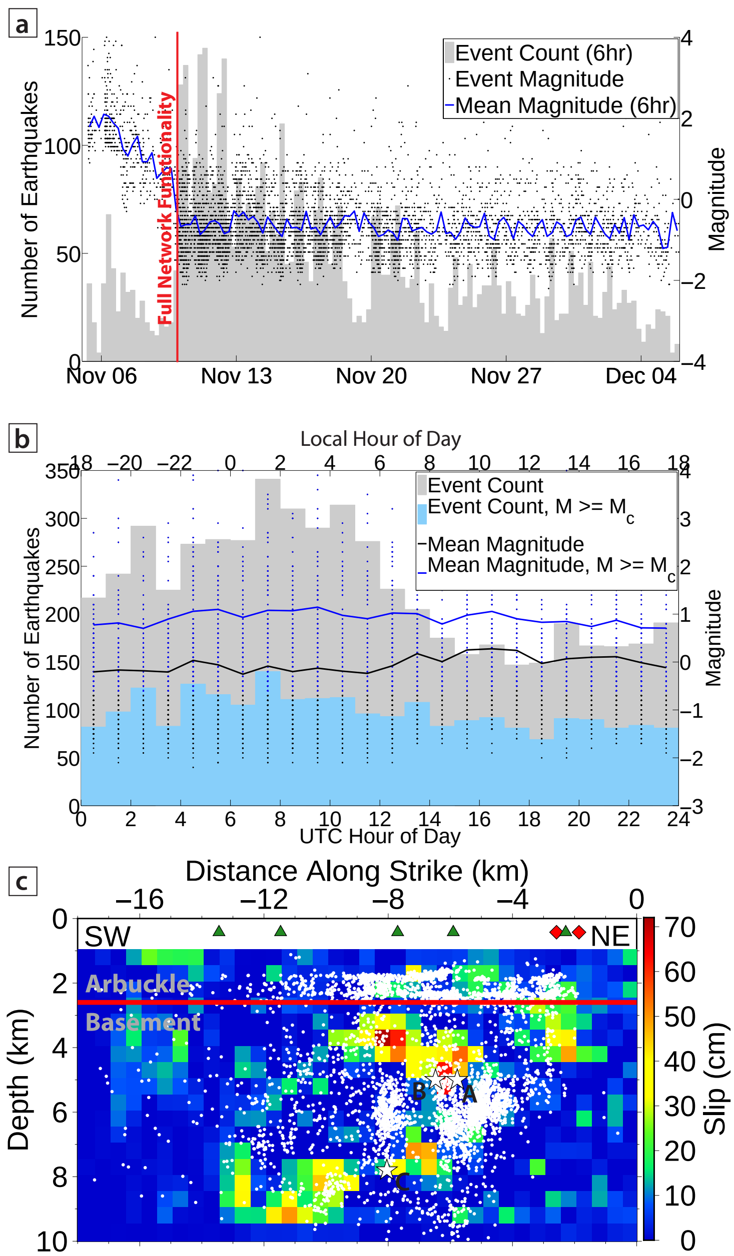

Figure 3.4. (a) Number of events and mean magnitude as a function of time. Event count per 6 h interval plotted as gray bars, mean magnitude as blue line, and magnitude of events occurring during the 6 h interval as black dots. (b) Examination of the diurnal variation seen in Figure 3.4a. Number of events per hour of the day for full catalog plotted in gray and catalog above the magnitude of completeness M_C plotted in blue with mean magnitude shown. Magnitude of events occurring during the 6 h interval plotted as black dots. (c) Finite-fault slip model from *Sun and Hartzell* [2014], depth indicated by scale on left and color-coded slip amplitude by scale on right, overlain by aftershock locations (white dots) from this study. The foreshock (A), mainshock (B), and largest aftershock (C) locations are shown by the white stars. The gray line indicates the basement-Arbuckle Group contact. As noted previously, large slip patches are predominantly free of aftershocks.

REFERENCES FOR CHAPTER 3

Albuquerque Seismological Laboratory (ASL)/USGS (1980), U.S. Geological Survey Networks, International Federation of Digital Seismograph Networks, Other/Seismic Network, doi:10.7914/SN/GS.

Barrett, S. A., and G. C. Beroza (2014), An empirical approach to subspace detection, *Seismol. Res. Lett.*, 85(3), 594-600, doi:10.1785/ 0220130152.

Benz, H. M., C. E. Johnson, J. M. Patton, N. D. McMahon, and P. S. Earle (2015a), *GLASS 2.0: An operational, multimodal, Bayesian earthquake data association engine*, Abstract S21B-2687 presented at 2015 Fall Meeting, AGU, San Francisco, Calif.

Benz, H. M., N. D. McMahon, R. C. Aster, D. E. McNamara, and D. B. Harris (2015b), Hundreds of earthquakes per day: The 2014 Guthrie, Oklahoma, earthquake sequence, *Seismol. Res. Lett.*, 86(5), 1318-1325, doi:10.1785/0220150019.

Beroza, G. C., and M. D. Zoback (1993), Mechanism diversity of the Loma Prieta aftershocks and the mechanisms of mainshock-aftershock interaction, *Science*, 259(5092), 201-213, doi:10.1126/science.259.5092.210.

Blackwell, D. D., M. C. Richards, Z. S. Frone, J. F. Batir, M. A. Williams, A. A. Ruzo, and R. K. Dingwall (2011), SMU geothermal heatflow map of the conterminous United States, 2011, accessed 15 Sep 2018, http://www.smu.edu/geothermal.

Byerlee, J. (1978), Friction of rocks, *Pure Appl. Geophys.*, 116(4-5), 615-626, doi:10.1007/BF00876528.

Chambers, D. J. A., K. D. Koper, K. L. Pankow, and M. K. McCarter (2015), Detecting and characterizing coal mine related seismicity in the western U.S. using subspace methods, *Geophys. J. Int.*, 203(2), 1388-1399, doi:10.1093/gji/ggv383.

Das, S. and C. H. Scholz (1983), Why large earthquakes do not nucleate at shallow depths, *Nature*, 305, 621-623, doi:10.1038/305621a0.

Das, S. and C. Henry (2003), Spatial relationship between main earthquake slip and its aftershock distribution, *Rev. Geophys.*, 41(3), 1013, doi:10.1029/2002RG000119.

Dycus, M. N. (2013), Structural characterization of the Wilzetta fault zone; Lincoln, Pottawatomie, and Creek Counties, Oklahoma, MS thesis, Dep. of Geosc., Univ. of Tulsa, Tulsa, Okla.

Friberg, P. A., G. M. Besana-Ostman, and I. Dricker (2014), Characterization of an earthquake sequence triggered by hydraulic fracturing in Harrison County, Ohio, *Seismol. Res. Lett.*, 85(6), doi:10.1785/0220140127.

Fritz, R. D., P. Medlock, M. J. Kiykendall, and J. L. Wilson (2013), The geology of the Arbuckle Group in the Midcontinent: Sequence stratigraphy, reservoir development, and the potential for hydrocarbon exploration, In J. Derby, R. Fritz, S. Longacre, W. Morgan, and C. Sternbach (Eds.), *The Great American Carbonate Bank: The Geology and Economic Resources of the Cambro-Ordovician Sauk Megasequence of Laurentia*, AAPG Memoir (Vol. 98, pp. 203-273), Tulsa: AAPG.

Gutenberg, B., and C. F. Richter (1944), Frequency of earthquakes in California, *Bull. Seismol. Soc. Am.*, 34(4), 185-188.

Hanks, T. C., and H. Kanamori (1979), Moment magnitude scale, *J. Geophys. Res.*, 84(B5), 2348-2350, doi:10.1029/JB084iB05p02348.

Harris, D. B. (2006), *Subspace detectors: Theory* (Rep. UCRL-TR-222758), Livermore, California: Lawrence Livermore National Laboratory.

Harris, D. B., and D. A. Dodge (2011), An autonomous system for grouping events in a developing aftershock sequence, *Bull. Seismol. Soc. Am.*, 101(2), 763-774, doi:10.1785/0120100103.

Holland, A. (2013), Optimal fault orientations within Oklahoma, *Seismol. Res. Lett.*, 84(5), 876-890, doi:10.1785/0220120153.

Holland, A (2015), Preliminary fault map of Oklahoma (Open File Rep. 03-2015, scale 1:750,000), Oklahoma Geological Survey.

IRIS Transportable Array (2003), USArray Transportable Array, International Federation of Digital Seismograph Networks, Other/Seismic Network, doi:10.7914/SN/TA.

Islam, Q. T. and J. Crump (1990), Simpson Group extent in Oklahoma focus of stud, *Oil Gas J.*, 88(24), accessed 15 Sep 2018, https://www.ogj.com/articles/print/volume-88/issue-24/in-this-issue/exploration/simpson-group-extent-in-oklahoma-focus-of-stud.html.

Johnson, K. S. (1991), Geological overview and economic importance of Late Cambrian and Ordovician rocks in Oklahoma, In K. S. Johnson (Ed.), *Late Cambrian-Ordovician Geology of the Southern Midcontinent, 1989 Symposium*, Oklahoma Geological Survey Circular (Vol. 92, pp. 3-14), Norman, Oklahoma: Oklahoma Geological Survey.

Joseph, L. (1987), Subsurface analysis, “Cherokee” Group (Des Monesian), portions of the Lincoln Pottawatomie, Seminole, and Okfuskee Counties: Oklahoma, *Oklahoma City Geological Society Shale Shaker*, Dec. 1986/Jan. 1987.

Keranen, K. (2011), Oklahoma RAMP, *International Federation of Digital Seismograph Networks*, Other/Seismic Network, doi:10.7914/SN/ZQ_2011.

Keranen, K. M., H. M. Savage, G. A. Abers, and E. S. Cochran (2013), Potentially induced earthquakes in Oklahoma, USA: Links between wastewater injection and the 2011 M_w 5.7 earthquake sequence, *Geology*, 41(6), 699-702, doi:10.1130/G34045.1.

Keranen, K. M., M. Weingarten, G. A. Abers, B. A. Bekins, and S. Ge (2014), Sharp increase in central Oklahoma seismicity since 2008 induced by massive wastewater injection, *Science*, 345(6195), 448-451, doi:10.1126/science.1255802.

Kisslinger, C., and L. M. Jones (1991), Properties of aftershock sequences in southern California, *J. Geophys. Res.*, 96(B7), 11,947-11,958, doi:10.1029/91JB01200.

Lapusta, N. and J. R. Rice (2003), Nucleation and early seismic propagation of small and large events in a crustal earthquake model, *J. Geophys. Res.,* 108(B4), 2205, doi:10.1029/2001JB000793.

Maceira, M., C. A. Rowe, G. Beroza, and D. Anderson (2010), Identification of low frequency earthquakes in non-volcanic tremor using the subspace detector method, *Geophys. Res. Lett.*, 37, L06303, doi:10.1029/2009GL041876.

McMahon, N. D., R. C. Aster, E. K. Myers, and A. C. Lough (2016), *Using subspace detection to study deep long-period seismicity beneath the Executive Committee Range, Marie Byrd Land, Antarctica*, Abstract S31E-04 presented at 2016 Fall Meeting, AGU, San Francisco, Calif.

McMahon, N. D., R. C. Aster, W. L. Yeck, D. E. McNamara, and H. M. Benz (2017), Aftershock catalog for the November 2011 Prague, Oklahoma, earthquake sequence, *U.S. Geol. Surv. Data Release*, doi:10.5066/F7FJ2FNT.

McNamara, D. E., H. M. Benz, R. B. Herrmann, E. A. Bergman, P. Earle, A. Holland, R. Baldwin, and A. Gassner (2015), Earthquake hypocenters and focal mechanisms in central Oklahoma reveal a complex system of reactivated subsurface strike-slip faulting, *Geophys. Res. Lett.*, 42, 2742-2749, doi:10.1002/2014GL062730.

Mendoza, C., and S. H. Hartzell (1988), Aftershock patterns and main shock faulting, *Bull. Seismol. Soc. Am.*, 78(4), 1438-1449.

Mogi, K. (1967), Earthquakes and fractures, *Tectonophysics*, 5(1), 35-55, doi:10.1016/0040-1951(67)90043-1.

Morton, E. A. (2013), Dynamic earthquake triggering above the Socorro magma body and automated event detection in the 2009 Socorro, New Mexico earthquake swarm, MS thesis, Dep. of Earth and Env. Sci., New Mexico Inst. of Mining and Tech., Socorro, New Mexico.

Myers, S. C., G. Johannesson, and W. Hanley (2007), A Bayesian hierarchical method for multiple-event seismic location, *Geophys. J. Int.*, 171(3), 1049-1063, doi:10.1111/j.1365-246X.2007.03555.x.

Myers, S. C., G. Johannesson, and W. Hanley (2009), Incorporation of probabilistic seismic phase labels into a Bayesian multiple-event seismic locator, *Geophys. J. Int.*, 177(1), 193-204, doi:10.1111/j.1365-246X.2008.04070.x.

Oklahoma Geological Survey (1978), Oklahoma Seismic Network, *International Federation of Digital Seismograph Networks*, Other/Seismic Network, doi:10.7914/SN/OK.

Skoumal, R. J., M. R. Brudzinski, and B. S. Currie (2015), Microseismicity induced by deep wastewater injection in southern Trumbull County, Ohio, *Seismol. Res. Lett.*, 86(5), 1326-1334, doi:10.1785/0220150055.

Song, F., N. R. Warpinski, M. N. Toksöz, and H. S. Kuleli (2014), Full-waveform based microseismic event detection and signal enhancement: An application of the subspace approach, *Geophys. Prospect.*, 62(6), 1406-1431, doi:10.1111/1365-2478.12126.

Suhm, R. W. (1997), Simpson stratigraphy of the southern midcontinent, In K. S. Johnson (Ed.), *Simpson and Viola Groups in the Southern Midcontinent, 1994 Symposium*, Oklahoma Geological Survey Circular (Vol. 99, pp. 3-38), Norman, Oklahoma: Oklahoma Geological Survey.

Sumy, D. F., E. S. Cochran, K. M. Keranen, M. Wei, and G. A. Abers (2014), Observations of static Coulomb stress triggering of the November 2011 M5.7 Oklahoma earthquake sequence, *J. Geophys. Res. Solid Earth*, 119, 1904-1923, doi:10.1002/2013JB010612.

Sun, X., and S. Hartzell (2014), Finite-fault slip model of the 2011 Mw 5.6 Prague, Oklahoma earthquake from regional waveforms, *Geophys. Res. Lett.*, 41, 4207-4213, doi:10.1002/2014GL060410.

Utsu, T., Y. Ogata, and R. S. Matsu'ura (1995), A centenary of the Omori formula for a decay law of aftershock activity, *J. Phys. Earth*, 43(1), 1-33, doi:10.4294/jpe1952.43.1.

Way, H. S. K. (1983), Structural study of the Hunton Lime of the Wilzetta Field, T12N-13N, R5E, Lincoln County, Oklahoma, pertaining to the exploration for hydrocarbons, MS thesis, Boone Pickens School of Geol., Okla. St. Univ., Stillwater, Okla.

Wessel, P., W. H. F. Smith, R. Scharroo, J. Luis, and F. Wobbe (2013), Generic Mapping Tools: Improved version released, *Eos. Trans. AGU*, 94(45), 409-410, doi:10.1002/2013EO450001.

Woessner, J., D. Schorlemmer, S. Wiemer, and P. M. Mai (2006), Spatial correlation of aftershock locations and on-fault main shock properties, *J. Geophys. Res.*, 111, B08301, doi:10.1029/2005JB003961.

Yeck, W. L., G. P. Hayes, D. E. McNamara, J. L. Rubinstein, W. D. Barnhart, P. S. Earle, and H. M. Benz (2017), Oklahoma experiences largest earthquake during ongoing regional wastewater injection hazard mitigation efforts, *Geophys. Res. Lett.*, 44, 711-717, doi:10.1002/ 2016GL071685.

Zhao, Z., K. Qike, K. Matsumura, and J. Xu (1992), p-values of continental aftershock activity in China, *Acta Seismol. Sin.*, 5(4), 683-690, doi:10.1007/BF02651015.

CHAPTER 4

Deep, Long-Period Seismicity Beneath the Executive Committee Range, Marie Byrd Land, Antarctica, Studied Using Subspace Detection

4.1 Introduction

Deep, long-period earthquakes (DLPs) are a relatively poorly understood, yet fairly ubiquitous type of seismicity found beneath and near volcanic centers. DLPs are typically smaller magnitude events (**M** < 2) characterized by (1) deep hypocenters below the crustal seismogenic or brittle-ductile transition zone (10-50 km, depending on region), (2) long-period/low-frequency energy (<5 Hz), (3) monochromatic or harmonic waveforms, (4) long-duration, ringing coda waves, and (5) emergent signals. DLPs are a part of background seismicity at volcanoes and can occur relatively persistently over years [e.g., *Aso et al*, 2011; *Lough et al.*, 2013], but they have also been correlated with various forms volcanic unrest, including eruptions [e.g., *Power et al.*, 2002; 2004].

DLPs have been observed worldwide in Alaska [*Power et al.*, 2004], Cascadia [*Pitt et al.*, 2002; *Nichols et al.*, 2011; *Vidale et al.*, 2014; *Han et al.*, 2018], Hawaii [*Aki and Koyanagi*, 1981; *Okubo and Wolf*, 2008; *Matoza et al.*, 2014], Iceland [*Soosalu et al.*, 2010], Japan [*Ukawa and Ohtake*, 1987; *Hasegawa and Yamamoto*, 1994; *Nakamichi et al.*, 2003; *Aso et al.*, 2013], the Philippines [*White*, 1996], northern California [*Hill et al.*, 2002; *Pitt et al.*, 2002], and Russia [*Shapiro et al.*, 2017].

A source mechanism for DLPs has not been well established, but the most favored source mechanism is the movement of fluid or magma within a volcano's plumbing system via forceful injection of fluid into cracks [e.g., *White*, 1996; *Hill et al.*, 2002; *Soosalu et al.*, 2010], magma movement/ascent [e.g., *Pitt et al.*, 2002; *Power et al.*, 2004; *Nichols et al.*, 2011], or resonance of fluid-filled cracks [e.g., *Okubo and Wolfe*, 2008; *Han et al.*, 2018].

Lough et al. [2013] used the Antarctic Network component of the Polar Earth Observing Network (POLENET/ANET) to identify DLPs beneath the Executive Committee Range (ECR) in Marie Byrd Land (MBL), Antarctica (Figs. 4.1 and 4.2c). A total of 1370 events were detected and located beneath the ice at 25-40 km depth. These events have been interpreted as a present location of active intraplate magmatic activity. Antarctica is generally characterized by low levels of intraplate seismicity; however, several types of tectonic, volcanic, and ice-related seismicity have been observed on the continent suggesting that the lack of recorded events is substantially a function of lack of instrumentation rather than lack of sources.

MBL is a remote continental region buried beneath the West Antarctic Ice Sheet (Fig. 4.1). The breakup of Gondwanaland in the Mesozoic and Cenozoic eras formed the West Antarctic Rift System between what is now East and West Antarctica [*Boger*, 2011]. The formation of the rift system introduced tensional stress and high heat flow into MBL [*Winberry and Ananadakrishnan*, 2003] and volcanism became widespread in the Cenozoic [*Behrendt*, 2013]. The ECR shows north-to-south progression of volcanism during the Holocene [*Behrendt*, 2013] (Fig. 4.2c).

Two swarms of events starting in January 2010 and March 2011 occurred beneath subglacial topographic and magnetic highs located 55 km south of the youngest subaerial volcano in the ECR, Mount Sidley (Fig. 4.2c). Magnitudes varied between **M** 0.8 and **M** 3.03 with a median of **M** 1.44. *Lough et al.* [2013] interpreted the earthquakes as DLP swarms indicating a present location of active magmatic activity. It is not believed, however, that volcanic eruptions accompanied the two swarms as there was no detectable shallow volcanic seismicity.

In this study, I utilized subspace detection methodology to detect and locate DLPs in MBL in 2010 as well as detect an additional seven years of DLPs on a lone, long-running seismic station. The analysis indicates that DLP activity is sustained and ongoing in the region.

4.2 DATA

I obtained the catalog of 1370 DLP swarm earthquakes identified by *Lough et al.* [2013] through 2010 and 2011, here forth referred to as the Lough catalog, via written communication with the author. This catalog was constructed through manually inspecting and picking *P*- and *S*-phases. All events with six or more combined *P*- and *S*-phase arrivals were picked for the January-February 2010 and March 2011 swarms. For the rest of the data period, five-day subsets of data were picked every 20 days. All picked data were initially located and all events with eight or more combined *P*- and *S*-phase arrivals were then relatively relocated. Events with less than 8 km location uncertainty were included in the final subset of 203 DLP events presented by *Lough et al.* [2013]. I utilized the entire catalog of 1370 events in this analysis, rather than the subset of 203 well-located events, in hopes that it would bolster the detection of smaller magnitude events as a well as more varied waveforms that might reflect changes in locations or source properties. The Lough catalog was used in the construction of the subspace detectors.

I analyzed one year of continuous waveform data, from January through December 2010, on nine POLENET/ANET seismic stations (Table 4.1) [*Wiens et al.*, 2007]. Two perpendicular transects of instruments were installed in the 2009-2010 field season (austral summer) intersecting in the Executive Committee Range (ECR) (Fig. 4.2a,b). The utilized stations were located 39 to 222 km from the center of the later identified swarm. These data were analyzed for the purpose of detecting and locating additional events in the subglacial swarm.

Furthermore, I analyzed an additional seven years (2011 through 2017) of continuous waveform data on station SILY, the only station of the eight remaining after MLB transect instruments were removed during the 2011-2012 field season to be redeployed elsewhere. SILY, coincidentally and fortunately, happened to be one of the closest stations to the swarm, only 60 km from the center of activity. Its continued operation provides an excellent resource for documenting sustained and ongoing DLP activity in the region.

4.3 METHODOLOGY

I utilized subspace detection methodology [e.g., *Harris*, 2006; *Harris and Dodge*, 2011; see Chapter 1.1] to identify DLP events in the continuous waveform data. Subspace detection invokes a model that represents the signals to be detected as a linear combination of multi-channel orthogonal basis waveforms formed by the singular value decomposition of a set of known events. Subspace detectors are more computationally efficient than matched filter techniques using all events and excel at identifying smaller events, particularly in low signal-to-noise environments. I follow the methods of *McMahon et al.* [2017] for subspace detector construction/execution, event association, and magnitude computation.

Detectors were developed exclusively for the *S*-phase. The initial catalog contained primarily *S*-phase picks because the *S*-phase is easily identifiable and contains the largest amplitude signal (Fig. 4.3). The highly emergent *P*-phase is much more difficult to identify, particularly on more distal stations. The number of *S*-phase picks available in the initial catalog for each station can be found in Table 4.1.

All waveform data were bandpass filtered between 1.5 and 4.0 Hz using a 3-pole Butterworth filter. Event waveform lengths varied by station from 17.5-31.7 s (Table 4.1) and included both *P*- and *S*-phases. All 7395 event waveforms were aligned on the S-phase and included 7.5 s of *S*-phase coda. The number of basis waveforms (templates) needed to describe 90% of the waveform energy on each station ranged from 15 to 95 (Table 4.1). Constant correlation coefficient thresholds were set for each station based on visual inspection attempting to minimize the number of false positives while still capturing small magnitude and low signal-to-noise ratio (SNR) events. Relative magnitudes were determined for each detection using *Benz et al.* [2015b]. Station-specific detections were associated into events using an arrival time associator [*Benz et al.*, 2015a] and events were located by colleagues at the National Earthquake Information Center (NEIC). Final event magnitudes were calculated by averaging the relative detection magnitudes across the network. SNRs were computed by dividing the root mean square (RMS) of the template length of detected signal by the RMS of a 30 s window of noise prior to the detection.

The subspace detection methodology was chosen for its efficiency and detection efficacy. A total of 7395 events identified on the 9 stations of interest was reduced to 547 subspace detection templates representing a 93% reduction in the number of templates cross correlated against the continuous data and an equivalent reduction in processing time.

DATA PROCESSING WOES

I had worked previously with colleagues at the NEIC on subspace detection methodology for studies other than Antarctica and it performed beautifully. The Antarctic data, however, presented a new challenge that the subspace detector software had not encountered before. The noisy background and emergent onset of these events reduced the accuracy of phase onset times. Improving this situation for highly emergent and band limited signals such as these data will require further methodological development at the USGS and within the broader community. For this reason, I here present only locations for a pilot group of events from 2010. Currently, times of the SILY detections over the full eight years are not sufficiently precise for location; however, the detections do represent real events and their occurrence and other statistics derived from this catalog are robust results of this study.

4.4 RESULTS

DETECTION AND LOCATION OF DLPS IN 2010

Subspace detection processing resulted in a total of 56,451 detections in 2010 across the nine studied seismic stations (Table 4.1; Fig. 4.4). Stations ST08, ST12, SILY, and ST13 exhibited the highest numbers of detections due to their close proximity to the cluster center (Fig. 4.2b). All stations exhibit a relatively high number of detections in January and February corroborating the Lough catalog identification of an intense swarm of DLP activity and low levels of sustained activity throughout the rest of the year. ST08 was not operational the last four months of 2010.

From 56,000+ detections, 1158 events were identified that had detections on at least 4 of the 9 stations and had location uncertainties less than 8 km (Figs. 4.5 and 4.6). These 1158 events show good temporal correlation with the Lough catalog (Fig. 4.5) exhibiting intense swarm activity in January and February with sporadic activity throughout the rest of the year. My processing did fail to identify some events contained in the Lough catalog (e.g., Jan 31-Feb1). I hypothesize that these missing events may be due to the restrictive analysis (4+ station association, < 8 km location uncertainty), and that relaxing these constraints may better capture them, but locations would be poorly constrained. The processing did, however, identify some additional low-level swarms that were missed in the Lough catalog (e.g., late July and late August). I note that up to 10 times more events are detected than could be accurately located, particularly on proximal stations. The majority of these events are likely too small to be detected on the requisite four stations for location purposes.

The subspace detected events are located in a geographically finite region where the Lough catalog also identified the swarm (Fig. 4.6). The new locations are more diffuse and lack the structure, particularly N-S and E-W elongations, present in the Lough catalog. The subspace detected events are also located at shallower depths. The original event locations clustered between 25 and 40 km depth whereas the subspace detected events appear to cluster between 15 and 30 km depth. The subspace detected event locations could be improved by utilizing a more appropriate velocity model. Locations were determined utilizing the *Kennett et al.* [1995] ak135

1-D reference earth velocity model, but a more specialized velocity model, such as that presented by *Lough et al.* [2013] which contains more shallow layers and higher velocities, would provide more precise hypocentral locations of these events defining greater structure at greater depths. The subspace detected events are located using only the *S*-phase arrivals, as this methodology has worked well in previous studies, but I not that adding *P*-phase arrivals would also help improve locations.

The frequency-magnitude distribution (FMD) of the subspace detected events exhibits a very high *b*-value (2.41) compared to the global mean value near 1.0 indicating a higher number of small magnitude events compared to large magnitude events (Fig. 4.7). This *b*-value is slightly lower but on par with the value calculated for the Lough catalog (2.75) and is broadly consistent with high *b*-values commonly observed in volcanic earthquake swarms [e.g., *McNutt*, 1996].

Improvements can be made in the further processing of the data (i.e., precise phase arrival picks, utilizing both *P*- and *S*-phases, utilizing a more appropriate velocity model), however, it is encouraging that the subspace detectors are capturing the sequence and facilitating the creation of an expanded catalog, even with such a sparse network and emergent waveforms. This shows that subspace detection can automate the detections of DLP events in Marie Byrd Land, greatly reducing analyst time, and provide an excellent tool for further study.

DETECTION OF DLPS ON SILY, 2010-2017

I detected a total of 120,937 events on the long-running station SILY from 17 January 2010 through 8 January 2018 (Fig. 4.8). These detections show sustained levels of DLP activity throughout the full eight-year time period with recent years 2015-2017 containing ~67% of the entire detected catalog. Intense swarms in January-February 2015 and January-March 2017 contain ~12% each of the entire detected catalog. While the POLENET/ANET network was most densely deployed in the region due to the MBL transect in 2010 and 2011, these years are perhaps two of the most inactive years observed.

I investigated a possible seasonality associated with the temporal distribution of DLP events. The austral summer months (January, February, March) appear to contain the most events when considering the entire catalog (Fig. 4.9) and the austral fall months (April, May, June) contain the fewest events. I considered the possibility that low-correlation events may be false positives that are more likely to be detected in the noisier summer months when sea ice is reduced and oceanic noise increases [*Aster et al.*, 2008]; however, the seasonality bias remains intact if the correlation coefficient threshold is raised. The seasonality is greatly reduced if the SNR of events is raised above five (Fig. A3.1), but this restriction eliminates ~80% of the catalog and negates the subspace detectors' enhanced capability of detecting events in low signal-to-noise environments. No evidence of diurnal variations is observed across the catalog as a whole or as a function of season or month (Figs. A3.2 and A3.3). A few years (2012, 2013, 2016) contain scant activity in summer months and 2016 contains relatively high levels of activity in the fall months. These observations indicate that the apparent seasonality is perhaps not a function of seasonal noise levels, but is, rather, coincidentally related to a few large swarms in the summer months of 2010, 2015, and 2017 that populated the catalog and produced a coincidental seasonality.

This detected catalog is dominated by small magnitude, low SNR events (Fig. 4.10). Approximately 80% of events are smaller than or equal to **M** 1.5 and have SNRs below 5. These magnitudes are broadly consistent with global observations of DLP events tending toward low magnitudes [e.g., *Aso and Tsai*, 2014]. The FMD of the extended SILY catalog is described by a *b*-value of 1.6 and a minimum magnitude of completeness (M_C) of 0.6 (Fig. 4.10a). This *b*-value is far below the value calculated for the located events in 2010 (2.41), but still high compared to global mean value near 1.0 determined for tectonic earthquakes [e.g., *Frohlich and Davis*, 1993] and still broadly consistent with higher *b*-values found in volcanic regions [e.g., McNutt, 1996]. The extended catalog FMD also exhibits a falloff of larger magnitude events (**M** > 1.7) in what I refer to as a maximum magnitude of completeness. Subspace detectors can be insensitive to larger events because the extended source duration reduces correlation sufficiently to make them difficult to detect using templates that are derived from smaller earthquakes [*McMahon et al.*, 2017].

I examined the catalog for evidence of triggering or modulation of event counts due to dynamic effects caused by seismic waves from large teleseismic earthquakes. Figure 4.11 shows event counts as a function of time with indicators for all earthquakes larger than or equal to moment magnitude ($\mathbf{M}_W$) 7.5 (Table A3.1). Table 4.2 and Figure 4.12 show the ratio of number of events occurring before and after the passing of these teleseismic waves in time windows of 1 hour (1 hour before and 1 hour after), 3 hours, 6 hours, 12 hours, 24 hours, 48 hours, and 72 hours, and 1 week. At first glance, the scatter indicates no distinct trends of numbers of DLP events increasing or decreasing after teleseismic earthquakes. There is an approximately equal number of data points above and below the 1:1 after:before ratio line in Figure 4.12 (111 above, 121 below; Table 4.2). However, there are twice as many data points above the 5:1 ratio line (33 points) as below the 1:5 ratio line (18 points). These large increases and decreases are most apparent after 24 hours. The data points above the 5:1 ratio line are dominated by smaller magnitude events (**M** ≤ ~8.0). I note a preference towards decreased numbers of events after larger magnitude teleseismic earthquakes (**M** ≥ ~8.2; red data points in Figure 4.12). This behavior has been observed before at Mauna Loa Volcano where *Okubo and Wolfe* [2008] showed that the rate of DLP events slowed significantly coincident with the occurrence of the 26 December 204 $\mathbf{M}_\mathbf{W}$ 9.3 Sumatra earthquake.

To investigate the possibility of triggering further, I generated randomized catalogs of detected event times. Inter-detection times were randomly generated from an exponential distribution with mean parameter ($1/\lambda$) where λ is the average number of detections that occur in a given year such that there is a Poissonian distribution of event times throughout the time frame. Each year of the 8 year time frame was assigned a λ equivalent to the true number of detections in that year. One hundred randomized detection time catalogs were generated. For each catalog, randomized detections were counted before and after the true teleseismic event times for the same windows used in the actual data and Figure 4.12. Results for all windows and all realizations are presented in Figure 4.13. These data points fall within a finite and well-defined region centered nearly symmetrically about the 1:1 ratio line with few points beyond the 5:1 and 1:5 lines in the entire dataset, and few points beyond the 2:1 and 1:2 lines when before or after event counts exceed 50. Many points in the actual data set in Figure 4.12 fall well outside the area defined by event ratios of the Poissonian distributed detected times in Figure 4.13. These extreme ratios may seem to suggest that events in the swarm are triggered or modulated by passing teleseismic waves.

However, the non-Poissonian distribution of events and swarmy nature (alternating times of high numbers of detections and low numbers of detections) was suspected as the source of extreme event count ratios, and I generated randomized catalogs of teleseismic event times. Inter-teleseism times were randomly generated in the same manner as the inter-detection times with λ equal to 5 for each year (45 teleseisms over an eight-year time periods is approximately 5 teleseisms per year). One hundred randomized teleseism time catalogs were generated. For each catalog, actual detections were counted before and after the randomized teleseism event times the same windows used previously. Results for all windows and all realizations are presented in Figure 4.14. These data points, while still centered nearly symmetrically about the 1:1 line as found in the randomized detection times, fall in a much broader and more poorly defined area, fully encompassing the area of the data points found in the actual data (Fig. 4.12). Extreme event count ratios in the actual data are reproduced when teleseism event times are randomized indicating that these variations are likely attributable to the swarmy, non-Poissonian nature of the sequence. A teleseism can come before a swarm which would result in an after:before ratio >> 1, in the middle of swarm which would result in an after:before ration of ~1, or after a swarm which would result in a after:before << 1. I find no strong evidence for triggering or other modulation in the current data set.

4.5 Conclusions

Two swarms of DLP activity in 2010 and 2011 were first identified beneath the ECR in MBL by *Lough et al.* [2013] and were interpreted as present location of active magmatic activity in the region. I utilized the Lough catalog and subspace detection methodology on the *S*-phase using nine stations in the POLENET/ANET network in an attempt to enhance detection and assessment of the seismicity cluster. While the total number of events in the catalog was not significantly increased, I did identify several low-level swarms in 2010 that were not identified in the *Lough et al.* [2013] study. The locations of these events, however, can be improved by improving phase picks, utilizing *P*- and *S*-phases, and utilizing a more appropriate velocity model.

Additionally, I analyzed eight years of continuous data from the long-running station SILY, located 60 km from the observed center of DLP activity. I detected a total of 120,937 events in this time period, with 2015-2017 being the most active years on record. The vast majority of these detections are low-magnitude, low SNR events that exhibit a high *b*-value. This high *b*-value, also present in the Lough catalog, is consistent with the statistics of other observed volcanic swarms. The catalog was examined for evidence of dynamic triggering or other modulation of event counts by passing waves from large teleseismic signals ($\mathbf{M_W} \geq 7.5$); however, no strong evidence for triggering or modulation was discovered.

My analysis corroborates the conclusions of the *Lough et al.* [2013] study regarding sustained deep, long-period earthquakes occurring beneath the Executive Committee Range in Marie Byrd Land, Antarctica. Indeed, DLP activity in recent years exceeds that studied by *Lough et al*. This region exemplifies the monitoring and analysis that is possible, even in remote-settings such as Antarctica, for the study of DLP earthquakes in volcanic regions worldwide.

4.6 ACKNOWLEDGEMENTS

The initial catalog of 1370 DLP events was obtained through written communication with A. Lough. I thank E. Myers for initiating this work as an IRIS intern at Colorado State University in 2014. I thank R. Aster and A. Lough for data support and guidance, P. Shore for expedited data access, and H. Benz and W. Yeck at the NEIC for software support as well as event association and locations.

4.7 TABLES FOR CHAPTER 4

Table 4.1: Seismic station and subspace detector information. Number of *S*-phase picks indicates the number of picks contained in the Lough catalog that were utilized in subspace detector template construction. Template length indicates the length of template waveforms and subspace rank indicates the number of basis waveforms used in the subspace detector on each station.

Station	Distance from Cluster Center (km)	Instrument	Dates (yyyy/mm/dd)		Number of *S*-phase picks	Template Length (s)	Subspace Rank	Correlation Coefficient Threshold
			Begin Processing	End Processing				
SILY	60	Nanometrics Trillium	2010/01/17	2018/01/10	1336	18.6	15	0.50
ST06	213	Nanometrics Trillium	2010/01/17	2010/12/31	98	31.0	51	0.31
ST07	125	Nanometrics Trillium	2010/01/17	2010/12/31	1244	23.5	74	0.50
ST08	39	Nanometrics Trillium	2010/01/17	2010/12/31	1315	17.5	16	0.41
ST09	136	Nanometrics Trillium	2010/01/17	2010/12/31	517	22.2	95	0.66
ST10	222	Nanometrics Trillium	2010/01/21	2010/12/31	121	31.7	33	0.31
ST12	107	Guralp CMG3T	2010/01/17	2010/12/31	1233	21.5	89	0.49
ST13	98	Nanometrics Trillium	2010/01/18	2010/12/31	1238	18.0	86	0.51
ST14	182	Nanometrics Trillium	2010/01/18	2010/12/31	293	25.9	88	0.51

Table 4.2: Triggering/Modulation data point counts. The after:before ratio indicates the ratio of events occurring after and before a passing teleseism and the geographic sections of Figure 4.12. Number of data points indicates the number of data points contained in each of the geographic sections of Figure 4.12.

After:Before Ratio	Number of Data points
>5:1	33
2:1 – 5:1	26
1:1 – 2:1	52
>1:1	111
1:1	128
<1:1	121
1:2 – 1:1	65
1:5 – 1:2	38
<1:5	18

4.8 Figures for Chapter 4

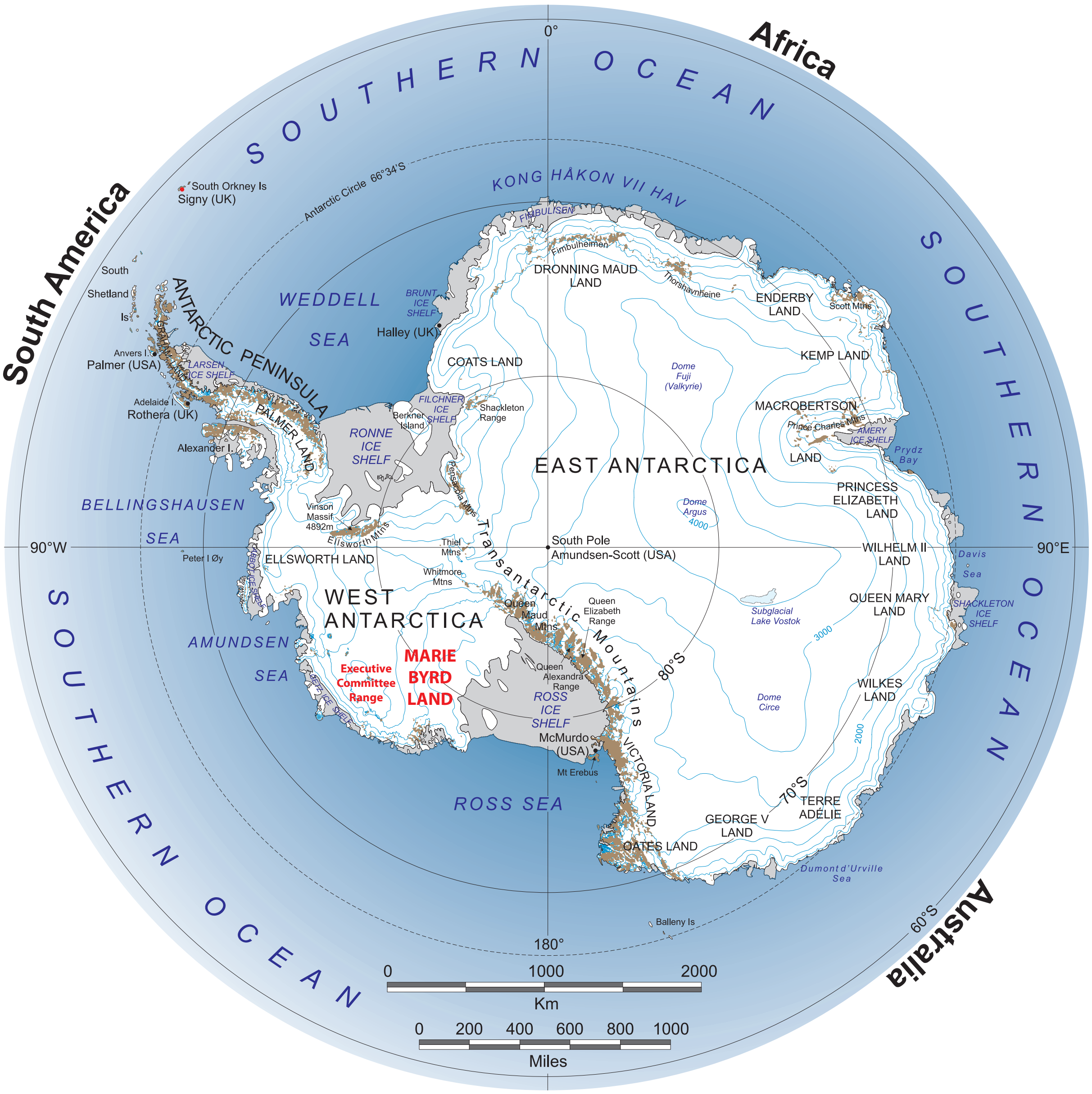

Figure 4.1. Location map of Antarctic features with Marie Byrd Land (MBL) and the Executive Committee Range (ECR) in red text. Adapted from *https://lima.usgs.gov*.

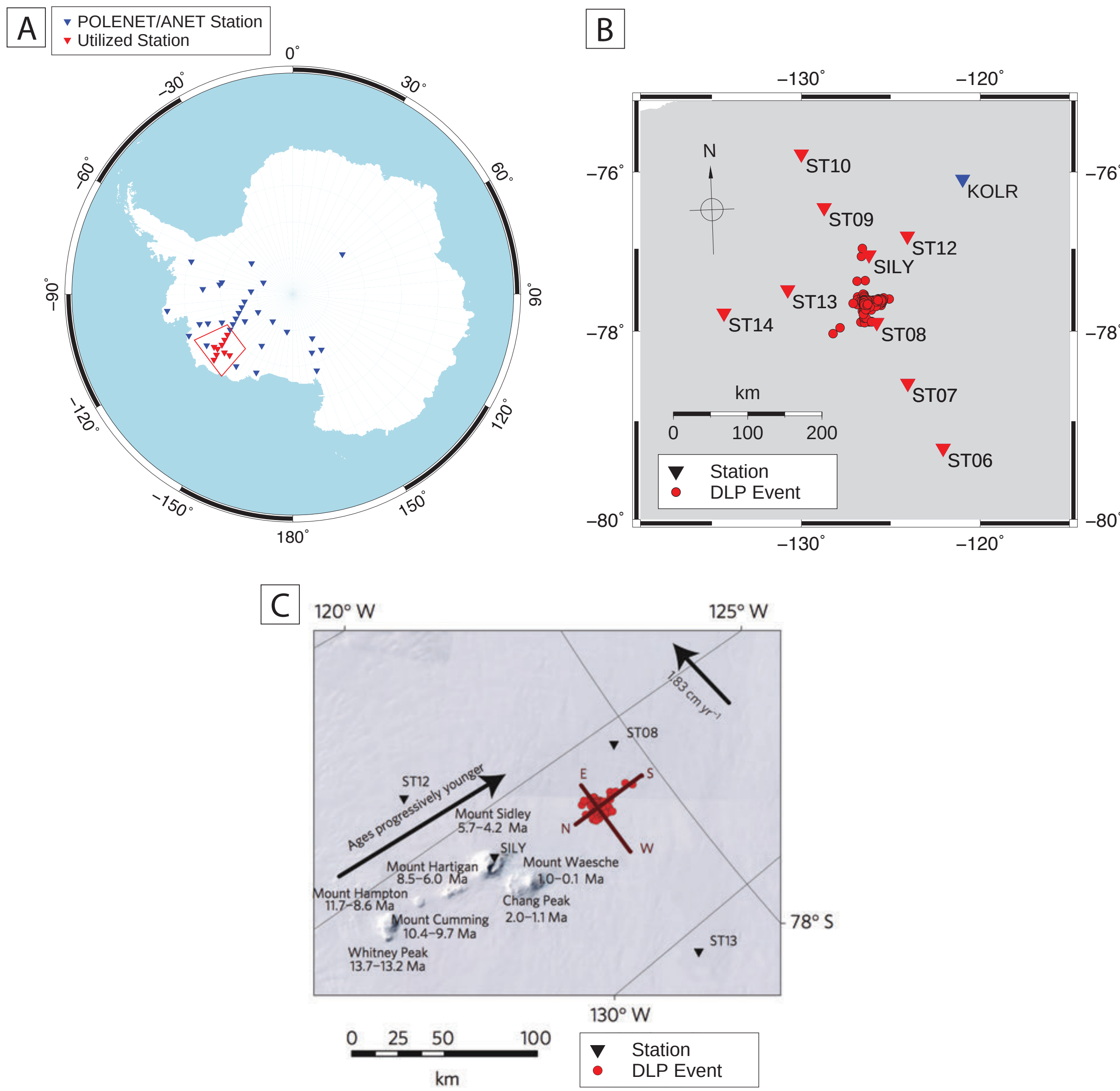

Figure 4.2. (A) Location map of 2010-2011 POLENET/ANET stations. Red stations are the nine stations utilized in this study. (B) Location map of utilized seismic stations and DLP events from the Lough catalog. DLP events are located near the intersection of two transects over the ECR. (C) ECR volcanoes labeled with dates of known volcanism. DLP swarms occur ~55 km south of Mount Sidley along the age-progression line. Arrow shows HS3-NUVELLA1A plate motions. Adapted from *Lough et al.* [2013].

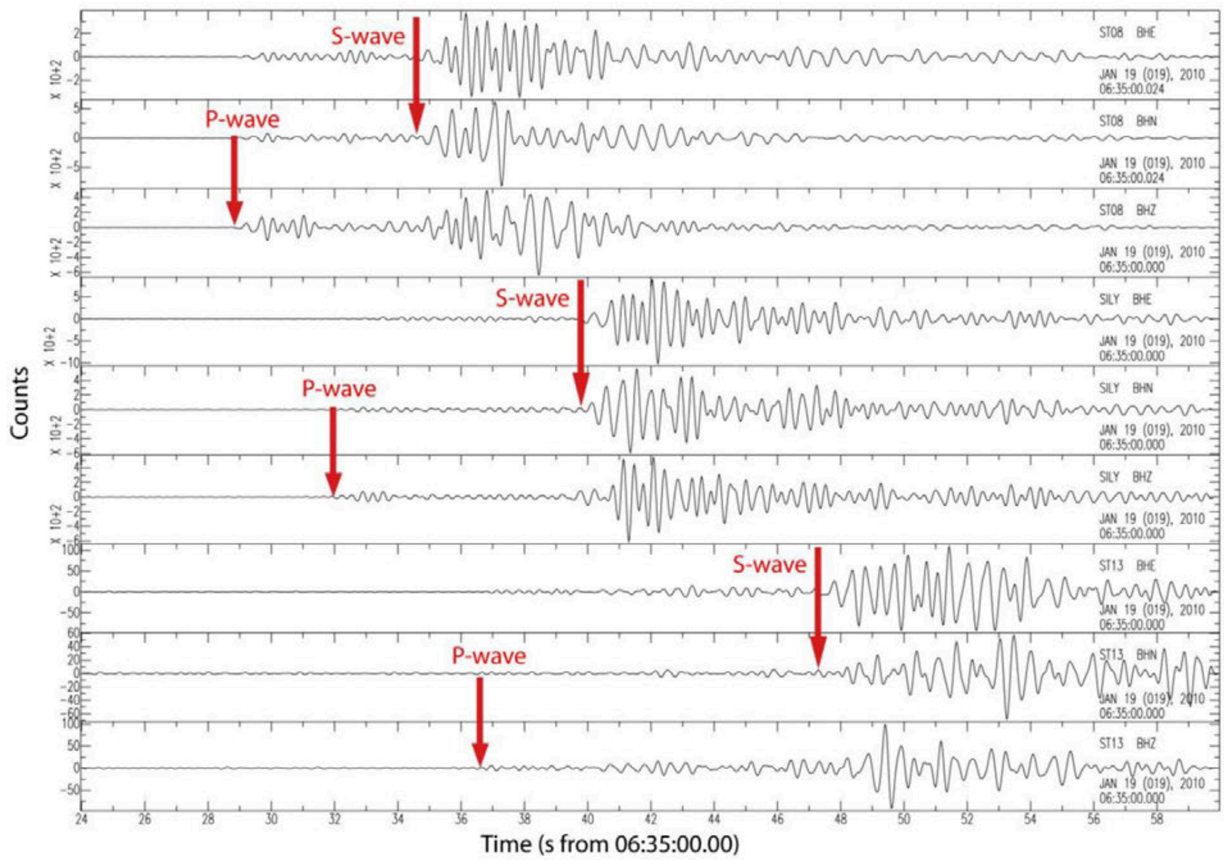

Figure 4.3. Three component seismogram of an example DLP event. Waveforms are bandpass filtered between 1.5 and 4.0 Hz. *P*- and *S*-phase arrivals are marked. Adapted from *Lough et al.* [2013]. Subspace detectors were developed exclusively for the *S*-phase because it is easily identifiable and contains the largest amplitude signal. The *P*-phase is much more difficult to identify on these emergent and distant events, particularly on more distal stations.

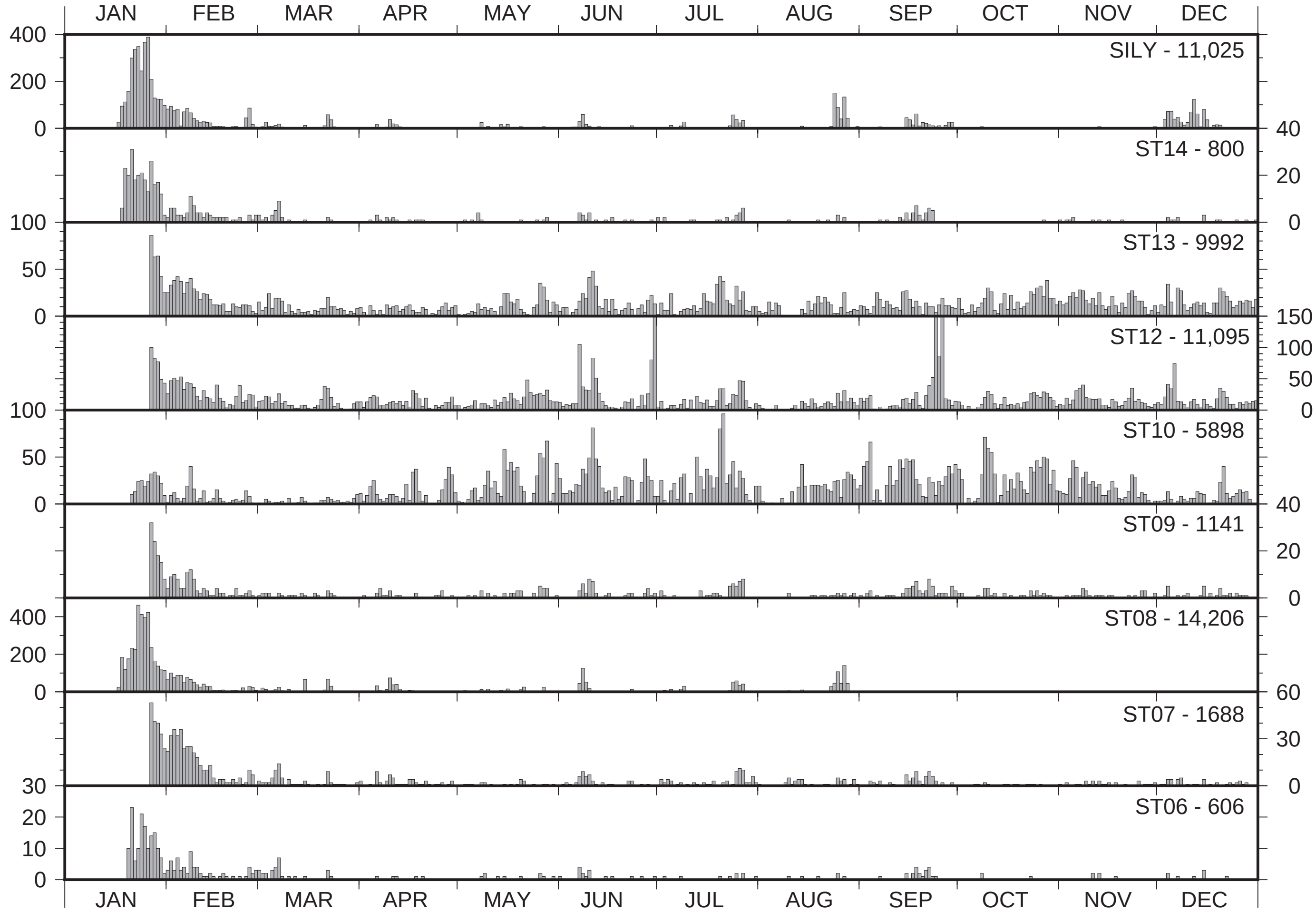

Figure 4.4. Subspace detector summary for each of the 9 seismic stations displayed as number events detected per day of 2010. Station name and total number of detections for that station are displayed in the upper right corner of each panel. A total of 56,451 detections were recorded across all nine stations. All stations exhibit a relatively high number of detections in January and February corroborating the Lough catalog identification of an intense swarm of DLP activity and low levels of sustained activity throughout the rest of the year. ST08 was not operational the last four months of 2010

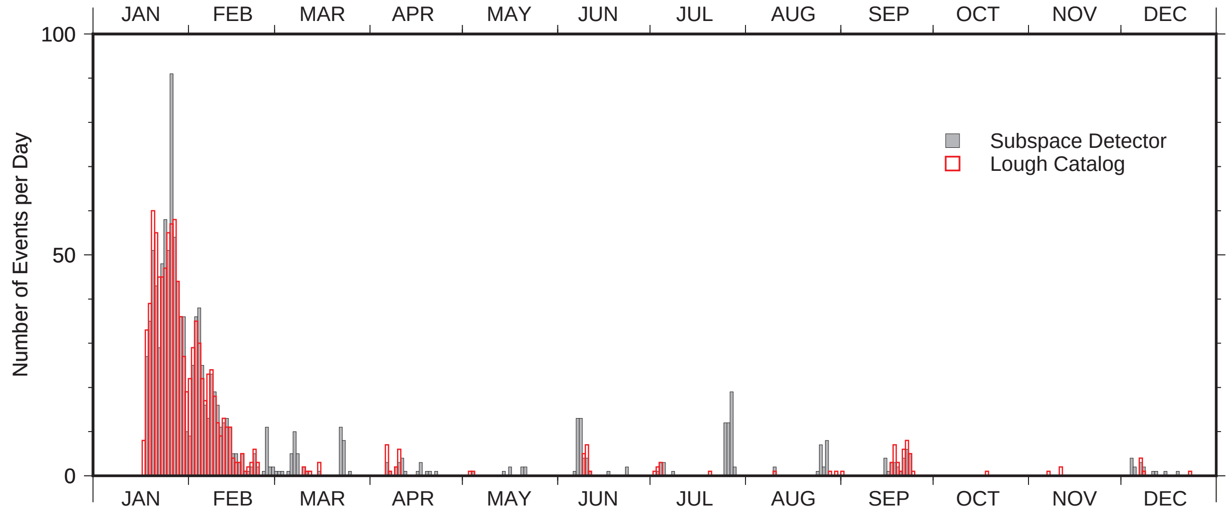

Figure 4.5. Number of events per day for the original Lough catalog (red outline) containing 1027 events and the subspace detector catalog (gray bars) containing 1158 events. The subspace detector events were detected on at least four stations and had location uncertainties less than 8 km. The two catalog show good temporal correlation exhibiting intense swarm activity in January and February with sporadic activity throughout the rest of the year. Processing did fail to identify some events contained in the Lough catalog (e.g., January 31 - February 1, but also succeeded in identifying a few additional low-level swarms that were not previously identified (e.g., late July).

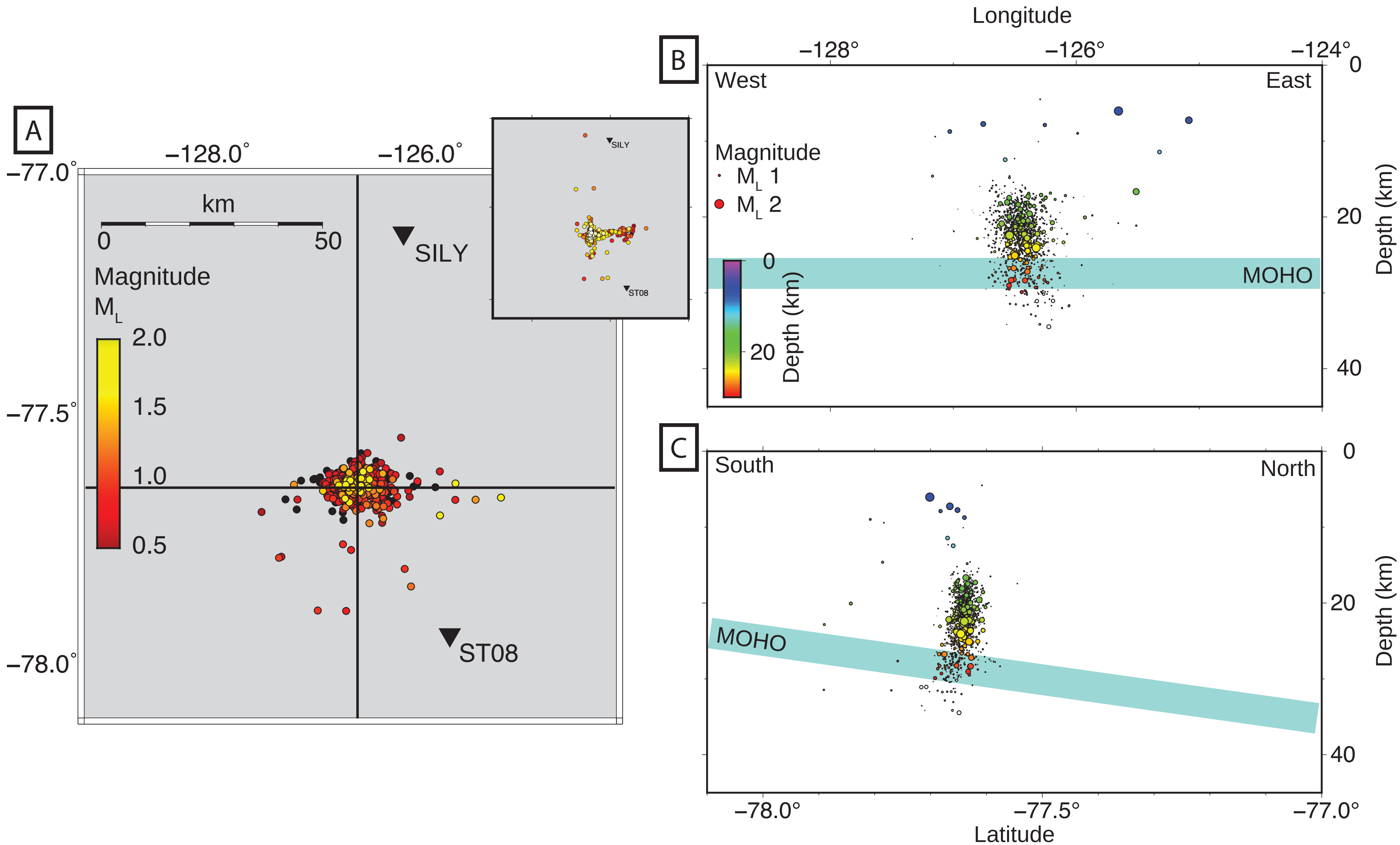

Figure 4.6. Locations of subspace detected events. (A) Map view showing the cluster of events locating approximately where the Lough catalog was originally located (inset). Black lines indicate the locations of the cross-sections present in B and C. (B) Longitudinal cross-section with the approximate location of the Moho indicated by the blue box. (C) Latitudinal cross-section with the approximate location of the Moho indicated by the blue box.

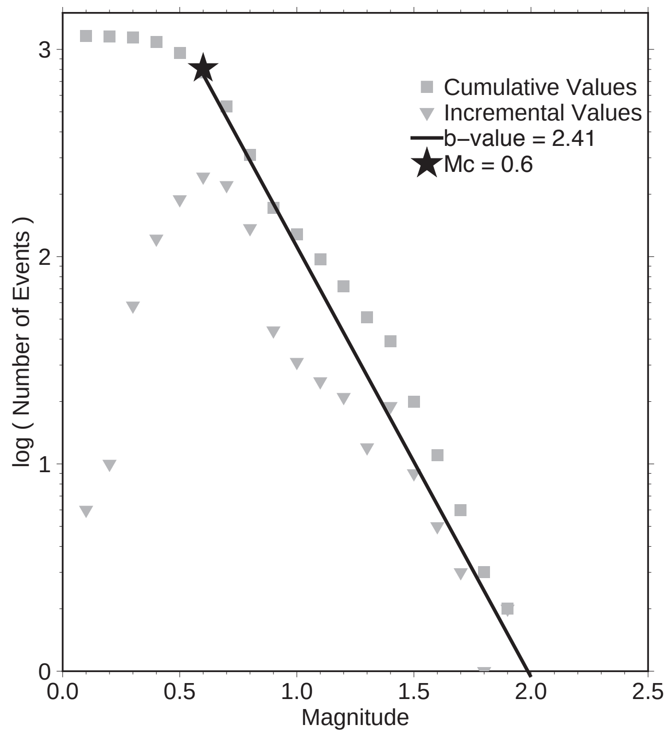

Figure 4.7. Frequency-magnitude distribution (FMD) of the 2010 subspace detected catalog. The *b*-value of 2.41 is very high for an earthquake catalog, and is broadly consistent with high *b*-values found for seismicity at other volcanic settings.

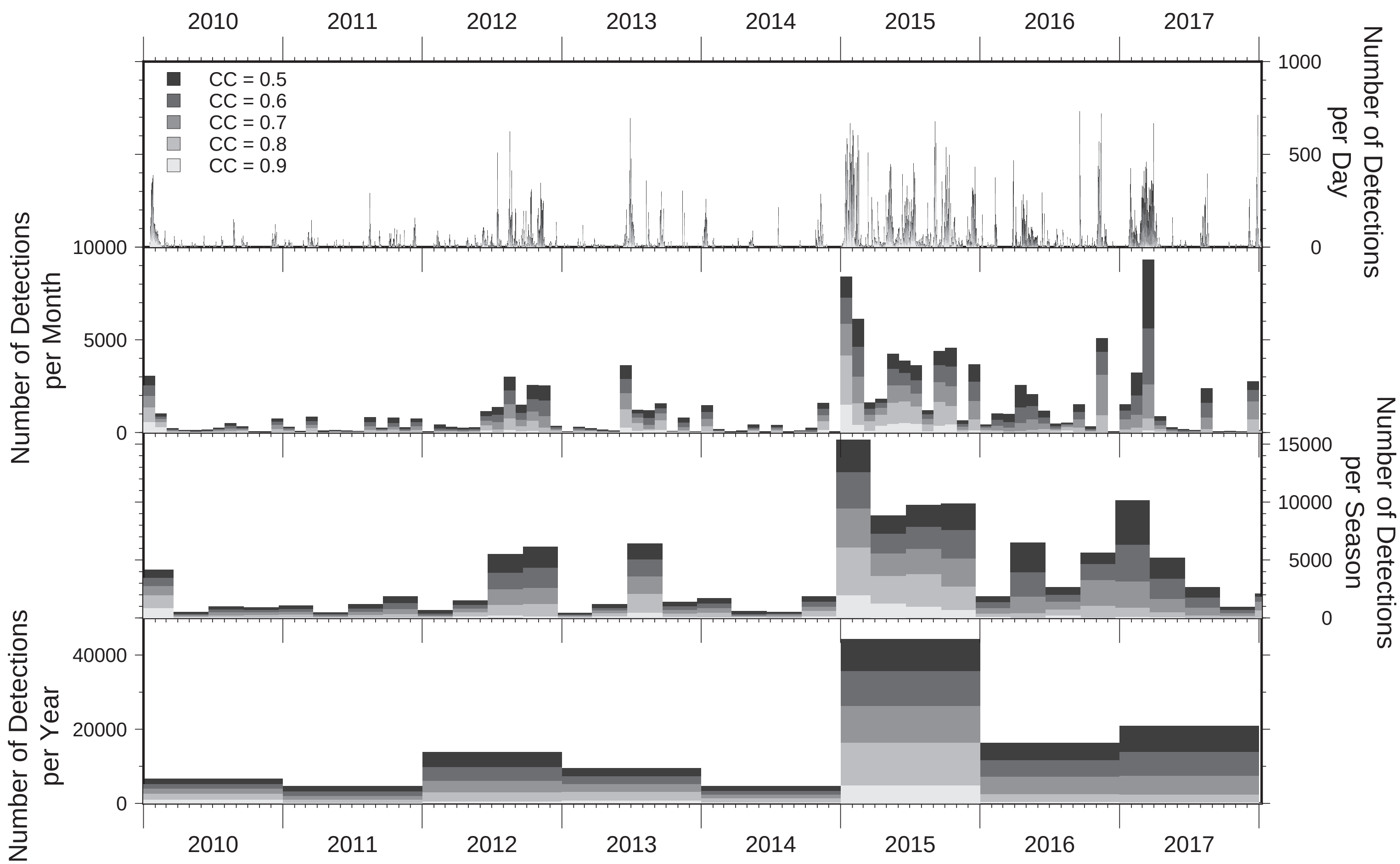

Figure 4.8. Summary of the extended catalog of events detected on SILY for 2010 through 2017, displayed as number of detections per day (top), month (second from top), season (second from bottom), and year (bottom). The detections are colored by cross-correlation coefficients (CC). There are 120,937 total detections on SILY from 17 January 2010 through 8 January 2018. This figure shows sustained levels of DLP activity throughout the eight-year time period with recent years 2015-2017 containing ~67% of the entire detected catalo

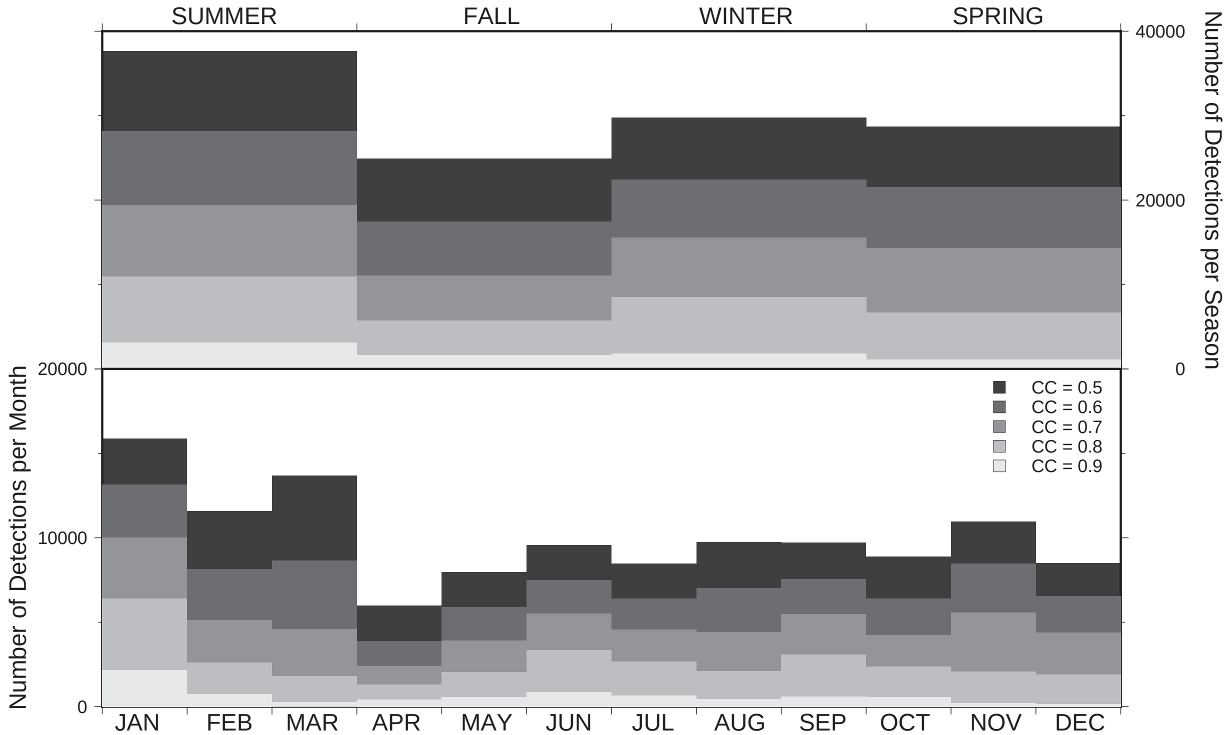

Figure 4.9. Summary of the extended catalog of events detected on SILY as a function of season (top) and month (bottom) across the entire catalog. The austral summer months (January, February, March) appear to contain the most events and the austral fall months (April, May, June) contain the fewest events. I conclude, however, that this observation of seasonality is not a function of sea noise levels, but is coincidentally caused by a few large swarms that occurred during the summer months of 2010, 2015, and 2017 (Fig. 4.8).

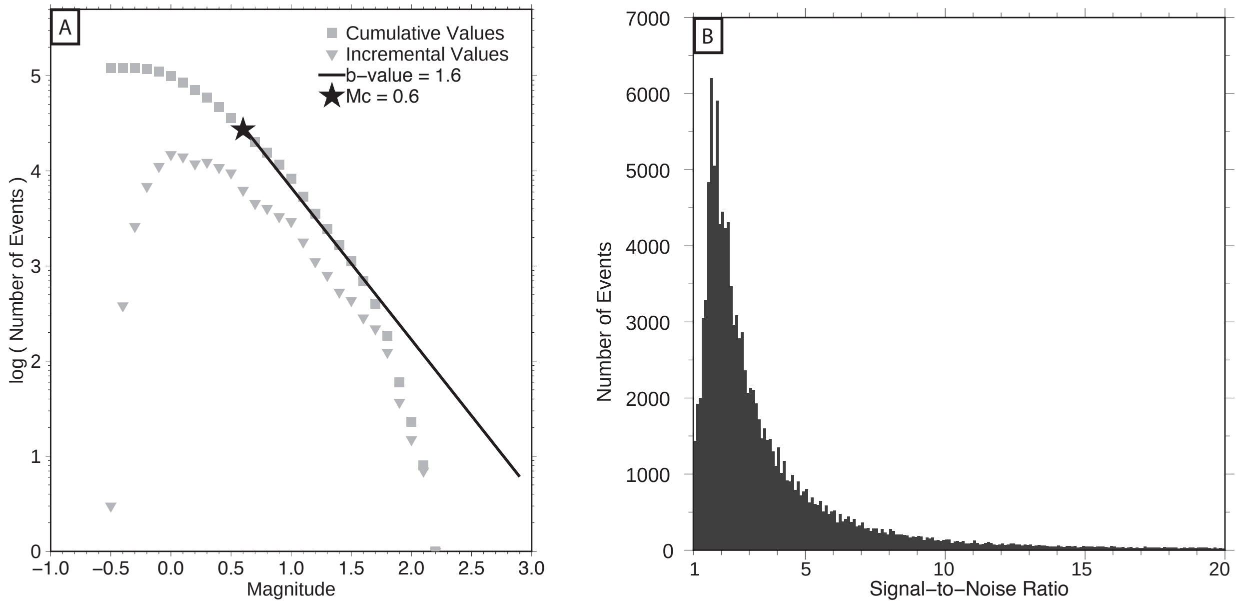

Figure 4.10. (A) FMD of the extended catalog of events detected on SILY, 2010-2017. There is a falloff of events above **M** 1.7 referred to as the maximum magnitude of completeness. This may be due to subspace detectors being insensitive to larger events when templates are constructed primarily of small events. (B) Histogram of signal-to-noise ratios (SNR) for the catalog. Approximately 80% of these events have SNRs below 5.

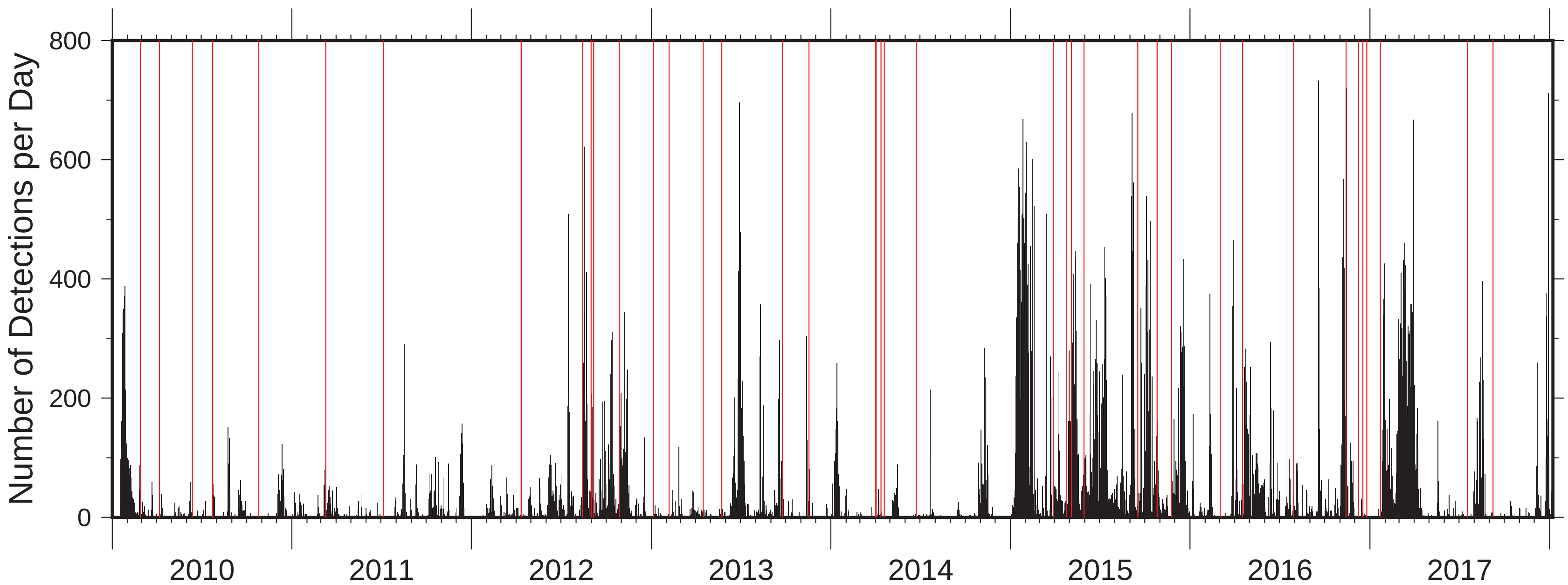

Figure 4.11. Number of detections per day on SILY (black columns) and times of all teleseismic events larger than or equal to $\mathbf{M_W}$ 7.5 (red lines).

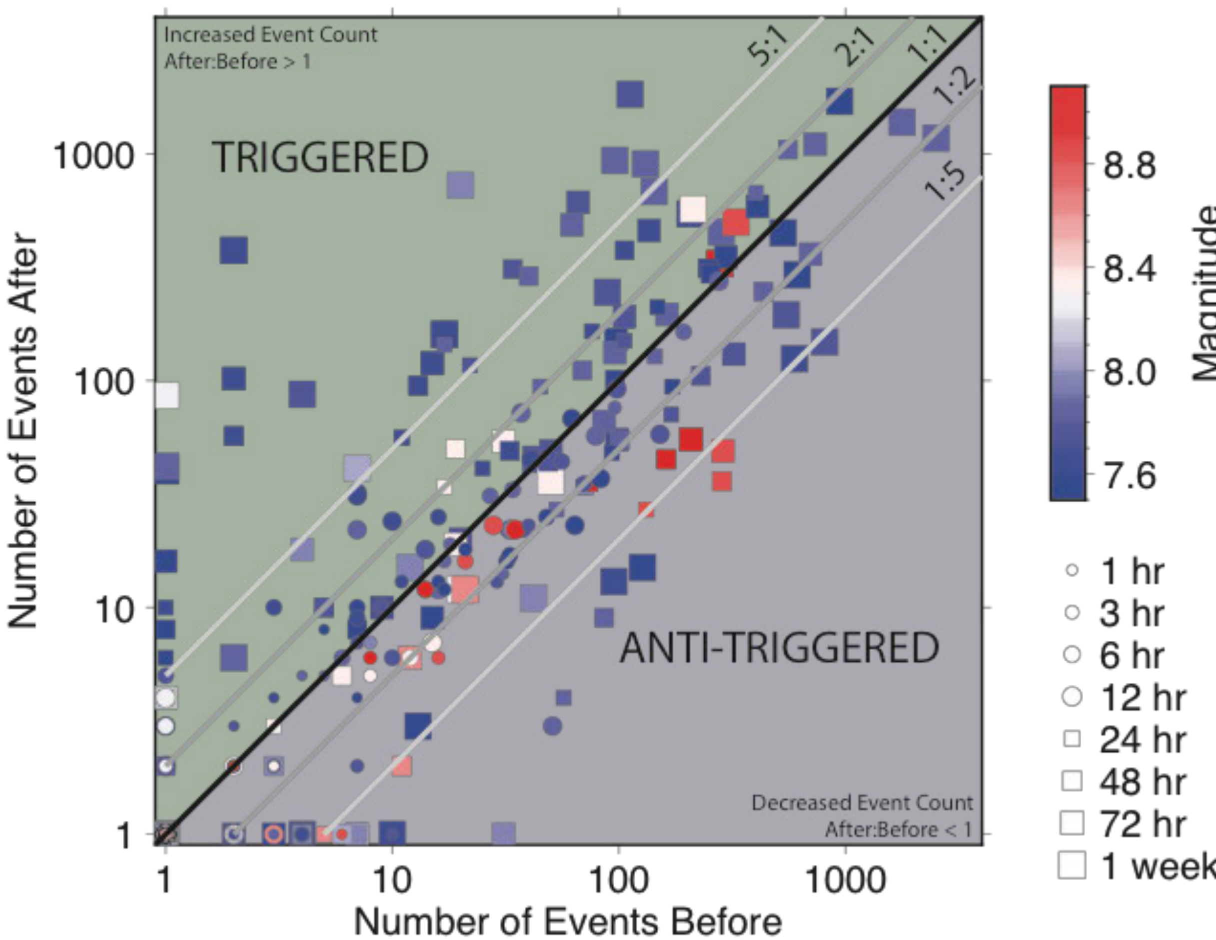

Figure 4.12. Scatter plot of ratio of SILY events detected after (y-axis) and before (x-axis) all teleseismic earthquakes $\mathbf{M_W} \geq 7.5$ during the studied time period. Note the axes are logarithmic. The shape of the symbols indicates the amount of time examined before and after the teleseismic earthquakes. The color of the symbols indicates the magnitude of the teleseismic earthquake. The green shaded area indicates an increase in number of events detected after the teleseismic earthquake and the purple shaded region indicates a decrease in number of events detected after the teleseismic earthquake. The solid black line indicates the 1:1 (After:Before) ratio. The dark gray lines indicate the 2:1 and 1:2 ratios. The light gray lines indicate the 5:1 and 1:5 ratios. There is an approximately equal number of data points above and below the 1:1 ratio line. There are twice as many data points above the 5:1 ratio line as below the 1:5 ratio line. The data points above the 5:1 ratio line are dominated by smaller magnitude events ($\mathbf{M} \leq \sim 8.0$). Larger magnitude events ($\mathbf{M} \geq \sim 8.2$; red data points) tend to show a decrease in events after teleseismic earthquakes.

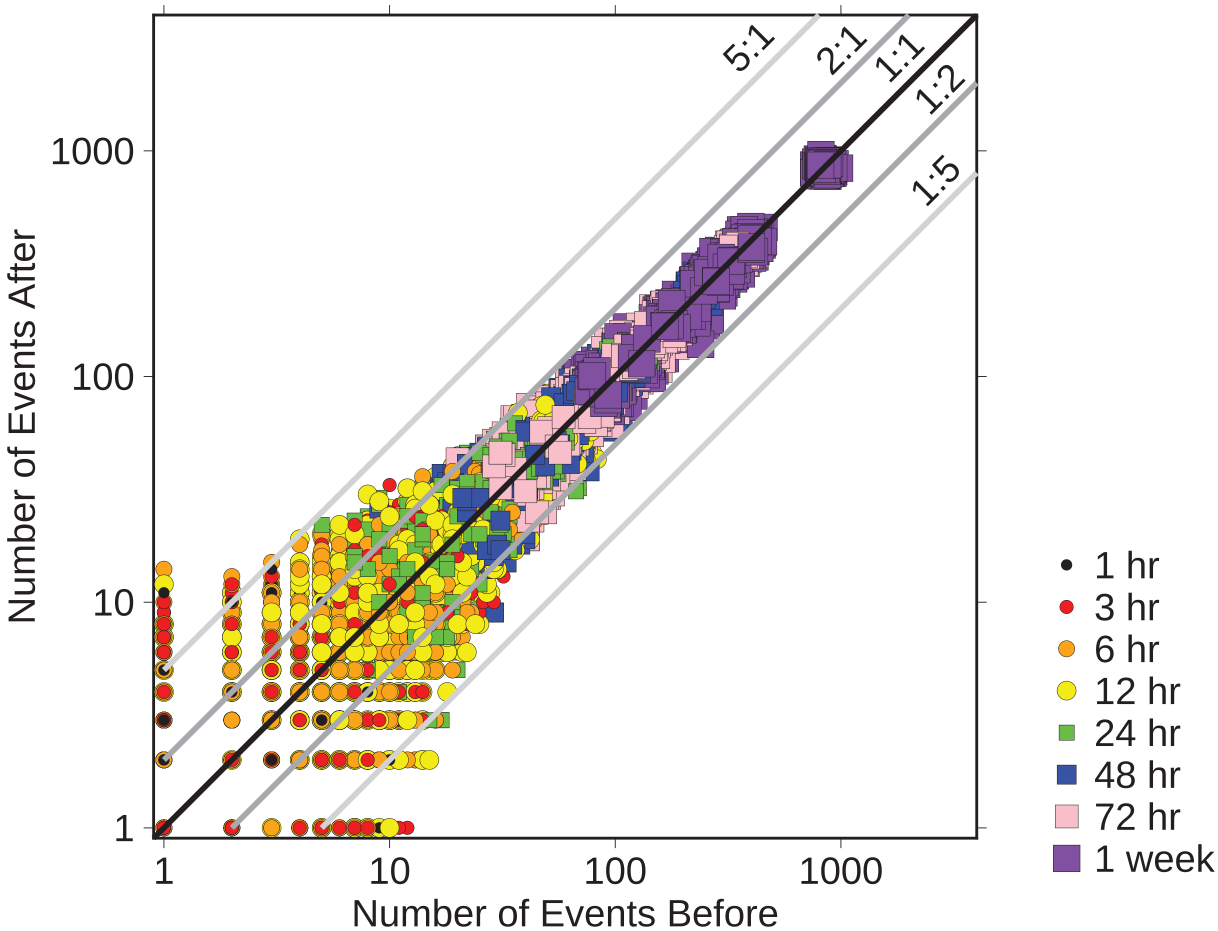

Figure 4.13. Scatter plot of event count ratios for 100 realizations of randomized Poissonian distributed detected events times. Figure format follows Figure 4.12. Data points fall within a finite and well defined area centered nearly symmetrically about the 1:1 ratio line.

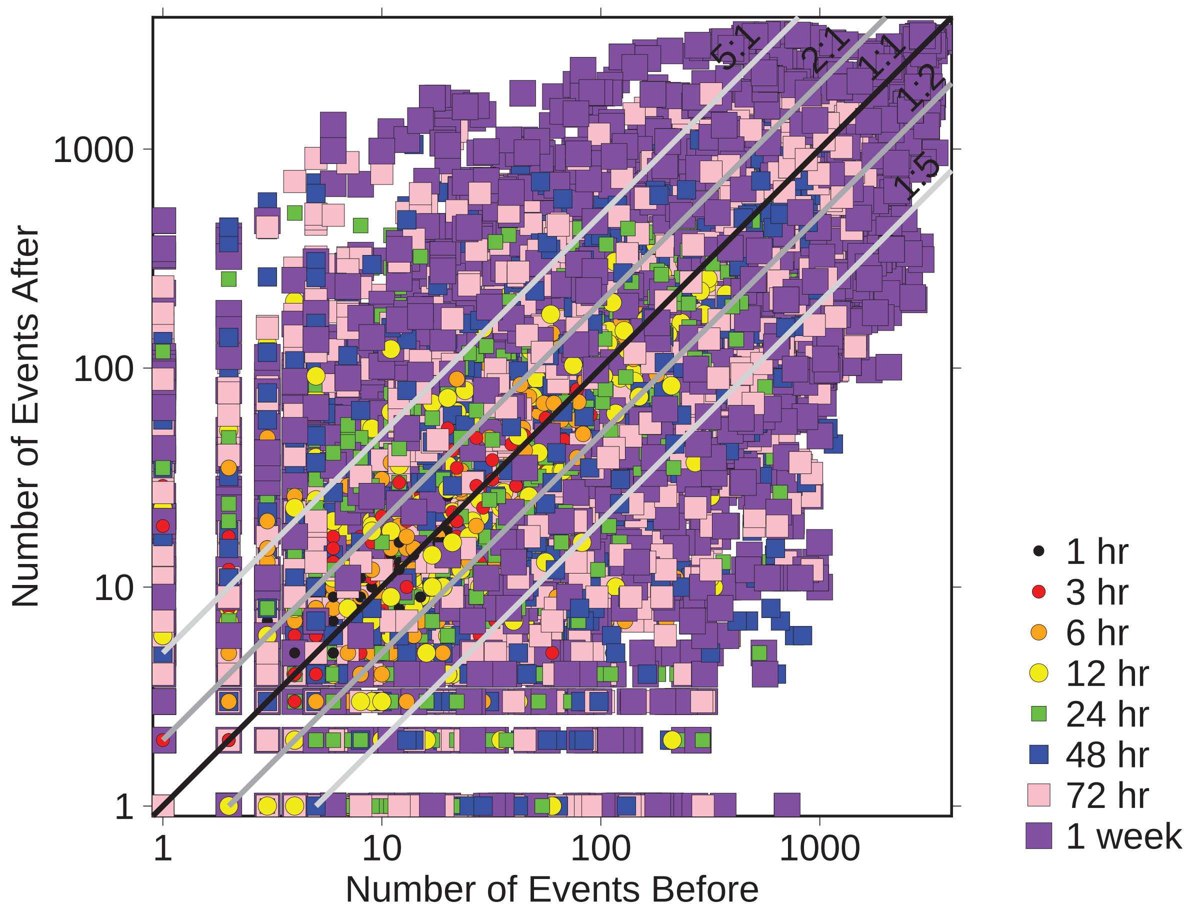

Figure 4.14. Scatter plot of event count ratios for 100 realizations of randomized Poissonian distributed teleseismic events times. Figure format follows Figure 4.12. Data points fall within a larger area centered nearly symmetrically about the 1:1 ratio line. This area completely encompasses the data points from the actual data shown in Figure 4.12.

REFERENCES FOR CHAPTER 4

Aki, K. and R. Koyanagi (1981), Deep volcanic tremor and magma ascent mechanism under Kilauea, Hawaii, *J. Geophys. Res.*, 86(B8), 7095-7109, doi: 10.1029/JB086iB08p07095.

Aso, N, K. Ohta, and S. Ide (2011), Volcanic-like low-frequency earthquakes beneath Osaka Bay in the absence of a volcano, *Geophys. Res. Lett.*, 38(8), L08303, doi: 10.1029/2011GL046935.

Aso, N. and V. C. Tsai (2014), Cooling magma model from deep volcanic long-period earthquakes, *J. Geophys. Res.-Sol.Ea.*, 119(11), 8442-8456, doi: 10.1002/2014JB011180.

Aso, N., K. Ohta, and S. Ide (2013), Tectonic, volcanic, and semi-volcanic deep low-frequency earthquakes in western Japan, *Tectonophysics*, 600, 27-40, doi: 10.1016/j.tecto.2012.12.015.

Aster, R. C., D. E. McNamara, and P. D. Bromirski (2008), Multidecadal climate-induced variability in microseisms, *Seismol. Res. Lett.*, 79(2), 194-202, doi: 10.1785/gssrl.79.2.194.

Behrendt, J. C. (2013), The aeromagnetic method as a tool to identify Cenozoic magmatism in the West Antarctic Rift System beneath the West Antarctic Ice Sheet – A Review: Theil subglacial volcano as possible source of ash layer in WAISCORE, *Tectonophysics*, 585, 124-136, doi: 10.1016/j.tecto.2012.06.035.

Benz, H. M., C. E. Johnson, J. M. Patton, N. D. McMahon, and P. S. Earle (2015a), *GLASS 2.0: An operational, multimodal, Bayesian earthquake data association engine*, Abstract S21B-2687 presented at 2015 Fall Meeting, AGU, San Francisco, Calif.

Benz, H. M., N. D. McMahon, R. C. Aster, D. E. McNamara, and D. B. Harris (2015b), Hundreds of earthquakes per day: The 2014 Guthrie, Oklahoma, earthquake sequence, *Seismol. Res. Lett.*, 86(5), 1318-1325, doi:10.1785/0220150019.

Benz, H. M., N. D. McMahon, R. C. Aster, D. E. McNamara, and D. B. Harris (2015), Hundreds of earthquakes per day: The 2014 Guthrie, Oklahoma, earthquake sequence, *Seismol. Res. Lett.*, 86(5), 1318-1325, doi:10.1785/0220150019.

Boger, S. D. (2011), Antarctica – Before and after Gondwana, *Gondwana Res.*, 19(2), 335-271, doi: 10.1016/j.gr.2010.09.003.

Frohlich, C. and S. D. Davis (1993), Teleseismic *b* values; Or, much ado about 1.0, *J. Geophys. Res.*, 98(B1), 631-644, doi:10.1029/92JB01891.

Han, J., J. E. Vidale, H. Houston, D. A. Schmidt, and K. C. Creager (2018), Deep long-period earthquakes beneath Mount St. Helens: Their relationship to tidal stress, episodic tremor and slip, and regular earthquakes, *Geophys. Res. Lett.*, 45(5), 2241-2247, doi: 10.1002/2018GL077063.

Harris, D. B. (2006), *Subspace detectors: Theory* (Rep. UCRL-TR-222758), Livermore, California: Lawrence Livermore National Laboratory.

Harris, D. B., and D. A. Dodge (2011), An autonomous system for grouping events in a developing aftershock sequence, *Bull. Seismol. Soc. Am.*, 101(2), 763-774, doi:10.1785/0120100103.

Hasegawa, A. and A. Yamamoto (1994), Deep, low-frequency microearthquakes in or around seismic low-velocity zones beneath active volcanoes in northeastern Japan, *Tectonophysics*, 233(3-4), 233-252, doi: 10.1016/0040-1951(94)90243-7.

Hill, D. P., P. Dawson, M. J. S. Johnston, and A. M. Pitt (2002), Very-long-period volcanic earthquakes beneath Mammoth Mountain, California, *Geophys. Res. Lett.*, 29(10), 1370, doi: 10.1029/2002GL014833.

Kennett, B. L. N., E. R. Engdahl, and R. Bulland (1995), Constraints on seismic velocities in the earth from travel times, *Geophys. J. Int.*, 122(1), 108-124, doi: 10.1111/j.1365-246X.1995.tb03540.x.

Lough, A. C. (2014), Studies of seismic sources in Antarctica using an extensive deployment of broadband seismographs, PhD dissertation, Dept. of Earth and Planetary Sci., Washington Univ., St. Louis, Missouri.

Lough, A. C., D. A. Weins, C. Grace Barcheck, S. Anandakrishnan, R. C. Aster, D. D. Blankenship, A. D. Huerta, A. Nyblade, D. A. Young, and T. J. Wilson (2013), Seismic detection of an active subglacial magmatic complex in Marie Byrd Land, Antarctica, *Nat. Geosci.*, 6(12), 1031-1035, doi: 10.1038/ngeo1992.

Matoza, R. S., P. M. Shearer, and P. G. Okubo (2014), High-precision relocation of long-period events beneath the summit region of Kilauea volcano, Hawaii, from 1986-2009, *Geophys. Res. Lett.*, 41(10), 3413-3421, doi: 10.1002/2014GL059819.

McMahon, N. D., R. C. Aster, W. L. Yeck, D. E. McNamara, and H. M. Benz (2017), Spatiotemporal evolution of the 2011 Prague, Oklahoma, aftershock sequence revealed using subspace detection and relocation, *Geophys. Res. Lett.*, 44(14), 7149-7158, doi: 10.1002/2017GL072944.

McNutt, S. R. (1996), Seismic monitoring and eruption forecasting of volcanoes: A review of the state-of-the-art and case histories, In R. Scarpa and R. I. Tilling (Eds.), *Monitoring and mitigation of volcano hazards* (pp. 99-146), Berlin: Springer-Verlag, doi: 10.1007/978-3-642-80087-0_3.

Nakamichi, H., H. Hamaguchi, S. Tanaka, S. Ueki, T. Nishimura, and A. Hasegawa (2003), Source mechanisms of deep and intermediate-depth low-frequency earthquakes beneath Iwate volcano, northeastern Japan, *Geophys. J. Int.*, 154(3), 811-828, doi: 10.1046/j.1365-246X.2003.01991.x.

Nichols, M. L., S. D. Malone, S. C. Moran, W. A. Thelen, and J. E. Vidale (2011), Deep long-period earthquakes beneath Washington and Oregon volcanoes, *J. Volcanol. Geoth. Res.*, 200(3-4), 116-128, doi: 10.1016/j.jvolgeores.2010.12.005.

Okubo, P. G. and C. J. Wolfe (2008), Swarms of similar long-period earthquakes in the mantle beneath Mauna Loa volcano, *J. Volcanol. Geoth. Res.*, 178(4), 787-794, doi: 10.1016/j.jvolgeores.2008.09.007.

Pitt, A. M., D. P. Hill, S. W. Walter, and M. J. S. Johnson (2002), Midcrustal, long-period earthquakes beneath northern California volcanic areas, *Seismol. Res. Lett.*, 73(2), 144-152, doi: 10.1785/gssrl.73.2.144.

Power, J. A., S. D. Stihler, R. A. White, and S. C. Moran (2004), Observations of deep long-period (DLP) seismic events beneath Aleutian arc volcanoes; 1989-2002, *J. Volcanol. Geoth. Res.*, 138(3-4), 243-266, doi: 10.1016/j.jvolgeores.2004.07.005.

Power. J. A., A. D. Jolly, C. J. Nye, and M. L. Harbin (2002), A conceptual model of the Mount Spurr magmatic system from seismic and geochemical observations of the 1992 Crater Peak eruption sequence, *Bull. Volcanol.*, 64, 206-218, doi: 10.1007/s00445-002-0201-x.

Shapiro, N. M., D. V. Droznin, S. Ya. Droznina, S. L. Senyukov, A. A. Gusev, and E. I. Gordeev (2017), Deep and shallow long-period volcanic seismicity linked by fluid-pressure transfer, *Nat. Geosci.*, 10(6), 442-455, doi: 10.1038/ngeo2952.

Soosalu, H., J. Key, R. S. White, C. Knox, P. Einarsson, and S. S. Jacobsdóttir (2010), Lower-crustal earthquakes caused by magma movement beneath Askja volcano on the north Iceland rift, *Bull. Volcan.*, 72, 55-62, doi: 10.1007/s00445-009-0297-3.

Ukawa, M. and M. Ohtake (1987), A monochromatic earthquake suggesting deep-seated magmatic activity beneath the Izu-Ooshima volcano, Japan, *J. Geophys. Res.*, 92(B12), 12649-12663, doi: 10.1029/JB092iB12p12649.

Vidale, J. E., D. A. Schmidt, S. D. Malone, A. J. Hotovec-Ellis, S. C. Moran, K. C. Creager, and H. Houston (2014), Deep long-period earthquakes west of the volcanic arc in Oregon: Evidence of serpentine dehydration in the fore-arc mantle wedge, *Geophys. Res. Lett.*, 41(2), 370-376, doi: 10.1002/2013GL059118.

Weins, D., A. Nyblade, and R. Aster (2007), IPY POLENET-Antarctica: Investigating links between geodynamics and ice sheets, *International Federation of Digital Seismograph Networks*, Other/Seismic Network, doi: 10.7914/SN/YT_2007.

White, R. A. (1996), Precursory deep long-period earthquakes at Mount Pinatubo: Spatio-temporal link to basaltic trigger, In C. G. Newhall and R. S. Punongbayan (Eds.), *Fire and mud: Eruptions and lahars of Mount Pinatubo, Philippines* (pp. 307-328), U.S. Geological Survey, accessed 15 Sep 2018, https://pubs.usgs.gov/pinatubo/.

Winberry, J. P. and S. Anandakrishnan (2003), Seismicity and neotectonics in West Antarctica, *Geophys. Res. Lett.*, 30(18), 1931, doi: :10.1029/2003GL018001.

APPENDIX 1

SUPPLEMENTARY INFORMATION FOR CHAPTER 2 – LINCOLN, MONTANA [3]

A1.1 INTRODUCTION

These supplementary tables provide information about the different catalogs mentioned and developed in this study, the location information for the 685 relocated events, as well as event and P-phase arrival information for the 3009 detected events associated with the 6 July 2017 $\mathbf{M}_\mathbf{W}$ 5.8 earthquake near Lincoln, Montana. Table A1.1 provides information about the catalogs in this study. Data Set A1.1 includes 685 relocated events larger than or equal to $\mathbf{M}_\mathbf{W}$ 1 contained in the U.S. Geological Survey's Comprehensive Catalog (ComCat) from 5 July through 14 October 2017. Data Sets A1.2 and A1.3 contain information for the 3009 events contained in the final catalog including 303 template events downloaded from ComCat, 3 additional foreshocks, and 2703 additional aftershocks occurring between 5 and 28 July 2017. I utilized a matched-filter technique for additional event detection, filtered detections for correlation coefficients greater than or equal to 0.5, screened for multiples, and associated detections to at least 5 of the 11 utilized seismic stations as detailed in the manuscript.

---

[3] **This appendix has been accepted and is currently in press for publication as supplementary information to:**

McMahon, N. D., W. L. Yeck, M. C. Stickney, R. C. Aster, H. R. Martens, and H. M. Benz (2018), Spatiotemporal analysis of the foreshock-mainshock-aftershock sequence of the 6 July 2017 M_W 5.8 Lincoln, Montana, Earthquake, *Seismol. Res. Lett.*, in press.

A1.2 Table

Table A1.1: Description of catalogs mentioned in this study associated with the Lincoln earthquake. ComCat is the online USGS Comprehensive Catalog of Earthquakes.

Catalog	Time Period (2017)	Number of Events	Magnitude Range	Notes
Entire ComCat Catalog	5 July – 31 December	> 1200	M_L -0.3 – M_W 5.8	• Not utilized in this study • Hosted at https://earthquakes.usgs.gov
Relocated Catalog	5 July – 15 October	685	M_W 1 – M_W 5.8	• These events were relocated in this study • All events larger than M 1 contained in ComCat for the time period • Includes 1 foreshock • Includes 261 template events • Event details in Data Set A1.1
Initial Catalog / Template Events	5 July – 27 July	303	M_L -0.3 – M_W 5.8	• All events contained in ComCat for the time period; utilized for correlation purposes • Includes 1 foreshock • Event details in Data Sets A1.2 and A1.3 with "IE" Event ID • Initial event locations can be found in ComCat
Final Catalog	5 July – 27 July	3009	M_{rel} -0.3 – M_{rel} 5.8	• These events were not located in this study • Includes 303 template events and 2706 newly detected events • Includes 4 foreshocks, 1 from the template events • Event details in Data Sets A1.2 and A1.3. Newly detected events have "ND" Event ID

A1.3 DATA SETS

Data Set A1.1: Attached as separate .txt file. Catalog of location information for the 685 relocated events in the $\mathbf{M}_W$ 5.8 Lincoln, Montana sequence. Columns are event ID (from ComCat), origin date, origin time, latitude, longitude, depth (km), and magnitude.

Data Set A1.2: Attached as separate .txt file. Catalog of event information for the 3009 events detected in the $\mathbf{M}_W$ 5.8 Lincoln, Montana sequence. Columns are event ID, origin date, origin time, and event magnitude ($\mathbf{M}_{rel}$). The 303 template events are identified by event IDs beginning with “IE,” and newly detected events are identified by event IDs beginning with “ND.”

Data Set A1.3: Attached as separate .txt file. Catalog of *P*-phase arrival information for events contained in Data Set A1.2. Columns are event ID, network, station, *P*-phase arrival date, and *P*-phase arrival time. Event IDs correspond to the event IDs in Data Set A1.2.

APPENDIX 2

SUPPLEMENTARY INFORMATION FOR CHAPTER 3 – PRAGUE, OKLAHOMA [4]

A2.1 INTRODUCTION

This supplementary information contains catalogs for the November 2011 Prague, Oklahoma, aftershock sequence (Data Sets A2.1 and A2.2), ancillary figures showing additional cross-sections (Fig. A2.1), magnitude estimate standard deviations (Fig. A2.2), earthquake density as a function of slip (Fig. A2.3), earthquake count over time in the Arbuckle Group and basement (Fig. A2.4), earthquake magnitude as a function of depth (Fig. A2.5), earthquake waveforms for varying magnitudes (Figs. A2.6-A2.8), average waveforms and spectra for detected events (Figs. A2.9-A2.10), figures including the 184 events excluded from analysis (A2.11-A2.15), ancillary tables of subspace detector construction parameters (Table A2.1) and the velocity profile (Table A2.2) used to relocate the aftershock seismicity, and an animation of the aftershock sequence through time (Movie A2.1).

---

[4] **This appendix has been previously published as supplementary information to:**

McMahon, N. D., R. C. Aster, W. L. Yeck, D. E. McNamara, and H. M. Benz (2017), Spatiotemporal evolution of the 2011 Prague, Oklahoma, aftershock sequence revealed using subspace detection and relocation, *Geophys. Res. Lett.*, 44(14), 7149-7158, doi: 10.1002/2017GL072944.

A2.2 TABLES

Table A2.1: Attached as separate .xlsx file. Station information and subspace detection construction parameters for 31 stations used in analysis.

Table A2.2: Input Velocity profile used in Bayesloc to relocate aftershock seismicity [*McNamara et al.*, 2015].

Depth (km)	P velocity (km/s)	S velocity (km/s)
0	3.4	2.0
1.9	3.4	2.0
1.9	5.5	3.3
8.0	5.5	3.3
8.0	6.25	3.6
21.0	6.25	3.6
21.0	6.4	3.7
42.0	6.4	3.7
MOHO		
42.0	8.15	4.6
121.0	8.15	4.6

A2.3 FIGURES

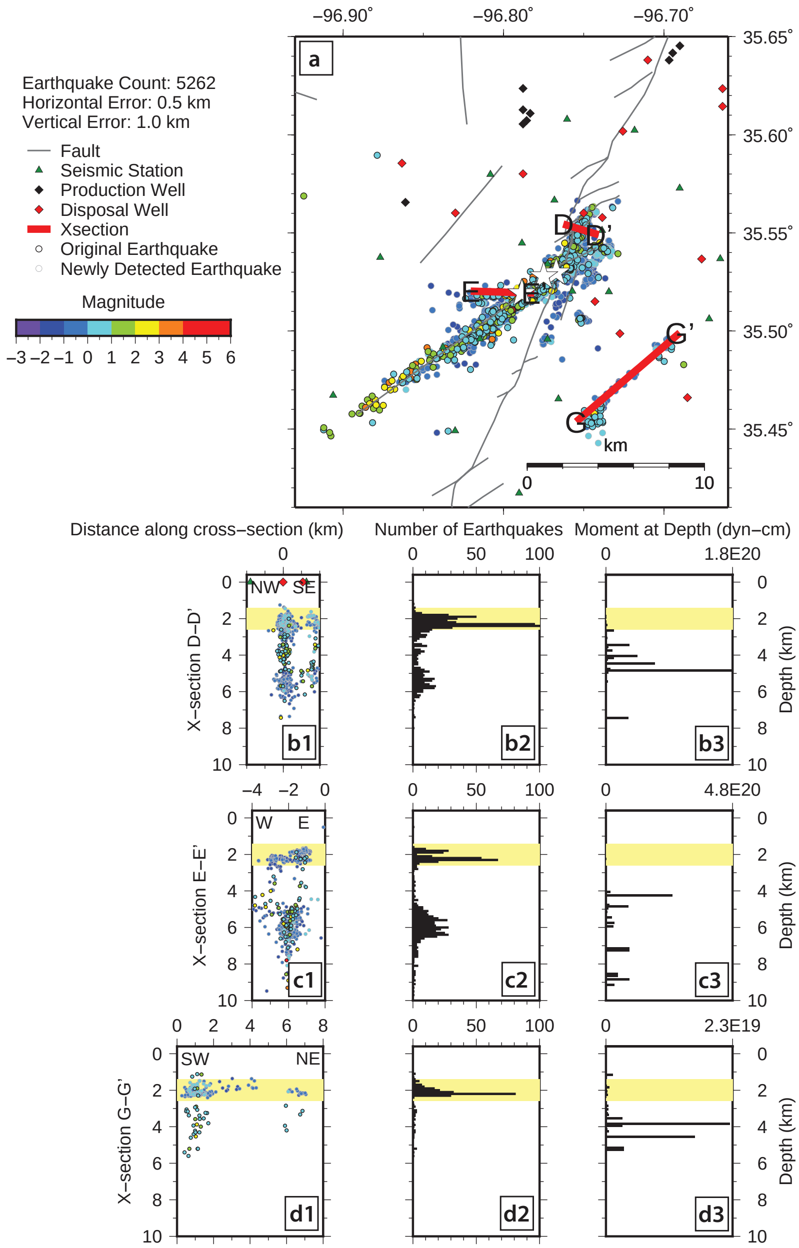

Figure A2.1. a) Map of final event catalog locations with epicentral uncertainties less than 500 m and depth uncertainties less than 1 km. The yellow depth range depicts the approximate extent of the Arbuckle Group in the region. Events are colored by magnitude as indicated in the legend. The three large events (Fig. 3.1) are plotted as white stars and cross-sections are indicated by red lines. b-1) Event locations within 1.5 km of cross section D-D' perpendicular to the main Wilzetta fault zone structure. b-2) Number of earthquakes in cross-section D-D' as a function of depth in 0.1 km depth bins. b-3) Seismic moment in cross-section D-D' as a function of depth in 0.1 km depth bins. c[1,2,3]) Follows b-[1,2,3] for cross-section E-E' along Meeker-Prague fault splay ruptured by the largest aftershock. d-[1,2,3]) Follows b-[1,2,3] for cross-section G-G' along strike of the subparallel fault perhaps triggered by the Prague sequence.

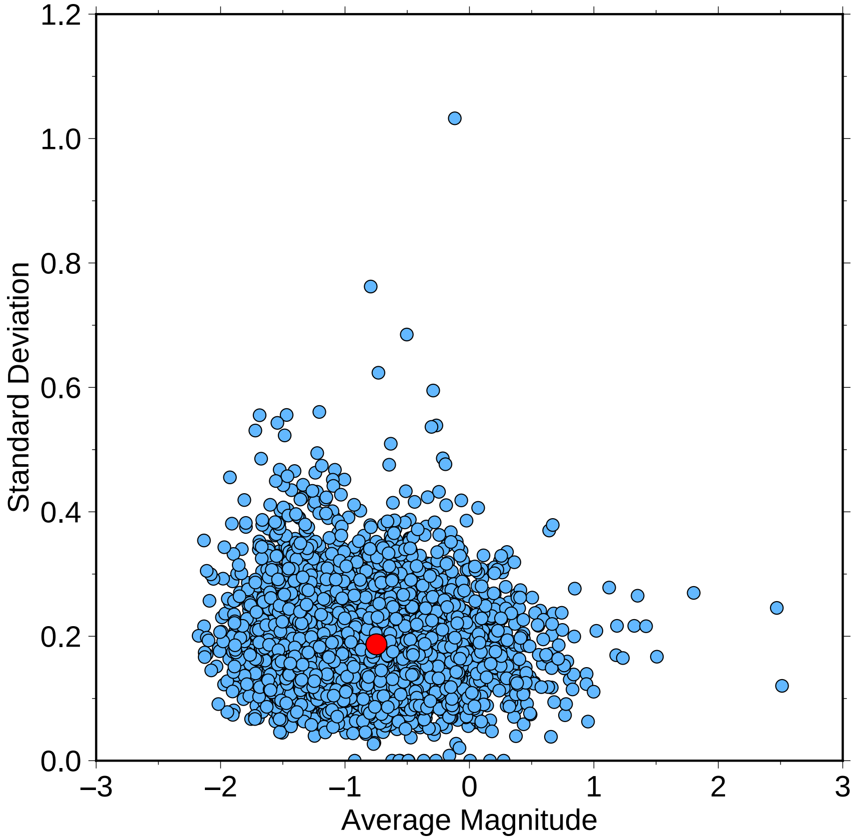

Figure A2.2. A plot showing the standard deviation of individual station magnitudes (determined from station averages) as a function of final average magnitude for each event in the catalog of subspace detected events. The red circle shows the mean.

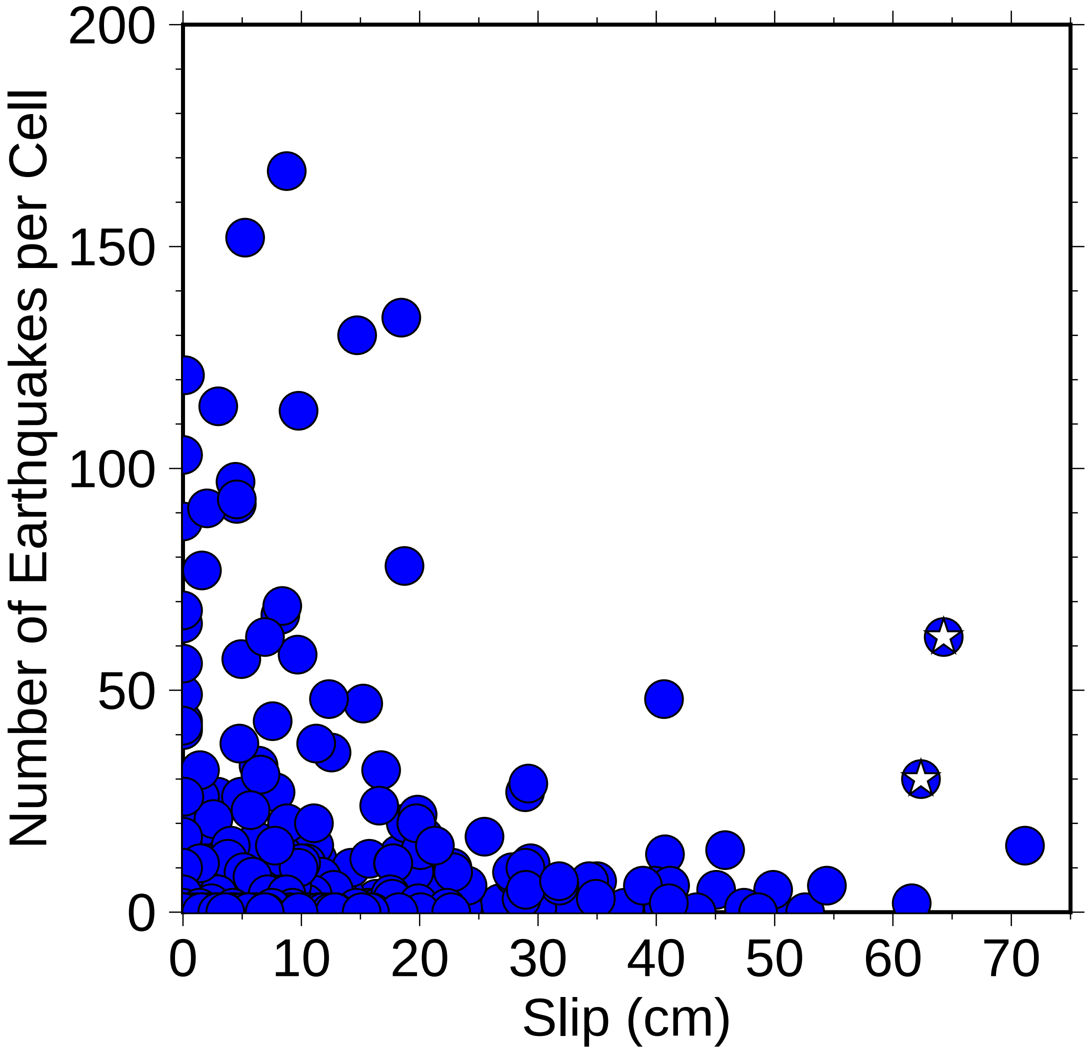

Figure A2.3. Corresponding to the finite-fault slip model of *Sun and Hartzell* [2014] (Fig. 3.4), number of earthquakes as a function of slip estimated for each cell. The white stars indicate the cells containing the hypocenters of the three largest events in the sequence. Note the inverse relationship between the number of earthquakes and amount of slip in each cell indicating that aftershocks are preferentially located in low-slip regions of the fault.

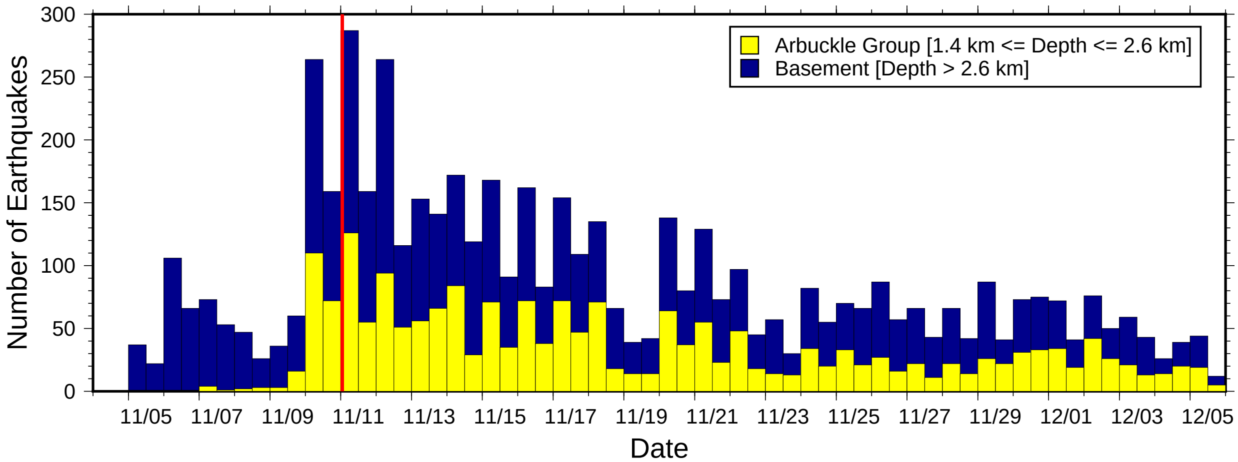

Figure A2.4. Stacked bar chart showing number of earthquakes over time separated into shallow, inferred Arbuckle Group events (yellow) and basement events (blue). Red vertical line indicates the time when the last temporary station became operational. Approximately 40% of aftershocks occur within the sedimentary Arbuckle Group. This proportion of earthquakes between the overlying Arbuckle Group and the crystalline basement remains relatively stable throughout the detection time period, ranging from 30 to 54% daily with a 7% standard deviation, after the temporary networks became fully operational. Prior to full temporary network functionality, it appears that a much smaller proportion of events is occurring in the Arbuckle Group; however, this phenomenon is likely a product of lack of station coverage.

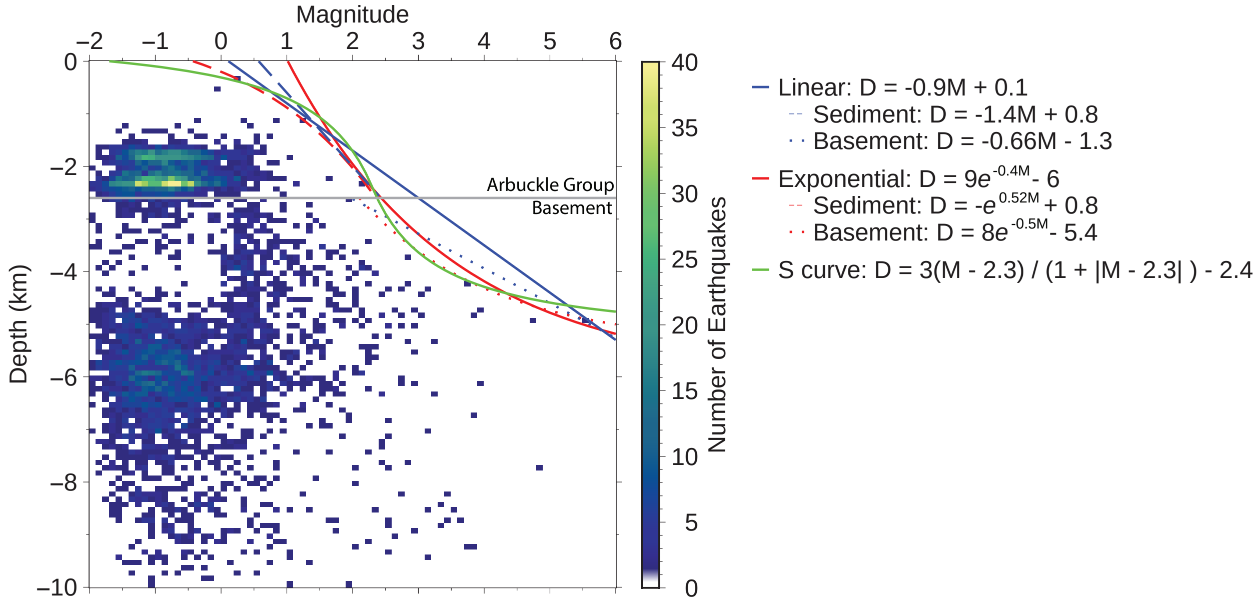

Figure A2.5. Earthquake magnitude vs. depth for the Prague aftershock catalog displayed as a function of earthquake density in 0.1 x 0.1 km cells. Various fits to the minimum depth as a function of magnitude are also shown. The fits show that events in the Arbuckle Group may reach a maximum magnitude of **M** 2-3, **M** 1 in the very shallow sediments in the Meeker-Prague region. Larger events, such as the **M**$_W$ 4.8 foreshock and **M**$_W$ 5.7 mainshock, are not likely to initiation much shallower than 5 km.

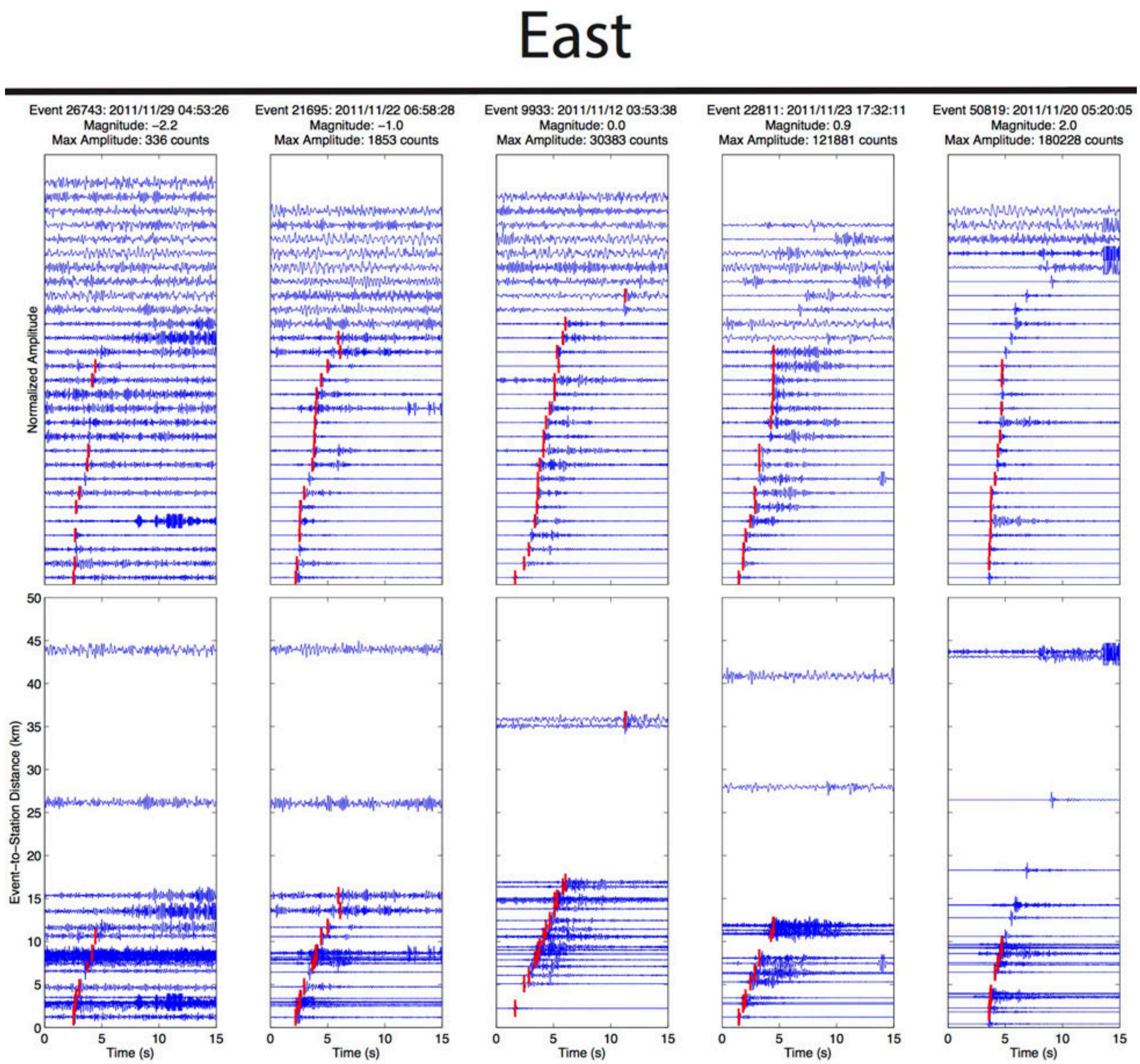

Figure A2.6. East-west component waveforms for five aftershocks ranging in magnitude from **M** -2.2 to **M** 2.0 (left to right). The top row displays normalized amplitude waveforms ordered by event-to-station distance, but displayed in equal vertical axis increments. The bottom row displays the normalized amplitude waveforms ordered by event-to-station distance and plotted vertical as a function of that event-to-station distance. Maximum amplitude for each event on the east-west component across the network displayed in the information text at top.

North

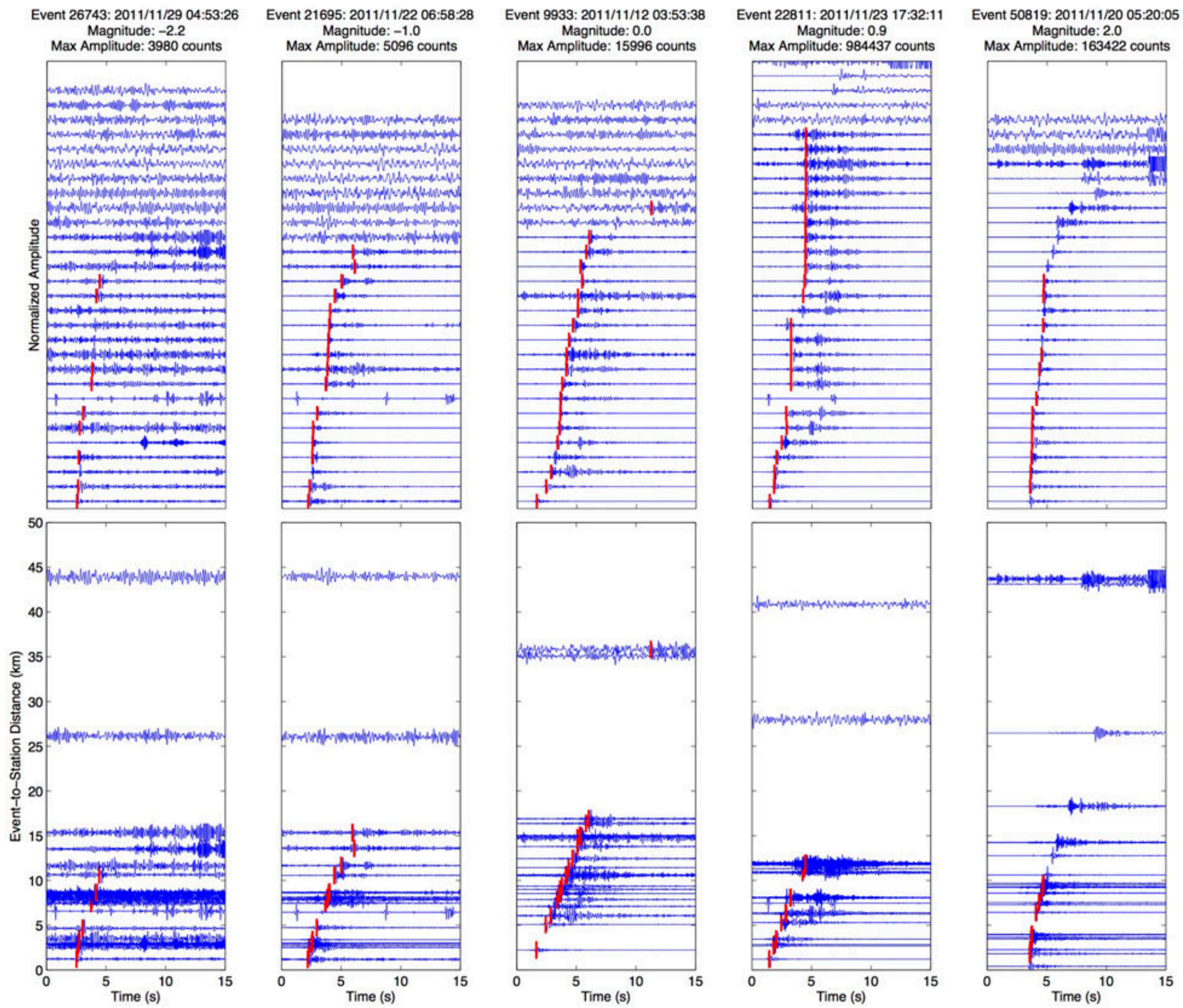

Figure A2.7. Follows Fig. A2.6 for north-south component.

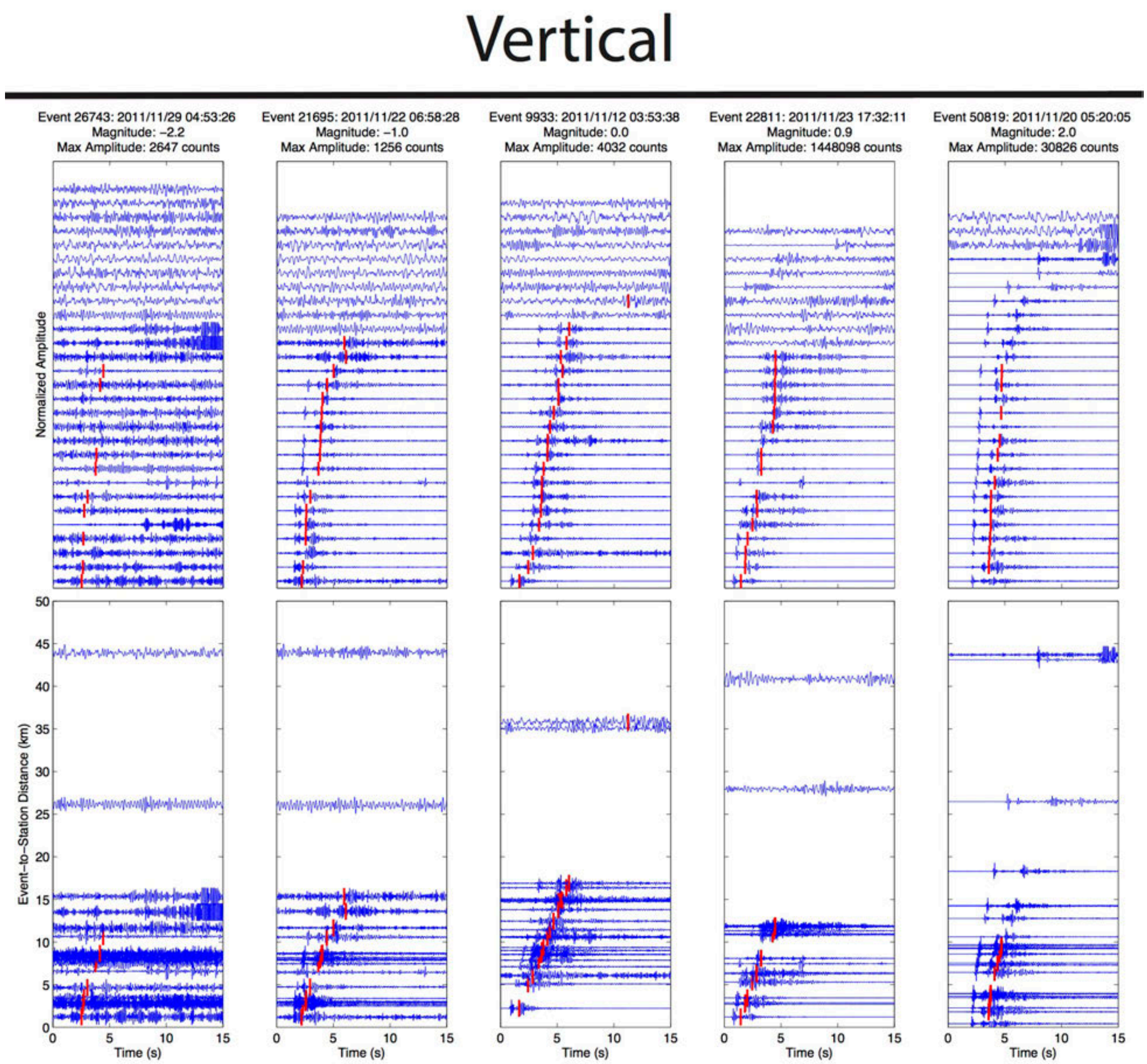

Figure A2.8. Follows Fig. A2.6 for vertical component.

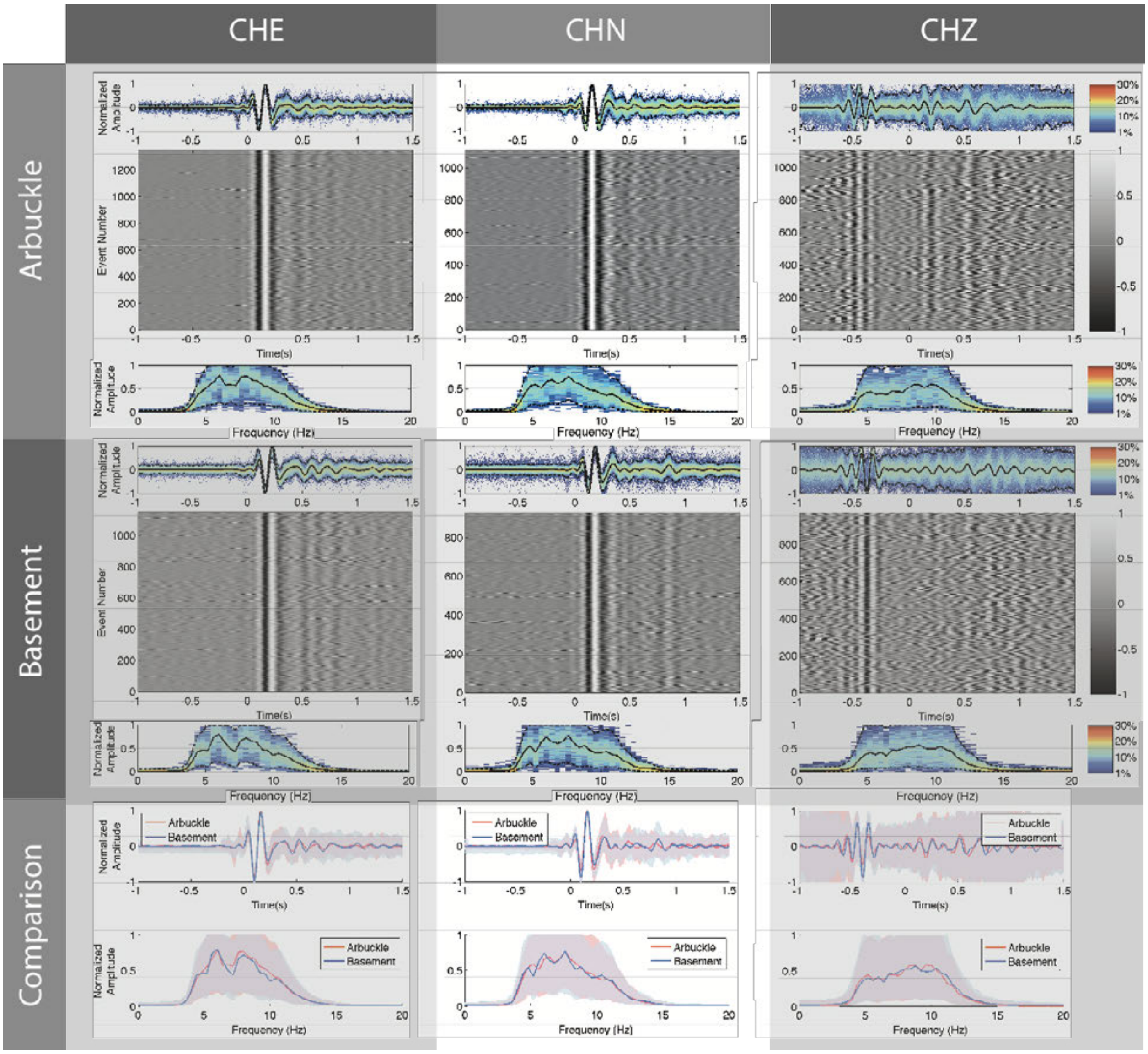

Figure A2.9. Waveforms and spectrums for aftershocks detected and located on station LC05 for the CHE (left), CHN (center), and CHZ (right) components. Top three rows (Arbuckle) are (from top to bottom): 1) probability density function (PDF) of the waveforms in the Arbuckle Group (1.4 < depth < 2.6 km) on the component specified at the top of the figure – median waveform defined by the solid black line and 95% confidence interval defined by dashed lines – probability defined by colorscale on far right; 2) waveforms in the Arbuckle Group on the component specified at the top of the figure – normalized amplitude defined by colorscale on far right; 3) PDF of the spectra calculated for the waveforms in (2) – median spectrum defined by the solid black line and 95% confidence interval defined by dashed lines – probability defined by colorscale on far right. Middle three rows (Basement) follow the top three rows (Arbuckle) for events in the basement (depth >2.6 km). Bottom two rows (Comparison) show the median waveforms (top) and the median spectra (bottom) for the Arbuckle and Basement for comparison – shaded backgrounds denote 95% confidence intervals. Shows that detected waveforms are very similar in the horizontal components where the *S*-phase energy shows best.

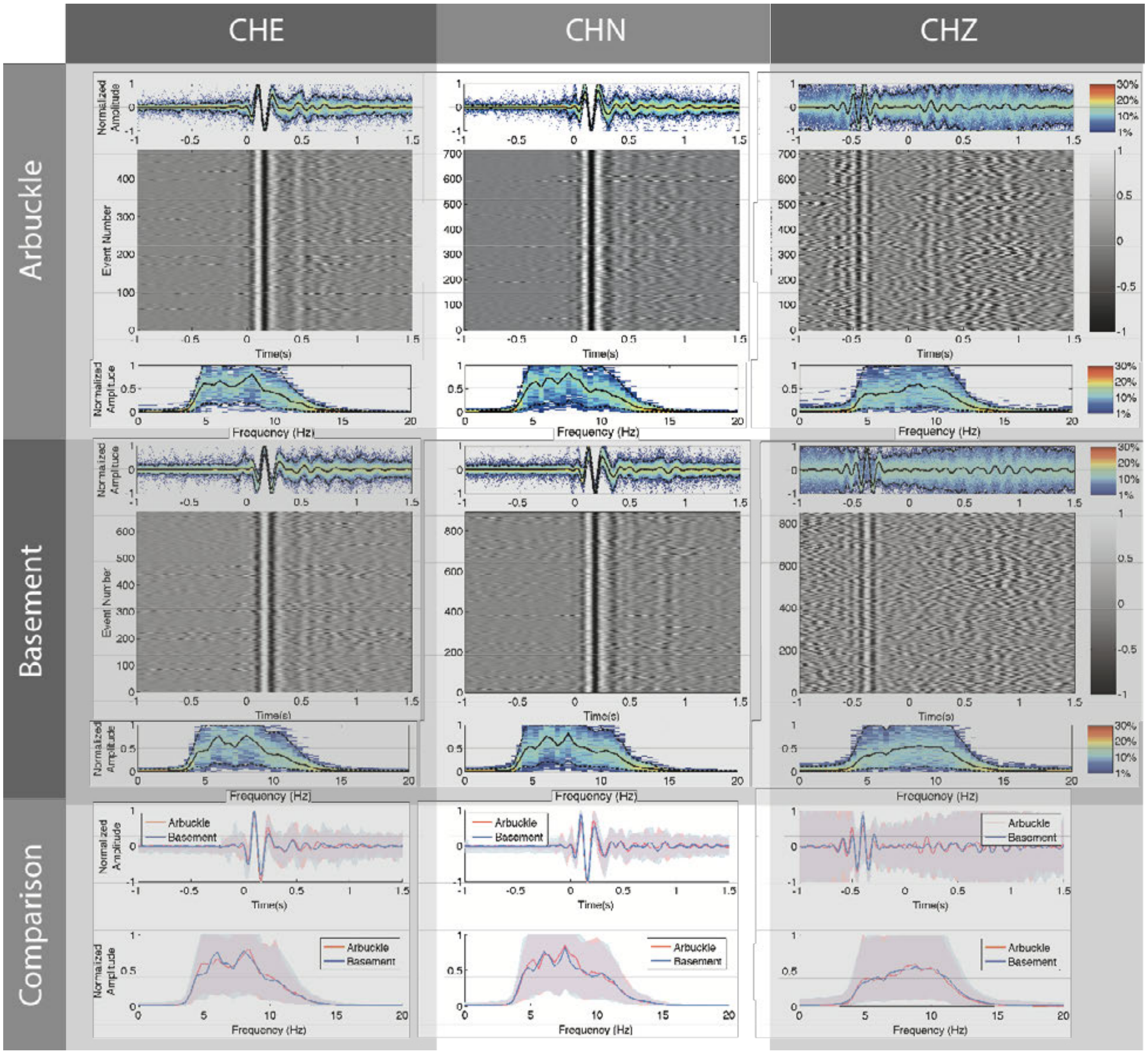

Figure A2.10. Follows Fig. A2.9 for waveforms with reverse polarity. I find no significant difference in either the average waveform or spectrum between the events occurring in the Arbuckle Group and the crystalline basement. Therefore, it's not particular templates that allowed for identification of additional Arbuckle Group events, but rather the nature of subspace detectors where event detections are represented as a linear combination of basis vectors rather than a cross-correlation with a single waveform, thus amplifying its ability to detect events in low signal-to-noise environments. This methodology applied to multiple nearby stations allowed for the detection and location of the low-magnitude events occurring in the Arbuckle Group.

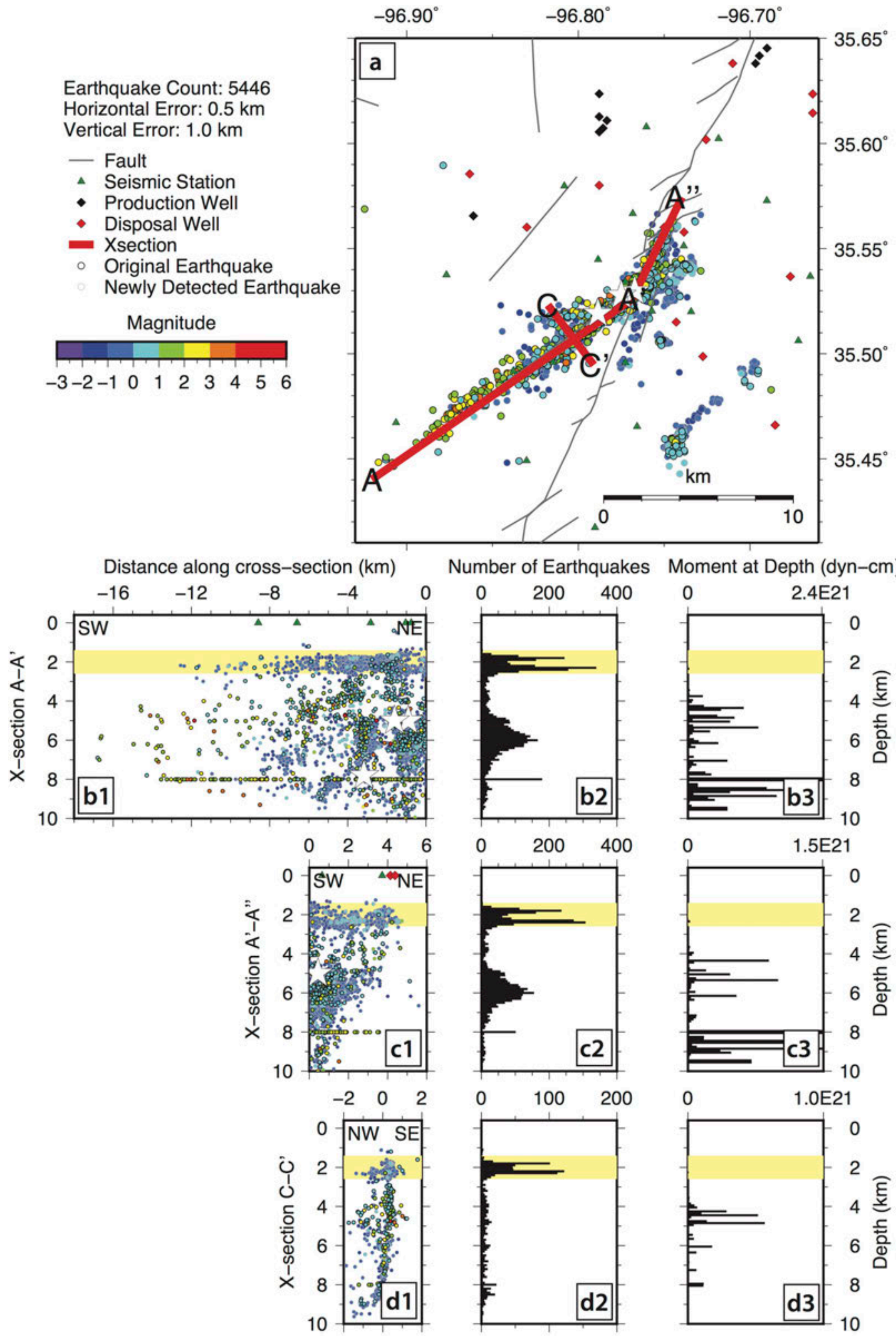

Figure A2.11. Follows Fig. 3.2, but includes the 184 events that were excluded from the original catalog that did not meet uncertainty constraints after relocation. These events occur at 5 and 8 km depth in accordance with standard USGS practices pinning earthquakes at these depths when the hypocentral depth is poorly constrained.

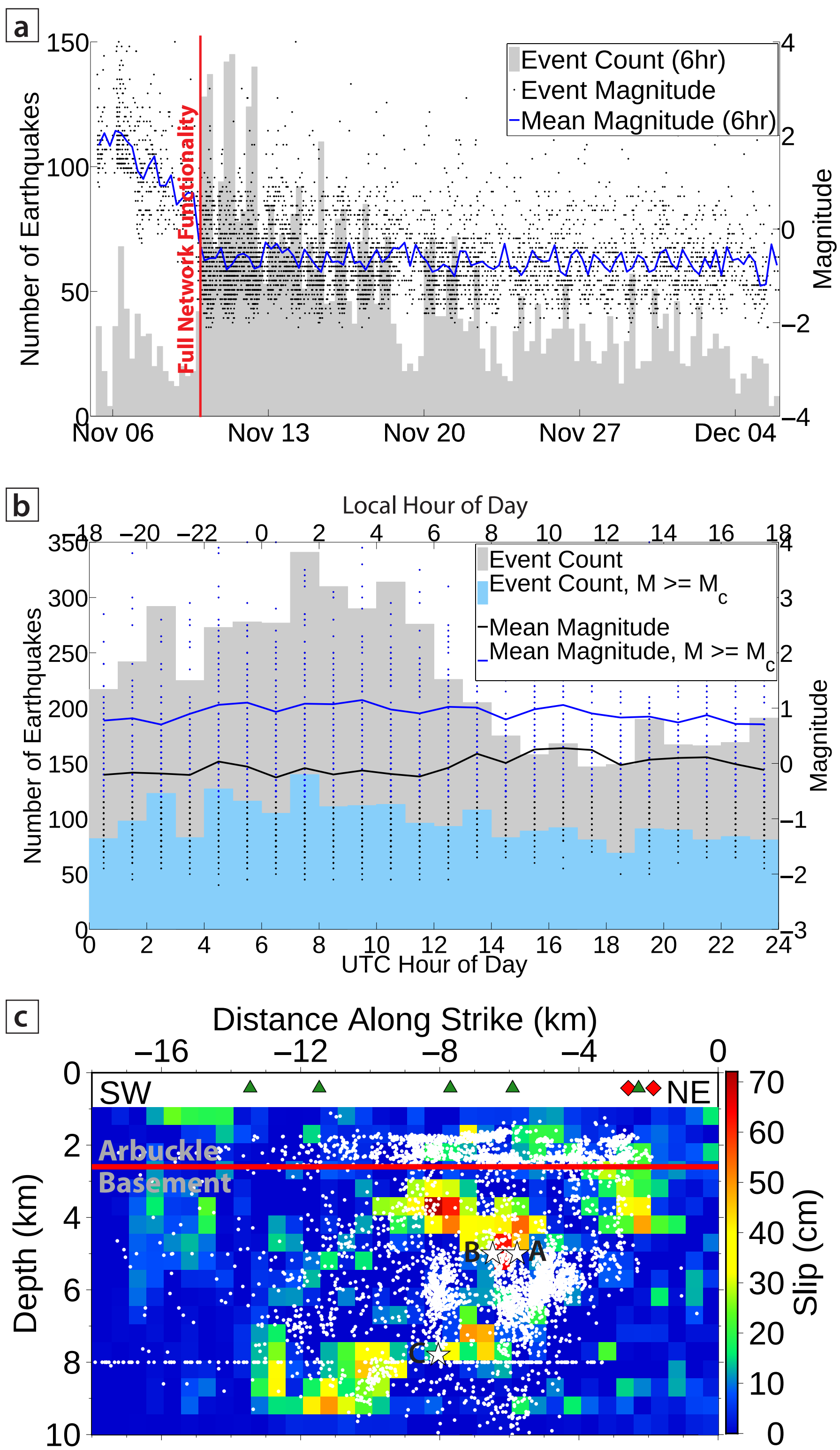

Figure A2.12. Follows Fig. 3.4, but includes the 184 events that were excluded from the original catalog that did not meet uncertainty constraints after relocation. These events occur at 5 and 8 km depth in accordance with standard USGS practices pinning earthquakes at these depths when the hypocentral depth is poorly constrained.

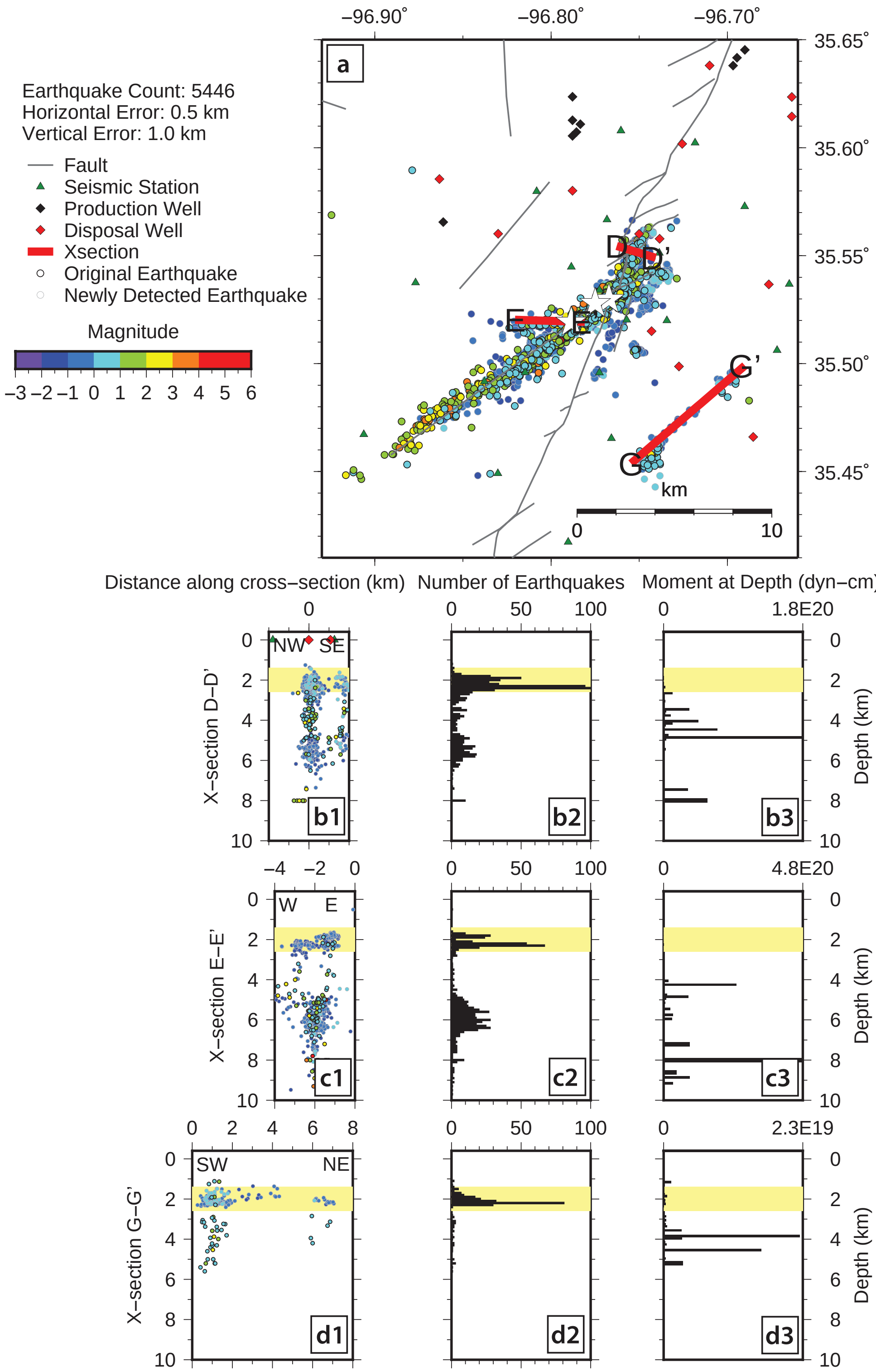

Figure A2.13. Follows Fig. A2.1, but includes the 184 events that were excluded from the original catalog that did not meet uncertainty constraints after relocation. These events occur at 5 and 8 km depth in accordance with standard USGS practices pinning earthquakes at these depths when the hypocentral depth is poorly constrained.

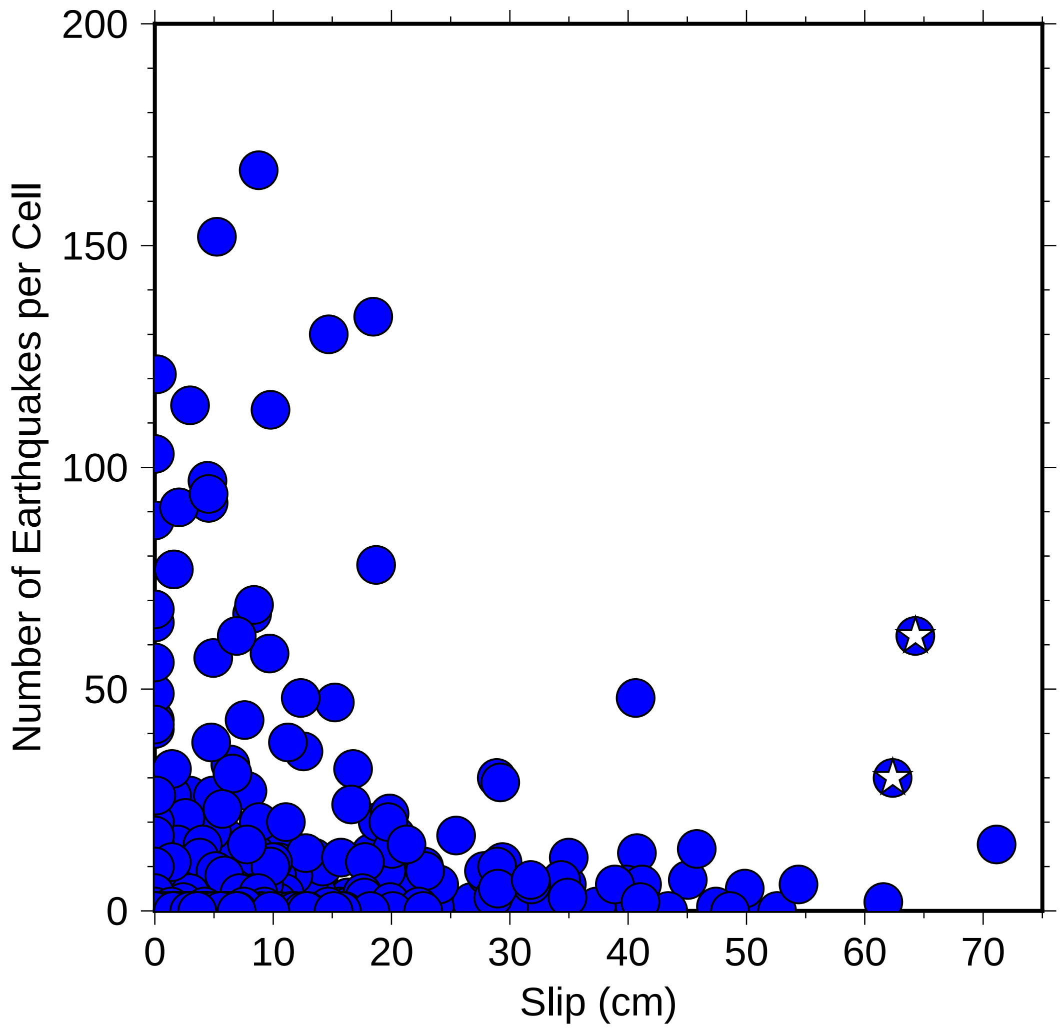

Figure A2.14. Follows Fig. A2.3, but includes the 184 events that were excluded from the original catalog that did not meet uncertainty constraints after relocation. These events occur at 5 and 8 km depth in accordance with standard USGS practices pinning earthquakes at these depths when the hypocentral depth is poorly constrained.

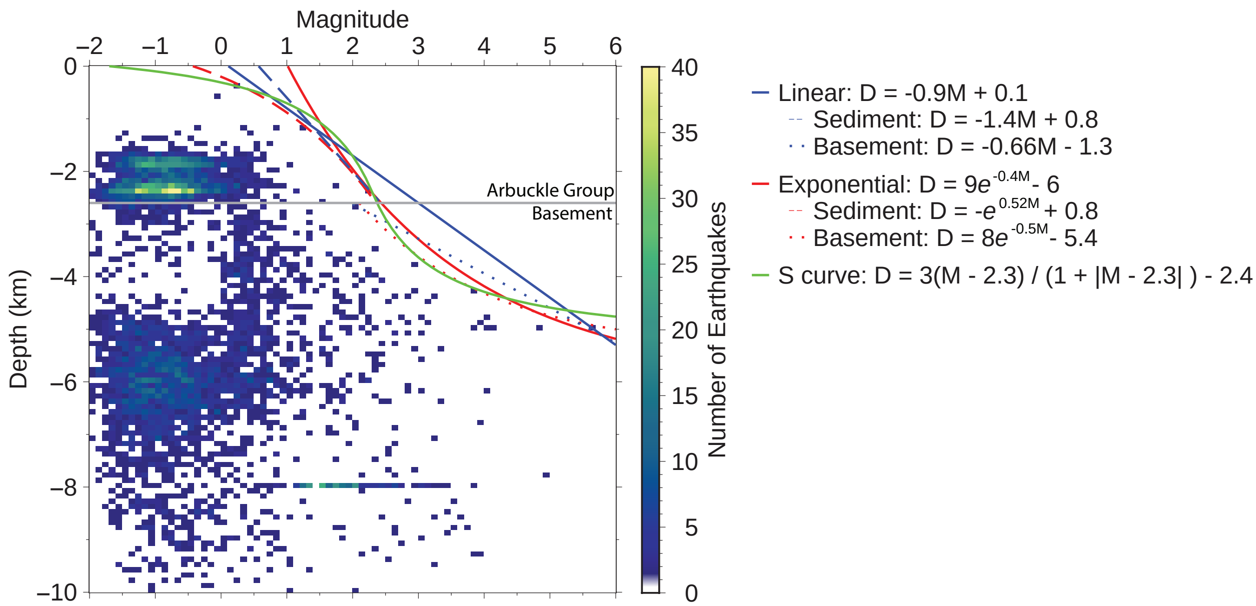

Figure A2.15. Follows Fig. A2.5, but includes the 184 events that were excluded from the original catalog that did not meet uncertainty constraints after relocation. These events occur at 5 and 8 km depth in accordance with standard USGS practices pinning earthquakes at these depths when the hypocentral depth is poorly constrained.

A2.4 DATA SETS

Data Set A2.1: Attached as separate .txt file. An initial catalog of events and arrival times used in the construction of the subspace detectors. A total of 998 events had *S*-phase arrivals on the 31 stations of interest in the month following the $\mathbf{M}_{W}$ 4.8 foreshock. Lines beginning with "E" contain event information in the following order: event ID, origin year, origin month, origin day, origin hour, origin minute, origin second, latitude, longitude, depth, and magnitude. Lines beginning with "P" contain *S*-phase information in the following order: event ID, station, phase arrival year, phase arrival month, phase arrival day, phase arrival hour, phase arrival minute, phase arrival second.

Data Set A2.2: Attached as separate .txt file. The final catalog of 5446 events and arrival times resulting from processing. Lines beginning with "E" contain event information in the following order: event ID, origin year, origin month, origin day, origin hour, origin minute, origin second, latitude, longitude, depth, and magnitude. Lines beginning with "P" contain phase information in the following order: event ID, station, phase, phase arrival year, phase arrival month, phase arrival day, phase arrival hour, phase arrival minute, phase arrival second.

A2.5 ANIMATION

Animation A2.1: Attached as separate .mp4 file. Animation of aftershock locations for the aerial view and cross-sections A-A', A'-A", and C-C'. Frames are separated by 10 minutes. Aftershock color intensity fades over 24 hours. This animation includes the 184 previously excluded from analysis due to error uncertainty in order to more fully understand the temporal nature of the sequence.

A2.6 ADDITIONAL METHODOLOGY INFORMATION

We utilized kurtosis-based methods of *Baillard et al*. [2014], to pick *S*-phase arrival times. Waveforms for each station were aligned using the correlation-based alignment and clustering approach of *Rowe et al*. [2002]. Proper alignment of initial events is essential to reduce the subspace rank, increasing computational efficiency [*Harris*, 2006].

The ideal filter band captures the broadest range of earthquake magnitudes while keeping the rank of the subspace low. For proximal temporary networks, a filter band of 4-12 Hz captured the unique waveform shape of the events, filtered out lower frequency noise that obscured smaller events, and kept the subspace rank sufficiently low (Table A2.1). For distal stations (>15 km from the mainshock epicenter), that were less likely to capture small events, the filter band was shifted to longer periods, 1-8 Hz. We used multi-channel templates that included the full *P*- and *S*-phase pulses. The template length for each station was dictated by the largest event-to-station distance and varied from 3.5 to 19.2 s (Table A2.1).

Detector templates were then computed through the singular value decomposition of a matrix with columns populated by aligned initial event waveforms.

Event detections were declared for variance peaks that exceeded the 6σ empirically estimated noise threshold as described by *Benz et al*. [2015b]. This relatively high threshold, which minimized false detections, was adaptively adjusted hourly. The resulting list of *S*-phase arrival times was then associated into multiple-station events using an arrival time associator [*Benz et al.*, 2015a].

Seismic moment was calculated using the formula of *Hanks and Kanamori* [1979].

REFERENCES FOR APPENDIX 2

Baillard, C., W. C. Crawford, V. Ballu, C. Hibert, and A. Mangeney (2014), An automatic kurtosis-based P- and S-phase picker designed for local seismic networks, *Bull. Seismol. Soc. Am.*, 104(1), 394-409, doi:10.1785/0120120347.

Benz, H. M., C. E. Johnson, J. M. Patton, N. D. McMahon, and P. S. Earle (2015a), *GLASS 2.0: An operational, multimodal, Bayesian earthquake data association engine*, Abstract S21B-2687 presented at 2015 Fall Meeting, AGU, San Francisco, Calif.

Benz, H. M., N. D. McMahon, R. C. Aster, D. E. McNamara, and D. B. Harris (2015b), Hundreds of earthquakes per day: The 2014 Guthrie, Oklahoma, earthquake sequence, *Seismol. Res. Lett.*, 86(5), 1318-1325, doi:10.1785/0220150019.

Hanks, T. C. and H. Kanamori (1979), Moment magnitude scale, *J. Geophys. Res.*, 84(B5), 2348-50, doi:10.1029/JB084iB05p02348.

Harris, D. B. (2006), *Subspace detectors: Theory* (Rep. UCRL-TR-222758), Livermore, California: Lawrence Livermore National Laboratory.

McNamara, D. E., H. M. Benz, R. B. Herrmann, E. A. Bergman, P. Earle, A. Holland, R. Baldwin, and A. Gassner (2015), Earthquake hypocenters and focal mechanisms in central Oklahoma reveal a complex system of reactivated subsurface strike-slip faulting, *Geophys. Res. Lett.*, 42(8), 2742-2749, doi:10.1002/2014GL062730.

APPENDIX 3

SUPPLEMENTARY INFORMATION FOR CHAPTER 4 – MARIE BYRD LAND, ANTARCTICA

A3.1 INTRODUCTION

This supplementary information contains the catalog of teleseismic earthquakes $\mathbf{M}_W \geq 7.5$ that occurred 2010-2017 and were examined for triggering/modulation on station SILY (Table A3.1) as well as figures describing the dissipation of perceived seasonality above SNR = 5 (Fig. A3.1) and the lack of observed diurnal variations on SILY (Figs. A3.2 and A3.3).

A3.2 TABLE FOR APPENDIX 3

Table A3.1: Attached as separate .xlsx file. Table of all teleseismic earthquakes $\mathbf{M}_W \geq 7.5$ that occurred 2010-2017 and were examined for triggering/modulation.

A3.3 FIGURES FOR APPENDIX 3

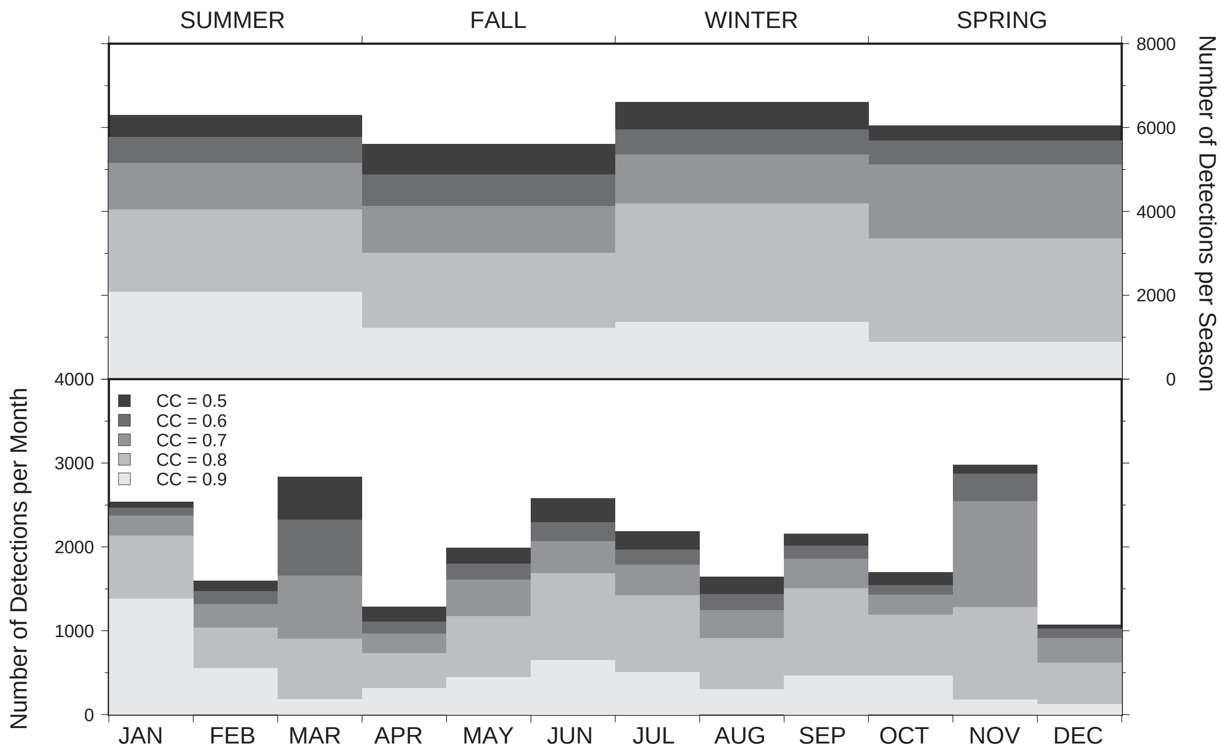

Figure A3.1. Summary of all events detected on station SILY with SNRs above 5. Displayed as the number of detections per season (top) and calendar month (bottom). Restricting catalog events to SNRs above 5 eliminates ~80% of the catalog.

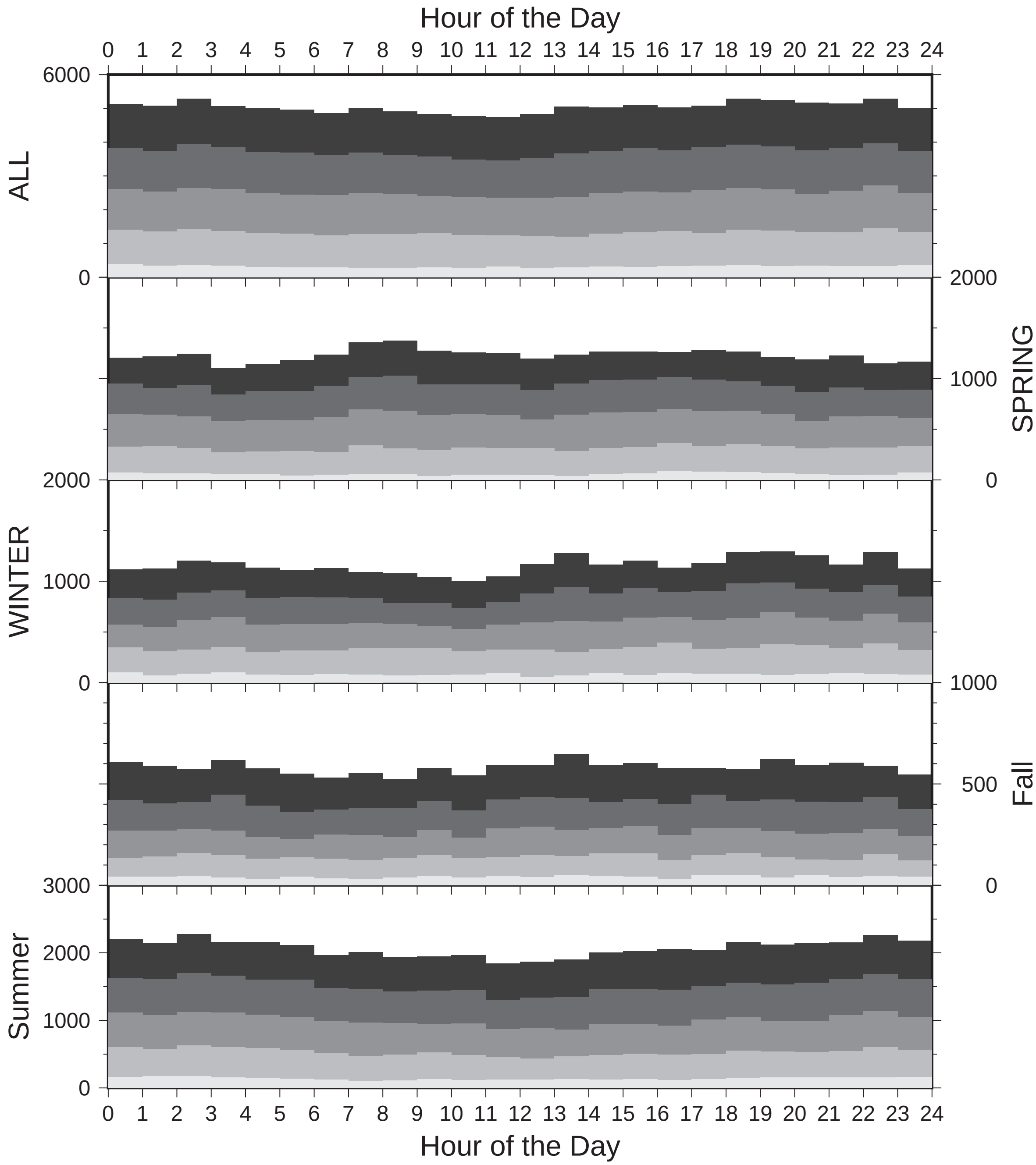

Figure A3.2. Summary of all events detected on station SILY, 2010-2017, displayed as the number of detections per hour of the day for the entire catalog (ALL; top) as well as each austral season. Colors correspond to CC thresholds shown in Figure A3.1. No strong diurnal variation is observed.

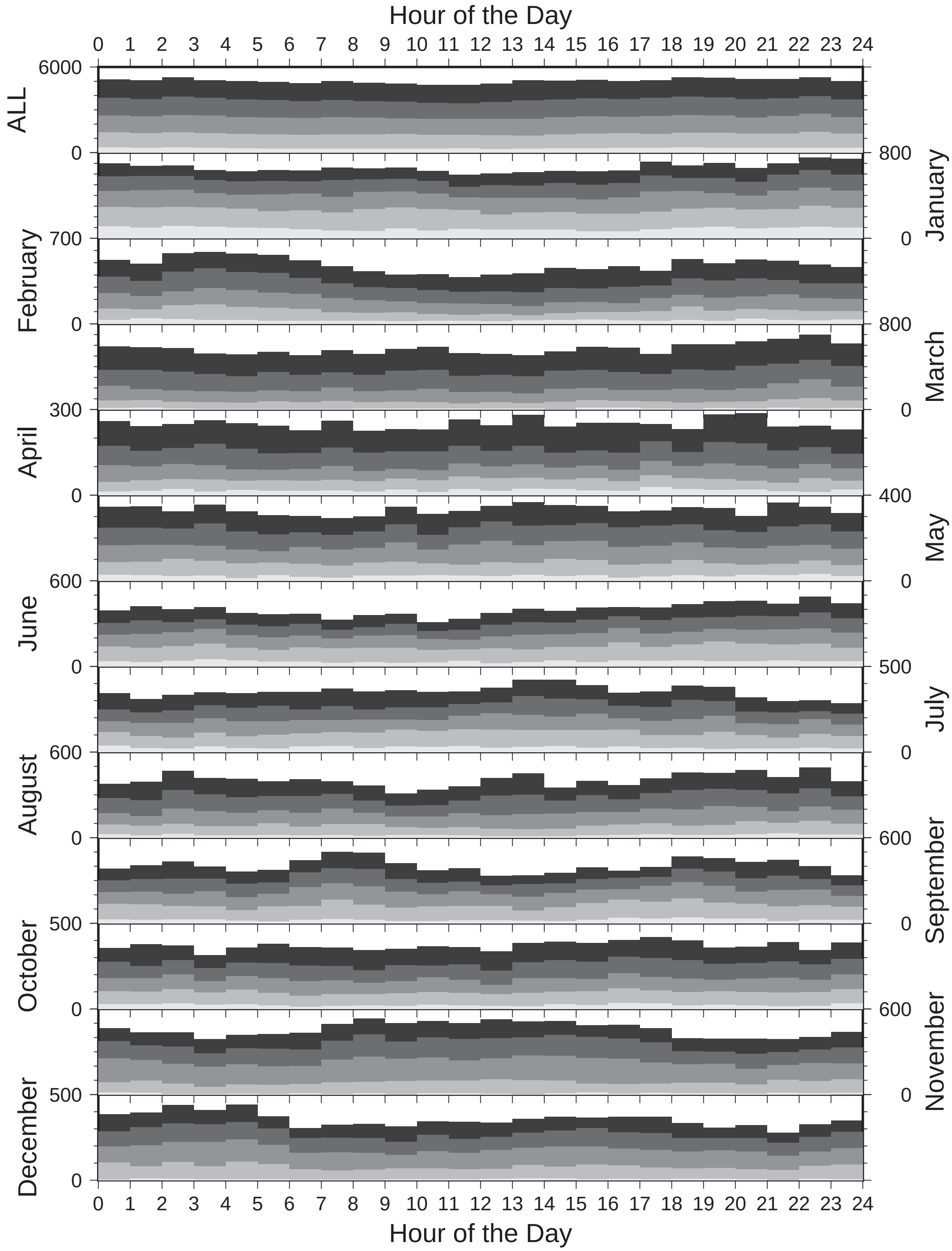

Figure A3.3. Summary of all events detected on station SILY, 2010-2017, displayed as the number of detection per hour of the day for the entire catalog (ALL; top) as well as each calendar month. Colors correspond to CC thresholds shown in Figure A3.1. No strong diurnal variation is observed.

APPENDIX 4

HUNDREDS OF EARTHQUAKES PER DAY: THE 2014 GUTHRIE, OKLAHOMA, EARTHQUAKE SEQUENCE [5]

A4.1 INTRODUCTION

A remarkable increase in seismic activity in Oklahoma since 2009 has been shown to correlate closely with enhanced hydrocarbon extraction and associated wastewater disposal; 99% of this recent Oklahoma earthquake activity has occurred within 15 km of a class II injection well [*Ellsworth*, 2013]. In response to this increase in seismic activity, the U.S. Geological Survey (USGS) partnered with the Oklahoma Geological Survey (OGS) to exchange waveform data from permanent and temporary seismic stations to improve the cataloging of earthquake source parameters for a broad region of north-central Oklahoma. For a particularly persistent earthquake sequence near Guthrie, Oklahoma, a subspace detection method is applied to data from nearby seismic stations. This approach documents the occurrence of hundreds of readily detectable, highly similar, earthquakes per day, with rates occasionally exceeding 1000 earthquakes per day. Time-varying changes in *b*-value appear episodic, suggesting a correlation with periods of reversible fault weakening and associated failure.

[5] **This appendix has been previously published:**

Benz, H. M., ***N. D. McMahon***, R. C. Aster, D. E. McNamara, and D. B. Harris (2015), Hundreds of earthquakes per day: The 2014 Guthrie, Oklahoma, earthquake sequence, *Seismol. Res. Lett.*, 86(5), 1318-1325, doi: 10.1785/0220150019.

Real-time seismic monitoring typically uses automated transient detection-based pickers to detect earthquakes and to define onset times of seismic phases. Such methods cannot reliably detect earthquake signals or time phases with low signal-to-noise, resulting in less complete earthquake catalogs than may be recovered by other means. Recognizing this limitation, recent studies of a suspected induced-seismicity sequence near Youngstown, Ohio, used waveform template matching [*Kim*, 2013; *Skoumal et al.*,2014] to significantly lower the detection threshold and to better characterize the spatiotemporal variability of seismicity. In this article, we build on these efforts using subspace detectors to objectively minimize the number of waveform templates required to fully characterize an earthquake sequence while increasing computational efficiency. Results demonstrate a new and scalable real-time procedure to better detect and characterize the rates, locations, magnitudes, and source processes of earthquake sequences of interest to the USGS National Earthquake Information Center (NEIC).

To better monitor and characterize Guthrie earthquake activity, we implemented optimal waveform detectors for a particularly active earthquake sequence, as identified by previously recorded earthquakes. What we found for the Guthrie sequence was extraordinary – hundreds of readily detectable earthquakes per day that continued throughout a seven-month study period. Using a relative amplitude master event method to estimate the magnitudes of these highly similar and nearly collocated earthquakes, temporal changes in *b*-value can be analyzed; the *b*-value is a number that describes earthquake frequency-magnitude distribution (FMD) and that provides possible physical insights into the earthquake-generation process. The correlation and detection processing was executed using NEIC acquisition systems and software processing subsystems, thus making it relatively easy to operationalize as a standard real-time procedure and to apply to other seismogenic areas of interest.

A4.2 SEISMICITY IN THE VICINITY OF GUTHRIE, OKLAHOMA

At the time of this study, the OGS operated 12 permanent broadband and short-period stations within Oklahoma, whereas the USGS and Incorporated Research Institutions for Seismology (IRIS) operated an additional three permanent broadband and strong-motion stations, as well as numerous stations in surrounding states. To augment existing USGS and OGS monitoring capabilities, the USGS and OGS coordinated the deployment of an additional 12 real-time temporary stations that provide additional coverage of fault systems that had recently become active. Two of these temporary stations, GS.OK027 and GS.OK029, were deployed to help monitor seismic activity that emerged in late 2013 and early 2014 near Guthrie and Langston, Oklahoma (Fig. A4.1).

The USGS earthquake catalog for central Oklahoma was improved using a multiple-event relocation procedure [*McNamara et al.*, 2015]. The relocated earthquakes show both well-defined clusters of seismicity and prominent linear trends of seismicity throughout the region (Fig. A4.1). Source mechanisms of the earthquakes are typically strike slip with fault planes striking either northwest-southeast or northeast-southwest and optimally oriented relative to the N85°E direction of maximum horizontal compression [*Holland*, 2013; *McNamara et al.*, 2015]. The Guthrie cluster southwest of station GS.OK029, centered at approximately 35.77° N and 97.44° W, is notable for generating a large number of earthquakes, including 79 located by the routine operations of the NEIC, with 33 events being **M** 3 or greater, and source depths ranging between 3 and 8 km. The region exhibited sustained seismic activity throughout 2014 within 5 km of two active class II disposal wells [http:// www.occpermit.com/WellBrowse/; last accessed May 2015]. Reported earthquake magnitudes in the cluster range from 2.0 to 4.0, with 10 earthquakes large enough for the NEIC to determine a regional moment tensor (RMT) solution [*Herrmann et al.*, 2011]. All ten RMT solutions are strike-slip mechanisms with one nodal plane aligning with the seismicity that is elongated in the northwest-southeast direction, suggesting earthquakes occurring on a steeply dipping, left-lateral strike-slip fault.

Station GS.OK029 (Fig. A4.1), which was installed on 15 February 2014, operates with three continuous broadband channels at 100 samples/s and three triggered strong-motion channels at 200 samples/s. This station's close proximity to the Guthrie cluster (~3.5 km from the cluster's centroid) makes it ideal for applying the subspace detector method to better characterize the size and the temporal and spatial patterns of the earthquake sequence. Station GS.OK027 (Fig. A4.1) was installed on 14 February 2014 and is configured similarly to GS.OK029. Applying the same processing to station GS.OK027 provides independent estimates of the source parameters and enables us to evaluate detector performance as a function of distance from this prolific source region.

A4.3 PROCESSING METHODS

SUBSPACE DETECTORS

Subspace detection is a powerful and adaptive tool that can improve earthquake catalogs by detecting small amplitude earthquake signals in the presence of noise within continuous data streams. This study closely follows the methodology of *Harris* [2006] and *Harris and Dodge*

[2011], in which an optimal set of subspace detectors are constructed by the singular value decomposition of a matrix with columns that represent a large set of aligned observed earthquake waveforms (which may be multichannel) previously recorded by a station of interest. The singular value spectrum provides both a direct measure of the similarity of the observed waveforms and a measure of how many orthogonal basis vectors (templates) are needed to adequately represent the observed data to a specified degree. The data space basis vectors associated with the highest-rank singular values become the set of component basis functions of a single multidimensional template that best describes the seismic sequence being evaluated. The number of basis functions (templates) needed to adequately describe seismograms from an earthquake sequence is a function of the variability of the observed waveforms, which is related to changes in source time history, source mechanism, and spatial distribution of the earthquakes.

Correlating the subspace detector templates with the observed data provides a point-by-point measure of the similarity of the detectors to the event space. In the implementation used here, the correlation is a least-squares estimate of the fit of the multidimensional (rank > 1) template (Fig. A4.2) to the observed data. For a single-rank multichannel template, the fit is equivalent to the square of the correlation coefficient with a range between 0 and 1. Detections are declared for peaks that exceed a specified threshold.

The detection threshold is determined by empirical estimates of noise. In the frequency domain, the spectral amplitude of the observed data is combined with the transformed filtered Gaussian random noise that is substituted for the phase, done on a channel-by-channel basis. The resulting empirical noise template mimics the spectral shape of each template but has randomized phase characteristics. For the Guthrie case, correlation of the empirical noise templates with the observed data shows that the histogram of the results has a Gaussian shape. In this study, detections are declared when the peak in the correlation results exceeds a 6σ threshold, which we judged to be low enough to detect most of the events above the noise floor of the sensor but high enough to minimize false detections.

Based on the similarity of RMT nodal planes and alignment of seismicity, we assume that detections within the Guthrie sequence will have a similar style of faulting. Consequently, we use the $\mathbf{M_W}$ and three-channel waveforms from a previously modeled earthquake (22 May 2014, $\mathbf{M_W}$ 3.5) as a reference for computing detection magnitudes. The detection magnitude (M) is determined by

$$M = M_{\text{ref}} + \log_{10}\left(\frac{x \cdot y}{x \cdot x}\right), \qquad \text{(A4.1)}$$

in which M_{ref} is the magnitude of the reference earthquake, $x \cdot y$ is the dot product of the multichannel waveforms for the reference earthquake (x) and the detected waveforms (y), and $x \cdot x$ is the dot product of the waveforms for the reference earthquake. Using different reference events for which we have a well-determined moment magnitude yields similar results.

ESTIMATING TIME-VARYING b-VALUE

The FMD of a population of earthquakes is commonly and successfully modeled as a power law relationship [*Ishimoto and Iida*, 1939; *Gutenberg and Richter*, 1944], such that

$$\log_{10} N = a - b\boldsymbol{M}\ , \qquad \text{(A4.2)}$$

in which N is the cumulative number of earthquakes greater than or equal to magnitude $\boldsymbol{M}$, and a and b are constants describing the activity and slope, respectively. The constant b, for a specific event population, characterizes the relative frequency of occurrence for different size events; a higher value indicates fewer large events and more small events than a lower value.

We estimate *b*-values via nonlinear parameter fitting for the parameters c and b over a specific magnitude range (M_c, M_{max}), assuming a magnitude-bounded Gutenberg-Richter law formulated as

$$N = c\ 10^{-bM}(M_c \leq \mathbf{M} \leq M_{max}). \qquad \text{(A4.3)}$$

The magnitude range was dynamically specified for each sample population of earthquakes. The minimum magnitude value M_c was estimated using the maximum curvature approach of *Wiemer and Wyss* [2000]. To combat the issue of underestimation of M_c in the case of gradually curved FMDs [*Woessner and Wiemer*, 2005] and to ensure catalog completeness, M_c was reset to include only the upper 85% of the magnitude range beyond the M_c estimated using maximum curvature. The maximum magnitude was the maximum magnitude event in each population. The magnitudes of each sample population were used to estimate a probability density function (PDF) with standard errors [*Brandon*, 1996]. A weighted least-squares nonlinear parameter estimation of c and b was then fit to the PDF estimate using a grid search, followed by refinement using the Levenberg-Marquardt method [e.g., *Aster et al.*, 2012]. The covariance matrix of the parameters was then calculated from the Jacobian of the weighted least-squares minimization function. Synthetic catalogs drawn from the Gutenberg-Richter law (equation A4.2) were generated to confirm that 95% confidence intervals on b estimated from the covariance matrix model were accurate for a range of synthetic catalog **M** and *b*-values, as well as magnitude-axis discretization. A *p*-value test was performed for each parameter determination to ensure χ^2-consistent adherence between parameter-predicted and empirical PDFs.

A4.4 RESULTS

Subspace detectors were used to detect recent earthquakes near Guthrie, Oklahoma, using the two closest seismic stations (GS.OK029 and GS.OK027). From empirical analysis of the observed waveforms recorded on station GS.OK029, a 4-16 Hz filter band was found to capture signals for the broadest range of earthquake magnitudes. For frequencies below ~4 Hz, smaller events could be filtered out, whereas above 16 Hz there was no improvement in the signal-to-noise ratio. For the 79 earthquakes used to determine an optimal set of subspace detectors, the waveforms were bandpass filtered on all three broadband channels, and each of them was aligned via cross correlation on the largest amplitude phase (*S* wave) observed on the horizontal components. A 1.4 s window starting 1.3 s before the onset of the direct *S*-wave arrival then was selected. The 1.4 s window of data includes both the *P* and complete *S* wave observed at the station. The singular value decomposition of the 79 three-component waveforms results in seven multichannel templates (orthonormal basis functions) that describe 90% of the observed event waveform data (Fig. A4.2b).

The templates are characterized by relatively low-amplitude *P*-wave phases (nodal, based on source mechanisms) and distinct *S*-wave phases on both horizontal components, making the signal generally unique. It is important to note that three-component processing is important in Oklahoma, where almost all observed earthquakes are relatively shallow and have predominantly strike-slip mechanisms of similar orientation [*McNamara et al.*, 2015]. Consequently, waveforms across the region can look similar, with relatively simple and strong *S*-wave pulses. Using a waveform that includes the nodal *P*-wave phase thus becomes an important constraint. Other source regions may have similar-looking *S*-wave pulses, but differences in the *P*-wave amplitudes and phase delays between the *P*- and *S*-wave pulses minimize detections of earthquakes from other source regions.

A 1.4-s-long multichannel template is the shortest template that contains the full *P*- and *S*-wave pulses in these data. This relatively short template length can increase the chance of false detections; however, we compensated for this using a high-detection threshold (6σ). In addition, we also reperformed the analysis using template lengths of 2.0 and 3.0 s, which include a significantly longer portion of the *S* coda. These longer templates produced results that were highly similar to those of the 1.4-s template length.

For the Guthrie cluster, variability in the observed waveforms is primarily associated with changes in source depth. Shallow earthquakes exhibit stronger dispersion of the surface waves due to the shallow low-velocity structure, whereas deeper earthquakes are typically characterized by relatively simple horizontal-component waveforms. The subspace templates also show polarity differences in the *S* wave that are likely related to changes in source mechanism or changes in spatial location along the fault zone.

Continuous correlation of the optimal detectors with station GS.OK029 from 15 February 2014 through 31 August 2014 resulted in 51,112 detections (Fig. A4.3) and a minimum magnitude of completeness of 0.1. A maximum number of detections per day of 2462 occurred on 17 February

2014, whereas the fewest number of earthquakes was 84 on 19 June 2014. The average number of detections per day was 258. None of the detected earthquakes are associated with previously reported earthquakes in other parts of Oklahoma.

All the detected waveforms recorded on the HH1 component (north-south-oriented channel) for station GS.OK029 are shown as a PDF (Fig. A4.3a) and as aligned normalized traces (Fig. A4.3b). The PDF was computed by stacking and binning trace-normalized waveforms on a point-by-point basis. Both figures show the remarkable similarity of the waveforms. The PDF also highlights that the highest probabilities are consistent with the highest-ranking templates (Fig. A4.2) and that low probabilities (less than a few percent) are primarily related to low signal-to-noise detections. The lack of significant variability in the templates indicates a relatively small active faulting region.

A summary of the detections with time (Fig. A4.4) shows that peaks in the number of detections per day generally associate with the occurrence of larger earthquakes (**M** > 3.0). Each peak in the seismicity rate exhibits two common features: (1) an increase in the number of earthquakes per day preceding the peak and (2) a rapid decay in the number of earthquakes occurring over several days following the peak. Although tectonic sequences generally follow an Omori-type exponential decay law [*Ishimoto and Iida*, 1939; *Gutenberg and Richter*, 1944] to a background rate, the Guthrie earthquakes decay only to a generally high-sustained rate of several hundred earthquakes per day with episodic pulses to higher rates.

Using the same processing procedures for the next closest station, GS.OK027, which is 16.5 km from the centroid of the earthquake cluster, we noted ~15% of the earthquakes detected on GS.OK029 with a minimum magnitude of completeness of 0.2 (Fig. A4.10.3). The temporal variations in *b*-value for station GS.OK027 are consistent with those observed for station GS.OK029.

A complication in the modeling of this earthquake sequence is the emergence of an earthquake cluster northeast of station GS.OK029 (Fig. A4.1), first documented by the occurrence of a 14 July 2014 **M** 2.5 event. The two earthquake sequences are spatially close and roughly equidistant to stations GS.OK027 and GS.OK029. Both sequences are also characterized by shallow seismicity and similar source mechanisms. Regional moment tensor solutions for events in the two clusters reveal two subparallel strike-slip faults oriented northeast-southwest (Fig. A4.1). Station GS.OK029 lies in the same part of the focal sphere for each cluster but on the opposite side of the mechanism. Consequently, subspace detectors constructed from earthquakes in the southwest cluster are likely to detect earthquakes in the northeast cluster. Using longer templates that included more of the coda was not diagnostic enough to significantly eliminate events in this second cluster. Separating the two clusters to very small magnitudes would require additional close stations that are not equidistant to the clusters. Data for the next closest stations were too intermittent to help identify when the northeast sequence began. We assume that prior to 1 June 2014 our detection results are dominated by activity within the southwest cluster, whereas after 1 June 2014 the results are a mix of activity from the two clusters.

Several studies [*Wiemer and Wyss*, 2000; *Schorlemmeret al.*, 2005; *Farrell et al.*, 2009; *Bachman et al.*, 2012] used *b*-value as a diagnostic indicator of seismogenic variability mechanisms that include changes in stress and/or thermal conditions, the presence of fluids, and variations in source zone constitutive properties (e.g., highly fractured versus competent rock). A global study of *b*-value [*Schorlemmer et al.*,2005] shows that areas of active tectonics generally exhibit a value near 1.0, whereas volcanic systems and induced-seismicity sequences are generally characterized by a *b*-value greater than 1.0. Earthquake sequences or regions characterized by high *b*-values are attributed to increased pore pressure from fluid migration or injection (i.e., magmatic or hydrothermal fluids or wastewater) that leads to fault weakening and associated increases in seismicity [*Farrell et al.*,2009; *Bachman et al.*, 2012].

The large number of earthquakes recorded per day combined with estimates of magnitude allows us to compute varying *b*-values for the sequence at high temporal resolution. Our *b*-value results show variations that range from as low as 0.5 to as high as 1.2, with an average *b*-value of 0.80 (Fig. A4.4). The calculated *b*-value for the catalog as a whole is 0.82 (Fig. A4.10.1). *Friberg et al.* [2014] suggest, in relation to hydraulic fracturing sequences, that higher *b*-values are associated with microearthquakes generated from the creation of new fractures, whereas lower *b*-values are associated with reactivation of preexisting faults. In the Guthrie sequence, we believe earthquakes are occurring along a preexisting fault in the shallow portion of the crystalline basement. We observed a sharp positive *b*-value gradient over approximately a few days to one week preceding the largest observed earthquakes, typically one magnitude unit larger than background levels. When the processing window encompasses the largest earthquake swarms, characterized by increased numbers of events per day and magnitude, *b*-value sharply drops for a few days. Following these larger earthquakes swarms, *b*-values trend gradually upward. These results suggest that variations in *b*-value are a direct measure of the changes of stress to the fault systems. If the subspace detector fails to detect events outside the predefined cluster, the trends seen before and after larger earthquakes will likely not change.

In the absence of information on the wastewater injection volumes and rates at the nearby disposal wells, we must speculate on the details of how injected wastewater may act to weaken faults via an increase in pore pressure. The results here show that the Guthrie sequence is atypical of tectonically controlled earthquake sequences where one would expect the rate and magnitude of earthquakes to decline with time after larger events. High sustained rates of seismicity and highly variable *b*-values over short time durations suggest that wastewater injection is a contributing factor in controlling the sustained seismicity in this area; and, as such, we can construct a hypothesis to explain our observations.

Our observations of progressive time-varying *b*-value variations suggest that fluid migration in the fault zone decreases the fault-normal stresses (i.e., increasing the seismogenic potential of the deviatoric stresses) on the fault [*Raleigh et al.*, 1976; *Nicholson and Wesson*, 1990]. This weakening process manifests itself as an increase in small earthquakes (higher *b*-value). This process continues to the point of critical failure where a larger patch of the fault system is able to slip in a series of larger earthquakes (**M** > 3). The larger earthquakes effectively strengthen the fault by eliminating the fluid pathways, resulting in a resetting of the system to higher normal stresses that inhibit earthquakes. The cycle repeats itself as migrating fluids reestablish pathways along the fault system and again decrease effective stress. For this to be sustained, the associated cumulative stress drops must be partial (significantly less than the available deviatoric stress) so that deviatoric stress remains to drive ongoing activity.

This article documents a novel approach for detailed characterization of spatiotemporal variations in clustered seismicity using a single station. The FMDs in seismicity are easily quantified from time-varying estimates of *b*-value, variations of which provide insight into possible mechanisms for earthquake generation in the presence of fluids.

A4.5 CONCLUSIONS

This study demonstrates that an optimal set of subspace detectors is effective at targeting and characterizing occurrence and magnitude of earthquake sequences of interest and, when combined with observations of time-varying *b*-values, provides possible insight into time-varying fault behavior and seismicity forecasting. The USGS catalog of earthquake source parameters for Oklahoma is sufficient to design optimal sets of waveform templates, both retrospectively and in real time, which can vastly improve monitoring of numerous earthquake sequences that have developed throughout Oklahoma in recent years [*McNamara et al.*, 2015].

A4.6 DATA AND RESOURCES

The waveform data used in this study can be obtained from the Incorporated Research Institutions for Seismology (IRIS) Data Management Center [http://www.iris.edu/; last accessed December 2015]. Earthquake source parameters and phase data used to construct optimal waveform templates were obtained from U.S. Geological Survey recent earthquake web pages (http://earthquake.usgs.gov/earthquake/search/; last accessed December 2014). Estimated origin times and magnitudes for detected earthquakes in this study can be found in the electronic supplement (see Data Set A4.10.1). Class II injection well information was obtained from the Oklahoma Corporation Commission electronic well database [http://www.occpermit.com/WellBrowse/; last accessed May 2015] and oil and gas data files [http://www.occeweb.com/og/ogdatafiles2.htm; last accessed May 2015]. Some figures were created using the Generic Mapping Tools software of *Wessel et al.* [2013].

A4.7 ACKNOWLEDGEMENTS

This research was supported by the U.S. Geological Survey (USGS) National Earthquake Hazards Reduction Program. Kevin Furlong, Paul Earle, Rob Williams, and Oliver Boyd of the USGS, Michael Brudzinski, and two anonymous reviewers provided thoughtful comments that improved this article. We thank J. Slate and J. McCarthy for editorial reviews. The authors greatly appreciate the hard work of the people who responded to the evolving earthquake sequence. Any use of trade, product, or firm names is for descriptive purposes only and does not imply endorsement by the U.S. Government.

A4.8 Figures for Appendix 4

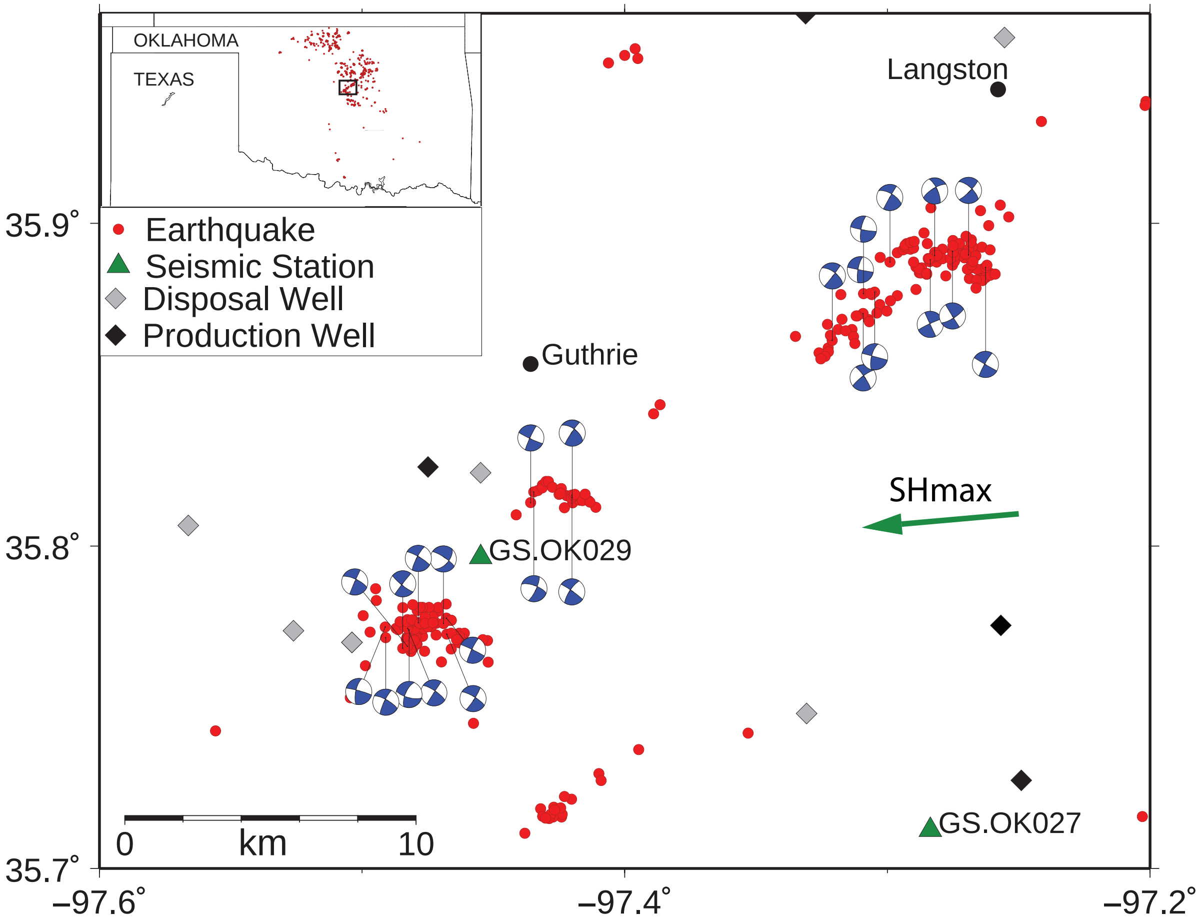

Figure A4.1. Location map of features near the Guthrie, Oklahoma, study site. The red dots show the distribution of earthquakes near Guthrie and Langston, Oklahoma, whereas the green triangles show the two closest seismic stations. The regional moment tensor solutions for the largest earthquakes in the various earthquake sequences and the active class II injection wells in the vicinity (gray and black diamonds) are also shown. The green arrow indicates the direction of maximum horizontal compression at N85°E. The inset map shows the study area within the Oklahoma region and seismicity from February 2014 through August 2014. Well information is available in Table A4.10.1.

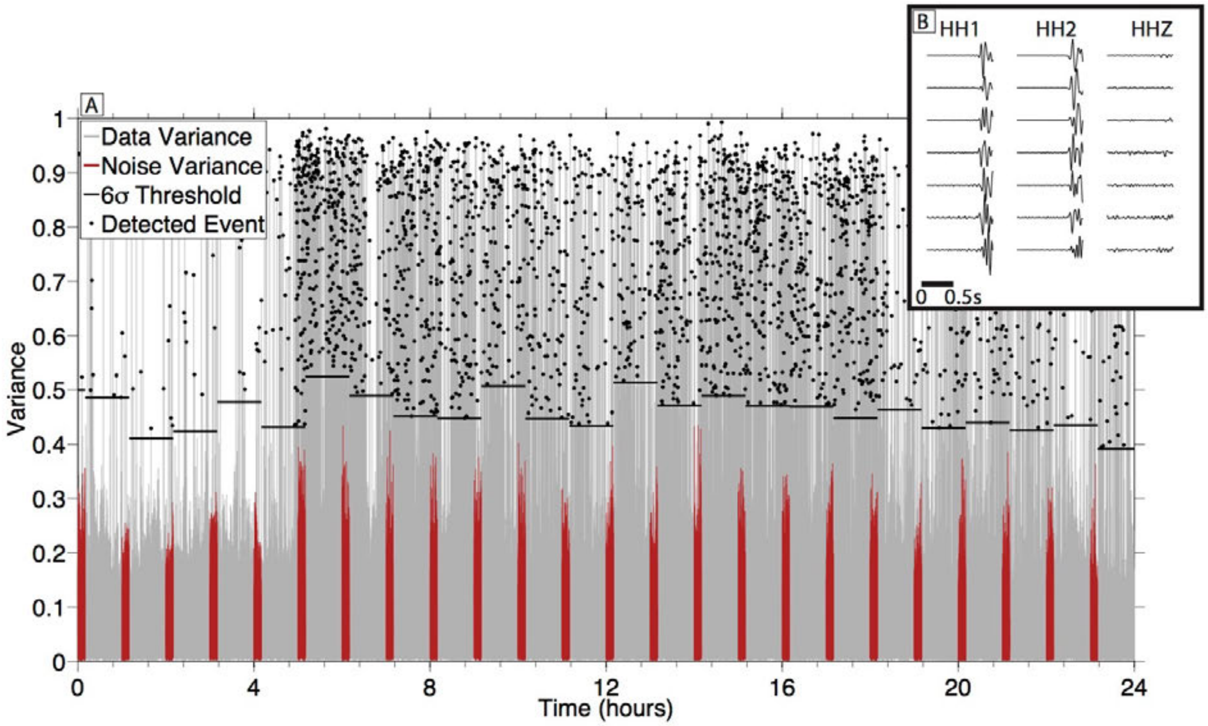

Figure A4.2. Station GS.OK029 subspace cross-correlation results for 17 February 2014. The light gray shows the variance of the cross correlation between the templates and continuous three-component data for station GS.OK029, and the red shows the variance using empirical noise templates to estimate the noise floor of the cross correlation. The horizontal black lines indicate the 6σ threshold above which peaks are considered as event detections. The small black circles show the location and value of the detection peaks. (Inset) The template set through rank 7 filtered in the 4–16 Hz frequency band, with the rank decreasing from top to bottom.

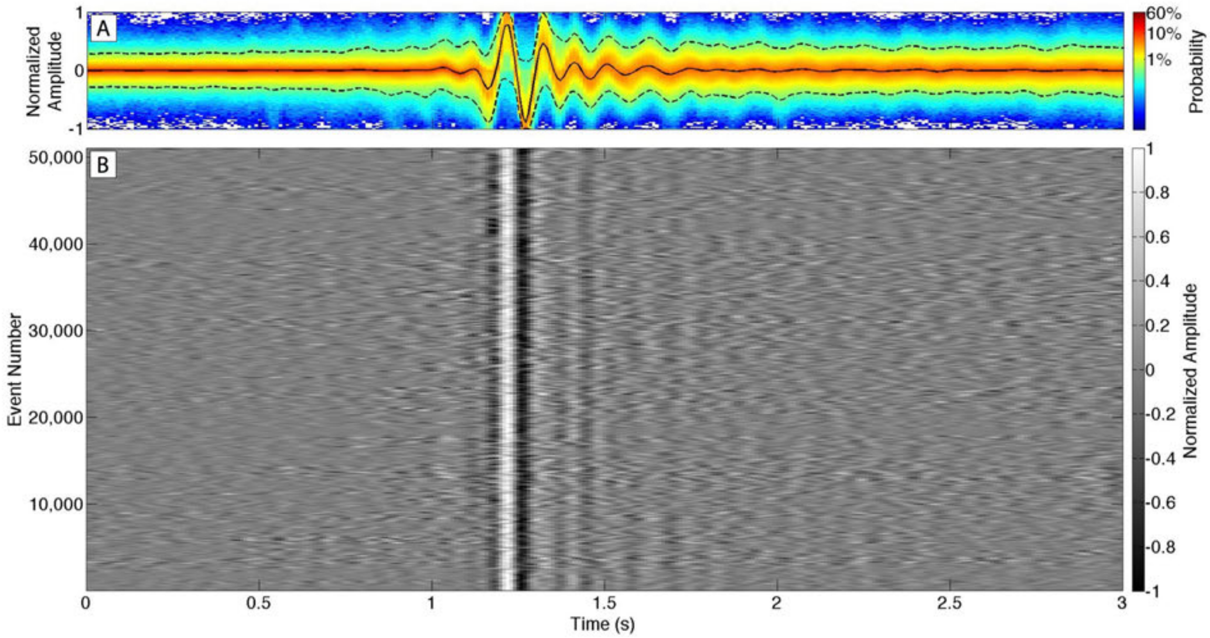

Figure A4.3. All detected waveforms observed on the horizontal channel HH1 (component oriented north-south) for station GS.OK029: (a) the probability density function stack was computed by trace-normalizing the detection waveforms and binning them as a probability on a point-by-point basis. The solid black line shows the median waveform, and the dashed lines show the $\pm 3\sigma$ envelope of the distribution. (b) Aligned waveforms of all 51,112 detections shaded by normalized amplitude.

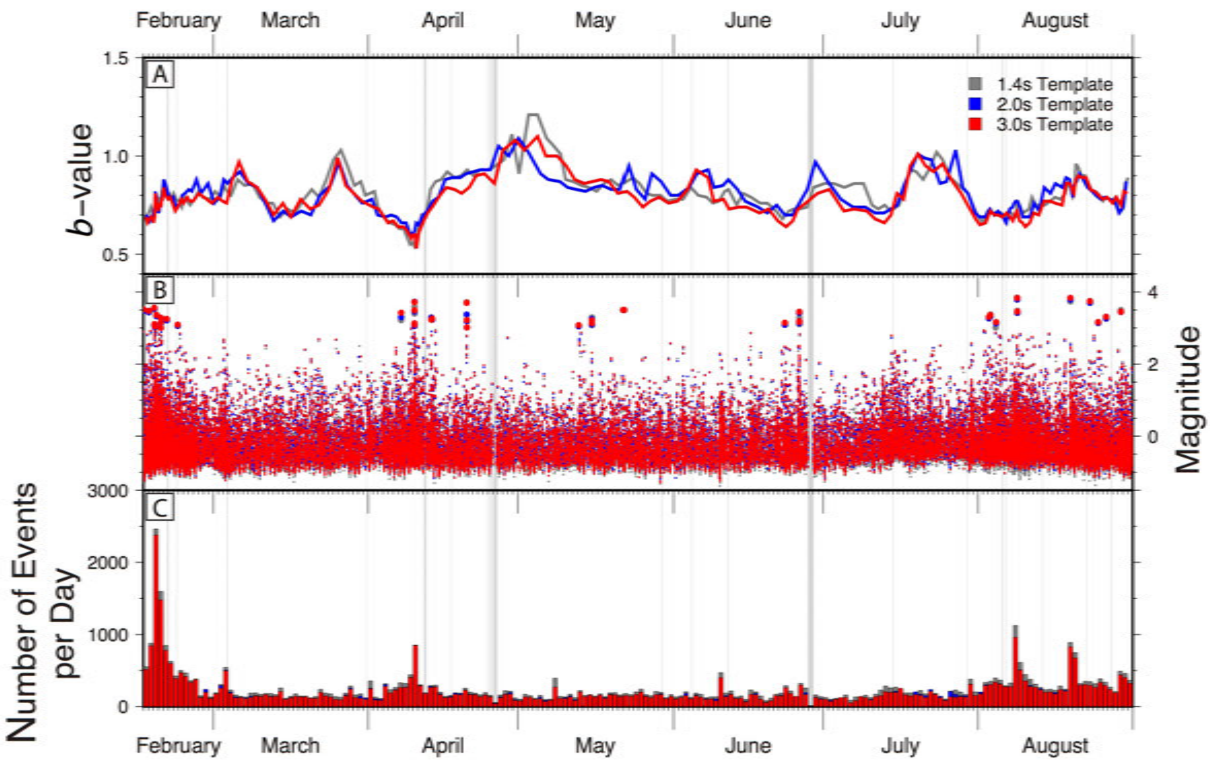

Figure A4.4. Detector summary as a function of time for data from station GS.OK029. All three figures display results using template lengths of 1.4 s (dark gray), 2.0 s (blue), and 3.0 s (red). (a) The time-varying *b*-value is estimated using a sliding window of 500 earthquakes; (b) detection magnitudes, larger dots indicating events larger than **M** 3.0; and (c) number of detections per day. The light gray vertical lines show time periods without data. The black arrows indicate the sharp positive *b*-value gradients that preceded larger earthquakes (**M** 3 or larger). The *b*-value decreases as the processing window encompasses the larger earthquakes and trends toward the background rate as the larger earthquakes slide out of the window. Note that all three template lengths show similar detection numbers, magnitudes, and *b*-value trends, indicating that results are not strongly affected by template length.

REFERENCES FOR APPENDIX 4

Aster, R., B. Borchers, and C. Thurber (2012), *Parameter Estimation and Inverse Problems* (Ed. 2), Amsterdam: Elsevier.

Bachman, C. E., S. Wiemer, B. P. Goertz-Allmann, and J. Woessner (2012), Influence of pore-pressure on the event-size distribution of induced earthquake, *Geophys. Res. Lett.*, 39(9), L09302, doi: 10.1029/2012GL051480.

Brandon, M. (1996), Probability density plot for fission-track grain-age samples, *Radiat. Meas.*, 26(5), 663-676, doi: 10.1016/S1350-4487(97)82880-6.

Ellsworth, W. L. (2013), Injection-induced earthquakes, *Science*, 341(6142), 1225942, doi: 10.1126/science.1225942.

Farrell, J., S. Husen, and R. B. Smith (2009), Earthquake swarm and *b*-value characterization of the Yellowstone volcanic-tectonic system, *J. Volcanol. Geotherm. Res.*, 188(1-3), 260-276, doi: 10.1016/j.jvolgeores.2009.08.008.

Friberg, P., G. Besana-Ostman, and I. Dricker (2014), Characterization of an earthquake sequence triggered by hydraulic fracturing in Harrison County, Ohio, *Seismol. Res. Lett.*, 85(6), 1295-1307, doi: 10.1785/0220140127.

Gutenberg, B., and C. F. Richter (1944), Frequency of earthquakes in California, *Bull. Seismol. Soc. Am.*, 34(4), 185-188.

Harris, D. B. (2006), *Subspace detectors: Theory* (Rep. UCRL-TR-222758), Livermore, California: Lawrence Livermore National Laboratory.

Harris, D. B., and D. A. Dodge (2011), An autonomous system for grouping events in a developing aftershock sequence, *Bull. Seismol. Soc. Am.*, 101(2), 763-774, doi:10.1785/0120100103.

Herrmann, R. B., H. Benz, and C. J. Ammon (2011), Monitoring the earthquake source process in North America, *Bull. Seismol. Soc. Am.*, 101(6), 2609-2625, doi: 10.1785/0120110095.

Holland, A. (2013), Optimal fault orientations within Oklahoma, *Seismol. Res. Lett.*, 84(5), 876-890, doi: 10.1785/0220120153.

Ishimoto, M., and K. Iida (1939), Observations sur les seisms euregistre par le microseisograph construite derniement (I), *Bull. Earthq. Res. Inst.*, 17, 443-478 (in French).

Kim, W. (2013), Induced seismicity associated with fluid injection into a deep well in Youngstown, Ohio, *J. Geophys. Res.*, 118(7), 3506-3518, doi: 10.1002/jgrb.50247.

McNamara, D. E., H. M. Benz, R. B. Herrmann, E. A. Bergman, P. Earle, A. Holland, R. Baldwin, and A. Gassner (2015), Earthquake hypocenters and focal mechanisms in central Oklahoma reveal a complex system of reactivated subsurface strike-slip faulting, *Geophys. Res. Lett.*, 42(8), 2742-2749, doi: 10.1002/2014GL062730.

Nicholson, C. and R. L. Wesson (1990), Earthquake hazard associated with deep well injection – A report to the U.S. Environmental Protection Agency, *U.S. Geol. Surv. Bull.*, 1951, doi: 10.3133/b1951.

Raleigh, C. B., J. H. Healy, and J. D. Bredehoeft (1976), An experiment in earthquake control at Rangely, Colorado, *Science*, 191(4233), 1230-1237, doi: 10.1126/science.191.4233.1230.

Schorlemmer, D., S. Wiemer, and M. Wyss (2005), Variations in earthquake-size distribution across different stress regimes, *Nature*, 437, 539-542, doi: 10.1038/nature04094.

Skoumal, R. J., M. R. Brudzinski, B. S. Currie, and J. Levy (2014), Optimizing multi-station earthquake template matching through re-examination of the Youngstown, Ohio, sequence, *Earth Planet Sc. Lett.*, 405, 274-280, doi: 10.1016/j.epsl.2014.08.033.

Wessel, P., W. H. F. Smith, R. Scharroo, J. Luis, and F. Wobbe (2013), Generic Mapping Tools: Improved version released, *Eos. Trans. AGU*, 94(45), 409-410, doi:10.1002/2013EO450001.

Wiemer, S., and M. Wyss (2000), Minimum magnitude of complete reporting in earthquake catalogs: Examples from Alaska, the western United States, and Japan, *Bull. Seismol. Soc. Am.,* 90(4), 859-869, doi: 10.1785/0119990114.

Woessner, J., and S. Wiemer (2005), Assessing the quality of earthquake catalogs: Estimating the magnitude of completeness and its uncertainty, *Bull. Seismol. Soc. Am.*, 95(2), 684-698, doi: 10.1785/0120040007.

A4.9 Supplementary Information for Appendix 4

Introduction

These supplementary figures show details about the parameters used in the estimations of the magnitude of completeness M_C and *b*-values, as well as the subspace detector results for an additional station, GS.OK027. Data Set A4.10.1 contains the catalog of events detected on station GS.OK029. Table A4.10.1 contains production and disposal information for the wells shown in Figure A4.1.

Table for Section A4.10

Table A4.10.1: Production and disposal data for the American Petroleum Institute (API) wells active in 2013 that are displayed in Figure A4.1 of the main text. Well class abbreviations: 2DNC, noncommercial disposal well; 2DCm, commercial disposal well; 2R/2RIn, enhanced recovery production well; 2RSI, enhanced recovery production well with simultaneous injection and disposal. Information was gathered from the Oklahoma Corporation Commission's oil and gas data files and electronic well database.

Well Function	API Well Number	Latitude (°)	Longitude (°)	Completion Date (mm/dd/yyyy)	Depth (km)	Well Class	Injected Fluid in 2013 (barrels)	Distance from Cluster Centroid (km)
Production	3508300368	35.775397	-97.25679	05/15/2008	1.80	2RSI	4320	19.88
	3508102778	35.964859	-97.33116	05/25/1951	1.00	2R	52994	24.92
	3508102784	35.824537	-97.47492	02/15/1951	0.99	2RIn	72807	5.57
	3508103749	35.727353	-97.249	02/20/1951	1.08	2RIn	15200	21.24
Disposal	3508320498	35.822723	-97.45489	04/3/1981	1.85	2DNC	75652	5.73
	3508322080	35.7481	-97.33078	07/16/1992	1.82	2DCm	1130	13.53
	*3508323254	35.770143	-97.50385	08/30/1994	2.04	2DNC	180358	2.46
	*3508323286	35.773762	-97.52611	07/7/1995	1.86	2DNC	69257	4.42
	3508323389	35.806374	-97.56617	04/27/1998	2.13	2DCm	108322	8.78
	3508335988	35.957502	-97.2554	12/27/1950	1.43	2DNC	18460	28.52

* Two closest class II injection wells located just west of cluster centroid

FIGURES FOR SECTION A4.10

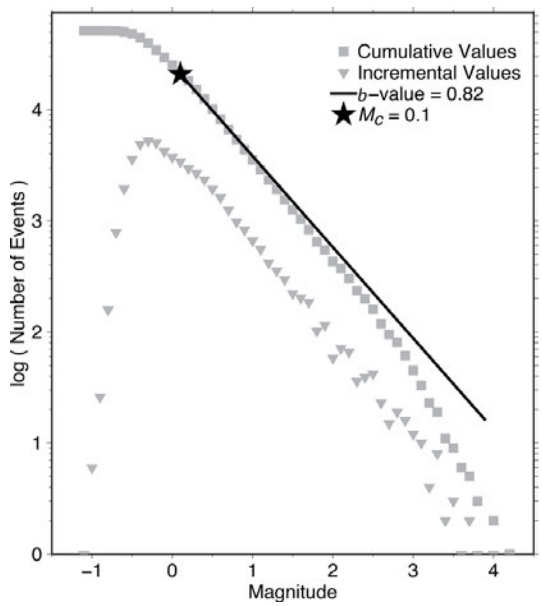

Figure A4.10.1. Gutenberg-Richter magnitude plot of the entire catalog (51,112 events in total) for the Guthrie cluster on station GS.OK029 with magnitude bins of 0.1. The estimated M_C (0.1) and *b*-value (0.82), calculated using methodologies described in Section A4.3, are plotted as a black start and black line, respectively.

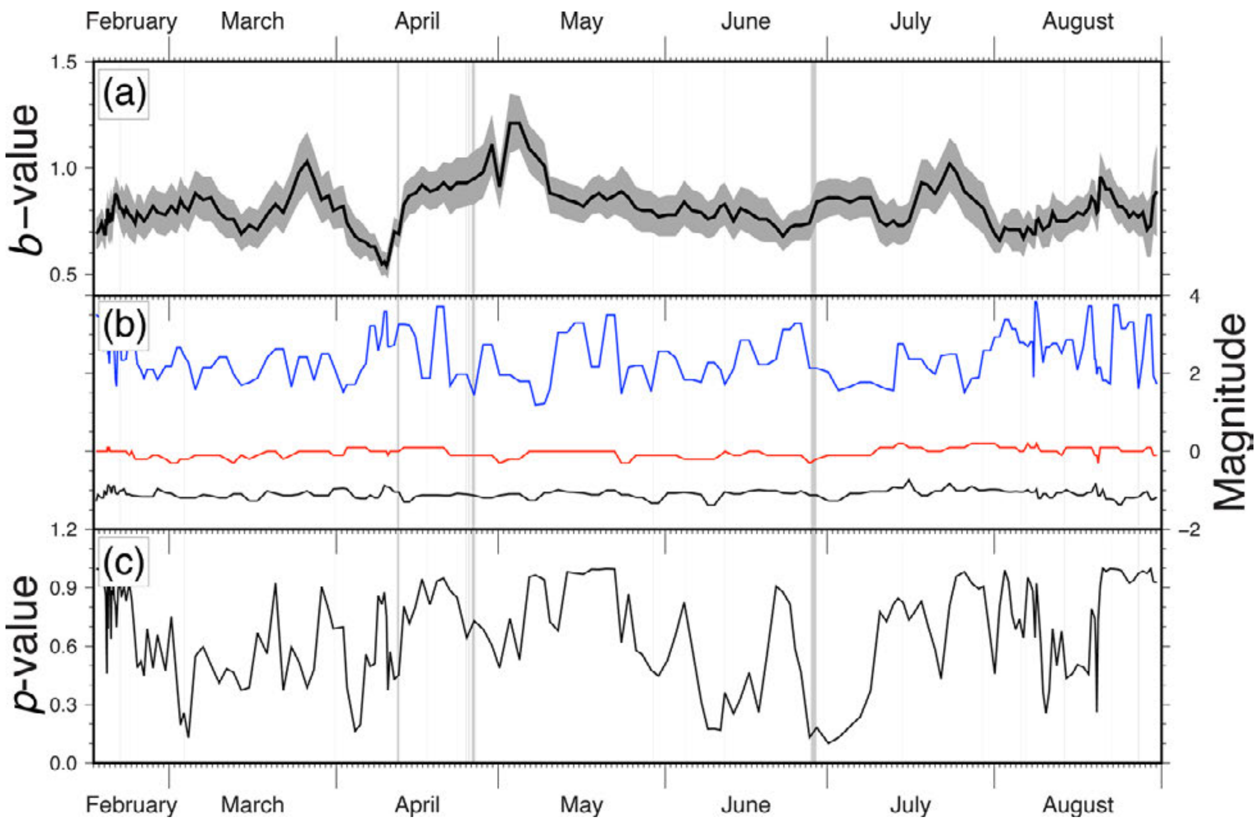

Figure A4.10.2. Summary of values used in and resultant from *b*-value calculations as a function of time for station GS.OK029: (a) the time-varying *b*-value using a sliding window of 500 earthquakes for each subcatalog (same as the dark gray line in Fig. A4.4), with the dark gray background indicating 95% confidence level; (b) the magnitude extremes in each *b*-value calculation (black, minimum magnitude in subcatalog; red, minimum M_C in subcatalog; blue, maximum magnitude in sub-catalog); and (c) the *p*-value statistic for each subcatalog [e.g., *Aster et al.,* 2012], a measure of how likely the observed data are to be produced from a random distribution produced with the predicted *b*-value and Gutenberg-Richter statistics.

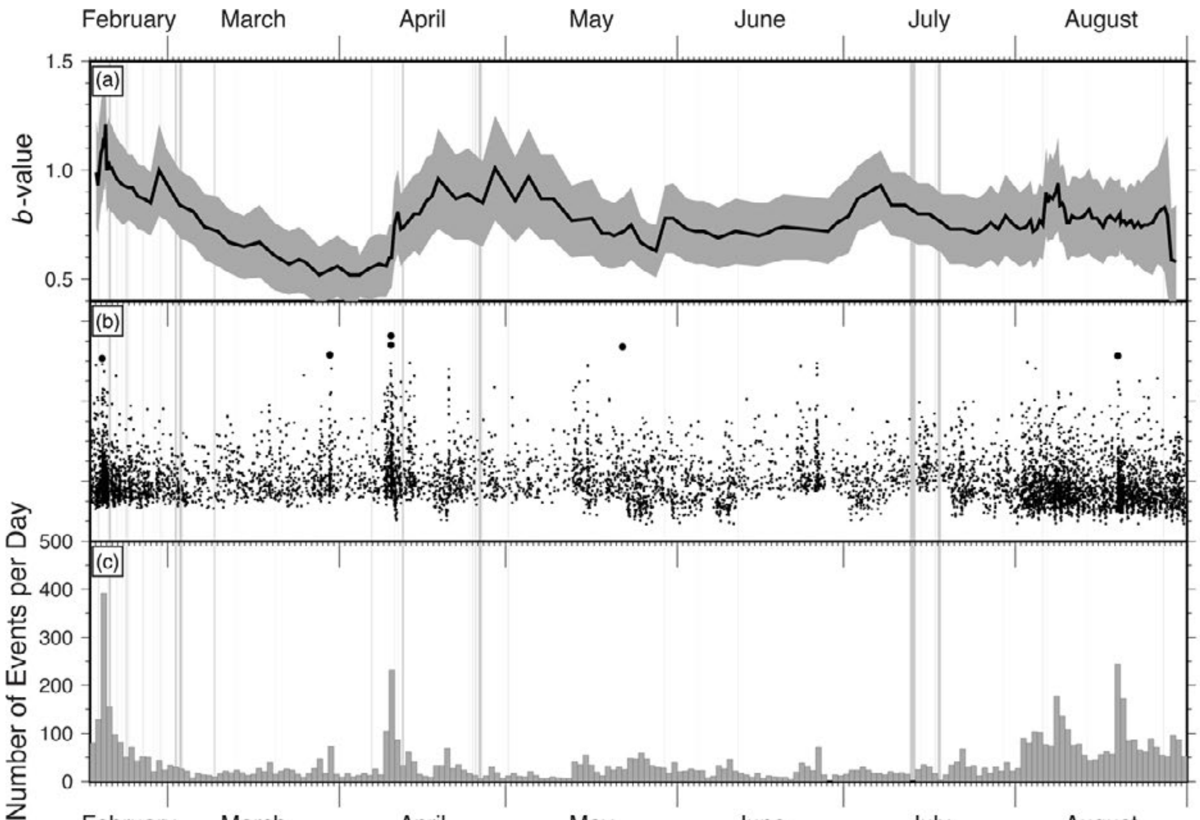

Figure A4.10.3. Detector summary as a function of time for station GS.OK027, located 16.5 km from the centroid of the Guthrie cluster using a template length of 3.5 s: (a) the time-varying *b*-value using a sliding window of 250 earthquakes, with the dark gray background indicating the 95% confidence interval; (b) the detection magnitudes (larger dots indicate events larger than magnitude 3.0); and (c) the number of detections per day. The light gray vertical lines show time periods without data. Approximately 15% of the events detected on station GS.OK029 were detected on station GS.OK027. All three panels show similar trends to those seen at station GS.OK029 (see Fig. A4.10.2).

DATA SET FOR SECTION A4.10

Data Set A4.10.1: Attached as separate .csv file. Catalog of the 51,112 events detected in the Guthrie cluster on station GS.OK029. Columns are event date (yyyy/mm/dd), estimated origin time (HH:MM:SS.FF), computed magnitude, and detector variance.

REFERENCES FOR SECTION A4.10

Aster, R., B. Borchers, and C. Thurber (2012), *Parameter Estimation and Inverse Problems* (Ed. 2), Amsterdam: Elsevier.

Oklahoma Corporation Commission, Oklahoma Corporation Commission's Well Data System (electronic well database), accessed May 2015, http://www.occpermit.com/WellBrowse/.

Oklahoma Corporation Commission, Oil and Gas Data Files, accessed May 2015, http://www.occeweb.com/og/ogdatafiles2.htm.